UNIVERSITÉ DE SHERBROOKE
Faculté de génie
Département de génie mécanique

DÉVELOPPEMENT DE RÉCUPÉRATEURS D'ÉNERGIE VIBRATOIRE PAR PIÉZOÉLECTRICITÉ AVEC MASSE SISMIQUE EN TUNGSTÈNE INTÉGRÉE AU NIVEAU DE LA TRANCHE POUR L'ALIMENTATION DE CAPTEURS SANS-FIL AUTONOMES ULTRA-FAIBLE PUISSANCE.

DEVELOPMENT OF MEMS PIEZOELECTRIC VIBRATION ENERGY HARVESTERS WITH WAFER-LEVEL INTEGRATED TUNGSTEN PROOF-MASS FOR ULTRA LOW POWER AUTONOMOUS WIRELESS SENSORS.

Thèse de doctorat
Specialité: génie mécanique

André DOMPIERRE

Sherbrooke (Québec) Canada

Février 2019

JURY MEMBERS

Luc FRÉCHETTE

Supervisor

Srikar VENGALLATORE

Co-supervisor

Patrice MASSON

Examiner

Serge CHARLEBOIS

Examiner

Shad ROUNDY

Examiner

RÉSUMÉ

La génération d'énergie localisée et à petite échelle, par transformation de l'énergie vibratoire disponible dans l'environnement, est une solution attrayante pour améliorer l'autonomie de certains noeuds de capteurs sans-fil pour l'Internet des objets (IoT). Grâce à des microdispositifs inertiels résonants piézoélectriques, il est possible de transformer l'énergie mécanique en électricité. Cette thèse présente une étude exhaustive de cette technologie et propose un procédé pour fabriquer des microgénérateurs MEMS offrant des performances surpassant l'état de l'art.

On présente d'abord une revue complète des limites physiques et technologiques pour identifier le meilleur chemin d'amélioration. En évaluant les approches proposées dans la littérature (géométrie, architecture, matériaux, circuits, etc.), nous suggérons des métriques pour comparer l'état de l'art. Ces analyses démontrent que la limite fondamentale est l'énergie absorbée par le dispositif, car plusieurs des solutions existantes répondent déjà aux autres limites. Pour un générateur linéaire résonant, l'absorption d'énergie dépend donc des vibrations disponibles, mais aussi de la masse du dispositif et de son facteur de qualité.

Pour orienter la conception de prototypes, nous avons réalisé une étude sur le potentiel des capteurs autonomes dans une automobile. Nous avons évalué une liste des capteurs présents sur un véhicule pour leur compatibilité avec cette technologie. Nos mesures de vibrations sur un véhicule en marche aux emplacements retenus révèlent que l'énergie disponible pour un dispositif linéaire résonant MEMS se situe entre 30 à 150 Hz. Celui-ci pourrait produire autour de 1 à 10 µW par gramme. Pour limiter la taille d'un générateur MEMS pouvant produire 10 µW, il faut une densité supérieure à celle du silicium, ce qui motive l'intégration du tungstène.

L'effet du tungstène sur la sensibilité du dispositif est évident, mais nous démontrons également que l'usage de ce matériau permet de réduire l'impact de l'amortissement fluidique sur le facteur de qualité mécanique Q_{m}. En fait, lorsque l'amortissement fluidique domine, ce changement peut améliorer Q_{m} d'un ordre de grandeur, passant de 10^3 à 10^4 dans l'air ambiant. Par conséquent, le rendement du dispositif est amélioré sans utiliser un boîtier sous vide.

Nous proposons ensuite un procédé de fabrication qui intègre au niveau de la tranche des masses de tungstène de 500 µm d'épais. Ce procédé utilise des approches de collage de tranches et de gravure humide du métal en deux étapes. Nous présentons chaque bloc de fabrication réalisé pour démontrer la faisabilité du procédé, lequel a permis de fabriquer plusieurs prototypes. Ces dispositifs ont été testés en laboratoire, certains démontrant des performances records en terme de densité de puissance normalisée. Notre meilleur design se démarque par une métrique de 2.5 $\mathrm{mW\text{-}s^{-1}/(mm^3(m/s^2)^2)}$, soit le meilleur résultat répertorié dans l'état de l'art. Avec un volume de 3.5 $\mathrm{mm^3}$, il opère à 552.7 Hz et produit 2.7 µW à 1.6 V RMS à partir d'une accélération de 1 $\mathrm{m/s^2}$. Ces résultats démontrent que l'intégration du tungstène dans les microgénérateurs MEMS est très avantageuse et permet de s'approcher davantage des requis des applications réelles.

Mots-clés : piézoélectricité, capteur sans-fil autonome, récupération d'énergie vibratoire, microsystème électromécanique, intégration au niveau de la tranche, microfabrication

ABSTRACT

Small scale and localized power generation, using vibration energy harvesting, is considered as an attractive solution to enhance the autonomy of some wireless sensor nodes used in the Internet of Things (IoT). Conversion of the ambient mechanical energy into electricity is most often done through inertial resonant piezoelectric microdevices. This thesis presents an extensive study of this technology and proposes a process to fabricate MEMS microgenerators with record performances compared to the state of the art.

We first present a complete review of the physical and technological limits of this technology to asses the best path of improvement. Reported approaches (geometries, architectures, materials, circuits) are evaluated and figures of merit are proposed to compare the state of the art. These analyses show that the fundamental limit is the absorbed energy, as most proposals to date partially address the other limits. The absorbed energy depends on the level of vibrations available, but also on the mass of the device and its quality factor for a linear resonant generator.

To guide design of prototypes, we conducted a study on the potential of autonomous sensors in vehicles. A survey of sensors present on a car was realized to estimate their compatibility with energy harvesting technologies. Vibration measurements done on a running vehicle at relevant locations showed that the energy available for MEMS devices is mostly located in a frequency range of 30 to 150 Hz and could generate power in the range of 1-10 µW per gram from a linear resonator. To limit the size of a MEMS generator capable of producing 10 µW, a higher mass density compared to silicon is needed, which motivates the development of a process that incorporates tungsten.

Although the effect of tungsten on the device sensitivity is well known, we also demonstrate that it reduces the impact of the fluidic damping on the mechanical quality factor Q_{m}. If fluidic damping is dominant, switching to tungsten can improve Q_{m} by an order of magnitude, going from 10^3 to 10^4 in ambient air. As a result, the device efficiency is improved despite the lack of a vacuum package.

We then propose a fabrication process flow to integrate 500 µm thick tungsten masses at the wafer level. This process combines wafer bonding with a 2-step wet metal etching approach. We present each of the fabrication nodes realized to demonstrate the feasibility of the process, which led to the fabrication of several prototypes. These devices are tested in the lab, with some designs demonstrating record breaking performances in term of normalized power density. Our best design is noteworthy for its figure of merit that is around 2.5 mW-s^{-1}/(mm^3(m/s^2)^2), which is the best reported in the state of the art. With a volume of 3.5 mm^3, it operates at 552.7 Hz and produces 2.7 µW at 1.6 V RMS from an acceleration of 1 m/s^2. These results therefore show that tungsten integration in MEMS microgenerators is very advantageous, allowing to reduce the gap with needs of current applications.

Keywords: piezoelectricity, autonomous wireless sensor, vibration energy harvesting, microelectromechanical system, wafer-level integration, microfabrication

REMERCIEMENTS

Je tiens d'abord à remercier mon directeur de recherche, Luc Fréchette, pour son soutien et sa confiance au cours des nombreuses années. J'ai eu la chance de le côtoyer pendant presque 10 ans et je considère avoir grandi immensément durant ce temps. Il a été un véritable mentor pour moi et a sans nul doute façonné ma manière d'approcher non seulement la recherche, mais les nouveaux défis en général. Dans les moments ou l'ampleur de la tâche me semblait insurmontable, ses paroles souvent rassurantes, positives, mais réalistes m'ont permis de garder la confiance nécessaire pour aller jusqu'au bout. Sa curiosité intellectuelle et sa confiance inébranlable sont une inspiration.

I would also like to thank my co-supervisor, Srikar Vengallatore, which has also been very supportive over these several years and has always provided insightful feedback on my work. Although he was not involved to the same extent as professor Frechette, he was always available and quick to respond to my interrogations when needed. Everytime I asked for his helped on something, he was willing to help and for that, I am very grateful.

I also want to thank the members of the jury, composed of Serge Charlebois, Patrice Masson and Shad Roundy, for accepting to read and evaluate this thesis. I consider it an honor to be evaluated by these highly successful researchers./Je tiens aussi à remercier les membres de mon jury, c'est-à-dire Serge Charlebois, Patrice Masson et Shad Roundy, qui ont accepté de lire et d'évaluer cette thèse. Ce sont des chercheurs chevronnés et c'est pour moi un honneur de recevoir leur avis sur ces travaux.

J'aimerais ensuite remercier le personnel du 3IT, plus spécifiquement le personnel du LCP et du LNN, sans qui il aurait été impossible de compléter ces travaux. J'ai aussi pu compter sur l'aide de plusieurs étudiants du groupe Micros pour mener à termes la fabrication et les tests réalisés dans cette thèse. Je veux donc remercier spécialement Étienne Léveillé, Mohamed Traore, Olivier Marconot et Amrid Amnache. J'ai aussi pu partager plusieurs moments de camaraderies sincères avec plusieurs autres étudiants du groupe Micros que j'ai côtoyés au fil des ans. Je me considère donc chanceux d'avoir pu former des amitiés franches avec plusieurs d'entre eux.

Je veux également remercier mes amis Simon Hamel et Évelyne Carbonneau, car ils m'ont apportés un support moral inestimable au travers d'étapes difficiles vécues au cours de ce projet. Je remiercie également de tout mon coeur mes parents, Gérald et Ginette, qui m'ont soutenu et encouragé de manière inconditionnelle durant tout ce temps. Ils n'ont jamais arrêté de croire en moi, même dans les moments où la motivation se faisait rare, et pour cela je tiens à leur exprimer mon appréciation et mon amour sincère.

TABLE OF CONTENTS

LIST OF FIGURES

LIST OF TABLES

LIST OF SYMBOLS

a	Acceleration (time signal)
A	Acceleration phasor
α	Dimensionless resistance (or time constant)
b	Beam width
β	Dimensionless inductance
β_{D}	Area normalized drag damping coefficient of cantilever
C_{D}	Lumped fluid drag coefficient
C_{m}	Lumped mechanical damping coefficient (SDOF)
C_{el}	Lumped electrical damping coefficient (SDOF)
C_{p}	Lumped piezoelectric capacitance
$\tilde{c} = f_{\mathrm{in}} / \left(M_{\mathrm{eq}} a\right)$	Equivalent force correction factor
D	Hydraulic diameter
d_{ijk}	Piezoelectric material coefficients
δ	Fluid boundary layer thickness
$\Delta\Omega_{\mathrm{el}}^2$	Non dimensional electrical stiffness
$\Delta\Omega$	Normalized noise bandwidth
E_{mech}	Mechanical energy
E_{el}	Electrical energy
E_{b}	Beam energy (stored)
E^*	Beam energy density FOM
ε_0	Permittivity of free space
ε_{ijk}	Piezoelectric material permittivity constants
η	Harvesting efficiency (FOM)
ξ	Harvesting effectiveness (FOM) without space constraints
ξ'	Harvesting effectiveness (FOM) with space constraints (packaged)
FoM_V	Volume figure of merit (Mitcheson)
f_{in}	Lumped inertial (or input) force
F_{in}	Lumped inertial (or input) force phasor
f_{D}	Damping force
γ	Mean free path
H	Piezoelectric thickness fraction (of beam thickness)
h	Piezoelectric block thickness
h_{g}	Gap function (from squeeze film model)
h_0	Static gap (for squeeze film)
h_{s}	Silicon beam layer thickness
h_{p}	Piezoelectric layer thickness
h_{el}	Electrode layer thickness
$h_{\mathrm{t,S}}$	Silicon tip mass thickness
$h_{\mathrm{t,W}}$	Tungsten tip mass thickness
i	Piezoelectric current (time signal)

k_b	Boltzmann constant (in J/K)
k_{ijk}	Piezoelectric material coupling factors
k_e^2	Lumped effective piezoelectric coupling factor
κ^2	Lumped piezoelectric coupling factor
K_m	Lumped mechanical stiffness
K_el	Lumped electrical stiffness
Kn	Knudsen number
L	Characteristic length
L_b	Cantilever beam length
L_el	Electrode length
L_t	Tip mass length
L_M	Mass length (generic design)
L_H	Packaged harvester (mass length plus travel range)
λ	Linear mass density ratio between proof mass and beam
Λ	Geometric reduction factor (stress concentration)
M_eq	Lumped equivalent mass
M_t	Tip mass
m_m	air molecular mass
μ	Fluid (air) viscosity
μ_eff	Fluid effective viscosity
P_in	Mechanical power input (complex)
$\bar{P}_\mathrm{in}$	Mechanical power input (active)
P_el	Electrical power output (complex)
$\bar{P}_\mathrm{el}$	Electrical power output (active)
P_ρ	Normalized power density FOM
P	Fluid induce local pressure
P_a	Ambient pressure
ϕ_f	Global geometric form factor (for piezocoupling)
Q_tot	Total quality factor
Q_m	Mechanical qualiy factor
Q_el	Electrical quality factor
Q_f	Fluidic quality factor
Q_int	Intrinsic quality factor (structural damping)
$r_{O'}^2$	Proof mass radius of gyration around beam tip axis O'
R_eq	Resistive load connected to piezoelectric device
ρ_M	Mass material density
ρ_s	Silicon density
ρ_p	Piezoelectric material density
ρ_el	Electrode material density
ρ_W	Tungsten tip mass density
S_0	Single sided power spectrum density of the acceleration source (white noise), normalized by units of Hz
S_a	Acceleration signal single sided power spectrum density (ASD), normalized by units of Hz

s_{ijk}	Piezoelectric material compliances
S_{ij}	Piezoelectric material strains tensor
σ_{mn}	Equivalent squeeze numbers
σ_{l}	Material dynamic tensile strength
t	Time
T	Natural period/Sampling period
T_{a}	Ambient temperature
T_{ij}	Piezoelectric material mechanical stresses tensor
θ	Lumped piezoelectric coupling coefficient
$\hat{\vartheta}$	Normalized mass rotation angle
Υ	Squeeze film to drag losses ratio
U_{S}	Stored energy
U_{D}	Energy losses per cycle
v	Piezoelectric voltage output
V	Piezoelectric voltage output phasor
Vol	Total effective volume of device (static volume)
Vol_{b}	Beam volume
Vol_{M}	Tip mass volume
$Volume$	Total device volume (with packaging)
w	Beam displacement, function of position x and time t
$\hat{w}$	Full geometry normalized displacement profile/shape
$\hat{w}_{\mathrm{b}}$	Beam normalized deflection shape
$\hat{w}_{\mathrm{m}}$	Rigid mass normalized displacement
W	Beam tip/mass displacement phasor
$W_{\max}$	Maximum allowed displacement by packaging (simplified model)
φ	Beam tip time response
φ_0	Beam tip/oscillator amplitude
ψ	Beam oscillation phase
ω	Radial frequency
ω_n	Radial natural frequency
ω_r	Radial resonance frequency
Ω	Frequency ratio
Ω_{r}	Resonant frequency ratio
x	Longitudinal position along structure
y_{s}	Vibration source displacement signal
Y_0	Vibration source displacement amplitude
Y_{p}	Piezoelectric material Young's modulus
Y_{s}	Silicon Young's modulus
Y_{el}	Electrode material Young's modulus (aluminum)
$\tilde{Y}$	Elasticity ratio between piezoelectric and structural layer
YI	Beam flexural modulus
ζ_{m}	Mechanical damping factor
ζ_{el}	Electrical damping factor
Z_{eq}	Connected circuit impedance (complex)

LIST OF ACRONYMS

ADC	Analog to Digital Converter
AFM	Atomic Force Microscopy
ASD	Acceleration Spectral Density
BOX	Buried Oxide
CMOS	Complementary Metal Oxide Semiconductor
DAQ	Data Acquisition modlue
DRIE	Deep Reactive Ion Etching
DUT	Device Under Test
FOM	Figure of Merit
FRF	Frequency Response Function
FWHM	Full Width at Half Maximum
IC	Integrated Circuit
IoT	Internet of Things
MCU	Microcontroller Unit
MEMS	Microelectromechanical System
MOCVD	Metal Organic Chemichal Vapor Deposition
PCB	Printed Circuit Board
PDF	Probability Density Function
PECVD	Plasma Enhanced Chemical Vapor Deposition
PSD	Power Spectral Density
PVEH	Piezoelectric Vibration Energy Harvesting
PZT	Lead Zirconate Titanate
RIE	Reactive Ion Etching
SEM	Scanning Electron Microscopy
SOI	Silicon On Insulator
TPMS	Tire Pressure Monitoring Systems
VEH	Vibration Energy Harvesting
VHM	Vehicular Health Monitoring
WDT	Watch Dog Timer
WLP	Wafer-Level Packaging
WSN	Wireless Sensor Network
XCVR	Transceiver

CHAPTER 1

Introduction

1.1 Wireless sensors for the Internet of Things

The futuristic vision of a smart world, as illustrated in Fig. 1.1, with its smart cities that include interconnected factories, buildings, cars and even smart pieces of clothing, emerges from the convergence of several technologies, such as the Internet, cloud computing and mass data storage. This concept of the "Internet of Things" (IoT) rests on the ability of the world and objects around us to gather, collect and transmit information to track or optimize all kinds of activities. Sensors, which are at the root of this idea, must be deployed seamlessly all around us to fully realize this vision. Coincidently, the mass production and adoption of low cost MEMS sensors (microelectromechanical system) along with the emergence of ultralow power microelectronic and wireless communication technologies all align to push these technologies forward. Deploying wireless millimeter scale sensor nodes all around us will create new wireless sensor network (WSN) communication architectures that will give access to new information and functionality in a wide range of fields (*e.g.*, industrial, vehicles [26, 200], medical).

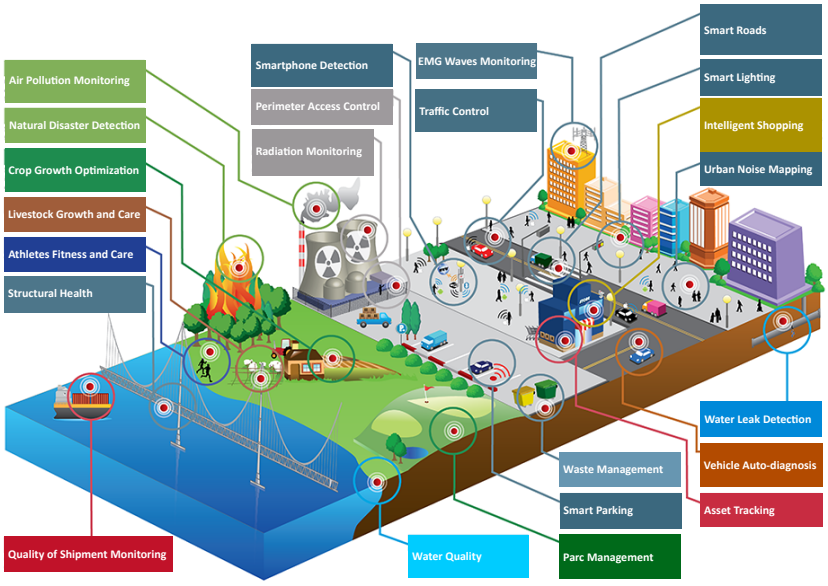

Figure 1.1 Representation of a connected smart world concept. Adapted from: [117]

1.2 Technological challenges

Alhtough this idea goes as far back as the early 90s, with its most ambitious incarnation pitched to DARPA by researchers at UC Berkeley [163] under the "Smart Dust" name, it is still far from maturity. Many challenges remain to be solved before it can be massively deployed. For instance, secure and reliable communication protocols still need to be established and standardized, there are numerous legal and ethical concerns regarding data privacy, and wireless channels have to be characterized in many different applications and environment [38, 142]. Last, but not least, the power consumption of the electronics (transceiver and power management modules) must be reduced further, as energy concerns raise critical issues of long term reliability and autonomy.

1.2.1 Power sources for wireless devices

Powering a wireless node requires a source of energy that is ideally localized, low cost, and durable. To this day, batteries remain mostly used, but this technology has its limits in the context of many of these new applications. One concern is that the widespread use of batteries will create many environmental hazards and could also lead to an unsustainable demand for lithium and other rare materials. More importantly, batteries have a limited lifetime, which is often insufficient for applications that need to be powered for many years. In automotive and industrial applications, the lifetime expectations are for the sensors to last 10 to 20 years. While batteries are rated to last from 3 to up to ten years in the best cases, they can be bulky compared to the other electronic components, as these can be miniaturized more easily. As a result, the sensor's size is typically limited by the battery. Furthermore, if a large number of wireless sensors are deployed in the environment to form a WSN, the power draw on each battery and their durability may vary greatly from one node to another. In the long run, the replacement and downtime costs make this solution unattractive [20].

1.2.2 Energy harvesting for autonomous sensors

Energy harvesting is proposed as a potential "fit and forget" solution to power wireless sensor nodes. Also called power harvesting or energy scavenging, it is defined as "*"the process by which energy is derived from external sources (e.g., solar power, thermal energy, wind energy, salinity gradients, and kinetic energy), captured, and stored for small, wireless autonomous devices, like those used in wearable electronics and wireless sensor networks."* [214] The use of ambient RF waves like Wi-Fi signals, in a way similar to wireless charging, is also considered as energy harvesting. According to Yole Development [145], the market for energy harvesting is

anticipated to reach 100 million USD in 2021, mainly from market demands for wireless sensors and WSN.

In the case of automotive, civil and industrial applications, ambient light (solar), thermal energy (temperature gradient) and kinetic energy (vibrations) usually come up as the most available sources of energy. Numerical estimates on their respective harvesting potential are presented in Table 1.1, whereas Fig. 1.2 presents an assessment of the expected lifetime against the power consumption for different energy storage systems of 1 cm^3 of volume. Based on these estimates, the combination of a smaller battery and an energy harvester could provide an adequate and durable trade off, as long as the charging capacity is preserved.

Table 1.1 Comparison of energy sources and their potential harvested power. Source: [205]

Source	Source power	Harvested power
Ambient light		
Indoor	0.1 mW/cm^2	10 $\mu W/cm^2$
Outdoor	100 mW/cm^2	10 mW/cm^2
Vibration/motion		
Human	1 m/s^2 @ 50 Hz	4 $\mu W/cm^2$
Industrial	10 m/s^2 @ 1 kHz	100 $\mu W/cm^2$
Thermal energy		
Human	20 mW/cm^2	30 $\mu W/cm^2$
Industrial	100 mW/cm^2	1-10 mW/cm^2
RF		
Cell phone	0.3 $\mu W/cm^2$	0.1 $\mu W/cm^2$

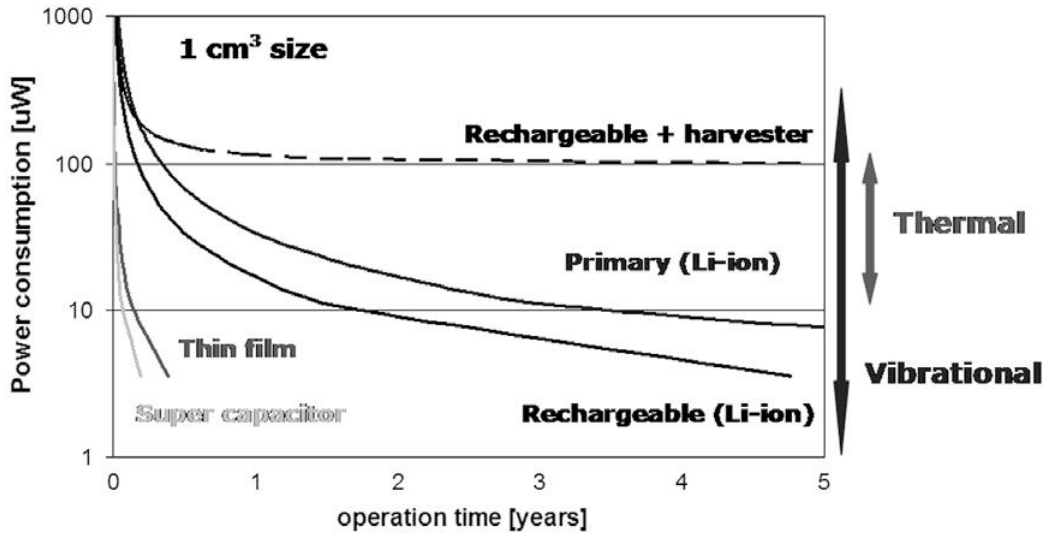

Figure 1.2 Comparison of power consumption vs. lifetime for various energy storage concepts of 1 cm^3 of volume. Source: [205]

Table 1.1 indicates that thermal energy in industrial environment and outdoor light are the two richest sources of energy, although they are not readily available everywhere. In contrast, vibrations provide less energy, but are more prevalent. This thesis focuses exclusively on vibration energy harvesting.

1.3 Kinetic energy harvesting: A brief overview

Vibration energy harvesting (VEH) typically refers to the process of converting ambient kinetic energy (mostly found in the form of vibrations) to generate electricity. Typically, a resonator is used to absorb the ambient energy by tuning its resonant frequency to the source frequency, although other device principles have also been proposed. Unless the harvester acts as a full fledged vibration absorber to suppress vibrations from the source, its scale must be much smaller than the host structure it is trying to harvest from to minimize its impact. The size of the device also affects the choice of an electromechanical conversion mechanism, as discussed in the following section.

1.3.1 Energy conversion mechanisms

Energy from mechanical vibrations is generally harvested via three conversion mechanisms:

- **Piezoelectricity:** a piezoelectric material converts strain into electrical energy;
- **Electromagnetism:** energy is produced by a moving magnet inducing current in a coil;
- **Electrostatics:** energy is produced by the relative motion between two charged particles or surfaces (also referred as capacitive transduction).

Nevertheless, other mechanisms have recently surfaced in the literature,

- **Electrostriction:** energy is produced by polarization of a dielectric material under a stress gradient. Electrostriction differs from piezoelectricity because it is not linear, but rather a second order phenomenon.
- **Triboelectricity:** a variant of electrostatic transduction where charges build up by contact/friction between different materials;
- **Magnetostriction:** a variant of electromagnetism where stress on a magnetostrictive material causes a varying magnetic field, which can then be converted to electricity through a coil.

Hybrid approaches incorporating more than one transduction principle have also been proposed and tested [49, 107, 146] to improve the harvesting capabilities. Each mechanism has advantages and drawbacks. For instance, electrostatic and piezoelectric transducers are better suited for microscale devices. In contrast, efficient coils are difficult to implement and fabricate using MEMS fabrication techniques because of their inherent 3D geometry. It is however a well known, cheap and mature technology that is well suited at the mesoscale. Although the electrostatic principle originally required a secondary voltage source, the introduction of electrets in recent years has addressed this problem. Electrets are made from dielectric materials that are able to maintain a quasi-permanent electric charge or polarisation and thus only need to be charged during initial fabrication. Table 1.2 summarizes the different characteristics of the various transduction mechanisms.

Table 1.2 Comparison of transduction mechanisms for vibration energy harvesting. Inspired by: [188]

Mechanism	Common materials	Pros	Cons
Piezoelectricity	PZT, AlN	Simple structure, easy to implement at small scale, high voltage output, high electromechanical coupling	Low current, high impedance, brittle materials
Electromagnetism	NdFeB (magnet)	Simple and mastered construction at larger scale, low impedance, high current	Low voltage, difficult to implement in microfabrication
Electrostatics	Common dielectrics	High output voltage, no exotic materials, compatible with standards IC technologies	Low current, bias voltage necessary (non electret), high impedance
Electrostriction	$BaSrTiO_3$	High strain limit, flexible	Difficult to implement in microfabrication, low energy density (low stress limit)
Triboelectricity	Polycarbonate, Teflon, PVDF	Cheap, high voltage	High impedance, low current, wear due to friction
Magnetostriction	Metglas, Galfenol	Flexible, No depolarization problem	Difficult to implement in microfabrication, nonlinear, requires coil

Due to its compatibility with MEMS microfabrication processes and our past knowledge of the technology, piezoelectric vibration energy harvesting (PVEH) is selected for this project.

1.3.2 Fundamentals of piezoelectricity

As briefly introduced in section 1.3.1, piezoelectric materials have the ability to convert mechanical stress to electrical energy. In essence, they accumulate a voltage gradient when stressed or, inversely, deform when subjected to a voltage gradient. Although asymmetric crystalline materials exhibit piezoelectricity at the crystal level due to the formation of an electric dipole when deformed (as depicted in Fig. 1.3), this characteristic is not sufficient to observe sizable piezo-

electricity in a material or device. The effective piezoelectric properties also depend on the microstructure (e.g, amorphous, polycrystal or monocrystal) and the general long range order of the crystallites. If the crystallites are well aligned in the material, either by design during its synthesis or by subsequent polarization (using a strong electric field on ferroelectric materials), and if the dipole moment is sufficiently strong, only then will the piezoelectric effect be effectively usable.

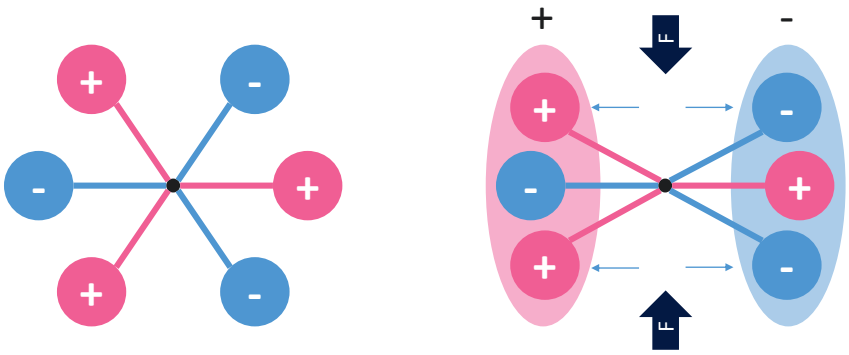

Figure 1.3 Creation of a piezoelectric dipole moment in the stressed crystal.

Material modeling

The linear modeling of piezoelectric materials is based on the 1987 IEEE standard on piezoelectricity [153]. Due to their anisotropic nature, their properties are defined by tensors. Figure 1.4 presents the usual axis system used and the subscripts associated with each direction. The polarization direction is attached to the third axis.

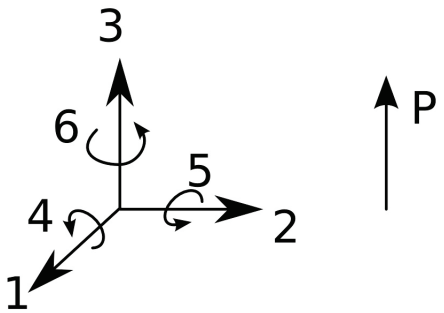

Figure 1.4 Typical axis system used to define the piezoelectric properties in each direction. Subscripts 4, 5 et 6 correspond to rotation around axis 1, 2 et 3 respectively.

Just like in non piezoelectric materials, the mechanical stresses T_{ij} and strains S_{ij} tensors are related by the compliances s_{ijk} (or stiffness c_{ijk}). However, due to the electromechanical coupling, a second fundamental equation is required to express quantities in the electrical domain.

These fundamental equations for piezoelectricity can take many forms. Equations 1.1 and 1.2 are expressed in the strain-charge form here. Hence, tensors for electrical fields E_{ij} and electrical displacements D_{ij} are added. The piezoelectric coefficients d_{ijk} as well as the permittivities ε_{ijk} are the properties describing the piezoelectric behavior of the material. Equation 1.3 defines the piezoelectric coefficients, which are typically expressed in m/V or in C/N. The superscripts E and T respectively denote that these properties are evaluated at constant electric fields and stresses. The superscript t denotes the transposed.

$$S = s^{\mathrm{E}}T + d^{\mathrm{t}}E \tag{1.1}$$

$$D = dT + \varepsilon^{\mathrm{T}}E \tag{1.2}$$

$$d_{ij} = \left(\frac{\partial D_i}{\partial T_j}\right)_{E=\text{const}} = \left(\frac{\partial S_i}{\partial E_j}\right)_{T=\text{const}} \tag{1.3}$$

Luckily, crystals often present planes of symmetry, simplifying the tensorial notation of the mechanical and piezoelectric properties as in Eqs. 1.4, 1.5 and 1.6.

$$d = \begin{bmatrix} 0 & 0 & 0 & 0 & d_{15} & 0 \\ 0 & 0 & 0 & d_{15} & 0 & 0 \\ d_{31} & d_{31} & d_{33} & 0 & 0 & 0 \end{bmatrix} \tag{1.4}$$

$$\varepsilon = \begin{bmatrix} \varepsilon_{11} & 0 & 0 \\ 0 & \varepsilon_{11} & 0 \\ 0 & 0 & \varepsilon_{33} \end{bmatrix} \tag{1.5}$$

$$s = \begin{bmatrix} s_{11} & s_{12} & s_{13} & 0 & 0 & 0 \\ s_{12} & s_{11} & s_{13} & 0 & 0 & 0 \\ s_{13} & s_{13} & s_{33} & 0 & 0 & 0 \\ 0 & 0 & 0 & s_{44} & 0 & 0 \\ 0 & 0 & 0 & 0 & s_{44} & 0 \\ 0 & 0 & 0 & 0 & 0 & 2(s_{11} - s_{12}) \end{bmatrix} \tag{1.6}$$

Further simplifications can be made depending on the geometry and the type of loading conditions. For instance, the fundamental equations for structures under uniaxial plane stress conditions can be simplified around the axial stress in direction 1, T_1, as it is the only one different

from zero. Additionally, if the electrodes are perpendicular to the polarization axis (the device thus operates in the so called "31-mode"), the fundamental equations simplify as in equation 1.7.

$$\begin{pmatrix} S_1 \\ D_3 \end{pmatrix} = \begin{bmatrix} s_{11}^{\mathrm{E}} & d_{31} \\ d_{31} & \varepsilon_{33}^{\mathrm{T}} \end{bmatrix} \begin{pmatrix} T_1 \\ E_3 \end{pmatrix} \tag{1.7}$$

Large d coefficients means that a large displacement is associated to a given voltage (actuator mode) or that a large voltage is generated under a given displacement (sensor mode). Generally, $d_{33} > d_{31}$. From an energetic standpoint, the coupling factors are usually used to describe the effectiveness of the material in converting energy from one form to another (either from electrical to mechanical or inversely). These dimensionless values are also anisotropic. The intrinsic coupling factors, noted by k_{ij}, are material properties that are generally obtained in static or quasi-static conditions and from specimens specifically designed to minimize geometric effects (e.g., an extended slender rod), like coupling between modes and directions. The ij subscripts again represent the piezoelectric loading mode and therefore k_{33} is for the longitudinal mode, k_{31} for the transverse mode and k_{15} for the shear mode. Equation 1.8 provides the k_{31} factor for a plane uniaxial stress loading.

$$k_{31}^2 = \frac{\text{Converted energy}}{\text{Applied energy}} = \frac{d_{31}^2}{s_{11}^{\mathrm{E}} \varepsilon_{33}^{\mathrm{T}}} \tag{1.8}$$

An effective coupling factor, k_{e}, is used to evaluate the conversion effectiveness for a specific topology subject to a given stress gradient, accounting for different material compositions. This topic is presented in more details in chapter 2, where we explain how this parameter is also used to assess the potential of an energy harvester. Modeling of devices and properties of various piezoelectric materials are also presented in the same chapter.

1.3.3 Survey of vibration harvesters: commercial offerings and research prototypes

This section presents a sample of PVEH devices proposed up to this day. First, we present some of the products that have been commercialized over the years, whereas the second part showcases results from prototypes produced by research laboratories. We finally discuss the issue of benchmarking and comparing these devices.

Commercial PVEH

Several VEH devices have made their way to market throughout the years, but very few have actually found commercial success. The most successful proposition to date comes from Perpetuum Inc, which started operation in 2004 when this market was still in its infancy. Their product is a mesoscale electromagnetic resonant generator specifically aimed at the industrial and transport sectors. They have mostly found success by addressing the niche market of railway and fleet management monitoring [158].

In the smart building sector, EnOcean has also seen success with its battery-free wireless switch and sensor product lines, which include a few VEH powered products (although none appear to be MEMS-based). The company's products are already found in more than 400 000 buildings worldwide. Founded in 2001 as a spin-off of Siemens AG, EnOcean holds an impressive range of patents for energy harvesting applications in the building and industrial automation sectors. They have also proposed their own proprietary low power wireless standard, which can be licensed [65].

Beside these two pioneering companies, others have also tried to enter this sector, but to varying degree of success:

- **Omron:** In partnership with the Holst Center/imec, they propose a small (but not MEMS-based) electret vibration generator. Their prototype has been put through field tests with customer beginning in 2014 [93] and they are still actively looking for commercialization partners.
- **Mide:** The Volture PPA product line consists of generic piezoelectric components marketed for VEH and other applications. They are made from a multilayer composite of a piezoelectric material sandwiched between copper electrodes and FR4 polymer for encapsulation [137].
- **Revibe Energy:** Founded in 2013, this company product line essentially consists of three main products, namely the modelA, modelD and modelQ, which are mesoscale electromagnetic harvesters of different volumes. Their main markets are railway monitoring, industries, construction, mines, machinery and aviation [172].
- **Lumedyne Technologies:** This company mainly focused on high sensitivity accelerometers, gyroscope and geophones, but they also developed and patented an electromagnetic VEH prototype in 2009 [213]. Their harvester was never launched on the market, but the company was reportedly bought by Google for 85 millions in 2015 [100].

- **LORD Microstrain:** This company offers inertial and other wireless sensors in many sectors (industrial, transport, aerospace, infrastructures). They introduced their MVEH and PVEH modules in 2011 (which are electromagnetic and piezoelectric respectively) [135, 136]. It is not clear if these products are still available for purchase.
- **Advanced Cerametrics:** This company launched the Harvestor-III product line in 2009, which consisted of PVEHs combined to a management circuit packaged in a lightweight mountable enclosure to provide continuous voltage out of the box [166]. The company now seems to be out of business.
- **8power:** This company is a spin-off of Cambridge University founded in 2015. Their product lines, the Track 100 and Track 200, launched in 2017 and consist in 100% self-powered energy harvesting sensors for creating WSN that run purely on ambient energy [1]. One of their product is a GPS tracker powered by vibrations, which is equipped with a complementary solar panel. It is not clear which transduction mechanism is used for the vibration harvester and if the harvester in these products is MEMS-based. They also have a patent for parametric MEMS vibration energy harvesters. Their target markets are civil infrastructures, machinery, and transport [2].
- **microGen Systems:** Launched in 2007, the company first product was the Bolt energy harvester, which consisted of the first MEMS PVEH available on the market. They later launched the AC Power Cell and the DC Power Cell, which also included the necessary power management circuits. They then expanded their offering to also include wireless sensors and data management. In July 2017, Wireless Sensor Solutions [131] acquired microGen Systems for an undisclosed amount. Their main markets are the sectors of Industrial IoT, construction, mines and machinery.

Some of these propositions are summarized in Table 1.4, which highlights that, for now, the majority of products use electromagnetism and are fabricated at the mesoscale. In addition, the low number of success stories in this space is a testament to the challenges and limitation of currently existing technologies. For one, it is now clear that vibration energy harvesters have not been accepted by the market on their own, but are successful when included in a complete sensor. Moreover, piezoelectric-based devices have mostly failed at the mesoscale, but appear to lead in the MEMS space. Still, comparing these products is challenging, because they offer different features and are not designed for the same vibration frequency and amplitude range, two parameters that directly relate to the source power and thus the device power output. Furthermore, little information is available on the details of each design and their power output specifications.

Table 1.3 Sample of commercial PVEH propositions.

Manufacturer	Model	Characteristics	Ref.
Perpetuum		• Mesoscale • Electromagnetic • 25 to 120 Hz • 1 kg • 3 mW @ 0.05 g's RMS	[159]
ReVibe Energy	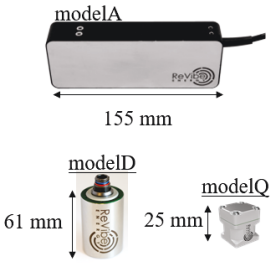	• Mesoscale • Electromagnetic • 15 to 100 Hz • 60 to 300 g • 1 mW @ 0.05 g (A,D) • 2 mW @ 0.2 g (Q)	[172]
OMRON	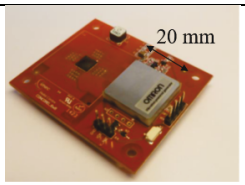	• Mesoscale • Electrostatic	[93]
8power	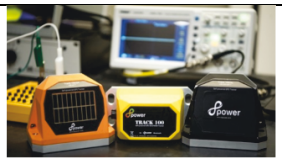	• Mesoscale? • Electromagnetic?	[1]
Microstrain	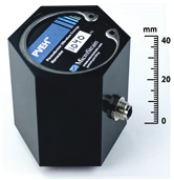	• Mesoscale • Piezoelectric • 1 kHz • 185 g • 30 mW @ 1.5 g's • Discontinued?	[136]
Advanced Cerametrics		• Mesoscale • Piezoelectric fiber composite bender • 30-220 Hz • Out of business	[3]

Continued on next page

Manufacturer	Model	Characteristics	Ref.
microGen Systems	µ-Recharger Cube (legacy) 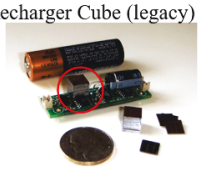 Bolt (legacy) 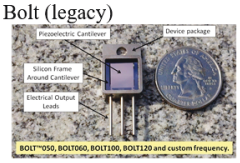 AC Power Cell  40.6 mm DC Power Cell  40.2 mm	• Piezoelectric MEMS • High Q-factor, > 200 (Vacuum packaged) <u>Bolt</u> • 50-120 Hz • 0.288 mW @ 1 g <u>Power Cells</u> • <20 g • 500-700 Hz • 200 µW max • 0.5 to 2.5 g's	[130, 132–134]

Nevertheless, Table 1.4 presents some specifications found specifically for piezoelectric devices. By comparing the output for the meso and microscale devices, we can clearly see the impact of a reduced size, as power goes from a few milliwatts to the hundred of microwatts range. Furthermore, the piezoelectric stack design used by Microstrain leads to a very high operation frequency compared to the bender designs. As far as MEMS designs are concerned, microGen Systems is the leader in this sector. Finally, it is worth noting that most of these products operate using the linear resonance principle to absorb vibrations.

Table 1.4 Specifications of commercial PVEH propositions.

Product	Advanced Cerametrics' Harvestor-III Power Module	microGen Systems' Bolt EH	Microstrain's PVEH
Power processing?	Yes	No	Yes
Size (cm^3)	141 to 231	0.8	74
Freq. range (Hz)	30-220	50-120	1000
Bandwith (Hz)	N/A	2	≈ 10
Power (mW)	N/A	0.288 @ 1 g	30 @ 1.5 g
Price (CAD)	> 100$	$\approx$ 33$	N/A
References	[3]	[130, 132]	[136]

PVEH in research

On the other hand, activities surrounding the development of PVEH modules in academia and research centers have been sustained through the last decade, with continued interest from companies such as ST Microelectronics, Intel, IBM, Texas Instruments and others. Significant efforts are dedicated to developing novel MEMS structures, materials, circuit and assembly processes. A large subset of activities is now dedicated to addressing the issue of the narrow bandwidth of linear resonators, which is assumed to be limiting the operational range of most harvesters. Although not presented more deeply here, this topic is touched upon in more details in chapter 2 and appendix A.

Table 1.5 features several published results for MEMS PVEH devices, with some of them pictured in Fig. 1.5. For the purpose of this comparison, all the data points collected are for devices tested with simple circuits (a resistive load, with or without a rectifier). It is also worth mentionning that Andosca *et al.* [10] device is effectively the prototype on which microGen's devices are based on.

Table 1.5 Assessment of several PVEH devices designed by researchers.

Reference	[148]	[61]	[169]	[10]	[5]	[216]
Piezo material	d_{33} PZT	d_{31} AlN	d_{31} AlN	d_{31} AlN	d_{31} PZT (2x)	d_{31} KNN
Substrate	Silicon	Silicon	Silicon	Silicon	PZT	Silicon
Process	sol-gel	sputtering	sputtering	sputtering	bonded/thinned	chemical solution
Beam volume (mm^3)	0.0029	0.23	0.061	0.47	0.75[a]	0.02[a]
Mass volume (mm^3)	0.32	12.5	6	12.5	15.6[a]	1.5[a]
Mass[a] (mg)	0.76	28	14	28.9	320	3.5
Mass material	Silicon	Silicon	Silicon	Silicon	Tungsten/PZT	Silicon
Frequency (Hz)	877	572	1082	58	158	132
Acceleration (m/s^2)	19.6	19.6	3.14	4.9	0.98	9.81
Power (µW)	1.4	60	3	32	1.58	3.62
Power/Volume (mW/cm^3)	4.34	4.71	0.49	2.55	0.13	2.41

[a]Estimated values

In general, microfabricated devices have larger quality factors than mesoscale ones, with values hovering between 100-1000. The work realized at IMEC [61, 169] on AlN-based MEMS PVEH devices introduced the use vacuum packaging to prevent degradation of the performances due to squeeze film damping. As shown by Table 1.5, many materials and fabrication processes have been used, but most devices are within one order of magnitude in terms of power output. The differences between designs stem from several factors, including the device size and acceleration input.

Power density, expressed as the ratio of the power divided by the volume (in mW/cm^3), is a frequently used metric in the PVEH literature to compare the performance of devices of different sizes. As far as this metric goes, the devices found in Table 1.5 range between 0.1-10 mW/cm^3. However, this metric is flawed in many ways because the contribution of the input vibration

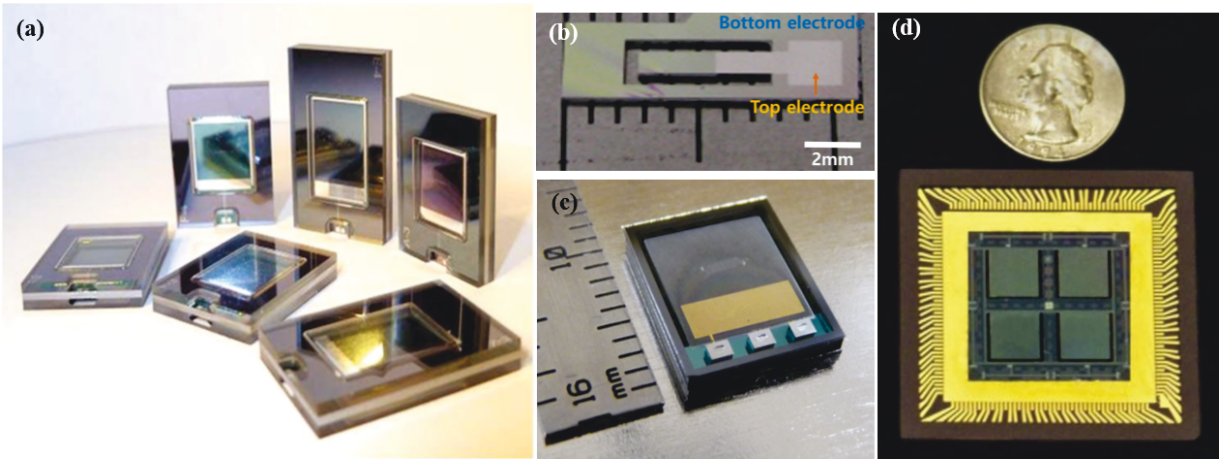

Figure 1.5 Sample of PVEH produced in research labs: (a) IMEC AlN-based, vacuum packaged devices [62], (b) Won *et al*. KNN-based device [216], (c) Aktakka *et al*. PZT-based, vacuum packaged device [5], (d) Andosca *et al*. AlN-based device [10].

is not accounted for. This point is addressed in more details in chapter 2, but we can still conclude that power levels of 1 to 60 µW are achieved by devices smaller than 15 mm^3 from sub-kHz vibrations of < 2 g's of amplitude. Nevertheless, it remains unclear how significant improvement can be achieved going forward.

In general, MEMS harvesters have not overtaken the market, because their power level remain small comparatively to larger devices. As we discuss in chapter 2, size itself is one reason, but MEMS fabrication also currently limits the type of materials that can be incorporated. As highlighted by Table 1.5, most are restricted to silicon to fabricate the mass, despite the fact that this material has a low mass density, which reduces the sensitivity.

1.4 Return on previous research work

In our previous studies, the influence of material properties and geometry on the power output of piezoelectric microresonators was studied extensively. As a starting point, the influence of the electrical load was restricted to the case of a purely resistive load and the source excitation was considered as harmonic. To accomplish this, a compact model formulation and an analytical design approach were proposed [56]. The details of these findings can be found in reference [53], but are also reviewed as part of chapter 2. Building on this knowledge, we believe that the next step of this project is to design, fabricate and test MEMS PVEH devices using innovative MEMS technology. This thesis also aims to address the following points:

- Several figures of merit are currently used in the literature, but some of them are deeply flawed, because they are sensitive to the vibration input rather than depending only on the device design. Adequate benchmarking tools and methodologies are needed to fairly compare devices, but also identify future paths of improvement. The amount of academic research activities on vibration energy harvesting has exploded in recent years, while several commercial offerings have come and gone cyclically. With the large number of new publications and results from newly fabricated device concepts comes a number of claims of continuous performance improvements. However, due to the lack of clear irrevocable figures of merits and firmly established physical limits, it is not yet clear to which extent and how these new designs really improve on their predecessors. It is therefore one goal of this work to investigate how to clarify these ambiguities.
- Contrary to batteries, which are fixed energy reservoirs, the power output of energy harvesters' is very dependent of the energy source on which they rely. Therefore, the specific design and fabrication of an harvester device is tied to the final application. Ideally, a system level design approach that also accounts for realistic values of ambient vibrations and their general characteristics in typical operation should be used.
- New fabrication approaches are continuously proposed, but most are focusing on increasing the electromechanical coupling (by improving the piezoelectric properties for instance), the device quality factor (using vacuum packaging) or the frequency response (via nonlinear mechanisms). However, few efforts have been made to integrate new materials to increase the device sensitivity to input vibrations.

1.5 Research objectives

In light of this situation, this thesis aims to answer this global research question:

How should cost effective and high power density piezoelectric vibration energy harvesters be designed and fabricated to provide a solution to power a wireless sensor node from ambient vibrations?

Based on this question, the main objective of this thesis is defined as:

Main goal

- Define and validate a wafer level batch fabricated MEMS PVEH with high density proof-mass for ultralow power autonomous wireless sensors.

This objective then leads to the formulation of the following secondary objectives:

Secondary objectives

- Identify the fundamental technological limits and define a comprehensive benchmarking framework to evaluate and guide the design of PVEH systems configurations, geometries and materials;
- Develop a methodology to define a harvesting application (configuration, power requirement, available ambient energy);
- Estimate the effect of fluid damping and a potential packaging on the performance of the device;
- Develop the detailed design and microfabrication process flow of the PVEH and characterize its performances.

1.6 Thesis outline and contributions

This chapter presented the motivations behind the proposed research project. Clearly, the development of novel power generation technologies generates a lot of research activities in many fields of engineering. Although most of the efforts in previous decades have focused on energy harvesting from macro sources, the field of micropower sources (or PowerMEMS) has emerged as a new topic because it is seen as a required stepping stone for the widespread integration of WSN in future intelligent systems and the IoT. Many avenues have been explored and vibration energy harvesting is considered as one possible solution. In the remaining chapters of this thesis, we present the numerous research areas tackled to address the objectives defined in section 1.5

In chapter 2, we review the general principles involved in the operation of PVEH devices as well as the current state of the art of this technology. The fundamental limits are presented, reviewed and discussed to present a system level design framework useful for benchmarking of various devices. All the important aspect are discussed, namely the impact of the material properties, geometry, electrical circuit and mode of operation. Part of the work presented in this chapter has been presented at the 2011 PowerMEMS international conference in Seoul, South Korea [57], and was also published in two book chapters published by CRC Press [52, 58].

Chapter 3 then presents an application case study for wireless automotive sensors. A general framework for identifying the best suited applications is first defined and a survey of sensors present in a vehicle is presented. Vibration measurements are then realized on an operating vehicle on the location associated to these sensors. Overall, more than 20 measurement points were monitored and extensive analyses were realized to characterize these vibration sources in term of their potential for vibration energy harvesting from an inertial MEMS device. Con-

jointly, a custom made wireless node design is evaluated to estimate a realistic power budget for a sensor application. Based on these results, we conclude that the most sensible solution to reach the required level of performance is to integrate higher density materials to fabricate the device proof mass. A previous version of this work was partly presented at the 2013 American Society of Mechanical Engineers' International Mechanical Engineers Congress and Exposition (ASME IMECE) in San Diego, USA [51].

In chapter 4, the effect of such a design change on the device interaction with the surrounding fluid is presented in details. We demonstrate analytically and experimentally that by integrating tungsten proof masses, the fluidic quality factor can be improved by close to an order of magnitude compared to pure silicon-based devices. Although not the only factor to consider, these results raise the possibility that new, vacuum-less packaging strategies can be viable by changing the mass density. This work was presented at the 2016th PowerMEMS international conference in Paris, France [50], and accepted for publication in the IEEE Journal of MEMS [59].

An original wafer-level process for integration of high density, bulk tungsten proof masses on silicon based devices is then presented in chapter 5. First, we propose the general process flow and then discuss the issues and challenges encountered during fabrication. Numerous short loop are realized and we present results that demonstrate the feasibility of the different fabrication blocks. This chapter then concludes by presenting some of the prototypes that were fabricated. A previous version of this work was presented at the 2017th Transducers' international conference in Khaoshung, Taiwan [55]. An international patent was also filed for the presented process flow (which also includes other versions not disclosed in this thesis) [54].

Experimental results for several piezoelectric devices fabricated using the fabrication technology introduced in chapter 5 are then presented in chapter 6. The general test methodology to measure the voltage and average power frequency response functions is explained and results for 8 different devices are reported. Their performances are evaluated and compared with the state of the art by using some of the metrics presented in chapter 2. Our results show that some of our designs provide record performances in terms of normalized power density, highlighting the many advantages of adding tungsten masses to MEMS vibration energy harvesters.

Finally, we conclude this thesis by summarizing the main results and contributions of this research project in chapter 8 and finish by discussing potential future research avenues and paths for technological improvements. The numeric, unsorted IEEE bibliography style is used throughout this document.

CHAPTER 2

General background and design framework

2.1 Introduction

Over the past twenty years, numerous device concepts have been proposed to solve the power supply issues associated to wireless sensor nodes, ranging from miniaturized engines and fuel cells to thermoelectric, thermophotovoltaic, and piezoelectric devices. Many crucial questions remain open in this field. What are the performance limits of different types of harvesters? Can we develop effective strategies for selecting harvesters for specific applications and environments? Can we develop rational design methodologies to optimize the performance, reliability, and manufacturability?

In this chapter, we seek answers to some of these questions for one particular type of harvester, namely, piezoelectric vibration energy harvesters (PVEH). Vibrations are of interest for energy harvesting because of their ubiquitous nature; contrary to traditional energy harvesting means, they do not require direct access to ambient wind or sun light. Vibration harvesting usually works by using a large suspended mass to inertially capture energy and create a force from the vibration at one point. For PVEH, this force is used to induce stresses in a piezoelectric material as the mean of energy conversion. MEMS harvesters typically use multi-layered cantilever or bridge beam geometries in a way very similar to accelerometers. For resonant devices, the large mass is attached to the structure to tune its resonant frequency and increase the applied stresses, thus boosting its output power. Thin film deposition processes are often used for the integration of the piezoelectric material into these small devices.

Many groups in academic and industrial research laboratories have designed and built miniaturized PVEH devices using different architectures, configurations, geometries, materials and electrical circuits. Their performance has also been tested under various operating conditions. Typically, power densities of the order of mW/cm^3 or less have been reported, but early estimates that motivated efforts to build PVEHs [174, 175, 178] suggest there is room for improvements. Therefore, increasing the power density is a major focus of current research, but it remains unclear whether there is indeed any significant potential for increasing these values. Recognizing the limits of VEH is also important to better understand which wireless sensor applications are compatible with this technology. To this end, we identify and discuss the various aspects that can limit the power density of PVEH, and quantify their impact using simple models. Figures

of merit (FOMs) are reviewed and proposed for benchmarking various designs, thus enabling a rigorous comparison of different devices that have been reported in the literature.

2.2 Energy transfer in PVEH devices

The general energy chain for typical piezoelectric energy harvesters is depicted in Fig. 2.1. An ambient source first supplies mechanical energy to the harvester, either inertially (*e.g.*, vibration, shocks) or directly (*e.g.*, impacts, fluid flows, pressure gradients). Part of the energy transferred is present as kinetic energy (from the mass motion) and potential energy (from the elastic energy in the strained spring and the electrical energy in the charged capacitance), with a continuous exchange between these two forms as the harvester vibrates. Under stress, the piezoelectric element generates an electrical potential on its electrodes, thus converting some of the mechanical energy into electrical energy, which is then partly extracted to be consumed, processed or stored for later use. During this process, losses usually occur in the form of mechanical damping and dielectric leakage. If electrical energy remains in the material, it is restored as mechanical kinetic energy. Once extracted and stored, the electrical energy can be used by the electronic device after it has been processed by the power distribution and control interfaces.

Note that the flow of energy can go both ways. For instance, the control interface could be used to electrically actuate and tune the harvester by injecting previously stored energy into the piezoelectric element [111], which would also affect the capture of ambient energy. For the miniaturized devices under consideration, the effects of the harvester on the source are assumed negligible. The performance is typically reported in terms of the power density (*i.e.*, power per unit volume of the device). Based on this energy conversion process, several limiting aspects can be identified as potential bottlenecks in terms of net power output and power density:

1. How much energy is transmitted to the structure? This depends on the vibration source and its mechanical coupling with the device. Is the excitation due to inertia or contact forces? Is transfer of energy based on resonance, impact, or plucking? This limit for linear resonators is discussed in section 2.4;

2. How much energy can the device collect, store and sustain? The traveling range allowed by the package imposes limits on the stored energy by the mass, whereas stress concerns (*i.e.*, distribution and concentration), fatigue and materials degradation limits how much energy can be stored in the spring materials. These items represent the upper bound for power density if we assume enough energy can be supplied and captured by the harvesting

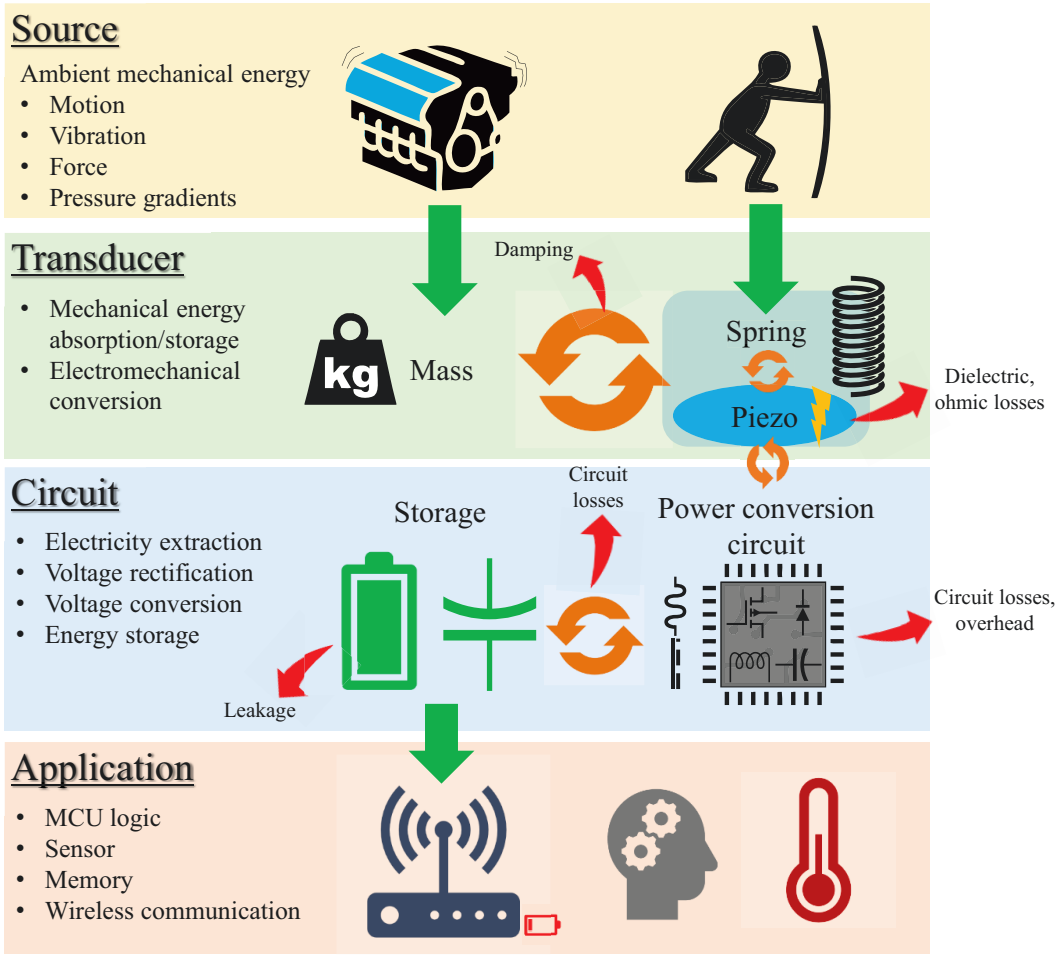

Figure 2.1 General energy chain of a PVEH device

device. These issues are discussed in section 2.5;

3. How much mechanical energy can be converted into electrical energy? This essentially depends on the device electromechanical coupling. For piezoelectric transducers, the generalized effective piezoelectric coupling factor, k_e^2, gives the fraction of the applied energy which is transformed in the electrical domain by the piezoelectric structure under a specific strain distribution. As we discuss in section 2.6, this coupling factor depends on material properties, mainly the material coupling factor expressed by its k_{ij} constants, and the device geometry;

4. How much electrical power can be extracted and stored? Even if a large part of the work applied on the device is converted into electrical energy, only a fraction may be extractable, depending on the load connected to the transducer. Many harvesting interfaces have been proposed to improve the extraction effectiveness and reduce losses. The impact of the extraction approach is presented in section 2.7.

All these aspects can be more or less interrelated depending on the design and device architecture. For instance, these influences are particularly strong for typical inertial resonant PVEHs because a single heterogeneous structure captures, receives and converts the energy, while energy injection and extraction also occur simultaneously.

This chapter explores each of these limits from a high level theoretical framework with the objective of introducing and reviewing relevant FOMs. The selection of an optimal piezoelectric material and electrical interface are also discussed. In section 2.9, we use the FOMs to compare the performance of various devices reported in the literature to paint a global picture of the current state of the art.

2.3 Single degree of freedom model of PVEH

Piezoelectric resonant structures can be modeled accurately using distributed parameter methods [69], which accounts for the multiple degrees of freedom (MDOF) of the structure and its numerous resonant modes. However, a simpler, lumped element approach is often sufficient and more convenient for design around a single resonant mode. Such a model is first presented here to introduce the dynamics, followed by a more exhaustive analysis of the parameters effects on the power output.

2.3.1 Lumped parameter modeling

Figure 2.2 illustrates the lumped modeling approach, shown here for an inertial device based on a piezoelectric unimorph cantilever beam of length L_b and with a tip mass, M_t. Although from a mechanical perspective such a continuous geometry has multiple degrees of freedom and resonant modes, the lumped representation of the piezoelectric device around its first mode resembles the traditional mechanical resonator, which includes a mechanical spring, K_m, an equivalent mass, M_{eq}, and a mechanical damper, C_m. However, an electrically coupled spring, K_{el}, and an electrical damper, C_{el}, are now introduced to wholly capture the piezoelectric effect [195]. Tied to the piezoelectric coupling θ, these two elements are also affected by the electrical load connected to the piezoelectric element, with a specific frequency response due to its capacitive nature.

From an electrical perspective, the piezoelectric device is comparable to a strain rate dependent current source connected in parallel to a piezoelectric capacitance C_p and a leakage resistance R_p (typically assumed very large, thus often neglected). Due to the electromechanical coupling with the mechanical resonator, this current source can be expanded to a series RLC circuit connected to a voltage source which depends on the applied external force or acceleration. In this representation, the resistance is tied to mechanical damping, the inductance to mass and the capacitance with mechanical compliance, whereas the coupling is presented as a transformer [89].

Model definition

For this analysis, we consider the transverse vibration mode of a weakly damped thin beam, such that its displacement can be characterized by [47]:

$$w(x,t) = \hat{w}(x)\varphi(t), \tag{2.1}$$

where $\hat{w}$ is the function providing the shape of the deformed beam, normalized to have $|\hat{w}(L_b)| = 1$, and $\varphi(t)$ is the beam tip displacement time response containing both the amplitude φ_0 and phase information ψ. For now, we consider the energy source to be an harmonic acceleration applied to the base of the cantilever beam,

$$\ddot{y}_s(t) = a(t) = \mathrm{Re}\{A\}\cos(\omega t), \tag{2.2}$$

where A expresses a phasor. Thus, the tip response $\varphi(t)$ is also harmonic,

$$\varphi(t) = \varphi_0 \cos(\omega t + \psi), \tag{2.3}$$

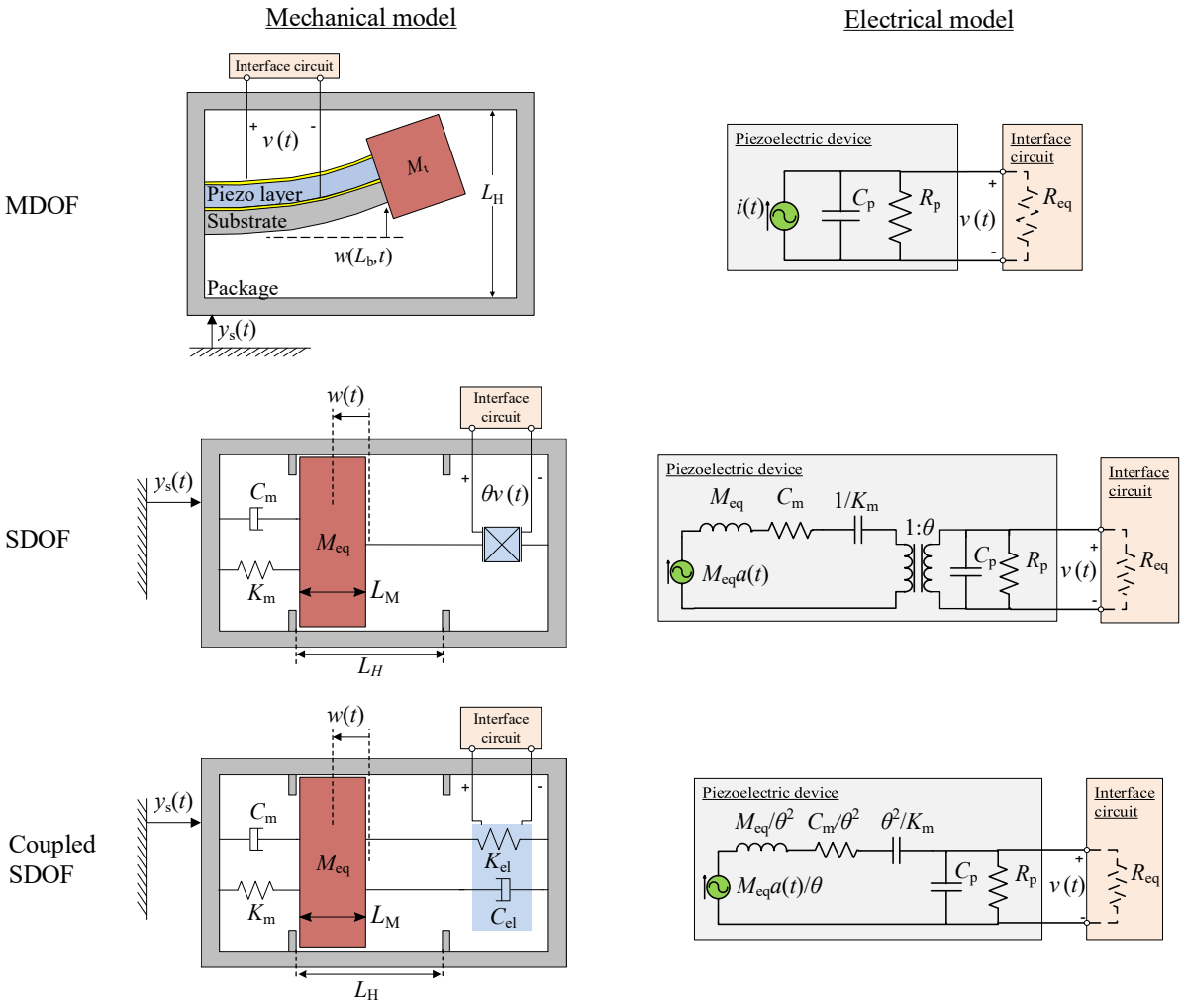

Figure 2.2 Equivalent lumped parameter model of a PVEH beam.

or expressed using phasor notations,

$$\varphi(t) = \mathrm{Re}\{\Phi\}\cos(\omega t), \tag{2.4}$$

$$w(x,t) = \mathrm{Re}\{W\}\cos(\omega t) = \hat{w}(x)\mathrm{Re}\{\Phi\}\cos(\omega t). \tag{2.5}$$

The mechanical domain equation of the lumped model at the beam tip is based on Newton's second law and can be reduced to Eq. 2.6. We then assume a purely resistive load R_{eq} as well as negligible leakage from the piezoelectric element (*i.e.*, $R_p \gg R_{eq}$). The electrical behavior is therefore captured by Eq. 2.7 and obtained from Kirchhoff circuit laws for an equivalent parallel

RC circuit connected with a variable current source.

$$M_{\text{eq}}\ddot{w}(L_{\text{b}},t)+C_{\text{m}}\dot{w}(L_{\text{b}},t)+K_{\text{m}}w(L_{\text{b}},t)-\theta v(t)=f_{\text{in}}(t), \tag{2.6}$$

$$\theta\dot{w}(L_{\text{b}},t)+C_{\text{p}}\dot{v}(t)+\frac{v(t)}{R_{\text{eq}}}=0 \tag{2.7}$$

The piezoelectric effect is completely captured through the coupling force, θv, and piezoelectric current, $\theta\dot{w}(L_{\text{b}},t)$, where $v(t)$ is the voltage and θ is the beam coupling coefficient. θ typically depends on the geometry and strain distribution of the beam and is proportional to the piezoelectric material coupling coefficient (*e.g.*, d_{31} if the structure uses the 31 mode). We do not discuss this point further for now, but it is an important aspect that is addressed in more detail in section 2.6.

We now complete the introduction of the model by describing the inertial forcing term, $f_{\text{in}}(t)$, in the right hand portion of Eq. 2.6. For a point mass, the applied force would be expressed by $a(t)M_{\text{eq}}$, but this does not account for the effect of the mass distribution of the beam and the tip mass. Hence, it can be corrected by a factor, here noted $\tilde{c}$, such that

$$f_{\text{in}}(t)=-M_{\text{eq}}a(t)\tilde{c}. \tag{2.8}$$

It is out of the scope of this chapter to provide detailed values for $\tilde{c}$, although it should be understood that if the proof mass M_{t} is large compared to the beam mass M_{b} and its motion linear with no rotation, $\tilde{c}$ will approach 1, whereas $M_{\text{eq}}\approx M_{\text{t}}$. By comparison, $\tilde{c}\approx 1.5$ and $M_{\text{eq}}\approx 0.25M_{\text{b}}$ for a beam with no tip mass. Interested readers are referred to [53, 70] for additional development on this subject.

Introducing the concepts of electrical stiffness and electrical damping

We can combine Eq. 2.6 and Eq. 2.7 using Laplace transforms and phasor notations to express the coupling force θv as electrical damping and stiffness explicitly. First, we isolate the voltage in Eq. 2.7 to obtain

$$V=-\left(\frac{j\omega R_{\text{eq}}}{1+j\omega R_{\text{eq}}C_{\text{p}}}\right)\theta W, \tag{2.9}$$

then multiply both the numerator and denominator by the complex conjugate of the denominator, $\left(1-j\omega R_{\text{eq}}C_{\text{p}}\right)$, to bring the complex term at the numerator,

$$V=-\left(\frac{j\omega R_{\text{eq}}+\omega^2R_{\text{eq}}^2C_{\text{p}}}{1+\omega^2R_{\text{eq}}^2C_{\text{p}}^2}\right)\theta W. \tag{2.10}$$

By substitution of the voltage in the Laplace transform of Eq. 2.6 we obtain

$$\left\{-\omega^2 M_{\text{eq}} + j\omega\left[C_{\text{m}} + \theta^2\left(\frac{R_{\text{eq}}}{1+\omega^2 R_{\text{eq}}^2 C_{\text{p}}^2}\right)\right] + \left[K_{\text{m}} + \theta^2\left(\frac{\omega^2 R_{\text{eq}}^2 C_{\text{p}}}{1+\omega^2 R_{\text{eq}}^2 C_{\text{p}}^2}\right)\right]\right\} W = F_{\text{in}}, \tag{2.11}$$

or alternatively

$$\left[-\omega^2 M_{\text{eq}} + j\omega\left(C_{\text{m}} + C_{\text{el}}\right) + \left(K_{\text{m}} + K_{\text{el}}\right)\right] W = F_{\text{in}}, \tag{2.12}$$

where [195]

$$K_{\text{el}} = \frac{\left(\omega R_{\text{eq}} C_{\text{p}}\right)^2}{1+\left(\omega R_{\text{eq}} C_{\text{p}}\right)^2}\left(\frac{\theta^2}{C_{\text{p}}}\right), \tag{2.13}$$

$$C_{\text{el}} = \frac{\left(R_{\text{eq}} C_{\text{p}}\right)}{1+\left(\omega R_{\text{eq}} C_{\text{p}}\right)^2}\left(\frac{\theta^2}{C_{\text{p}}}\right). \tag{2.14}$$

Equations 2.13 and 2.14 show how the electrical stiffness and damping are tied to the relative impedance difference of the external load, R_{eq}, with respect to the capacitive layer, $(\omega C_{\text{p}})^{-1}$. We discuss this behavior in more details in subsection 2.3.2.

The tip displacement phasor, W, and the coupling force phasor, θV, can now be expressed as:

$$W = \frac{\tilde{c} M_{\text{eq}} A}{\left(K_{\text{m}} + K_{\text{el}} - \omega^2 M_{\text{eq}}\right) + j\omega\left(C_{\text{m}} + C_{\text{el}}\right)} \tag{2.15}$$

$$\theta V = -\left(K_{\text{el}} + j\omega C_{\text{el}}\right) W. \tag{2.16}$$

The undamped natural frequency, traditionally given by $\omega_n = \sqrt{K_{\text{m}}/M_{\text{eq}}}$, does not consider the effect of electrical stiffness. Therefore, the system's true resonant frequency is instead expressed by

$$\omega_{\text{r}} = \sqrt{\frac{K_{\text{m}} + K_{\text{el}}}{M_{\text{eq}}}}. \tag{2.17}$$

For convenience, each parameter can be expressed in dimensionless form. As defined in Eqs. 2.18 to 2.21, Ω is the frequency ratio, ζ_{m} the mechanical damping factor, α the dimensionless time constant and κ^2 the dimensionless coupling ratio. This last parameter gives the ratio of electrical to mechanical potential energy stored in the structure in open circuit condition. It is also related

to the effective coupling factor, k_e^2, via Eq. 2.22 [153]:

$$\Omega = \frac{\omega}{\omega_n}, \tag{2.18}$$

$$\zeta_m = \frac{C_m}{2\omega_n M_{eq}}, \tag{2.19}$$

$$\alpha = \omega_n R_{eq} C_p, \tag{2.20}$$

$$\kappa^2 = \frac{\theta^2}{K_m C_p} = \frac{E_{el}}{E_{mech}}, \tag{2.21}$$

$$k_e^2 = \frac{\kappa^2}{1+\kappa^2} = \frac{E_{mech}}{E_{input}}. \tag{2.22}$$

Finally, we rearrange Eqs. 2.16 and 2.15 to get partially dimensionless expressions for the output voltage and the tip deflection [56]:

$$V = -\frac{K_m}{\theta}\left(\Delta\Omega_{el}^2 + 2j\Omega\zeta_{el}\right)W, \tag{2.23}$$

$$W = \frac{\tilde{c}A}{\omega_n^2\left[1+\Delta\Omega_{el}^2 - \Omega^2 + 2j\Omega\left(\zeta_m+\zeta_{el}\right)\right]}, \tag{2.24}$$

where $\Delta\Omega_{el}^2$ and ζ_{el} are the dimensionless forms of the electrical stiffness and damping, respectively, given by:

$$\Delta\Omega_{el}^2 = \frac{K_{el}}{K_m} = \kappa^2\left(\frac{\Omega^2\alpha^2}{\Omega^2\alpha^2+1}\right), \tag{2.25}$$

$$\zeta_{el} = \frac{C_{el}}{2\omega_n M_{eq}} = \frac{\kappa^2}{2}\left(\frac{\alpha}{\Omega^2\alpha^2+1}\right). \tag{2.26}$$

Physically, $\Delta\Omega_{el}^2$ is responsible for the resonant frequency shift typically observed on piezoelectric devices. A dimensionless form for Eq. 2.17 is similarly obtained,

$$\Omega_r = \omega_r/\omega_n = \sqrt{1+\Delta\Omega_{el}^2}. \tag{2.27}$$

Solving for power output

The electrical power generated by the piezoelectric element can be evaluated by considering the equivalent impedance of the RC circuit shown in Fig. 2.2,

$$Z_{eq} = \left(\frac{1}{R_{eq}} + j\omega C_p\right)^{-1} = \frac{R_{eq}}{1+j\omega R_{eq}C_p}. \tag{2.28}$$

The complex electric power, P_{el}, is therefore given by

$$P_{\text{el}} = \frac{VV^*}{2Z_{\text{eq}}^*} = \frac{|V|^2}{2Z_{\text{eq}}^*}, \tag{2.29}$$

where the asterisk denotes the complex conjugate. Based on Eqs. 2.23 to 2.26, we can expand and rearrange to get

$$\begin{aligned} P_{\text{el}} &= \frac{1}{2}\frac{K_{\text{m}}^2}{\theta^2}\left(\Delta\Omega_{\text{el}}^4 + 4\Omega^2\zeta_{\text{el}}^2\right)\frac{\left(1 - j\omega R_{\text{eq}}C_{\text{p}}\right)}{R_{\text{eq}}}|W|^2, \\ &= \frac{1}{2}\omega\kappa^2 K_{\text{m}}\left(\frac{\Omega\alpha - j\Omega^2\alpha^2}{\Omega^2\alpha^2 + 1}\right)|W|^2 = \omega\kappa^2 E_{\text{mech}}\left(\frac{\Omega\alpha - j\Omega^2\alpha^2}{\Omega^2\alpha^2 + 1}\right) \end{aligned} \tag{2.30}$$

The real part of Eq. 2.30 is called the active power, which is the actual average power dissipated by the load resistance. In contrast, the imaginary reactive power represents electrical energy which is stored in the device capacitance but not extracted. Looking at Eqs. 2.25 and 2.26, it is clear that the active and reactive powers are respectively tied to the electrical damping and the electrical stiffness. Hence, the average harvestable power output, $\bar{P}_{\text{el}}$, can be rearranged as in Eq. 2.31.

$$\begin{aligned} \bar{P}_{\text{el}} &= \omega K_{\text{m}}\Omega\zeta_{\text{el}}|W|^2 = 2\omega\Omega\zeta_{\text{el}}E_{\text{mech}}, \\ &= \frac{K_{\text{m}}\tilde{c}^2|A|^2}{\omega_n^3}\frac{\Omega^2\zeta_{\text{el}}}{\left[\left(1 + \Delta\Omega_{\text{el}}^2 - \Omega^2\right)^2 + 4\Omega^2\left(\zeta_{\text{m}} + \zeta_{\text{el}}\right)^2\right]}, \\ &= \frac{\tilde{c}^2 M_{\text{eq}}|A|^2}{\omega_n}\frac{\Omega^2\zeta_{\text{el}}}{\left[(1 + \Delta\Omega_{\text{el}}^2 - \Omega^2)^2 + 4\Omega^2\left(\zeta_{\text{m}} + \zeta_{\text{el}}\right)^2\right]}. \end{aligned} \tag{2.31}$$

The first factor of Eq. 2.31 regroups parameters such as the vibration amplitude and frequency, as well as the equivalent mass of the device. The second term provides the frequency response and the effect of damping on the output power. Figures 2.3, 2.4 and 2.5 illustrates the frequency response trends for this second term with variations of κ^2, ζ_{m} and α respectively. In the next subsection, we analyze further the reasons for the behaviour observed.

2.3.2 Piezoelectricity effects on resonance and closed loop solutions

As previously discussed, the piezoelectric effect can be captured by the addition of a spring and a damper which are frequency and load dependent. The response of both components, provided by Eqs. 2.13 and 2.14, is tied to the relative difference of impedance between the harvester and the extracting load. Figure 2.6 illustrates the trends based on their dimensionless

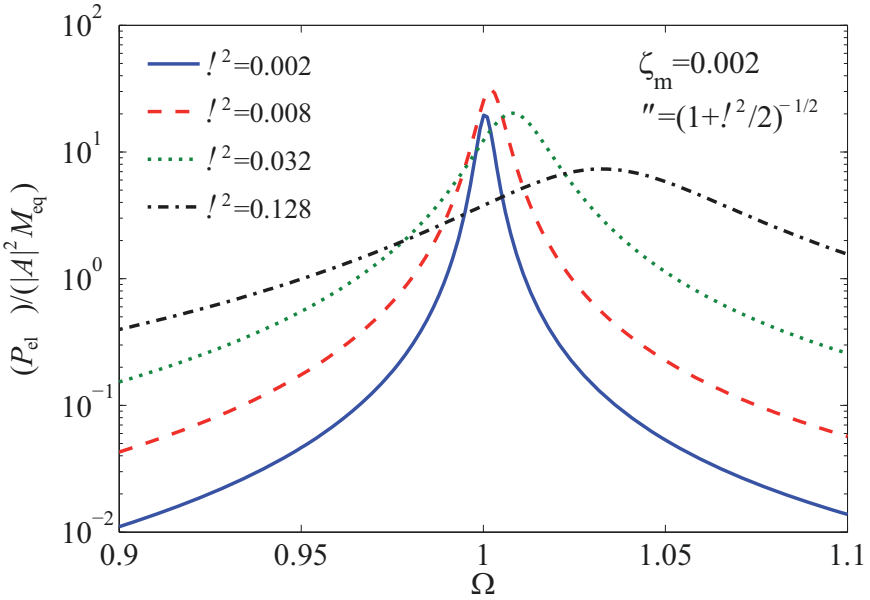

Figure 2.3 Effect of the coupling ratio, κ^2, on the power frequency response

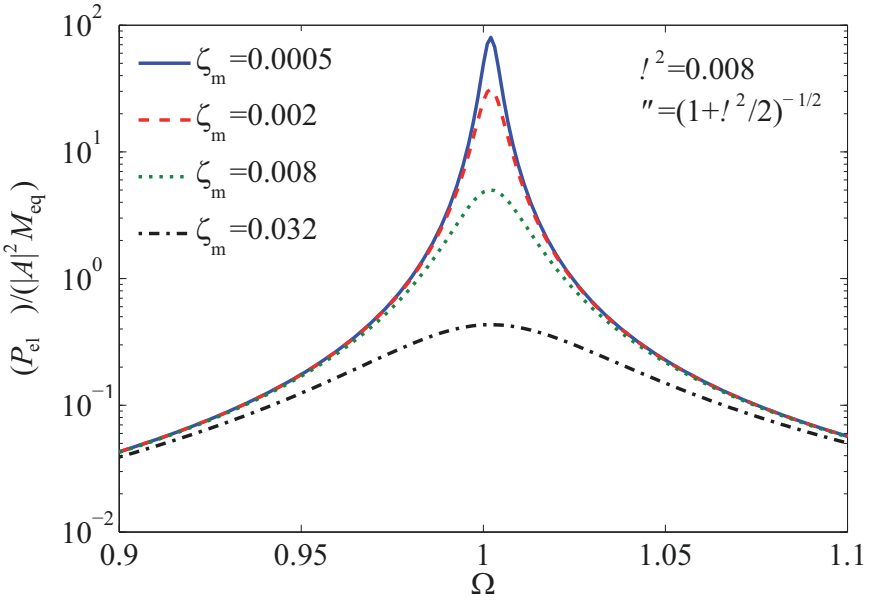

Figure 2.4 Effect of the mechanical damping factor, ζ_m, on the power frequency response

formulation. We observe that K_{el} increases with the relative impedance of the external load. This stiffening behavior occurs because more electrical potential energy is stored in the material as the impedance increases. Hence, the term θ^2/C_p effectively represents the maximum electrical stiffness issued from the piezoelectric feedback force acting on the structure in open circuit condition. It is possible to directly measure the effective coupling factor of the piezoelectric

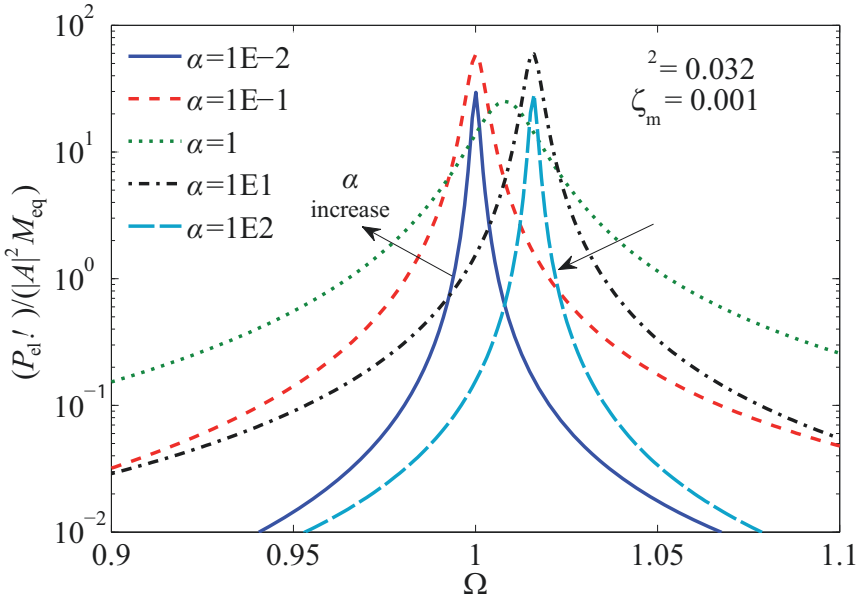

Figure 2.5 Effect of the electric load, α, on the power frequency response

transducer by observing the frequency shift occurring between the short circuit and open circuit conditions [1]. In contrast, there is no electrical damping occurring in both the open and short circuit conditions, but it is maximized when $R_{eq} = (\omega C_p)^{-1}$, which is the condition of impedance matching. We can express this in dimensionless form,

$$\alpha = \Omega^{-1}. \tag{2.32}$$

Knowing the relationship between the electrical stiffness and the load, as well as its impact on the resonant frequency, a closed loop solution for the resonant frequency ratio which only depends on the load can be obtained by solving Eq. 2.17 for $\Omega = \Omega_r$,

$$\begin{aligned} \Omega_r^2 &= 1 + \frac{\Omega_r^2 \alpha^2 \kappa^2}{1 + \Omega_r^2 \alpha^2}, \\ 0 &= \alpha^2 \Omega_r^4 + \Omega_r^2 \left[1 - \alpha^2 \left(1 + \kappa^2\right)\right] - 1. \end{aligned} \tag{2.33}$$

From the four solutions of Eq. 2.33, two are complex and two are real. The only valid solution is the positive real root provided by Eq. 2.34,

$$\Omega_r = \sqrt{\frac{\alpha^2 (1+\kappa^2) - 1 + \sqrt{\left[1 - \alpha^2 (1+\kappa^2)\right]^2 + 4\alpha^2}}{2\alpha^2}}. \tag{2.34}$$

1. This is true if dielectric leakage and parasitic capacitance are small.

For any Ω_r, an associated electrical damping factor (Eq. 2.26) can also be expressed as a function of the load only,

$$\zeta_{el}|_{\Omega=\Omega_r} = \frac{\alpha\kappa^2}{1+\alpha^2(1+\kappa^2)+\sqrt{\left[1-\alpha^2(1+\kappa^2)\right]^2+4\alpha^2}}. \tag{2.35}$$

At the resonance, the expressions for the tip displacement and power output (Eqs. 2.24 and 2.31) can also be simplified to

$$|W|_{\Omega=\Omega_r} = \frac{\tilde{c}|A|}{2\omega_n\omega_r(\zeta_m+\zeta_{el})}, \tag{2.36}$$

$$\bar{P}_{el}|_{\Omega=\Omega_r} = \frac{\tilde{c}^2 M_{eq}|A|^2}{4\omega_n}\frac{\zeta_{el}}{(\zeta_m+\zeta_{el})^2}. \tag{2.37}$$

It is important to again stress that both expressions are implicitly dependent on the load only, through Eqs. 2.34 and 2.35. This expression can therefore be used to evaluate the optimal load at the resonance peaks.

2.3.3 Resistive load optimization

Equation 2.37 is optimized by solving

$$\frac{\mathrm{d}|\bar{P}_{el}|_{\Omega=\Omega_r}}{\mathrm{d}\zeta_{el}} = 0, \tag{2.38}$$

which yields $\zeta_{el} = \zeta_m$. The resulting maximum average electrical power output, $\bar{P}_{lim}$, is therefore given by

$$\bar{P}_{lim} = \frac{\tilde{c}^2 M_{eq}|A|^2}{16\omega_n\zeta_m}. \tag{2.39}$$

It is worth mentioning that these results are independent of the transduction mechanism and were also derived for electromagnetic harvesters [215]. This conclusion therefore allows to optimize the load connected to the PVEH device, based on its known relationship with the electrical damping at resonance in Eq. 2.35. This expression is plotted in Fig. 2.7 for several coupling ratios κ^2.

For a specified mechanical damping level, shown here by a dotted line, we observe that matching both damping components is impossible if the coupling ratio is small because it limits the electrical damping achievable. In this case, the power output is maximized by a single load

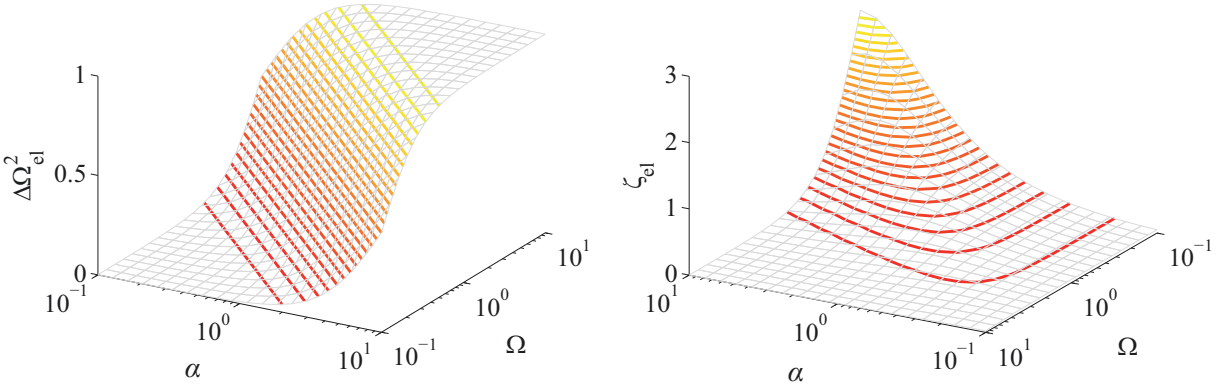

(a) (b)

Figure 2.6 (a) Electrical stiffness and (b) damping trends with the load and frequency variations. The values are normalized by κ^2.

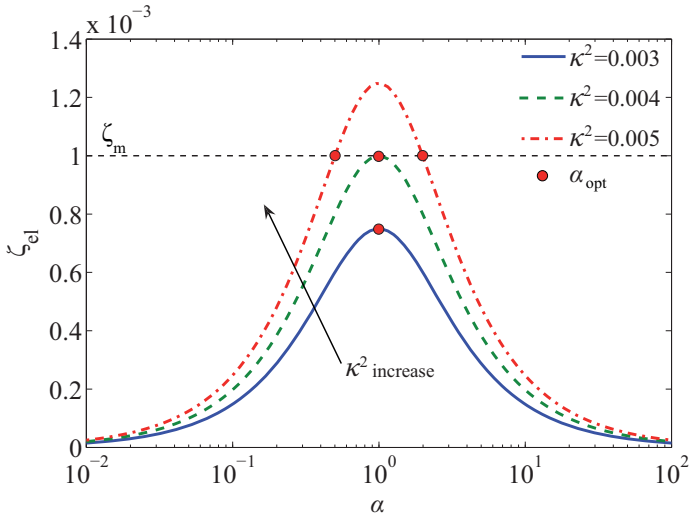

Figure 2.7 Electrical damping at resonance for several coupling ratio κ^2. The optimal loads are marked with circles and the dotted line is the corresponding mechanical damping level considered.

that matches the impedance of the piezoelectric layer. In contrast, a large coupling ratio leads to cases where the electrical damping can be the main damping mechanism and two loads can maximize the power output. One is a low impedance load, closer to the short-circuit condition and results in a low voltage output, whereas the second one is a high impedance load, which is closer to the open-circuit condition and leads to a high voltage output [2]. Between these two loads, the electrical damping dominates and the power output reduces, but an increase of the device bandwidth is observed, as shown on Fig. 2.5. Hence, beyond a certain coupling threshold, it is not possible to increase the power output for single frequency harmonic sources. We explain the reason for this phenomenon in section 2.4.1.

The comparison of the coupling with the mechanical damping is therefore an effective method to identify the type of load optimization required. A FOM that accomplishes such comparison is the resonator figure of merit. Frequently used to characterize the performance of piezoelectric surface acoustic wave (SAW) devices, we reintroduce this FOM, here in the context of VEH.

2.3.4 Resonator figure of merit

The piezoelectric resonator FOM is expressed by $\kappa^2 Q_m$ [153], where Q_m is the mechanical quality factor of the resonator. The quality factor is more generally defined as

$$Q = \frac{1}{2\zeta} = \omega_r \frac{\text{Energy Stored}}{\text{Power Dissipated}}. \tag{2.40}$$

For the piezoelectric resonator, the stored energy is the sum of the electrical energy stored in the capacitor, the potential energy stored in the spring and the kinetic energy in the mass. The power dissipated is the sum of all the power dissipation sources. Since power can be dissipated mechanically or electrically, this definition is applicable to both mechanical damping and electrical damping. Hence, the total quality factor of the device can be expressed as

$$Q_{tot} = \left(\frac{1}{Q_m} + \frac{1}{Q_{el}} \right)^{-1}. \tag{2.41}$$

Using the equations introduced in this section, we can establish a coupling criterion to state under which condition the electrical damping becomes more dominant.

2. It is worth noting that if this load becomes large, it will become sensitive to the effect of dielectric losses and the effective output power can be lower as a result.

Maximum electrical damping occurs when the impedances are matched, hence substitution of the load in Eqs. 2.25 and 2.26 by its value from Eq. 2.32 gives,

$$\Delta\Omega_{\mathrm{el}}^2|_{\alpha=\Omega^{-1}} = \frac{\kappa^2}{2}, \tag{2.42}$$

$$\zeta_{\mathrm{el}}|_{\alpha=\Omega^{-1}} = \frac{\kappa^2}{4\Omega}. \tag{2.43}$$

By then putting the result of Eq. 2.42 in Eq. 2.27, we see that there is a unique frequency ratio and load for which there is both resonance and maximization of the electrical damping,

$$\Omega_{\mathrm{r}}|_{\alpha=\Omega^{-1}} = \sqrt{1+\kappa^2/2}. \tag{2.44}$$

Taking Eq. 2.44 in Eq. 2.43, we can express the resulting maximum achievable electrical damping at resonance operation by

$$\zeta_{\mathrm{el}}|_{\Omega=\Omega_{\mathrm{r}},\alpha=\Omega_{\mathrm{r}}^{-1}} = \frac{\kappa^2}{4\sqrt{1+\kappa^2/2}}. \tag{2.45}$$

When $\zeta_{\mathrm{el}} \geq \zeta_{\mathrm{m}}$, the transition occurs, which is to say

$$\kappa^2 \geq 4\zeta_{\mathrm{m}}\left(\zeta_{\mathrm{m}} + \sqrt{\zeta_{\mathrm{m}}^2+1}\right). \tag{2.46}$$

For low coupling systems, Eq. 2.45 can be approximated to

$$\zeta_{\mathrm{el}}|_{\Omega=\Omega_{\mathrm{r}},\alpha=\Omega_{\mathrm{r}}^{-1}} \approx \frac{\kappa^2}{4}. \tag{2.47}$$

The error introduced by Eq. 2.47 is less than 2.5% for $\kappa^2 < 0.1$. Equation 2.46 can also be reduced to

$$\kappa^2 \geq 4\zeta_{\mathrm{m}}. \tag{2.48}$$

Finally, based on Eq. 2.40, the value of the resonator FOM for which the transition occurs is approximately

$$\kappa^2 Q_{\mathrm{m}} \approx 2. \tag{2.49}$$

As a criterion for PVEH, the resonator FOM basically compares the electrical damping with the mechanical damping and states that devices with low piezoelectric coupling or a low mechanical quality factor ($\kappa^2 Q_{\mathrm{m}} \ll 2$) may not be able to reach the optimal power generation condition. It is therefore useful to identify the design state of a resonator. There is an optimal design state, for which $\kappa^2 Q_{\mathrm{m}} > 2$, where:

- Mechanical damping is the only limiting factor.

- Mechanical damping and electrical damping should be matched by adjusting the load to maximize the power output at a single frequency resonance peak.

- There are two optimal loads and their value are strictly tied to mechanical damping and the coupling. These two values are obtained by solving Eq. 2.35 for $\zeta_{el} = \zeta_m$ [53]:

$$\alpha_{opt} \approx \frac{1}{1+\kappa^2}\left\{\frac{\kappa^2}{4\zeta_m} + \zeta_m\left[1 \pm \sqrt{1 - \frac{\kappa^2}{2\zeta_m^2} + \frac{1}{\zeta_m^2}\left[\left(\frac{\kappa^2}{4\zeta_m}\right)^2 - 1\right]}\right]\right\}. \tag{2.50}$$

The second design state, for which $\kappa^2 Q_m < 2$, implies that:

- Coupling and mechanical damping are both limiting factors.

- Electrical damping should be maximized.

- There is a single optimal load at resonance and it only depends on coupling,

$$\alpha_{opt} = \frac{1}{\sqrt{1+\frac{\kappa^2}{2}}}. \tag{2.51}$$

These equations make it possible to fully appreciate the relative importance of all the parameters in the optimization of the power output of resonant PVEH and, more precisely, the influence of the coupling factor and the mechanical damping. In the following sections, we discuss what they imply in terms of fundamental limits and how they impact the device design, by considering geometry optimization, the choice of an interface for electrical energy extraction and the selection of a suitable piezoelectric material. The equations developed here are used to give numerical estimates for those limits and the performance of a baseline PVEH design.

2.3.5 Baseline parameters for assessment

For future reference, the parameters found in Table 2.1 are used for a baseline design. The piezoelectric and mechanical properties considered are for a common hard lead zirconate titanate ceramic material, PZT4 [95], and the density of silicon is used for the tip mass because it can be readily micromachined. It is also worth mentioning that for thin beams made from an anisotropic material, the elasticity Y_p is derived from the compliance of the material, such as [66]

$$Y_p = (s_{11}^E)^{-1}, \tag{2.52}$$

where s_{11}^{E} is the first term of the compliance tensor of the material[3]. Also note that in the generator mode, the piezoelectric material coupling factor, k_{31}, is the ratio between the electrical energy transformed to the energy provided (*i.e.*, $k_{31}^2 = E_{\mathrm{el}}/E_{\mathrm{input}}$). For a single direction plane stress situation like in typical cantilevers, the piezoelectric 31 mode is solicited and thus [66, 153]

$$k_{31}^2 = \frac{d_{31}^2 Y_{\mathrm{p}}}{\varepsilon_{33}^{\mathrm{T}}}, \tag{2.53}$$

$$\varepsilon_{33}^{\mathrm{T}} = \varepsilon_{33}^{\mathrm{S}} + d_{31}^2 Y_{\mathrm{p}}, \tag{2.54}$$

where $\varepsilon_{33}^{\mathrm{S}}$ is the permittivity of the piezoelectric material measured with constant strain, whereas $\varepsilon_{33}^{\mathrm{T}}$ is the permittivity measured with a constant and preferably null stress.

Table 2.1 Baseline parameters used for estimates.

Young modulus Y_{p} (GPa)	Dynamic tensile strength σ_{l} (MPa)	Coupling factor k_{31}	Quality factor Q_{m}	Frequency f (Hz)	Acceleration amplitude $\lvert A\rvert$ (m/s^2)	Density ρ_{M} (kg/m^3)
81.3	24	0.33	250	150	1	2330

2.4 Mechanical power absorption

How much energy is absorbed by the device fundamentally limits what it can harvest. In this section, we seek to evaluate how the intensity of the vibration source, the quality of the mechanical coupling and the process of harvesting energy affects this quantity for resonant PVEH. First, we assume that the piezoelectric device has a large tip mass which oscillates in a purely transverse motion, hence $M_{\mathrm{eq}} \approx M_{\mathrm{t}}$ and $\tilde{c} = 1$. For now, let's also assume that the volume of this mass, Vol_{M}, occupies most of the space of the device and neglect the effect of its sweeping motion. We also assume that the frequency shift due to the piezoelectric effect is small, hence $\omega_n \approx \omega_{\mathrm{r}}$. Finally, we consider the situation of steady state vibrations so that the transfer of energy to the harvester is equal to what it dissipates:

$$\bar{P}_{\mathrm{in}} = \bar{P}_{\mathrm{el}} + \bar{P}_{\mathrm{m,loss}}. \tag{2.55}$$

3. The superscript E indicates that the property is measured with a constant or null electric field *i.e.*, in short circuit condition.

2.4.1 Inertial coupling limit of the linear resonator

The expected power output of an inertial piezoelectric resonator is fundamentally tied to the rate it can capture kinetic energy from the ambient source. To maintain its steady-state oscillations, mechanical energy must be continuously supplied by the inertial force acting on the oscillating mass. The instantaneous power transfer effectively results from the product of the applied force on the mass, $f_{\text{in}}(t)$, and its velocity, $\dot{w}(L_{\text{b}},t)$. The average power transfer, $\bar{P}_{\text{in}}(t)$, over an amount of time T is therefore given by

$$\bar{P}_{\text{in}} = \frac{1}{T}\int_0^T f_{\text{in}}(t)\dot{w}(L_{\text{b}},t)dt. \tag{2.56}$$

In the frequency domain, the vibration power input is obtained by computing the cross spectrum between these quantities [11, 124]:

$$P_{\text{in}} = \frac{\dot{W}^* F_{\text{in}}}{2} = \frac{-j\omega W^* M_{\text{eq}} A}{2}. \tag{2.57}$$

After substitution of Eq. 2.24 in Eq. 2.57,

$$P_{\text{in}} = \frac{M_{\text{eq}}A}{2}\frac{-j\omega A^*}{\omega_n^2\left[1+\Delta\Omega_{\text{el}}^2-\Omega^2-2j\Omega\left(\zeta_{\text{m}}+\zeta_{\text{el}}\right)\right]}. \tag{2.58}$$

Equation 2.58 is then rearranged to bring all complex terms to the numerator,

$$P_{\text{in}} = \frac{M_{\text{eq}}|A|^2}{2\omega_n}\frac{\left[2\Omega^2\left(\zeta_{\text{m}}+\zeta_{\text{el}}\right)-j\Omega\left(1+\Delta\Omega_{\text{el}}^2-\Omega^2\right)\right]}{\left[\left(1+\Delta\Omega_{\text{el}}^2-\Omega^2\right)^2+4\Omega^2\left(\zeta_{\text{m}}+\zeta_{\text{el}}\right)^2\right]}. \tag{2.59}$$

The reactive imaginary part represents energy temporarily stored in the mass or spring due to the phase difference between the inertial force and the mass velocity. The real part, the active power, is the time average net power transferred to the resonator. Previously defined in Eq. 2.56, it is this time explicitly expressed as function of the frequency ratio in Eq. 2.60,

$$\bar{P}_{\text{in}} = \frac{M_{\text{eq}}|A|^2}{\omega_n}\frac{\Omega^2\left(\zeta_{\text{m}}+\zeta_{\text{el}}\right)}{\left[\left(1+\Delta\Omega_{\text{el}}^2-\Omega^2\right)^2+4\Omega^2\left(\zeta_{\text{m}}+\zeta_{\text{el}}\right)^2\right]}. \tag{2.60}$$

At the resonance the applied force is in phase with the mass velocity. Hence, the active power is maximized while Eq. 2.59 shows the reactive power is zero. The input power at resonance

therefore simplifies to

$$\bar{P}_{\text{in}}|_{\Omega=\Omega_{\text{r}}} = \frac{M_{\text{eq}}|A|^2}{4\omega_n(\zeta_{\text{m}}+\zeta_{\text{el}})} = \frac{(\omega_n|W|)(M_{\text{eq}}|A|)}{2}. \tag{2.61}$$

Equation 2.61 explicitly shows that the input power continuously increases when damping is reduced. Resonance amplifies the power input, but the process of harvesting energy has a backward effect here, which explains the result presented in section 2.3.3.

2.4.2 Relevant figures of merit

Power densities

By neglecting the mass oscillation in the device volume and assuming the beam volume is much smaller than the mass, the power density is basically obtained by normalizing by the mass volume. Based on these simplifying assumptions, and considering the matching of the damping components and substitution by the mechanical quality factors via Eqs. 2.40 and 2.41, the input and output power density limits are given by

$$\frac{\bar{P}_{\text{in}}}{Vol_{\text{M}}} = \frac{\rho_{\text{M}}|A|^2 Q_{\text{tot}}}{2\omega_n} = \frac{\rho_{\text{M}}|A|^2 Q_{\text{m}}}{4\omega_n}, \tag{2.62}$$

$$\frac{\bar{P}_{\text{lim}}}{Vol_{\text{M}}} = \frac{\rho_{\text{M}}|A|^2 Q_{\text{tot}}^2}{2\omega_n Q_{\text{el}}} = \frac{\rho_{\text{M}}|A|^2 Q_{\text{m}}}{8\omega_n}. \tag{2.63}$$

Based on our baseline parameters, the resulting input power density is estimated at 154 $\mu W/cm^3$ whereas the electrical power density is exactly half this value at 77 $\mu W/cm^3$. Based only on the mass volume, the power density therefore scales with the mass density as well as the device Q_{m}. Although they provide orders of magnitude for expected power output versus the mass volume, power densities also depend on the vibration source characteristics, described by its acceleration amplitude, $|A|$, and frequency, ω. They do not provide intuitive insight regarding device performances, hence other metrics must also be considered.

Normalized power density

Although simple to evaluate, it is misleading to use power density as a metric to compare designs operating under different conditions. Beeby *et al.* [21] instead proposed its normalization by the square of the acceleration amplitude, $|A|^2$, but this neglects the effect of frequency. To account for the input power (Eq. 2.60), the power density should rather be normalized by $|A|^2/\omega$, as this

term effectively characterizes the intensity of the source. An adequate normalized power density FOM, P_ρ, can therefore be defined as [126, 140]:

$$P_\rho = \frac{\bar{P}_{\text{el}}}{Vol}\frac{\omega}{|A|^2} = \frac{M_{\text{eq}}}{4Vol}\frac{\zeta_{\text{el}}}{(\zeta_{\text{m}}+\zeta_{\text{el}})^2}. \tag{2.64}$$

Here, $Vol = Vol_{\text{b}} + Vol_{\text{M}}$ is the total effective volume of the transducer with its tip mass. We see here that P_ρ scales with ρQ_{m} to enable a fair comparison of the power output from different vibration conditions. A similar FOM was also proposed by Mitcheson *et al.* [140], who suggested normalizing the output power by $Y_0^2\omega^3 M_{\text{eq}}$, where Y_0 is the source vibration amplitude of displacement. However, we propose using the volume instead of the mass to reward designs that integrate high density materials. At the same time, normalizing by the volume instead of the mass provides an indication of how much of the device mass is useful in capturing energy.

Harvesting efficiency and harvesting effectiveness

Another useful metric is the harvesting efficiency, which can be expressed for any frequency by the ratio of output electrical power expressed in Eq. 2.31 over the input mechanical power in Eq. 2.60,

$$\eta = \frac{\bar{P}_{\text{el}}}{\bar{P}_{\text{in}}} = \frac{\zeta_{\text{el}}}{(\zeta_{\text{m}}+\zeta_{\text{el}})}. \tag{2.65}$$

Logically, a larger fraction of the energy pumped into the system is consumed electrically if $\zeta_{\text{el}} > \zeta_{\text{m}}$. A relationship between the maximum harvesting efficiency and the resonator FOM can also be defined by simply replacing ζ_{el} by Eq. 2.47 and ζ_{m} by its equivalent Q_{m}. With an impedance matched resistance, this efficiency is approximated by [173, 186]:

$$\eta_{\max} \approx \frac{\kappa^2 Q_{\text{m}}}{2+\kappa^2 Q_{\text{m}}}. \tag{2.66}$$

However, we have shown previously that the optimal power output condition occurs for $\zeta_{\text{m}} = \zeta_{\text{el}}$, thus increasing the efficiency over the 50% mark does not necessarily improve the electrical power. In fact, excessive damping reduces the amplitude, $|W|$, and the input mechanical power by extension. Although the device is more *efficient*, it produces less power from the same source because it is less *effective* at capturing energy. This trade-off is especially apparent for monochromatic sources [168], but is less so for broadband sources, as we discuss in more detail in section 2.8.1 and appendix A.

Because of these considerations, we feel it is appropriate to define another FOM, ξ, to describe the harvesting effectiveness. It is expressed as the ratio of the average electrical power output

over the electrical power limit of the device (Eq. 2.39),

$$\xi = \bar{P}_{el}/\bar{P}_{lim} = 4\frac{\zeta_m \zeta_{el}}{(\zeta_m + \zeta_{el})^2}. \tag{2.67}$$

Figure 2.8 shows the general trend expected for these FOMs as a function of the piezoelectric resonator FOM in the condition of matched impedance and resonance. For $\kappa^2 Q_m < 2$, both of the FOMs increase. However, once the coupling threshold is achieved, the resonant device can either be operated to optimize the efficiency (by matching the load impedance to the transducer) or the effectiveness (by adjusting the load to match the electrical damping with the mechanical damping) [168].

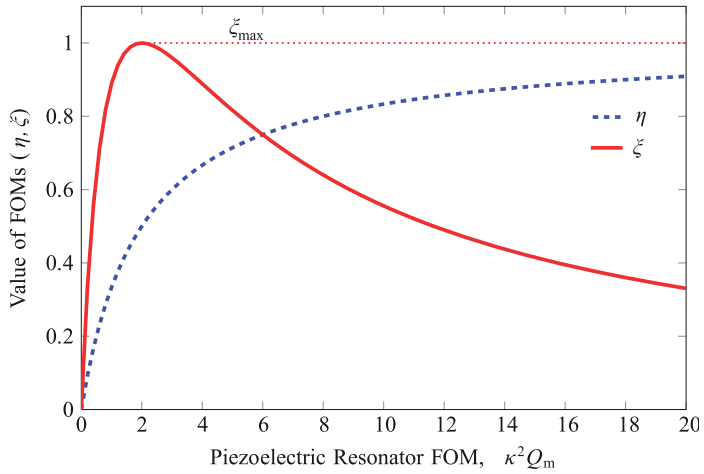

Figure 2.8 Variation of the FOMs with the resonator FOM, $\kappa^2 Q_m$.

Still, these FOMs also have their limits. To demonstrate, consider two scenarios, one where energy dissipation is caused by both mechanical and electrical damping ($\zeta_m = 0.002$ and $\zeta_{el} = 0.002$) and a second one where energy dissipation is the same but entirely caused by the piezoelectric damping ($\zeta_m = 0$ and $\zeta_{el} = 0.004$). Although the average mechanical power input would be the same in both cases, it is evident that the second case is better, because the efficiency would jump from 50% to 100% and conversely, the harvested power would also double. However, because the energy dissipation is completely controlled by the piezoelectric damping in the second situation, one could in principle indefinitely amplify $\bar{P}_{in}$ by reducing the electrical damping on purpose, thus $\bar{P}_{lim} \to \infty$. The effectiveness would then be 1 in the first scenario, but zero in the second. This result is not practical, because it requires an infinite mass displacement, which will either be restricted by the device package or lead to the harvester springs failure due to intense stresses. In this case, the power density as defined in section 2.4.2 is also not an adequate repre-

sentation of the actual power density. These additional limits on performance therefore need to be addressed and are the focus of the next section.

2.5 Mechanical energy storage

Regardless of the source, the size of the harvester eventually limits the amount of energy it can store and harvest. The space available for the mass oscillations, but also the tolerable stress in the spring elements, which is tied to their dimensions, define this limit. In this section, we address both of these aspects and develop equations to first consider the effect of the mass motion on the power density and then identify under which conditions the beam and mass size may become similar.

2.5.1 Constraints on mass oscillations from size and device package

Let's first assume the geometry of the system can be simplified to a mass moving through a rectangular slot with the same surface area as the mass, as depicted in the SDOF model of Fig. 2.2. Ideally, the size of the beam is negligible and the device package is designed to accommodate the amplitude of the mass motion $|W|$ as well as the mass length L_M, such that $W_\mathrm{max} = |W|$ and the length L_H of the packaged harvester is given as

$$L_\mathrm{H} = L_\mathrm{M} + 2W_\mathrm{max}. \tag{2.68}$$

If we then assume the device operates at resonance, the input power is real and maximized, thus we can simply express the power density based on Eq. 2.61,

$$\frac{\bar{P}_\mathrm{in}}{Volume} = \frac{\rho_\mathrm{M} L_\mathrm{M} |A| \omega_n W_\mathrm{max}}{2L_\mathrm{H}}, \tag{2.69}$$

where *Volume* is the volume of the packaged device. For a given size, L_H, two strategies are possible to optimize the power density: 1) increase the mass, by changing its density ρ_M or its size L_M, or 2) favor the mass travel W_max, by instead reducing the mass length L_M. The optimum is found by replacing W_max using Eq. 2.68 in Eq. 2.69, which gives:

$$\frac{\bar{P}_\mathrm{in}}{Volume} = \frac{\rho_\mathrm{M} |A| \omega L_\mathrm{H}}{4} \left[\tilde{L}_\mathrm{M} \left(1 - \tilde{L}_\mathrm{M}\right)\right], \tag{2.70}$$

where $\tilde{L}_\mathrm{M} = L_\mathrm{M}/L_\mathrm{H}$ is the ratio between mass and device lengths. Solving for the derivative of Eq. 2.70 with respect to $\tilde{L}_\mathrm{M}$ yields $\tilde{L}_\mathrm{M}|_\mathrm{opt} = 1/2$, the same result found by Mitcheson *et al.* [141]. In other words, although the mass density should always be maximized, there is an

ideal trade-off between its size and allowed traveling distance. Practically, half the space should be occupied by the mass volume with the rest allowing for its oscillations. The optimal input power density is hence equal to

$$\left.\frac{\bar{P}_{\text{in}}}{Volume}\right|_{\text{opt}} = \frac{\rho_{\text{M}}|A|\omega L_{\text{H}}}{16}. \tag{2.71}$$

Contrary to Eq. 2.62, Eq. 2.71 explicitly shows that power does not simply scale with the device volume. When the travel range is considered, the input power density is rather proportional to the device length L_{H}, which is unfortunately not ideal for miniaturization.

This solution is also the upper limit on the power density, although it considers that the quality factor can be adjusted to allow the mass to vibrate with just the right amplitude for any given input vibration at exactly a quarter of the device size, such that

$$Q_{\text{tot}} = \frac{\omega^2 W_{\text{max}}}{|A|} = \frac{L_{\text{H}}}{4}\frac{\omega^2}{|A|}. \tag{2.72}$$

However, this is not always possible based on the following considerations [140, 141]:

- When the source displacement is much smaller than the device size ($L_{\text{H}} \gg |A|/\omega^2$), a resonator offers optimal performance if its Q-factor is high enough to get $|W| = W_{\text{max}}$. Consequently, Q_{tot} will be limited by the material or device Q_{m}. This scenario relates to high frequency or low amplitude vibration sources, typical of machine vibrations;
- Inversely, when the source displacement is comparable or large relatively to the device size, amplification by resonance becomes less viable due to the space constraints. As a result, the mass must be damped accordingly and electrical damping will now limit the power density. For PVEH, this is effectively limited by the harvester piezoelectric coupling factor (κ^2), the harvesting circuit and the dielectric breakdown voltage. This scenario is typically representative of low frequency and high amplitude sources, such as body motion for instance. Alternative harvesting architectures, different than the linear resonator, have however been suggested for these applications to alleviate these issues [75, 76, 84, 170]. These are briefly discussed in section 2.8.2 and appendix A.3.
- Once fabricated, the device package and mass size are fixed, whereas the vibration source can change at any time. Thus, any variations in the vibration characteristics may deviate the harvester from this optimal value.

From these considerations, Mitcheson *et al.* [139] have defined four operation regions:

1. If $Q_{\text{tot}} > \frac{\omega^2 W_{\max}}{|A|}$, the mass displacement cannot be harmonic because there is not enough damping to prevent collisions with the end-stops. Electrical damping should be maximized.
2. If Q_{tot} can be adjusted to its optimal value by tuning the electrical damping, the mass should be intentionally over damped ($\zeta_{\text{el}} > \zeta_{\text{m}}$) to optimize the power output given the available space and mechanical damping.
3. If $\kappa^2 Q_{\text{m}} \geq 2$ [4] and $Q_{\text{m}} \leq 2\frac{\omega^2 W_{\max}}{|A|}$, optimal power is generated if $\zeta_{\text{el}} = \zeta_{\text{m}}$, while the mass displacement occupies as much of the available space as possible.
4. If $\kappa^2 Q_{\text{m}} < 2$ [4] and $Q_{\text{tot}} \leq \frac{\omega^2 |W|}{|A|}$, the mass displacement is confined in the available space ($|W| < W_{\max}$), even though $\zeta_{\text{el}} < \zeta_{\text{m}}$. Coupling and mechanical damping are both limiting factors, which means that a transducer offering more coupling and less mechanical damping could improve the performances.

For reference, regions 3 and 4 were effectively covered in section 2.3.4, whereas regions 1 and 2 now account for limits on the mass displacement. The general conclusion is that efficiency should be increased when the mass displacement is space constrained. Otherwise, maximizing effectiveness is preferable. Overall, region 2 represents the ideal mode of operation, since ζ_{el} can be tuned as required depending on the situation to optimize the power density and power output.

Harvesting effectiveness under space constraints

It can be argued that the effectiveness should be redefined if space limitations are now dominant. Proposed in [141], this alternate definition of the harvesting effectiveness is given as

$$\xi' = \frac{\bar{P}_{\text{el}}}{\frac{1}{2}\omega W_{\max} M_{\text{eq}} |A|} = \frac{\bar{P}_{\text{el}}}{\bar{P}_{\text{in,lim}}}, \tag{2.73}$$

where $\bar{P}_{\text{in,lim}}$ is the upper bound on the power that can be transfered to an harmonically oscillating linear resonant harvester with specified dimensional limits. It is also the upper bound on the power output if a device efficiency of 100% is assumed. This definition makes sense when the harvester is operating in regions 1 and 2. In this context, however, ξ' will tend toward the harvester's efficiency, η. For operation in regimes 3 and 4, limits on Q_{tot}, and namely on Q_{m}, prevent the mass from occupying the full device volume. Q_{m} should therefore be increased, although as we discuss in section 2.5.2, stress in the materials eventually imposes limits on this parameter as well.

4. This threshold changes depending on the circuit. See section 2.7.3 for more details.

Volume FOM

Because the effectiveness does not provide insight regarding the optimization of space inside the harvester package, Mitcheson [141] proposed the volume figure of merit, FoM_V, to compare the performance of harvesters with regard to their overall size. This metric is obtained by normalizing the electrical power output of the test device, $\bar{P}_{\text{el}}$, by the maximum power output achievable with a reference design, $\bar{P}_{\text{el,ref}}$, assuming an efficiency of 100%. For simplicity, this reference design has a cubic geometry with the same overall package volume as the test device (*i.e.*, $Volume = L_{\text{H}}^3$), but features an optimally sized gold proof mass, with a density $\rho_{\text{Au}} = 19.3$ kg/m^3, occupying half this volume. Based on equation 2.71,

$$FoM_V = \frac{\bar{P}_{\text{el}}}{\bar{P}_{\text{el,ref}}} = \frac{\bar{P}_{\text{el}}}{\frac{1}{16}\omega|A|\rho_{\text{Au}} Volume^{\frac{4}{3}}}, \tag{2.74}$$

where $Volume$ is the packaged volume of the test device.

Baseline estimates

The baseline parameters of Table 2.1 are now used to assess the impact of size constraints on the power density. The specified source characteristics, $|A| = 1$ m/s^2 and $f = 150$ Hz, yield a source displacement of 1.13 µm. Assuming $\zeta_{\text{el}} = \zeta_{\text{m}}$, and thus $Q_{\text{tot}} = 125$, the resulting amplitude of oscillation would be 141 µm. The optimal power density would therefore be obtained for a mass thickness of 282 µm and a total package thickness of 563 µm. Based on Eq. 2.71, the resulting input power density would be of 77 µW/cm^3, for an electrical power density of 39 µW/cm^3. These values are exactly half of those found in section 2.4.2, since half of the device volume is occupied by the mass. In term of maximum power, a device with a 1 cm^2 footprint could then deliver approximately 2.2 µW. However, the size of the springs is still unaccounted for. In the next section, we evaluate the effect of stress on the spring relative size compared to the mass.

2.5.2 Stress considerations

Resonant harvesters amplify energy absorption by leveraging energy stored in the mass and springs. From the definition of the quality factor in Eq. 2.40, we can express the energy stored in the springs, E_{b}, as

$$E_{\text{b}} = \frac{\bar{P}_{\text{in}} Q_{\text{tot}}}{\omega_{\text{r}}}. \tag{2.75}$$

Stored as stress, this energy must be limited to prevent device failure. The ultimate tensile stress of piezoceramics can be as high as a few hundred megapascals, but this value can be

significantly larger for microfabricated structures prepared with higher crystalline quality and lower defect densities compared to bulk ceramics [94]. For some materials, however, only a fraction (20 to 30 %) of this value can be applied during operation to avoid degradation or failure due to depolarization and fatigue [27, 162]. In addition, the spring design can create stress concentrations, which also affect the overall sustainable mechanical load.

The goal of this section is to quantify the effect of such considerations on the spring energy density and thus the necessary spring size. To do so, we first examine the best case scenario of the uniform stress distribution and then quantify the effect of a stress gradient for the typical beam configuration.

Energy density with uniform stress

The springs energy density is maximized when the highest strain possible is applied over the full volume of the transducer without leading to its failure. Hence, this optimum is achieved by uniformly stressing the material to its limit, here noted by σ_l. Such a uniform stress field can be represented by a piezoelectric block of length L_b, thickness h and width b, which is stressed along its axis. The stiffness of this block is simply given by

$$K_m = Y_p(bh/L_b), \tag{2.76}$$

where Y_p represents the Young's modulus of the piezoelectric material. It also follows that the resulting displacement is

$$|W| = (bh\sigma_l)/K_m. \tag{2.77}$$

and the energy stored in the spring material is given by

$$E_b = \frac{1}{2}K_m|W|^2. \tag{2.78}$$

By substitution of Eqs. 2.76 and 2.77 in Eq. 2.78, we get the energy stored in terms of the maximum applied stress,

$$E_b = \frac{1}{2}\frac{(\sigma_l)^2}{Y_p}bhL. \tag{2.79}$$

By normalizing Eq. 2.79 by $Vol_b = bhL$, we express the spring energy density,

$$\frac{E_b}{Vol_b} = \frac{1}{2}\frac{(\sigma_l)^2}{Y_p}. \tag{2.80}$$

Finally, we rearrange Eq. 2.80 using Eq. 2.75 to get the beam power density. This value will be used to compare with the values found in section 2.4.

$$\frac{\bar{P}_{\text{in}}}{Vol_{\text{b}}} = \frac{1}{2}\frac{\omega_{\text{r}}}{Q_{\text{tot}}}\frac{(\sigma_{\text{l}})^2}{Y_{\text{p}}}. \tag{2.81}$$

Assuming matching of the damping components, an input power density of 26.7 mW/cm^3 is obtained using our baseline parameters, whereas the electrical power density would be half of that. This value is more than two orders of magnitude larger than the 154 µW/cm^3 density obtained via Eq. 2.62 for the mechanical power density based on the mass volume. This therefore suggests that, relatively speaking, a very large mass is needed to achieve such stress levels with the specified source and quality factor. In these conditions, the size of the device is thus driven by its mass.

We will now evaluate how the electrical power density compares in a case where electrical damping is maximized. In this case, Q_{tot} is replaced by Q_{el}, which based on Eq. 2.47 and Eq. 2.40 we know can be approximated to

$$Q_{\text{el}} \approx \frac{2}{\kappa^2}. \tag{2.82}$$

Due to the uniform stress field, the conversion factor is also simply given by

$$\kappa^2 = \frac{k_{31}^2}{1-k_{31}^2}. \tag{2.83}$$

For this block of PZT4, $\kappa^2 = 0.122$ and $Q_{\text{el}} \approx 16$, which suggests an average electrical power density limit of 208 mW/cm^3. Once more, this electrical power density based on the beam stress limit is much larger than the 77 µW/cm^3 value estimated from the mass volume and the vibration source input. This value is also larger than the previous one because the transducer is now much more efficient.

However, most spring structures in resonators are more complex and are subject to stress gradients during operation, which effectively reduce their maximum energy density. This reduction is evaluated in the next sub-section for the widely used cantilever beam geometry.

Energy density reduction due to stress profile - Case of the cantilever

We now assume that this same block of piezoelectric material is subjected to a transverse force and is shaped to instead behave like a bending cantilever beam. Its stiffness is therefore given

by [53, 69]

$$K_{\mathrm{m}} = YI \int_0^{L_{\mathrm{b}}} \left(\frac{\mathrm{d}^2 \hat{w}(x)}{\mathrm{d}x^2} \right)^2 \mathrm{d}x, \tag{2.84}$$

where $YI = Y_{\mathrm{p}} bh^3/12$ is the bending modulus of the beam. Further assuming for simplicity that the deformed shape is that of a statically deformed cantilever subject to a point tip force,

$$\hat{w}(x) = \frac{1}{2}\left[-\left(\frac{x}{L_{\mathrm{b}}}\right)^3 + 3\left(\frac{x}{L_{\mathrm{b}}}\right)^2 \right]. \tag{2.85}$$

From Eq. 2.85, we then evaluate stress and stiffness using Eq. 2.84,

$$K_{\mathrm{m}} = \frac{bh^3 Y_{\mathrm{p}}}{4L_{\mathrm{b}}^3}, \tag{2.86}$$

$$\sigma_{\mathrm{l}} = \frac{3}{2}\frac{hY_{\mathrm{p}}}{L_{\mathrm{b}}^2}|W|. \tag{2.87}$$

Equation 2.78 remains valid and an additional assumption is made for simplicity. For the sake of the current argument, we consider that the piezoelectric conversion factor of the material, κ^2, specified in Eq. 2.83 remains adequate to represent the conversion effectiveness of the transducer. We know this assumption is not accurate, but we will apply the necessary correction in section 2.6.

By replacing Eqs. 2.86 and 2.87 into Eq. 2.78, and again normalizing by the beam volume, we find that the cantilever beam energy density can be written as

$$\frac{E_{\mathrm{b}}}{Vol_{\mathrm{b}}} = \frac{1}{18}\frac{(\sigma_{\mathrm{l}})^2}{Y_{\mathrm{p}}} = \frac{1}{9}\left(\frac{E_{\mathrm{b}}}{Vol_{\mathrm{b}}}\right)_{\mathrm{uniform}} \tag{2.88}$$

Comparing Eqs. 2.88 and 2.80 shows that the energy density is reduced by a factor of 9 due to the distribution of the strain along the length and across the thickness of the beam (see Fig. 2.9). The actual input power density of the cantilever therefore goes down to 3 mW/cm^3 (*i.e.*, 1.5 mW/cm^3 in terms of electrical power density) when the damping are matched, which is about 20 times the power density based on the mass. It is however much larger when maximum electrical damping is considered, with a value of 23 mW/cm^3. This again suggests that the mass is typically much larger than the beam.

The magnitude of spring energy density reduction evidently changes for other stress distributions. For instance, if the stress can be maintained over the entire length of the beam, with only a linear stress distribution through the thickness, the reduction factor is limited to 3. Such a stress distribution is notably found in triangular tapered beams subject to a tip force [53, 79] or

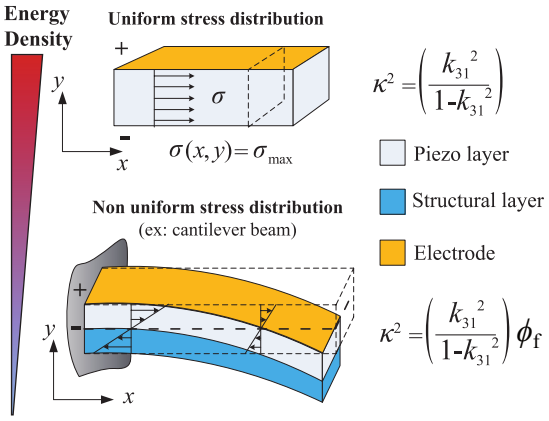

Figure 2.9 Effect of stress distribution on energy density

rectangular beams where the load is a moment instead of a transverse tip force. This type of load can occur if the tip mass length is important relatively to the beam's length, as we show in chapter 4.

Conclusion regarding relative beam size

Strictly from the mechanical strain distribution, the energy density reduction in the beam is significant [5] compared to the ideal uniform stress; on a general basis, the effect of stress concentration diminishes the spring energy density. As a result, more spring material is necessary to support the stresses induced while the harvester operates. The relation of the quality factor with the stored energy also implies that, similarly, the volume of the spring must be larger if the quality factor is increased.

By comparison with the inertial limit established previously in section 2.4, an expression for the mass to spring volume ratio for a given power output is established from the ratio of Eqs. 2.62 and 2.81. If we also replace Q_{tot} by its ideal value found in Eq. 2.72, we get

$$\frac{Vol_{\text{M}}}{Vol_{\text{b}}} = \left(\frac{\omega_{\text{r}}^2}{\rho_{\text{M}}|A|^2 Q_{\text{tot}}^2}\right)\left(\frac{\sigma_{\text{l}}^2}{Y_{\text{p}}}\right)\Lambda = \left(\frac{16}{\rho_{\text{M}} L_{\text{H}}^2 \omega_{\text{r}}^2}\right)\left(\frac{\sigma_{\text{l}}^2}{Y_{\text{p}}}\right)\Lambda, \tag{2.89}$$

where Λ is the geometric reduction factor, which we have derived as $\Lambda = 1/9$ for an homogeneous beam. Equation 2.89 further indicates that the necessary beam volume rapidly becomes important compared to the mass volume if Q_{tot} is increased, although a material with high stress and strain limits will allow for a compact beam design. More generally, it clearly indicates that the volume of the mass becomes much larger than the beam in small scale devices designed for low frequency operation. Although the density of the mass ρ_{M} also affects this ratio, its impact

5. Although it is worth considering that this property is also exploited to reduce the device resonant frequency.

is limited to an order of magnitude at most based on the density range of existing materials relative to silicon.

2.6 Electromechanical conversion

Up to this point, we have assumed the piezoelectric conversion factor, κ^2, was only dependent of the piezoelectric material based on Eq. 2.83. However, this is only true for bulk piezoelectric specimens uniformly stressed in a single direction. The conversion factor is reduced, and can even reach small values approaching zero, when a non-uniform stress is applied and passive layers are used. In this section, the effect of geometry and material properties are considered to better assess the conversion effectiveness.

2.6.1 Geometrical considerations

A useful framework for comparing and optimizing different configurations can be developed by expressing κ^2 in a way that separates the piezoelectric properties from the geometrical and mechanical parameters [53, 56]. We demonstrate this approach using a cantilever beam, although it could be extended to any transducer configuration. Here, the bending cantilever works in d_{31} mode and we assume that the electrodes cover a length $L_{\mathrm{el}} \leq L_{\mathrm{b}}$, which starts from the base of the cantilever beam because this region is the most stressed. For this configuration [53, 69],

$$\theta = Y_{\mathrm{p}} d_{31} \left(b \bar{h}_{\mathrm{p}} \int_0^{L_{\mathrm{el}}} \frac{\mathrm{d}^2 \hat{w}(x)}{\mathrm{d}x^2} \mathrm{d}x \right) = Y_{\mathrm{p}} d_{31} \phi_1, \tag{2.90}$$

$$C_{\mathrm{p}} = \varepsilon_{33}^{\mathrm{S}} \left(\frac{b L_{\mathrm{el}}}{h_p} \right) = \varepsilon_{33}^{\mathrm{S}} \phi_2, \tag{2.91}$$

where $\bar{h}_{\mathrm{p}}$ represents the distance between the beam neutral axis and the mid plane of the piezoelectric layer (see Fig. 2.10). Meanwhile, the variables ϕ_1 and ϕ_2 respectively define the impact of geometry on the piezoelectric coupling coefficient θ and the piezoelectric capacitance C_{p}. These terms can then be expressed as

$$\phi_1 = \left(b \bar{h}_{\mathrm{p}} \int_0^{L_{\mathrm{el}}} \frac{\mathrm{d}^2 \hat{w}(x)}{\mathrm{d}x^2} \mathrm{d}x \right) = b L_{\mathrm{el}} \bar{\hat{S}}_1, \tag{2.92}$$

$$\phi_2 = \frac{b L_{\mathrm{el}}}{h_p}, \tag{2.93}$$

where $\bar{\hat{S}}_1$ in Eq. 2.92 is effectively the mean strain in the volume of piezoelectric material that forms the capacitance normalized by the beam tip displacement. Based on Eq. 2.21, the coupling

factor can then be rewritten as

$$\kappa^2 = \frac{d_{31}^2 Y_\mathrm{p}^2}{\varepsilon_{33}^\mathrm{S}} \frac{\phi_1^2}{\phi_2 K_\mathrm{m}} = \frac{k_{31}^2}{1-k_{31}^2}\phi_\mathrm{f} \tag{2.94}$$

with ϕ_f being the global geometric factor, expressed as

$$\phi_\mathrm{f} = \frac{Y_p (b L_\mathrm{el} h_\mathrm{p}) \bar{\tilde{S}}_1^2}{K_\mathrm{m}}. \tag{2.95}$$

Equation 2.95 is essentially the fraction of the strain energy stored in the piezoelectric capacitor relatively to the spring full geometry. To evaluate the integrals in Eq. 2.92, stemming from θ, and Eq. 2.84, relating to K_m, we again use the simplified static deflection shape (Eq. 2.85):

$$\int_0^{L_\mathrm{el}} \frac{\mathrm{d}^2 \hat{w}(x)}{\mathrm{d}x^2} \mathrm{d}x = \frac{3}{2L_\mathrm{b}} \left[-\left(\frac{L_\mathrm{el}}{L_\mathrm{b}}\right)^2 + 2\left(\frac{L_\mathrm{el}}{L_\mathrm{b}}\right) \right], \tag{2.96}$$

$$\int_0^{L_\mathrm{b}} \left(\frac{\mathrm{d}^2 \hat{w}(x)}{\mathrm{d}x^2}\right)^2 \mathrm{d}x = \frac{3}{L_\mathrm{b}^3}. \tag{2.97}$$

Finally, the layer stacking configuration needs to be considered to evaluate the neutral axis position and the resulting bending modulus YI.

Unimorph beam

For the unimorph beam depicted in Fig. 2.10, with piezoelectric and substrate layer thicknesses respectively denoted by h_p and h_s, the distance $\bar{h}_\mathrm{p}$ is given by

$$\bar{h}_\mathrm{p} = \frac{\bar{h}_b + \bar{h}_c}{2}, \tag{2.98}$$

$$\bar{h}_a = -\frac{\frac{h_\mathrm{s}}{2} Y_\mathrm{s} h_\mathrm{s} + \left(h_\mathrm{s} + \frac{h_\mathrm{p}}{2}\right) Y_\mathrm{p} h_\mathrm{p}}{Y_\mathrm{s} h_\mathrm{s} + Y_\mathrm{p} h_\mathrm{p}}, \tag{2.99}$$

$$\bar{h}_b = h_\mathrm{s} + \bar{h}_a, \tag{2.100}$$

$$\bar{h}_c = h_\mathrm{p} + \bar{h}_b, \tag{2.101}$$

where Y_s is the Young modulus of the substrate layer, whereas the terms $\bar{h}_a$, $\bar{h}_b$ and $\bar{h}_c$ are respectively the distance between the lower surface, the piezo/substrate interface and the top surface from the neutral axis.

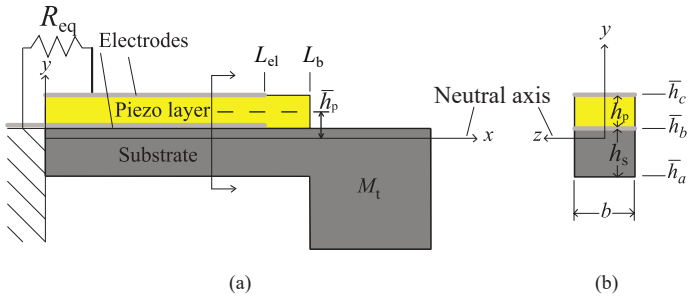

Figure 2.10 Considered beam geometry and relevant dimensions. a) Sideview, b) cross section.

The electrodes are assumed to be much thinner than the beam, thus their effect on stiffness and mass are negligible. Based on these assumptions, the bending modulus of the composite unimorph cantilever is given by

$$YI = \frac{b}{3}\left[Y_s(\bar{h}_b^3 - \bar{h}_a^3) + Y_p(\bar{h}_c^3 - \bar{h}_b^3)\right]. \tag{2.102}$$

After some algebraic manipulations, ϕ_f for the unimorph beam can finally be expressed as [53]

$$\phi_f = \frac{9}{4}\frac{\tilde{Y}H(1-H)^2\frac{L_{el}}{L_b}\left(2-\frac{L_{el}}{L_b}\right)^2}{\left[(\tilde{Y}-1)H+1\right]\left[(\tilde{Y}-1)^2H^4+(\tilde{Y}-1)H(4H^2-6H+4)+1\right]} \tag{2.103}$$

where $\tilde{Y} = Y_p/Y_s$ is the elasticity ratio between the active and structural layers, $H = h_p/h_{total}$ is the fraction of piezoelectric material that composes the beam and L_{el}/L_b is the partial coverage ratio of the electrode. The global geometric form factor ϕ_f is thus a function of both the elasticity ratio and the spatial distribution of the piezoelectric material on the structural layer.

Equation 2.103 is plotted in Fig. 2.11.a) for several elasticity ratios. The first notable thing concerns the conversion effectiveness of a bending beam made entirely from piezoelectric material. Such a configuration would be completely ineffective, with $\phi_f = 0$, due to the charge cancellation between the bottom and top halves of the cantilever, which are stressed in opposite directions. Moreover, each elasticity ratio presents an optimal thickness fraction. For instance, with $\tilde{Y} = 1$ and $L_{el}/L_b = 1$, the form factor simplifies to $\phi_f = 9/4[H(1-H)^2]$; the optimal thickness fraction is then $H = 0.33$, which gives $\phi_{f,opt} = 0.33$. This figure also demonstrates that coupling for the unimorph configuration is ideally increased by using a thick and compliant piezoelectric layer on a thin, rigid substrate. However, if we consider the thin film deposition techniques usually used in MEMS fabrication, the low fraction region is more relevant and in this case, the trend rather favors a stiff and thin layer on a thick and compliant substrate.

Bimorph beam

Equation 2.104 is obtained by evaluating YI for a symmetric bimorph beam and using the same simple scheme [53]; the results are similarly illustrated in Fig. 2.11.b).

$$\phi_f = \frac{9}{16} \frac{\tilde{Y} H \left[H^2 + 4(1-H)\right] \frac{L_{el}}{L_b} \left(2 - \frac{L_{el}}{L_b}\right)^2}{\left[\left(\tilde{Y}-1\right) H \left(H^2 - 3H + 3\right) + 1\right]} \tag{2.104}$$

Contrary to the unimorph configuration, the value of H here is $H = 2h_p/h_{total}$. We also note that the bimorph made exclusively from piezoelectric material does not suffer from the same charge cancellation problem, thanks to the segregation of the regions that are stressed in opposite directions. While the form factor remains far from unity, it is much better than for the unimorph with a value of $\phi_f \approx 0.56$. In general, the bimorph configuration works best when stiffer and relatively thinner piezoelectric films are used on a compliant base. In both cases, using piezoelectric material near the neutral axis decreases the effective coupling.

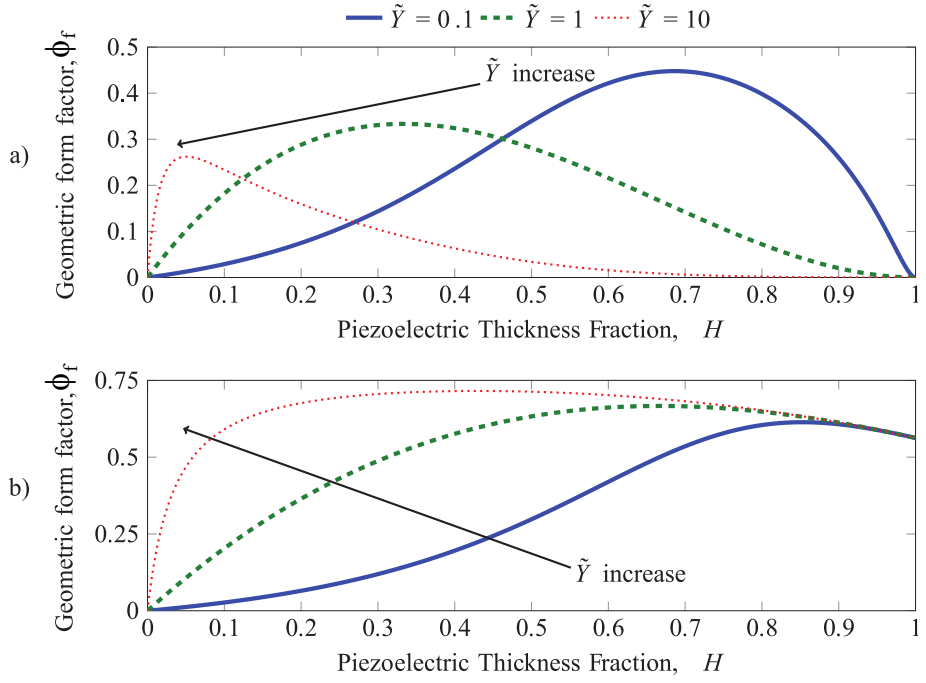

Figure 2.11 Form factor charts for various material stiffness ratio and thickness fraction for the a) unimorph and b) bimorph configurations. $L_{el}/L_b = 1$

Electrode coverage length

In addition, Eqs. 2.103 and 2.104 show that the geometric factor can also be optimized by restricting the length of the electrode on the beam. With the assumption of a point tip force, the optimal coverage ratio is $L_{el}/L_b = 2/3$, which increases ϕ_f by about 19% (to 0.39 for a

unimorph). As was the case for the energy density, this occurs because the last third of the beam does not contribute as much to the conversion of energy, since the bending moment in this portion is weaker. Extending the electrode further contributes to an overall decrease of the conversion effectiveness. This charge redistribution phenomenon was also validated experimentally by Stewart *et al.* [194] and their results are consistent with the numbers we provide here. If the stress distribution can be kept constant over the full length of the beam (*e.g.*, if the load on the rectangular beam tip is a moment), the optimal electrode design instead covers the full length of the beam. The general conclusion is that the piezoelectric material and its electrode pattern must be located on portions of the spring that are under the most stress to optimize the conversion effectiveness of the device.

Other configurations

Numerous configurations can similarly improve the conversion factor. For instance, tapered cantilevers [86] subject to a point tip force conserve a constant stress distribution over the beam length, whereas air spaced cantilevers [209] effectively reduce the impact of material near the neutral axis. In fact, Fig. 2.11.b) can be extended to cover the case of air-spaced cantilevers, since the curves tend to maximum asymptotic values as $\tilde{Y}$ increases. According to Yen *et al.*, corrugated cantilevers can also be optimized to reach form factors which are similar to bimorph beams [219]. The advantages of this geometry are that it is easier to process than a bimorph while also eliminating the need for a passive support layer.

Geometric factor impact summary

The global geometric factor can therefore be used to obtain supplementary insight on the transducer design, although it does require knowledge of the materials Young modulus. Table 2.2 summarizes the assessments made in this section by collecting values of the global geometric factor estimated for various configurations, generally assuming similar Young modulus between active and passive layers, $\tilde{Y} = 1$. The estimate for the air spaced cantilever is based on the results for the bimorph, but instead assumes $\tilde{Y} \to \infty$ and that the bending of the beam is not dominated by a S-shape, which can occur when the layers are thin and far apart [209]. In this case, the electrode has to be segmented to avoid charge cancellation [71]. Moreover, the results for the tapered beam and moment loads are based on previous mathematical demonstrations [53].

Based on the results reported in Table 2.2, several configurations can theoretically reach form factors close to unity if the thickness ratio is optimized properly, notably those subject to moment load. Fabrication of optimal MEMS structures can however be challenging considering the limited thicknesses that can be deposited by standard thin film fabrication processes.

Table 2.2 Global geometric factor for various configurations ($\tilde{Y} = 1$)

Configuration	Load	$(L_{el}/L_b)_{opt}$	H_{opt}	$\phi_{f,opt}$
Unimorph	point tip force	2/3	1/3	0.4
Symmetric bimorph	point tip force	2/3	2/3	0.79
Unimorph	moment load	1	1/3	0.44
Symmetric bimorph	moment load	1	2/3	0.89
Tapered unimorph	point tip force	1	1/3	0.44
Tapered symmetric bimorph	point tip force	1	2/3	0.89
Air spaced (symmetric)	point tip force	2/3	-	≤ 0.89
Air spaced (symmetric)	moment load	1	-	≤ 1
Corrugated (optimized)	point tip force	2/3	-	0.79
Corrugated (optimized)	moment load	1	-	0.89

2.6.2 Piezoelectric material considerations

Perhaps even more important than geometry, the piezoelectric material properties also influence the conversion effectiveness. Piezoelectric materials, which come in a variety of compositions and crystallographic structures, can be synthesized from a large range of processes. Each material and integration process present their issues and challenges, affecting the cost as well as the performances of the device [206]. A complete review of these aspects is out of the scope of this chapter, but we provide here a brief overview of existing materials by reporting how they are processed and their resulting properties. Table 2.3 and 2.4 contain data collected for a wide variety of bulk, thick and thin film piezoelectric materials.

It is also worth stressing some of the major differences between bulk piezoelectric materials and their thin film counterparts. First, the mechanical compliance of thin films is often dominated by the underlying thick substrate. Hence, they are subject to the influence of residual stresses due to mismatch in lattice constant, coefficient of thermal expansion differences, as well as coupling with other piezoelectric modes. Because these phenomena cannot be completely eliminated, it is difficult to directly measure the compliance of the film and measurements rather lead to effective film properties. Most notably, the $e_{31,f}$ constant (in stress-charge notation) generally includes some coupling with the thickness mode. Equations 2.105 and 2.106 express the relationship of this constant with the d_{ij} piezoelectric constants in the strain-charge notation for two stress

conditions [66, 198, 199].

$$\text{Thin beam, main stress in one direction :} \quad e_{31,\mathrm{f}} = \frac{d_{31}}{s_{11}^{\mathrm{E}}}. \tag{2.105}$$

$$\text{Thin plate, main stresses in two directions :} \quad e_{31,\mathrm{f}} = \frac{d_{31}}{s_{11}^{\mathrm{E}}+s_{12}^{\mathrm{E}}}. \tag{2.106}$$

For this reason, an energy harvesting FOM, noted by $e_{31,\mathrm{f}}^2/(\varepsilon_0\varepsilon_{33})$, is frequently used in the thin film processing literature instead of the usual coupling factor, k_{31}^2, that is used for bulk materials [198, 199]. The data points in Tables 2.3 and 2.4 show that some materials pro-

Table 2.3 Reported piezoelectric properties for bulk materials

Material	Type	$(s_{11}^{\mathrm{E}})^{-1}$ (GPa)	$\varepsilon_{33}^{\mathrm{T}}/\varepsilon_0$	d_{31} (pC/N)	k_{31}(%)	Q_{m}	Ref
PZT-5A	ceramic	61/71	1500/1928	-171/-190	34/37	75/80	[60, 95, 128]
PZT-5H	ceramic	58/63	3200/3935	-250/-320	36/44	30/75	[60, 95, 128]
PZT-4	ceramic	72/81	1135/1494	-120/-150	33/36	500/600	[60, 95, 128]
PZT-8	ceramic	87/96	1000/1205	-93/-127	30/36	900/1050	[60, 95, 115, 128]
PMN-0.25PT	ceramic	184	1167	-74	31	283	[16]
PMN-0.25PT	single crystals	37.3	2560	-240/-569	33/73	131/362	[16]
PMN-0.29PT	single crystals	-	5500	-1350	87	100	[37]
PMN-0.3PT	single crystals	17.5/50	6610/7800	-742/-1395	49/90	44	[156, 183, 221]
PMN-0.32PT	single crystals	15/34.8	650/5700	-160/-930	32/78	31/68	[12]
PMN-0.33PT	single crystals	14.5	8200	-1330	59	-	[222]
PMN-0.345PT	ceramic	75.4	4952	-255	75	-	[48]
PMN-0.42PT	single crystals	106	660	-91	39	-	[33]
Soft PMN-PZT	single crystals	7.87	4500/8000	-1400/-2252	90/95	100	[37, 67]
Hard PMN-PZT	single crystals	-	3100/4000	-850/-1200	86/88	>500	[37]
PZN-0.045PT	single crystals	9.35/28.6	2553/5600	-690/-1540	43/85	95/430	[108, 115]
PZN-0.045PT + 0.01Mn	single crystals	13.2/43.5	1572/3491	-542/-830	42/80	375/441	[108]
PZN-0.045PT + 0.02Mn	single crystals	27	1626/1873	-458/-502	69	336	[108]
PZN-0.07PT	single crystals	14.8	3180	478	35	-	[223]
PZN-0.08PT	single crystals	11.5	7700	-1455	60	40	[99, 183]
PZN-0.12PT	single crystals	54	612.4	-148	50	-	[48]
$BaTiO_3$	single crystals	124	168	-35	32/59	400	[60, 116, 156]
$BaTiO_3$	ceramics	110/125	625/1700	-32/-78	15/21	300/1400	[60, 95, 128]
ZnO	-	127	11/12.64	-5.2/-5.43	18/19	N/A	[95]
$LiNbO_3$	-	173	30	-1	2.6	-	[60]

vide interesting properties despite their much lower d_{31} constant. For example, barium titanate ($BaTiO_3$) offers comparable or better coupling factors than PZT ceramics because of its higher stiffness and lower dielectric constant. Thin film aluminum nitride (AlN) also compares favorably. However, we also want to stress that considering materials on the unique basis of their piezoelectric properties can be misleading. Indeed, materials with a very high coupling factor are commonly assumed to be highly desirable for high performance energy harvesters (*e.g.*, sin-

Table 2.4 Reported piezoelectric properties for some thin film materials

Material	Type	Substrate	$\varepsilon_{33}^{S}/\varepsilon_0$	$e_{31,f}$ (C/m^2)	$e_{31,f}^2/\varepsilon_0\varepsilon_{33}$ (GPa)	Q_m	Ref
AlN	MOCVD Epitaxial	Sapphire	9.5	-1.37	22.3	2490	[147]
AlN	Sputtering	Si	10.2	-1.3	18.7	-	[147]
AlN	Sputtering	-	10.5	-1.05	11.9	-	[199]
AlN	Sputtering	Si	-	-	-	120/500	[39, 126]
ZnO	Sputtering, single crystal	Si	10.9	-1.0	10.3	1770	[35, 147, 199]
PZT (53/47)	Single crystal, sputtering	MgO	200	-6.2	21.7	-	[103]
PZT (53/47)	Polycrystalline, sputtering	Si	200	-7.7	33.48	-	[103]
PZT	Sol-gel	SiO_2/Si	1100/1300	-4/-6	6/18	54/237	[147, 149]
PZT (48/52)	-	MgO	-	-3.98	-	114	[211]
PMnN-0.94PZT (48/52)	Single crystal, sputtering	MgO	100	-12.0	163	185	[211]
PMnN-0.94PZT (50/50)	Polycrystaline, sputtering	SiO_2/Si	834	-14.9	30	-	[211]
PMN-0.33PT	Single crystal, sputtering	MgO	500	-5	5.65	20	[210]
PMN-0.33PT	Single crystal, sputtering	$SrTiO_3$/Si	1600	-27	50	-	[17]

gle crystal relaxors). Even if high coupling is indeed a desirable property, we must also consider the conclusions relative to the inertial coupling limit established in section 2.4. This limit states that an increase of the coupling beyond a critical point does not always provide benefits on the net power output or power density of the resonator due to excessive damping which reduces the captured energy. In addition, the power output limit and efficiency are also closely tied to mechanical damping. It is therefore important to consider the material mechanical quality factor, Q_m, as well. In the next section, we discuss the importance of this property in the selection process by also considering the impact of the electric load.

2.7 Electrical energy extraction

To be properly harvested, the energy converted by the transducer must be extracted by the connected load. Therefore, the performance of an interface circuit can also be considered in terms of *effectiveness* and *efficiency*. The first considers the fraction of converted energy extracted and the second, the fraction of successfully extracted energy, accounting for losses like Joule effect or current leakage for instance. It is out of the scope of this work to discuss the different circuits' efficiencies. This section rather touches on the effectiveness aspect of the extraction process and its impact on the electrical damping.

2.7.1 Linear interfaces

Resistive load

In section 2.3 we presented how the piezoelectric element can be modeled as a current source connected in parallel to a capacitance, C_p. Based on this approach, we then derived the actual output power, $\bar{P}_{el}$, from the active power delivered to the resistive load. Going back to the complex power expression (Eq. 2.30) can provide indications on the level of performance achieved by this simple architecture:

$$P_{el} = \omega \kappa^2 E_{mech} \left(\frac{\Omega\alpha - j\Omega^2\alpha^2}{\Omega^2\alpha^2 + 1} \right).$$

Here, the electrical power is simply expressed by the product of the radial frequency with the electrical energy conversion, which is then modulated by a function dependent of the operating frequency and the load. This function also indicates the portions of real and reactive powers. For a short circuit ($\Omega\alpha = 0$), its modulus is 0, thus no electrical power is generated. For an open circuit ($\Omega\alpha \to \infty$), the modulus is instead 1, but the generated power is now purely reactive. In contrast, a matched impedance leads to an even distribution of active and reactive power, but the modulus is slightly lowered to $\sqrt{1/2}$. This expression therefore implies that 1) extracting energy at the same time as the capacitance is charging is not optimal to fully convert mechanical energy into electricity and 2) only half of the converted energy is dissipated by the passive resistive load, whereas the rest remains stored in the transducer and acts as a spring. Moreover, a resistance represents a permanent AC power draw and cannot be used to store energy, which is necessary in a real application.

Generalized complex load

Equation 2.7 can be easily modified to account for the effect of an added inductance L_{eq} in parallel to the circuit.

$$\theta \ddot{w}(L_b, t) + C_p \ddot{v}(t) + \frac{\dot{v}(t)}{R_{eq}} + \frac{v(t)}{L_{eq}} = 0. \tag{2.107}$$

The equivalent impedance of the resulting RLC circuit therefore becomes

$$Z_{eq} = \left[\frac{1}{R_{eq}} + j \left(\omega C_p + \frac{1}{j\omega L_{eq}} \right) \right]^{-1}. \tag{2.108}$$

Using the phasor notation and the Laplace transform, the voltage can be expressed as

$$V = \frac{\theta}{C_\mathrm{p}} \left(\frac{\omega R_\mathrm{eq} C_\mathrm{p}}{\left[\frac{R_\mathrm{eq}}{\omega L_\mathrm{eq}} - \omega R_\mathrm{eq} C_\mathrm{p} \right] + j} \right) W, \tag{2.109}$$

and using the same strategy as before to bring the complex term at the numerator to rearrange V:

$$V = \frac{\theta}{C_\mathrm{p}} \left[\frac{\frac{R_\mathrm{eq}^2 C_\mathrm{p}}{L_\mathrm{eq}} - \omega^2 R_\mathrm{eq}^2 C_\mathrm{p}^2 - j\left(\omega R_\mathrm{eq} C_\mathrm{p}\right)}{1 + \left(\frac{R_\mathrm{eq}}{\omega L_\mathrm{eq}} - \omega R_\mathrm{eq} C_\mathrm{p} \right)^2} \right] W. \tag{2.110}$$

We then substitute the terms by their dimensionless form. First, we introduce the variable β,

$$\beta = \omega_n^2 L_\mathrm{eq} C_\mathrm{p},$$

which is the impedance ratio between the inductance and the piezo layer. It is also equivalent to $\omega_{n,\mathrm{mech}}^2 / \omega_{n,\mathrm{el}}^2$, the squared ratio of the resonant frequency of the short-circuited beam (mechanical resonator) relative to the resonant frequency of the RLC circuit (electrical resonator). Hence, the circuit impedance and voltage can respectively be rewritten using non dimensional terms as

$$Z_\mathrm{eq} = R_\mathrm{eq} \frac{1}{1 + j\Omega\alpha \left(1 - \frac{1}{\Omega^2 \beta}\right)}, \tag{2.111}$$

$$V = \frac{\theta}{C_\mathrm{p}} \left[\frac{\Omega^2 \alpha^2 \left(\frac{1}{\Omega^2 \beta} - 1 \right) - j\Omega\alpha}{1 + \Omega^2 \alpha^2 \left(\frac{1}{\Omega^2 \beta} - 1 \right)^2} \right] W. \tag{2.112}$$

Finally, by using Eqs. 2.111 and 2.112 in Eq. 2.30, we finally obtain the complex electrical power with a generalized load as

$$P_{\text{el}} = \frac{1}{2}\omega\kappa^2 K_{\text{m}} \left[\frac{\Omega\alpha - j\Omega^2\alpha^2\left(1-\frac{1}{\Omega^2\beta}\right)}{1+\Omega^2\alpha^2\left(1-\frac{1}{\Omega^2\beta}\right)^2} \right] |W|^2,$$
$$= \omega\kappa^2 E_{\text{mech}} \left[\frac{\Omega\alpha - j\Omega^2\alpha^2\left(1-\frac{1}{\Omega^2\beta}\right)}{1+\Omega^2\alpha^2\left(1-\frac{1}{\Omega^2\beta}\right)^2} \right]. \tag{2.113}$$

Renno *et al*. [171] showed that the power output could be optimized for any frequency by adding the inductor. Cammarano *et al*. [29] also observed similar possibilities. The resulting RLC circuit effectively introduces a second tunable resonance mode, which is equivalent to electrically tuning both the effective stiffness and damping of the harvester. In other words, this interface affects the energy input by changing the transducer mechanical response. Based on Eqs. 2.23 and 2.113, we can easily infer the circuit effects:

$$\Delta\Omega_{\text{el}}^2 = \kappa^2 \left[\frac{\Omega^2\alpha^2\left(1-\frac{1}{\Omega^2\beta}\right)}{\Omega^2\alpha^2\left(\frac{1}{\Omega^2\beta}-1\right)^2+1} \right], \tag{2.114}$$

$$\zeta_{\text{el}} = \frac{\kappa^2}{2} \left[\frac{\alpha}{\Omega^2\alpha^2\left(\frac{1}{\Omega^2\beta}-1\right)^2+1} \right]. \tag{2.115}$$

Overall, optimal power transfer is achieved by matching the complex impedance of the circuit with that of the transducer, which in theory allows resonance at any frequency. However, it is very difficult to implement in practice over the whole frequency spectrum due in part to limits on the electrical components tuning; for low operating frequencies, matching the impedances would require very large inductances. In addition, losses due to dielectric leakage from the piezoelectric capacitance can also become limiting when the circuit impedance increases.

Nevertheless, the added inductance also allows the electrical power to be fully active when the circuit resonant frequency is matched with the source ($\beta = \Omega^{-2}$). In this condition, the voltage is in phase with mass velocity and the electrical stiffness becomes zero, whereas electrical damping can be maximized, thereby improving the effectiveness of the transducer and simplifying Eq. 2.113 to:

$$\bar{P}_{\text{el}}|_{\beta=\Omega^{-2}} = \omega\kappa^2 E_{\text{mech}}(\Omega\alpha). \tag{2.116}$$

Although here ζ_{el} effectively scales with α, suggesting it is not bounded by the same coupling limit as the pure resistance, its value cannot be increased indefinitely due to the dielectric leakage concerns mentioned above. Finally, this interface remains impractical, considering the generated power is still AC, whereas electronic components need a stable DC source.

2.7.2 Nonlinear interfaces

Because the raw output of the harvester is AC current that can vary greatly based on the live ambient conditions, other circuit components are necessary to store and convert the harvester output into a stable and usable source of energy [205]. Rectification, filtering, smoothing and voltage regulation are needed, but require diodes, capacitors, batteries and numerous other components. Conversely, these additional elements can be used as a buffer between the application and the harvester to reduce the influence of load variations on the harvesting process. However, these components also introduce losses and threshold voltages, which respectively affect the global efficiency and effectiveness of the circuit. The rest of this section presents a brief overview of the existing nonlinear circuit topologies and their impact on the harvesting process. For reference, Fig. 2.12 presents an overview of some of these topologies.

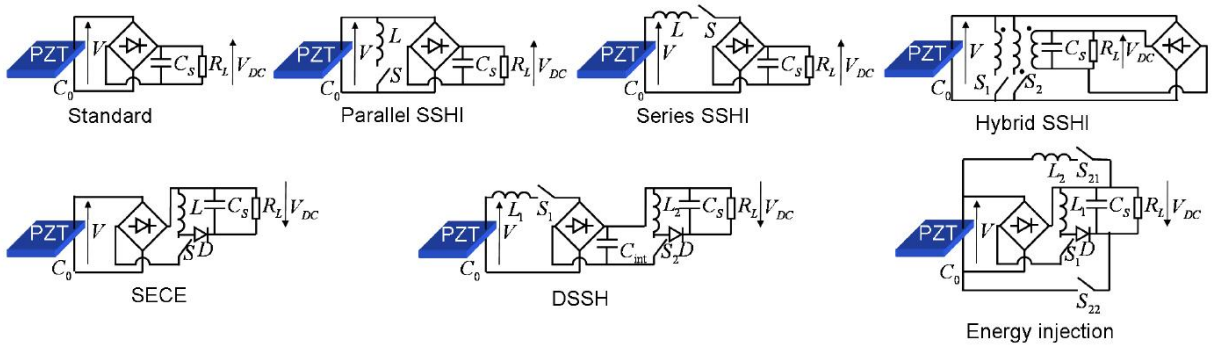

Figure 2.12 Simplified schematics of energy energy harvesting circuit topologies. Source: [112]

Diode rectifier

The most basic, but still mostly adopted passive nonlinear circuit is the diode rectifier, which allows storage of the extracted energy in an external capacitive bank to provide a DC current source. The diode rectifier is typically presented either in a half (2 diodes, half cylce rectification) or full bridge (4 diodes, full cycle rectification) configuration. With this interface, the

transducer is in open circuit condition as long as its voltage is below the operating voltage, which is the capacitor voltage at the steady state. At this point, and assuming the capacitive bank is much larger than C_p, the voltage on the transducer remains constant and current flows out as long as the stress and displacement increase. To extract the maximum amount of energy, the optimal operating voltage for the half and full bridge topologies are respectively V_{OC} and $V_{OC}/2$, where V_{OC} is the open circuit voltage amplitude on the transducer for the same input force [6] [123]. The resulting optimal power can be expressed as [81]

$$\bar{P}_{el} = \frac{\omega \kappa^2}{\pi} E_{mech}. \tag{2.117}$$

Equation 2.117 shows that the fraction of energy harvested is slightly lower, by a ratio of $2/\pi$, compared to the pure resistance (Eq. 2.30), which is due to the operating voltage threshold. Although this interface enables energy storage, it still extracts charges while the transducer is not fully stressed.

Synchronized energy extraction

Energy transfer can be improved by closing the circuit only at the peak stress of the cycle using a peak detector. Several nonlinear extraction schemes have been proposed to operate in this manner, but they are essentially based on the synchronous electric charge extraction (SECE) architecture, which allows the storage stage to be decoupled from the piezoelectric transducer [81, 112]. The basic principle is to separate the extracting process in two steps. First, the energy from the piezoelectric element is transfered to an inductance at the peak stress. The inductance and switch are located after the diode bridge. In the second step, the inductance is disconnected from the diode bridge and piezoelectric capacitance, and the stored energy is transfered to the storage capacitance. This topology can extract up to four times the energy per cycle of the standard diode rectifier interface [81, 123].

Voltage inversion

To increase even more the effect of the piezoelectric feedback force during the harvesting cycle, the voltage on the piezoelement can be inverted after each energy extraction process, which typically ends when the transducer reaches its peak displacement. The inversion process effectively allows to increase the operation voltage for a given displacement [81]. To do so, the inductor and switch are instead connected directly to the piezoelectric element in the synchronized switch

6. This is true for quasi-static operation or when the backward coupling effect on the transducer amplitude of displacement is negligible.

harvesting on inductor (SSHI) principle. Here, the energy stored in the inductance is therefore used to induce the voltage inversion. According to Guyomar *et al.* [81], this circuit architecture can extract up to 10 times the energy of the standard diode rectifier. Finally, the double synchronized switch harvesting (DSSH) is obtained by combining the SSHI and SECE topologies to simultaneously leverage the benefits of voltage inversion and synchronized energy transfer.

2.7.3 General effect of the interface circuit

Therefore, nonlinear harvesting interfaces induce a nonlinear electrical feedback force on the transducer. Because they are designed to improve the extraction process by making it more effective, they can increase the degree of damping on the structure for a given coupling level compared to a passive resistance or a standard diode rectifier.

However, we have shown in section 2.4.1 that a backward coupling effect can limit the net output power. We have also shown in section 2.3.4 that the corresponding resonator FOM for which this backward limiting effect occurs with a resistive load is $\kappa^2 Q_m = 2$. We remind that this corresponds to the value where mechanical and electrical damping can be matched, since $\zeta_{el} \approx \kappa^2/4$ at the resonance. Based on Eq. 2.117, we can also infer the maximum electrical damping induced by the optimized diode bridge as $\zeta_{el} = \kappa^2/(2\pi)$, and therefore the transition rather occurs for $\kappa^2 Q_m = \pi$ with this circuit topology.

As a result, the value of the resonator FOM where the transition occurs is lower for more effective circuits, as shown by the plots on Fig. 2.13, adapted from [112]. The figure also shows that every interface tends toward the same limit, P_{lim}, with the increase of $\kappa^2 Q_m$. The only exception is the injection technique, which actually surpasses the inertial limit, although this comparison is not entirely fair considering that previously stored electrical energy is added in the system [81]. Hence, the benefits of these circuits are significant for highly damped or lightly coupled devices that have a low $\kappa^2 Q_m$. In some of these cases, gains of more than 400% were observed in terms of power output. As pointed out in section 2.5.1, these circuits are also of interest for space constrained applications. On the other hand, the advantages of these very effective extraction schemes are diminished if used in conjunction with highly coupled or weakly mechanically damped devices [187], because they cannot overcome the inertial limit stated by Eq. 2.39. Yet, these interfaces can also improve both the harvesting efficiency and the bandwidth [119], which, as we discuss later in section 2.8.1, can be of interest in some scenarios. To conclude, Table 2.5 presents a summary of the characteristics of the different topologies presented here in terms of maximum electrical damping and transition resonator FOM (*i.e.*, $\kappa^2 Q_m$ allowing for 50% efficiency). We also estimate the value of the maximum efficiency, η, by assuming $\kappa^2 Q_m = 2$ (and $\alpha = 1$ for the linear circuit interfaces).

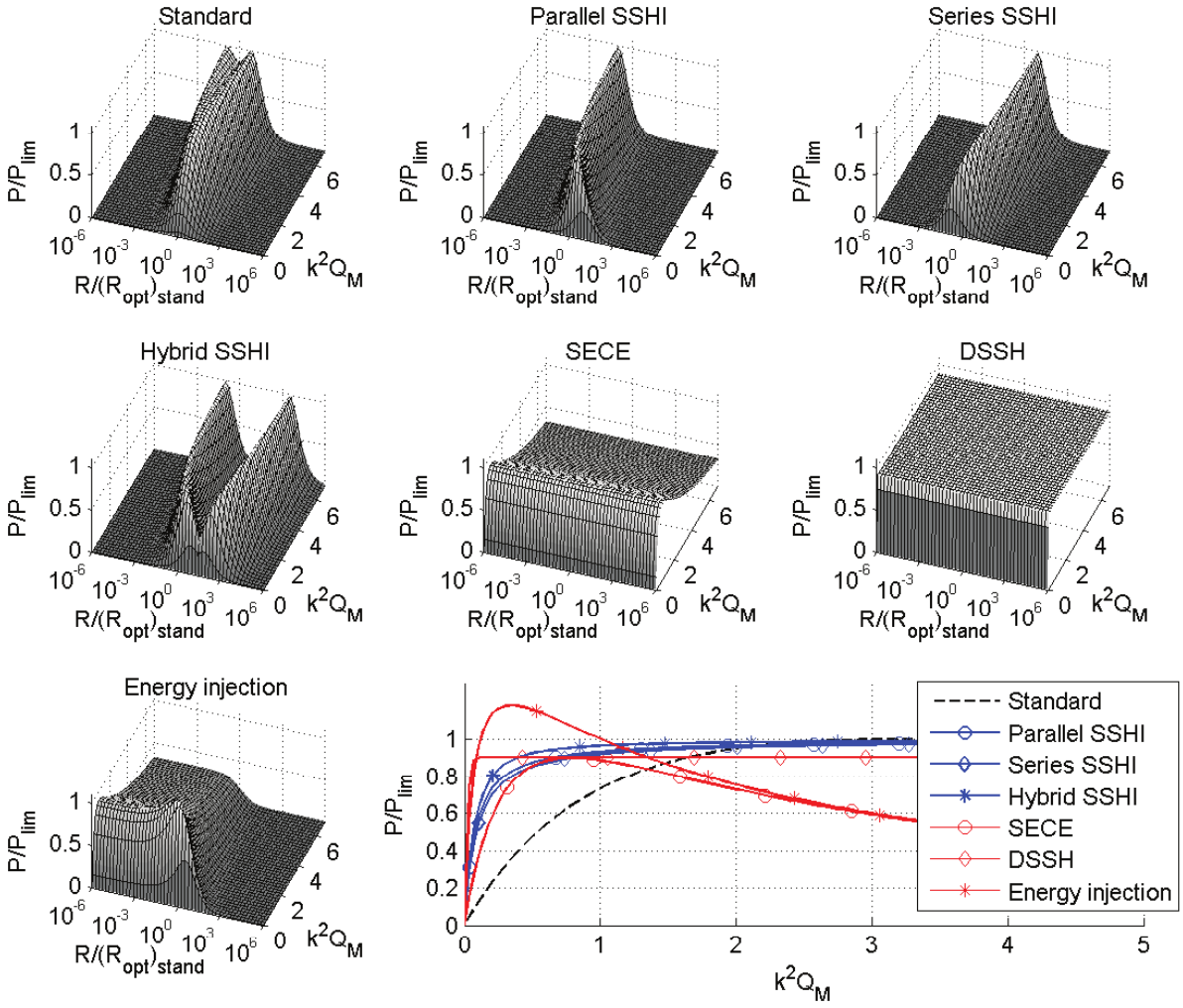

Figure 2.13 Normalized harvested power as a function of load and normalized maximum power for several extraction interfaces under a constant force magnitude. Here, the standard interface refers to the diode rectifier topology. Source: [112]

Table 2.5 Maximum electrical damping induced with transition resonator FOM, $\kappa^2 Q_{\mathrm{m}}$, for several circuit topologies

Circuit	$\zeta_{\mathrm{el,max}}$	$\kappa^2 Q_{\mathrm{m}}$	η (%)
Resistance	$\kappa^2/4$	2	50
Resistance + inductance	$\kappa^2\alpha/2$	$1/\alpha$	66
Diode rectifier	$\kappa^2/(2\pi)$	π	39
SECE	$2\kappa^2/\pi$	$\pi/4$	71
SSHI	$\approx 5\kappa^2/\pi$	$\approx \pi/10$	86
DSSH	$\approx 20\kappa^2/\pi$	$\approx \pi/40$	96

2.7.4 Possible compromise considering materials and extraction circuits

To complete our discussion regarding the selection of piezoelectric materials, we mapped the quality factor Q_m with estimates of κ^2 on Fig. 2.14. This figure considers the 31 mode properties for the materials that are reported in Tables 2.3 and 2.4, without the effect of the geometry of the composite structure (*i.e.*, a geometric form factor $\phi_f = 1$ is assumed). For comparison, some of the devices benchmarked in section 2.9.1 are also added to this figure. The dashed line is the condition $\kappa^2 Q_m = 2$, which corresponds to the critical coupling value with a resistive load. We note that most of the materials and reported devices are located in the optimal design region, which suggests that coupling should not be the only criteria for PVEH material selection. In fact, other considerations should be taken into account depending on the application.

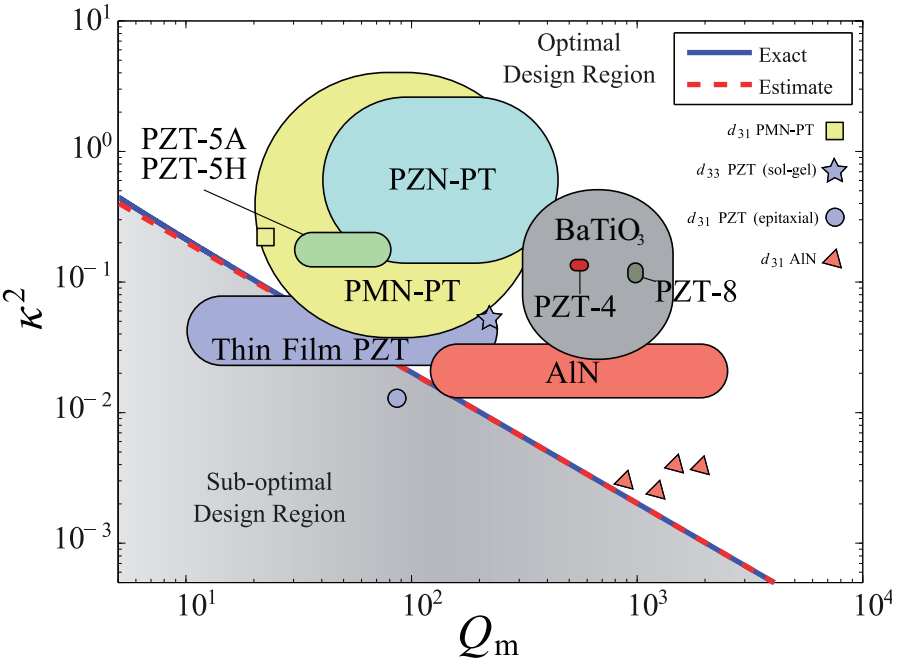

Figure 2.14 Critical coupling factor with respect to Q_m and mapping of materials for this criteria.

It is also possible to improve the performance of designs which have a lower resonator FOM by using nonlinear extraction interfaces, which therefore allow multiple design trade-offs. For instance, with a high coupling material and a highly effective extracting interface, the size of the piezoelectric active element can be reduced significantly [15, 16]. Alternatively, the use of more effective extraction schemes allows a wider selection of piezoelectric materials to produce the same power output.

2.8 Other considerations

This chapter focused primarily on linear resonant PVEH operating under a single frequency harmonic excitation. In this section, however, we broaden the scope with a discussion on wide band vibration energy harvesting. More specifically, we introduce some nuances concerning wide band sources and nonlinear approaches for vibration energy harvesting.

2.8.1 Linear resonator inertial coupling limit for broadband vibration

Resonant devices must operate at a specific frequency, which is a major setback for many field applications. A high mechanical quality factor, Q_{m}, improves the device efficiency and power density, whereas a higher Q_{tot} also improves power input amplification. However, this also implies a small operation bandwidth. If the mechanical energy source is broadband or non stationary in nature, which is the case for many ambient vibrations, it is assumed that the harvester may collect only a small portion of the available energy, resulting in a low power output and a poor power density due to frequency mismatch with the source. Reducing the quality factor improves the bandwidth, but potentially at the expense of the power output. Addressing this problem is an active area of current research.

For a single harmonic source, the optimal power is harvested by matching the electrical damping with the mechanical damping. However, the optimization is different for broadband sources [168]. Figures 2.3, 2.4 and 2.5 show the power output frequency response changes with the different damping types. If only the mechanical damping increases, the power at the resonant peak is reduced, but remains largely the same outside of the peak. Therefore, the bandwidth increase only comes from a diminution of the main peak and the average output power is lower. By instead increasing the electrical damping, it is possible to improve the frequency response outside of the peak. Although the peak is lower, the response for the nearby frequencies is increased. This general broadening of the response can be sufficient to compensate for the main peak diminution, but this depends on the shape of the power spectral density (PSD) of the harvested vibration.

Broadband noise

A more detailed analysis of random wide band vibration harvesting is presented in appendix A, where broadband and band limited Gaussian white noise vibration sources are used instead of narrow band harmonic sources. These analyses show that it is not always optimal to match the damping components for wide band sources; in fact, improving the efficiency is rather preferable. Similar results were also discussed in [87, 168]. One major consideration is that, contrary

to the narrow band situation, the power absorbed by an inertial resonator subject to random broadband white noise no longer depends on the device damping. Rather, it only depends on the source vibration power density, S_0, and the system's mass, as described in Eq. 2.118:

$$\bar{P}_{\text{in}} = \frac{S_0 M_{\text{eq}}}{4}. \tag{2.118}$$

Here, S_0 is defined using the single sided spectrum definition and is normalized by frequency units of Hz, it is thus expressed in $(\text{m}^2/\text{s}^4)\text{Hz}^{-1}$. Because Eq. 2.118 states that the input power is constant, regardless of the quality factor, increasing the electrical damping always leads to a higher power output due to an improved efficiency. The device power density simultaneously increases, since the mass displacement amplitude is reduced at the same time.

Band limited noise

For band limited sources, which can have power densities described by Eq. 2.119,

$$S_{\text{a}}(\Omega) = \begin{cases} S_0 & \text{for } \Omega_1 \leq \Omega \leq \Omega_2 \\ 0 & \text{for } \Omega_1 > \Omega > \Omega_2 \end{cases}, \tag{2.119}$$

the optimal damping level is found somewhere between the values for narrow band and broadband excitations. Figure 2.15 plots the electrical power output (normalized by the absorbed power from a white noise from Eq. 2.118) with respect to the normalized noise bandwidth $\Delta\Omega$,

$$\Delta\Omega = \Omega_2 - \Omega_1,$$

and the system total damping ratio. Here, we have assumed a constant mechanical damping of $\zeta_{\text{m}} = 0.0001$ and have also kept S_0 constant, regardless of the change of $\Delta\Omega$ (*i.e.*, the energy content increases with $\Delta\Omega$). This figure provides several informations regarding the impact of the source bandwidth on the harvester performances.

The inclined dashed isolines represent constant input power levels and correspond to specific ratios of $\frac{\Delta\Omega}{\zeta_{\text{tot}}}$, with the 50% valued isoline following $\frac{\Delta\Omega}{\zeta_{\text{tot}}} = 2$ (the half-power bandwidth of a linear oscillator by definition). The absorbed power per unit of mass is effectively function of the source power density, S_0, and bandwidth ratio between the harvester and source. In effect, the limited band noise can be approximated to a broadband white noise (95% absorbed power for $\frac{\Delta\Omega}{\zeta_{\text{tot}}} = 25$), or a monochromatic noise (5% absorbed power for $\frac{\Delta\Omega}{\zeta_{\text{tot}}} = 0.15$), depending on

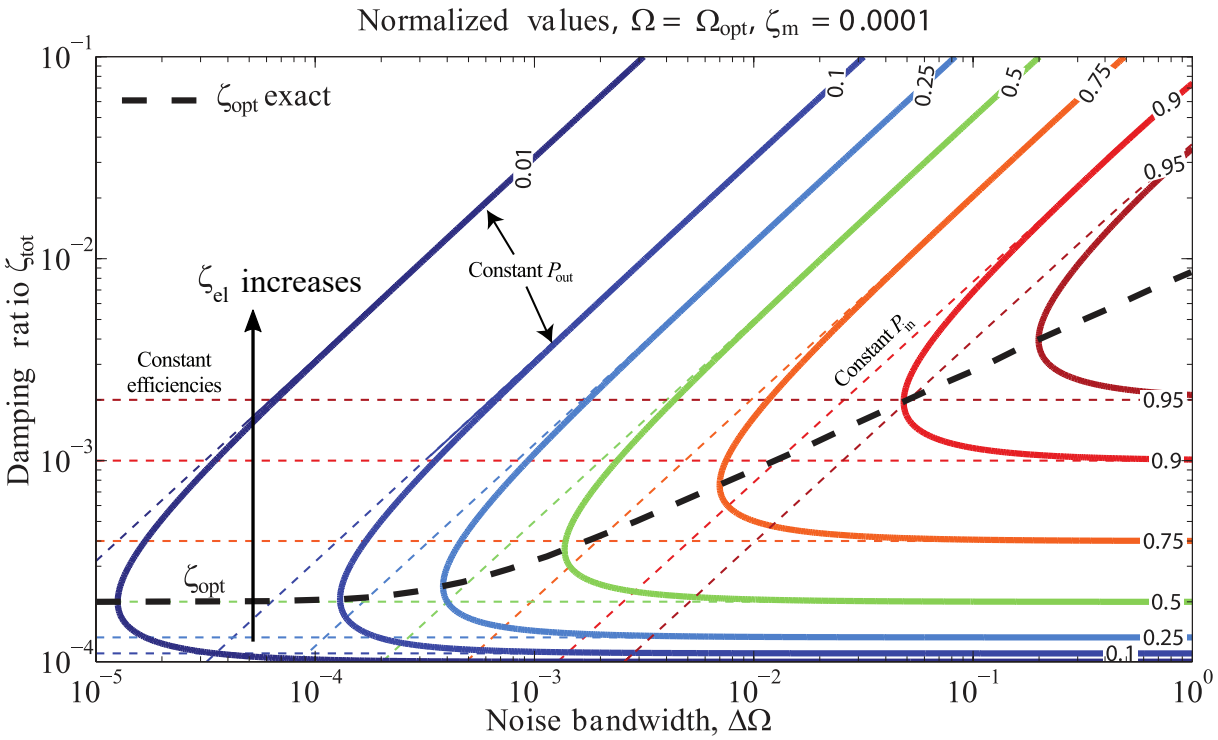

Figure 2.15 Isocurves of the normalized electrical power output by a linear oscillator subject to band limited white noise centered at the resonant frequency with $\zeta_m = 0.0001$. The dashed horizontal and diagonal lines respectively correspond to harvesting efficiencies and mechanical power inputs.

these characteristics. Nevertheless, Fig. 2.15 clearly illustrates how the harvester input power always decreases as the device bandwidth increases relatively to a specified source bandwidth.

Meanwhile, the horizontal isolines correspond to constant harvesting efficiencies, which continuously increase with ζ_{el}. By combining both values, we can find the optimal electrical damping level for given vibration characteristics. For example, for very low bandwidths, we find the optimal power is obtained when $\zeta_{el} = \zeta_m$, which corresponds to the monochromatic case. On the other hand, the electrical damping should be increase with the source bandwidth to leverage the improved harvesting efficiency and maintain an optimal power generation. Overall, the optimal power output is obtained from the ideal trade-off between the efficiency and the absorbed power. Figure 2.15 also shows that this trade-off begins between $1 \leq \frac{\Delta\Omega}{\zeta_m} \leq 10$. The optimal damping ratio then increases steadily with $\sqrt{\Delta\Omega}$.

2.8.2 Other strategies for broadband vibration harvesting

Other approaches are investigated to increase the bandwidth and improve the power output of harvesters subject to non-stationary vibrations. One simple solution is to use multimodal structures or even arrays of piezoelectric linear resonators sensitive to different frequencies [105, 118]. This approach broadens the operational bandwidth by adding degrees of freedom, but at the expense of the volumetric power density. Several papers have proposed methods to mechanically [92] or electrically [29] tune the resonant frequency or damping level to provide broadband operation while limiting the total size of the device. Nevertheless, continuous active tuning consumes energy, which has been demonstrated incapable of providing net power gains [177]. Only semi-active strategies, which are discontinuous and operate by duty-cycling, can improve the net energy balance over time. The conditions necessary for this strategy to pay-off then greatly depend on the application.

Nonlinear resonators

To avoid power consumption issues, novel approaches are investigated to passively change the frequency response of the the transducer. For example, devices incorporating nonlinear compliant structures [82, 83, 125, 127, 181, 182], magnetic coupling [8, 68, 120], stoppers [24, 24, 25, 121, 189] and buckled structures [9, 40, 217] have been the topic of numerous papers in recent years. All these schemes are based on the principle of introducing instabilities and nonlinearities to change the effective mass or stiffness of the oscillator. More recently, many research groups have shifted their focus on nonlinear bistable oscillators, as they are seen as a promising solution [88]. A critical review of these approaches is presented in [42] as well as in appendix A, where several types of vibration source are again considered.

However, based on our analyses, it is not clear that theses strategies can effectively lead to significant power density improvement. Several authors have also demonstrated this in recent years [22, 30, 42]. Although the frequency response is indeed modified by implementing these strategies, an apparent larger bandwidth is only obtained if the system is supplied enough energy to operate in its optimal state, which is not always guaranteed. Moreover, the maximum power output is reduced compared to the linear system at the nominal resonant frequency [30]. In the case of broadband white noise, most of these approaches have, in fact, no impact on the overall output power [113, 114]. Nonetheless, these strategies may present benefits in the case of non stationary narrow band vibrations, but it then becomes challenging to identify when this occurs and do general comparison of performances, because the results are greatly affected by the specific conditions considered.

Nonresonant architectures

Other device architectures have been proposed to address these challenges. Among those are so-called frequency up converter [75, 76, 110], impact based [80, 170] or latch-assisted harvesters [84]. Although these devices also operate nonlinearly, they are not based on resonance. They effectively decouple the mechanical energy absorption and the harvesting phases by using a secondary structure to transfer and absorb the kinetic energy stored in the mass upon contact between the two. This secondary structure then oscillates at its natural frequency, which is typically much higher than the source dynamics, and can extract the energy more efficiently by maximizing its electrical damping. These devices are however best suited for low frequency applications, where the scale of the device is typically smaller than the amplitude of motion of the source. Because of this, they are fundamentally restricted by the limits discussed in section 2.5.1.

According to Hosseinloo [84], an optimal strategy for this type of device is the latch principle. In this architecture, the mass is released from one end-stop when the vibration source reaches its peak, therefore allowing the mass to travel to the other end-stop as rapidly as possible. For the simple case of an harmonic vibration, and assuming the end-stops can efficiently absorb and convert all the energy stored in the mass on each contact, it is fairly simple to show, as demonstrated in section A.3, that the power input limit for this architecture is

$$\bar{P}_{\text{in,latch}} = \frac{2}{\pi} M_{\text{eq}} W_{\text{max}}^2 \omega^3 \left(\frac{|A|}{\omega^2 W_{\text{max}}} - 1 \right). \tag{2.120}$$

If $\frac{|A|}{\omega^2 W_{\text{max}}} \gg 1$, Eq. 2.120 simplifies to

$$\bar{P}_{\text{in,max}} = \frac{2}{\pi} M_{\text{eq}} |A| \omega W_{\text{max}}, \tag{2.121}$$

which only differs by a factor of $4/\pi$ with Eq. 2.61 for a linear resonant oscillator operating inside a travel range of $\pm W_{\text{max}}$. This factor was also noted by Mitcheson in [141], although he derived this value by assuming energy was rather harvested by a constant friction force of magnitude $M_{\text{eq}}|A|$. The origin of this factor is explained in appendix A.3, where nonresonant architectures are compared to an ideal harvesting cycle. As $\frac{|A|}{\omega^2 W_{\text{max}}} \gg 1$, latch based devices tend to passively replicate the optimal mass displacement waveform of an ideal cycle with the same displacement constraints, which is square signal that is synchronized with each acceleration peaks. It is worth noting that this is demonstrated for arbitrary vibration sources in [84, 87], hence this conclusion can be extended to any type of vibration waveform. Based on the analyses presented in Fig. A.21(b), which compares the power absorbed by different nonresonant architectures, we can see that the latch-based architecture is optimal only for $W_{\text{max}}/Y_0 \leq 0.19$, whereas the impact based architecture outperforms it for $W_{\text{max}}/Y_0 > 0.19$. Then, a sufficiently damped linear device can be better than both if $W_{\text{max}}/Y_0 > 1.18$. Hence, Eq. 2.121 can be extended to any harvester architecture, regardless of its operating principle or transduction mechanism, to compare their performance under given displacement constraints. The harvesting effectiveness under these conditions can then be generally redefined has

$$\xi' = \frac{\bar{P}_{\text{el}}}{\bar{P}_{\text{in,max}}} = \frac{\bar{P}_{\text{el}}}{2M_{\text{eq}}|A|\omega W_{\text{max}}/\pi}. \tag{2.122}$$

2.9 Benchmarking: review and propositions

In light of this work, it is clear that the benchmarking of PVEH devices is not trivial. Although there have been several attempts at proposing metrics for device comparison, there is currently no standard framework or procedure which has been adopted. In this context, we have presented in this chapter the different limits that can affect the performances of vibration harvesters. Along the way, we have also reviewed and discussed some of the different approaches that have been presented by numerous authors and suggested several standard metrics going forward. These FOMs are summarized in Table 2.6 with brief explanations. However, not all are used for the assessment that follows. The fact is many of the harvesters reported are either unpackaged or miss key information. We therefore focus on evaluating 5 metrics: the resonator FOM ($\kappa^2 Q_{\text{m}}$), the power density (P_{el}/Vol), the normalized power density (P_ρ), the maximum efficiency (η_{max}) and the unpackaged device effectiveness (ξ).

Table 2.6 Summary of the figures of merit.

FOM	Expression	Purpose
Normalized Power Density	$P_\rho = \bar{P}_{\mathrm{el}}\omega/(A^2 Vol) \propto \rho Q_{\mathrm{tot}}\eta$	Normalizes the power output by the specific power of a single frequency harmonic source vibration and the device static volume. It is used to compare devices designed for different harmonic sources, packaged or not.
Piezoelectric Resonator FOM	$\kappa^2 Q_{\mathrm{m}}$	Compares the mechanical losses to the electromechanical coupling of the structure. This dimensionless FOM is used to compare the levels of mechanical damping and electrical damping.
Harvesting Efficiency	$\eta = \frac{\bar{P}_{\mathrm{el}}}{\bar{P}_{\mathrm{in}}} = \frac{\zeta_{\mathrm{el}}}{(\zeta_{\mathrm{m}}+\zeta_{\mathrm{el}})}$	Gives the fraction of energy pumped in the device that is used to produce power. Essentially depends on the mechanical damping, the piezoelectric coupling and the electrical circuit.
Harvesting Effectiveness[a]	$\xi = \frac{\bar{P}_{\mathrm{el}}}{\bar{P}_{\mathrm{lim}}} = 4\frac{\zeta_{\mathrm{m}}\zeta_{\mathrm{el}}}{(\zeta_{\mathrm{m}}+\zeta_{\mathrm{el}})^2}$	Indicates if the device is close to the maximum power limit imposed by inertial coupling for a single frequency harmonic source.
Harvesting Effectiveness[b]	$\xi' = \frac{\bar{P}_{\mathrm{el}}}{\bar{P}_{\mathrm{in,max}}} = \frac{\bar{P}_{\mathrm{el}}}{2\omega W_{\mathrm{max}} M_{\mathrm{eq}}\lvert A\rvert/\pi}$	Indicate if the device is close to the maximum power limit imposed by its package size for a single frequency harmonic source.
Volume FOM	$FoM_V = \frac{\bar{P}_{\mathrm{el}}}{\bar{P}_{\mathrm{el,ref}}} = \frac{\bar{P}_{\mathrm{el}}}{\frac{1}{16}\omega\lvert A\rvert\rho_{\mathrm{Au}} Volume^{\frac{4}{3}}}$	Compares the device output power to the power output of an hypothetical design subject to a single frequency harmonic source. The baseline design is packaged and features an optimized high density gold mass occupying half the device volume.
Global geometric factor	$\phi_{\mathrm{f}} = \kappa^2\left(\frac{1-k_{31}^2}{k_{31}^2}\right)$	Evaluates the impact of the transducer geometry on the coupling factor. Describes the stress gradient in the transducer and its effectiveness for electromechanical conversion.

[a] When limited by mechanical damping

[b] When limited by package

2.9.1 Device assessments

This section compares the performance of different PVEH resonators reported in the literature plus three designs from IMEC (which agreed to provide partial for this study). The results of this investigation are summarized in Table 2.7, which focuses on PZT-based devices, and Table 2.8, which reports lead-free designs. All the designs reported produce power on the order of 1 to 60 µW across a frequency range going from 50 Hz to 3 kHz. One can also notice that they generally feature a proof mass that is much larger than the beam. PZT based devices also generally have a lower mechanical quality factor compared to those that uses AlN, which is consistent with Fig. 2.14.

Table 2.7 Assessment of PZT-based PVEH devices reported in the literature.

	Ref.	[148]	[143][c]	[67][c]	[5][b]	[72]	[185]
Design	Piezo	d_{33} PZT	d_{31} PZT	d_{31} PMN-PT	d_{31} PZT (bimorph)	d_{31} PZT	d_{31} PZT
	Substrate	Si	SS	Al	-	Si	Si
	Process	Sol-gel	Epitaxial	Bonded bulk	Bonded/Thinned	Sol-gel	Sol-gel
	Piezo thickness (µm)	2	2.8	500	20/25	1.64	1
	Beam thickness (µm)	9	56	1330	60	16.3	36.63
	Thickness fraction	0.222	0.050	0.376	0.750	0.101	0.027
	Mass[a] (mg)	0.76	38	490	320	1.6	1.4
	Mass material	Si	-	-	W	Ni	Si
	Vol_b (mm^3)	0.0029	5.1	106	0.75	0.0137	0.0469
	Vol_M (mm^3)[a]	0.32	0	0	15.625	0.18	0.6051
	Vol (mm^3)	0.3229	5.1	106	16.375	0.1937	0.652
Test cond.	f (Hz)	877	126	1835	158	609	461.15
	$\|A\|$ (m/s^2)	19.6	5	9.81	0.98	9.81	19.6
	$\|A\|^2/\omega$ (m^2/s^3)	0.07	0.032	0.0083	0.00097	0.025	0.13
Perf.	Q_m	220[a]	85	22	40[a]		400[a]
	k_e^2	0.05	0.013	0.18	0.15[a]		
	$\kappa^2 Q_m$	11.6[a]	1.1	4.8	6.8[a]		
	P_{el} (µW)	1.4	5.3	7.3	1.58	2.16	2.15
FOM	P_{el}/Vol (µW/mm^3)	4.36	1.04	0.0689	0.0965	11.2	3.30
	P_ρ $\left(\frac{\mu W s^{-1}}{mm^3 (m/s^2)^2}\right)$	62	33	8	100	443	25
	η_{max}[a] (%)	85	36	71	77		
	ξ	0.96	0.68	1.1	1.0		0.23

[a]Estimated values

[b]Operating at maximum efficiency

[c]Calculations corrected for lack of tip mass

Some of the FOMs for these various designs are plotted against one another in Fig. 2.16. In terms of normalized power density, Fig. 2.16(a) shows that both of Nguyen's devices [150, 151] dominate, with values around 2 mW-s^{-1}/(mm^3(m/s^2)^2). These two devices use doped aluminum nitride as their active material, but the device presented in [151] also has a tungsten proof mass, whereas the one in [150] is made of standard silicon. Although they have reportedly high me-

Table 2.8 Assessment of lead-free PVEH devices reported in the literature.

	Ref.	[61]	[169]	[10]	[216]	[151]	[150]	[138]	[34]	[201]	IMEC1A[b]	IMEC4B[b]	IMEC7A[b]
Design	Piezo	d_{31} AlN	d_{31} AlN	d_{31} AlN	d_{31} KNN	d_{31} (MgHf)AlN	d_{31} (MgHf)AlN	d_{31} (MgZr)AlN	d_{31} AlN	d_{31} KNN	d_{31} AlN	d_{31} AlN	d_{31} AlN
	Substrate	Si	Si	Si	Si	Si	Si	Si	SS	SS	Si	Si	Si
	Process	Sputtering	Sputtering	Sputtering	Chemical solution	Co-Sputtering	Co-Sputtering	Co-Sputtering	Sputtering	Sputtering	Sputtering	Sputtering	Sputtering
	Piezo thickness (µm)	0.8	1.2	1	1	0.7	0.7	2	1.89	2.2	2	2	2
	Beam thickness (µm)	45	51.2	13.9	10	40	50	12	52	32.7	52	52	52
	Thickness fraction	0.018	0.023	0.072	0.100	0.018	0.014	0.167	0.036	0.067	0.038	0.038	0.038
	Mass[a] (mg)	28	14	28.9	1.5	6.3	0.6	0.6	1617	25	15	15	40
	Mass material	Si	Si	Si	Si	W/Si	Si	Si	Cu	SS	Si	Si	Si
	Vol_b (mm^3)	0.23	0.061	0.47	0.02	0.008	0.01	0.00492	3.23	0.65	0.22	0.27	0.37
	Vol_M (mm^3)[a]	12.5	6	12.5	1.5	0.686	0.258	0.24	180.5	3.25	6	6	16.9
	Vol (mm^3)	12.73	6.061	12.97	1.52	0.694	0.27	0.24492	183.73	3.9	6.22	6.27	17.27
Test cond.	f (Hz)	572	1082	58	132	926	2497	792	66.4	393	1178	1002	620
	$\|A\|$ (m/s^2)	19.6	3.14	4.9	9.81	4.9	8.83	8	9.81	10	6.28	6.28	6.28
	$\|A\|^2/\omega$ (m^2/s^3)	0.11	0.0015	0.066	0.12	0.0041	0.005	0.013	0.23	0.040	0.0053	0.0063	0.010
Perf.	Q_m	160	1200			920[a]	1000 [a]	800[a]		90	1900	1450	865
	k_e^2		0.0025								0.0039	0.004	0.003
	$\kappa^2 Q_m$		3								7.4	5.8	2.6
	P_{el} (µW)	60	3	32	3.62	5.8	2.6	1.3	51.74	1.6	10	10	32
FOM	P_{el}/Vol (µW/mm^3)	4.71	0.495	2.47	2.38	8.36	9.63	5.31	0.282	0.410	1.61	1.59	1.85
	P_ρ $\left(\frac{\mu W s^{-1}}{mm^3 (m/s^2)^2}\right)$	44	341	37	21	2025	1938	413	1	10	302	255	183
	η_{max}[a] (%)		60								79	74	57
	ξ	1	0.99			1.9	7	1.7		0.14	0.53	0.59	0.73

[a] Estimated values

[b] Operating at maximum efficiency

chanical quality factors (both close to 1000), a desirable property that can partly explain this level of performance, the device with the high density tungsten proof mass should theoretically provide close to an order of magnitude improvement over the device with the silicon mass, assuming that similar piezoelectric coupling properties have been achieved for both. Most of the other devices that have a silicon proof mass and a Q_m value of similar order of magnitude, such as those from Minh [138], Renaud [169] and IMEC, follow this trend as well. Figure 2.16(c) however shows an effectiveness $\xi \approx 7$ for the design presented in [150], which strongly violates the inertial limit (here shown by the thick red line at $\xi = 1$). Hence, the results reported in [150] may contain discrepancies and can be questioned. To a lesser extent, it is also the case for the results reported in [138, 151].

As noted previously, P_ρ generally scales with ρQ_m. For example, Renaud's device [169] achieves a relatively large P_ρ due to its high Q_m and despite its silicon mass. On the other hand, a low value of Q_m can be compensated by using materials with higher density, as can be seen from the devices reported by Aktakka *et al*. [5], which uses tungsten. Despite a poor quality factor of approximately 40, which is 30 times worse than what is reported by Renaud *et al*., it is able to reach a normalized power density that is only 3.5 times less. It is also probable that Fang's [72] and Morimoto *et al*.' [143] designs, which respectively use nickel and stainless steel, also benefit from using slightly denser materials than silicon.

In terms of maximum efficiency, η_{max}, the devices made of AlN fabricated by IMEC generally do well compared to the others despite their relatively low coupling, highlighting the benefits of their high quality factor. The PZT based devices reported in [5, 67, 148] provide similar or better efficiency because of their high piezoelectric coupling. Muralt's design [148] achieves the best result by leveraging a moderately good Q_m and using an interdigitated electrodes design that benefits from the better d_{33} mode properties. Akatakka's design [5] poor Q_m is similarly compensated by its bimorph configuration that minimizes the use of passive materials. The device reported by Erturk *et al*. [67] achieves its good efficiency by using PMN-PT, a high coupling single crystal relaxor material. Nevertheless, these three devices do not have the best normalized power density, because they are limited by Q_m.

In addition, Fig. 2.16(b) shows that devices with $\kappa^2 Q_m \geq 2$ have been fabricated numerous times, both at the MEMS scale and at the mesoscale [67]. This is also reflected in Fig. 2.16(c), which shows that multiple devices reaching the inertial coupling limit have been fabricated.

Finally, Fig. 2.17 maps the normalized power density for all the reported devices versus their frequency of operation. The general trend seems to be that this FOM decreases in the lower frequency range. One hypothesis for the lower performances registered could originate from

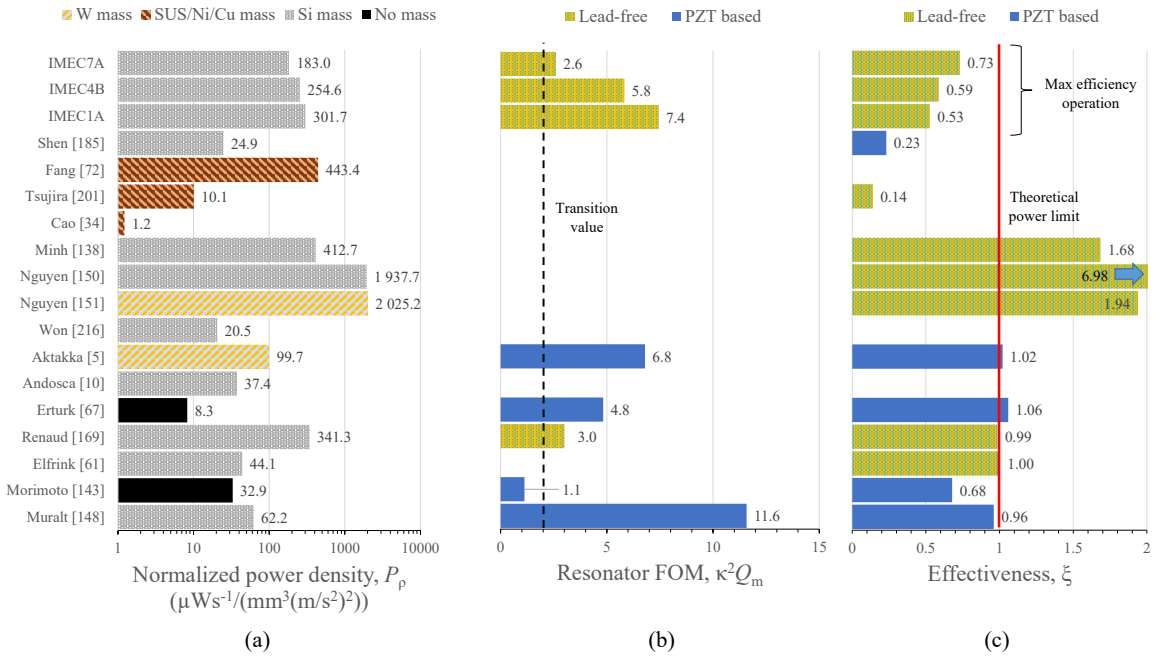

Figure 2.16 Comparison of the normalized power density (a), resonator FOM (b) and harvesting effectiveness (c) for the reported devices.

lower Q_m values. Harvesters that target low frequencies are generally built at the mesoscale, but their Q_m rarely match those achieved by silicon MEMS devices designed to operate at higher frequencies. Even then, silicon MEMS devices become more sensitive to the effects of fluid damping as the frequency decreases [23]. Because the amplitude of motion also increases, squeeze film can become significant as well. Although vacuum packaging can alleviate these effects [63], the space constraints introduced will also impact the maximum power achievable, as discussed in section 2.5.1. Many piezoelectric materials are reported here, but it appears the main characteristics allowing for high performance are a high mass density and a high Q_m value.

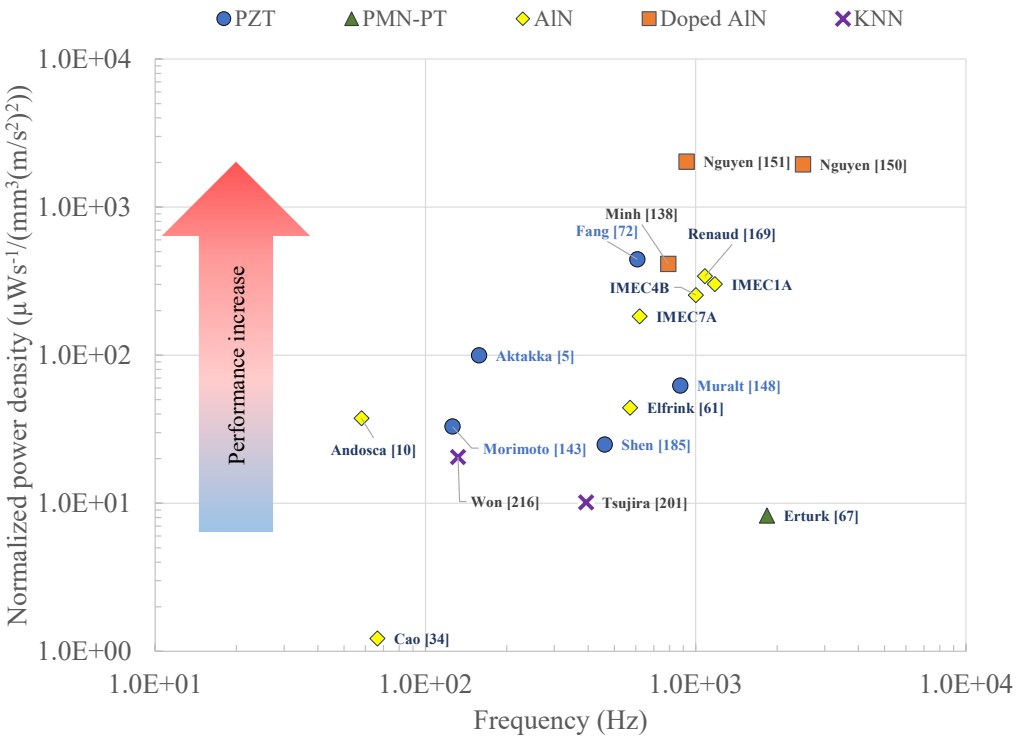

Figure 2.17 Normalized power density versus frequency of reported devices.

2.10 Conclusion

This chapter reviewed the various aspects that can limit the power output and the power density of piezoelectric vibration energy harvesters, with a focus on linear resonant devices. To support the analyses, we introduced a streamlined, lumped parameter modeling approach and addressed the need for relevant metrics of comparison for PVEH system design by investigating several ways to assess the performance. We did so by:

1. comparing the amount of energy captured by the device with the intensity of the source;
2. comparing the amount of energy produced by the device with how much energy it can capture (with and without size constraints);
3. comparing the maximum amount of energy that can be stored by the mass versus the springs;
4. evaluating the fraction of energy that can be converted into electricity by the transducer based on its geometry and material properties;
5. evaluating the fraction of electric energy extracted from the device by the circuit and how it impacts the overall system efficiency.

For typical values, a power density limit below the 100 μW/cm^3 range was estimated for silicon based devices, a limit that is mostly due to the inertial coupling limit. However, to reach this power density, the PVEH must be well designed. If the device is packaged, a good design will allow the mass to take at least half of the device volume, whereas the rest of the volume will give room for the mass displacement. Meanwhile, the piezoelectric transducer must provide sufficient coupling to not limit the achievable power output and support the induced stress without failure.

However, we have shown that for low amplitude vibrations, capturing a significant amount of energy remains the most important bottleneck, because of the large mass required compared to the size of the beam. Therefore, the power density will be first limited by the mass density of the device and then by stress. Nonetheless, for large accelerations or forces (in harsh environments for instance), the size of the package or the strength of the materials may become concerning factors. For designs which provide low coupling, nonlinear circuits can be alternatively used to improve the performance. The inertial coupling limit however still prevents significant gains for devices with already high Q_{m}.

To summarize, an ideal harvester has the following characteristics:

- A proof mass made from a high density material and sized to occupy approximately half of the space available in the package volume;
- Minimal mechanical losses, which translates to a high mechanical quality factor, Q_{m};
- Enough coupling to provide at least 50% efficiency (although more coupling is beneficial and can improve the bandwidth if necessary);
- Tuned properly to the vibration source characteristics (*e.g.*, resonant frequency and mass travel range versus source amplitude).

Based on the extensive investigation presented here, we proposed several standard FOMs such as the normalized power density, the harvester's efficiency and the harvester's effectiveness to properly compare devices operating under variable conditions. Interestingly, all three depend on the piezoelectric resonator FOM, $\kappa^2 Q_{\mathrm{m}}$. An assessment of several resonant devices published in the literature was then conducted, revealing that many have already reached the inertial limit expected for resonators. Moreover, the devices lagging behind could reach this limit with some geometric optimization or by using a more effective extraction interface. As expected, devices with a large quality factor or a high density proof mass generally presented better normalized power densities. While our assessment focused on linear resonant harvesters, the topic of broadband energy harvesting using nonlinear resonators or nonlinear architectures was also briefly addressed. Although we came to the understanding that these approaches are fundamen-

tally bounded by the same limits as the linear system, a similar assessment of fabricated devices based on these principles would be interesting to conduct.

In conclusion, this global analysis suggests that the technology for piezoelectric generator energy conversion is quite developed. Research to synthesize high coupling materials is well underway and analytical tools for the design and optimization of piezoelectric transducers have also been developed. Moreover, an array of circuit topologies that allows for highly effective energy extraction have been proposed by numerous authors, although their implementation and performance at the microscale still pose unresolved challenges. Overall though, the power density of miniature PVEH devices is inherently limited by the power input due to their size and mass density. It is assumed that vibrational energy is readily available in large amount in the environment, but it remains challenging to scavenge energy from these unpredictable, low quality sources. The theoretical performance limits of resonant harvesters seem to have been reached and significant research efforts are underway to bring the same level of performance to a broader range of operating frequencies and scenarios. Although frequency tuning methods, novel nonlinear resonators and nonresonant architectures have been investigated for several years to this end, no clear winning proposition has emerged has a perfect answer to the limited bandwidth problem. In fact, it is quite possible that no single solution can address every type of solicitations. Any optimal PVEH design is probably intimately tied to its intended environment and application.

CHAPTER 3

Case study of autonomous sensors in vehicles

This chapter presents a study to assess the potential to power sensors via VEH in consumer vehicles by measuring car vibrations under typical driving conditions. To do so, we surveyed potential sensor applications in vehicles and measured the characteristics of vibrations present on the car body.

First, locations of sensors currently used in vehicles were listed and sorted. Their requirements were then used as criteria to narrow down the location of interests for this study. A total of 20 locations were retained after keeping the sensors with lower requirements. Spectral analyses were then conducted to evaluate the vibration characteristics. Random vibrations due to the road perturbations as well as part of the structural responses of the vehicle from changing speed were observed, as noted by vibration peaks which shift in frequency and others which are steady despite the changing conditions. This study also indicates that most of the available vibration energy is in a frequency range below 200 Hz. In our dataset, we found harvestable consistent peaks below 140 Hz on the front chassis, the rear and front plastic bumpers and the brake fluid tank. Although these results relate to a specific vehicle and a limited data set, the methodology proposed here can be extended to any vehicle or machinery to consider several conditions of operation.

Conjointly, a wireless node was developed to evaluate realistic power requirements. We chose a temperature sensor among several applications studied due to its low power requirements. The node was optimized to reduce its power consumption in the 10s µW range in sleep mode. This low power level can be leveraged by duty cycling. Considering this power budget, potential linear harvester designs subjected to the measured sources were finally assessed by analytical modeling. Based on these studies, we estimate that a mass of at least 1 gram would be necessary to provide enough power to the sensor.

3.1 Introduction

Modern consumer cars use more than 200 individual sensors [1] and switches. Most of these on board devices are connected with their Electronic Control Units (ECUs) through the Controller

1. We consider here as sensors all types of transducers (position, chemical, temperature, accelerometer, flow, pressure, etc.)

Area Network (CAN), a serial bus standard widely used since 1986 and still largely prevalent to this day. It was originally designed for multiplex electrical wiring inside vehicles to save on copper, but it often requires expensive shielded wires and connectors to work properly in such an hostile environment subject to intense heat and interferences. The Local Interconnect Network (LIN) protocol was later introduced in 2002 to complement CAN and provide a cheaper alternative for non-critical subsystems where data transmission speed and reliability requirements are less critical. Nevertheless, the increasing number of features in consumer cars is complexifying their design and assembly, as more wires are necessary. In addition, wires restrict sensor implementations in several locations of the vehicle (*e.g.*, steering wheel and tires), whereas their weight also represents a significant load that can impact fuel efficiency [200]. These concerns are expected to become even more significant with the advent of smart autonomous cars.

To alleviate these burdens, it has been proposed that next generation vehicles integrate more wireless sensor nodes, such as those already used in tire pressure monitoring systems (TPMS). However, battery maintenance remains a major obstacle to their widespread deployment and better autonomy is necessary to avoid frequent, exhaustive and expensive maintenance procedures [20]. Alternatively, localized energy production through energy harvesting is also an emerging avenue. Vibrations in running vehicle structures are considered as a potential source for continuously powering wireless nodes via a vibration energy harvesting (VEH) system. Using MEMS technologies, it is conceivable that these generators could be integrated seamlessly with the sensors.

In his thesis work, Shad Roundy measured vibration levels in various environments, including some parts of a vehicle, to compare their potential for VEH [176]. Similar studies have since been conducted in other environments and ambient vibration databases are being built [64, 152]. However, few studies have expanded on the specific characteristics and potential of car vibrations for this type of application.

In this work, we take an exhaustive look at their potential in terms of magnitude of harvestable power, frequency range and variability. Vibrations occurring at several locations on a car under various road types and driving conditions were measured to get a broad range of scenarios that reflect typical usage of a consumer vehicle. We therefore propose a methodology using time-frequency analyses to assess the harvestable power from a given source. Several sensor applications are then considered to evaluate the power consumption of a typical wireless node, which leads to the development of a wireless temperature sensor node. This sensor is optimized to consume around 10 µW. Based on these results, we extract the basic specifications necessary for the harvester, namely its mass, quality factor and conversion efficiency.

3.2 Measurement points identification

3.2.1 Selection criteria

Before proceeding with any measurement, we narrowed down the accelerometers mounting locations based on two criteria: (1) the current locations of wired sensors or potential locations of wireless nodes and (2) their requirements. The second point effectively regroups the data transmission rate and the criticality level relating to the sensor function. The data transmission rate reflects the frequency of communication between the sensor and the ECU, thus a higher rate is logically more energy demanding, which reduces the node autonomy or asks for high performances from the harvester. Alternatively, the criticality level of a sensor is tied to the severity of the consequences to the passenger's safety or vehicle condition if it fails to transmit its information. Hence, critical sensors (*e.g.*, shock accelerometers, ABS yaw sensors, chemical sensors of the powertrain system, etc.) are considered riskier and less suited for wireless connection due to safety and reliability concerns. For this work, both criteria are weighted using a 3-tier qualitative scale (low, medium, high) and are evaluated based on our own judgment. A global score is then generated by multiplying both criteria.

A list of typical automotive sensors is presented and grouped by functions in appendix C. This list shows possible locations for vibration measurement and include our evaluation based on those two criteria. Control switches in the driver cabin (*e.g.*, A/C, windows, radio and other control buttons) are not included, although many of them could be wireless based switches and are thus considered as relevant measuring points.

3.2.2 Selected points of measurement

Among the sensors found in Table C.1, those with the lowest data transmission rate and criticality level [2] are selected as references for the vibration measurements. For the purpose of this work, 26 locations were selected, but due to redundancy in the collected data, only 20 were retained for further analyses. Figure 3.1 roughly depicts where the vibration sensors were installed on a 2012 Chevrolet Impala LS, the car model used for our experiments.

2. Although there can be multiple types of sensors (*e.g.*, pressure, temperature, oxygen, air-flow, position, rotational motion, angular-rate, accelerometer) to accomplish one sensor application, here we generally limit to one type to globally describe the sensor.

Location		Sensor
(1)	Front bumper, metal	Outside temp°
(2)	Front bumper, plastic	Outside temp°
(3)	Windshield, behind mirror	Rain
(4)	Driver side mirror	Mirror limit switch
(5)	Driver side door	Window limit switch
(6)	Front door	Ajar sensor (potential)
(7)	Front door	Ajar sensor
(8)	Rear door	Ajar sensor
(9)	Rear bumper side, metal	Blind spot sensor
(10)	Rear bumper, plastic	Park-aid sensor
(11)	Rear chassis, metal under vehicle	-
(12)	Rear bumper, metal	Park-aid sensor
(13)	Trunk door	Ajar sensor
(14)	Driver seat metallic track	Limit switch
(15)	Next to windows controls	Buttons
(16)	Next to hand brake	Switch
(17)	Lights, side mirrors controls	Buttons
(18)	Steering wheel, next to controls	Buttons
(19)	Brake pedal	Switch (for brake lights)
(20)	Sun load sensor	Sunlight sensor
(21)	Next to A/C controls	Buttons
(22)	Below glove compartment, plastic	Cabin temp° (potential)
(23)	Passenger seat metallic track	Limit switch
(24)	Instrument panel	-
(25)	Next to windshield washer fluid tank	Windshield washer fluid level
(26)	Below brake fluid tank	Brake fluid level

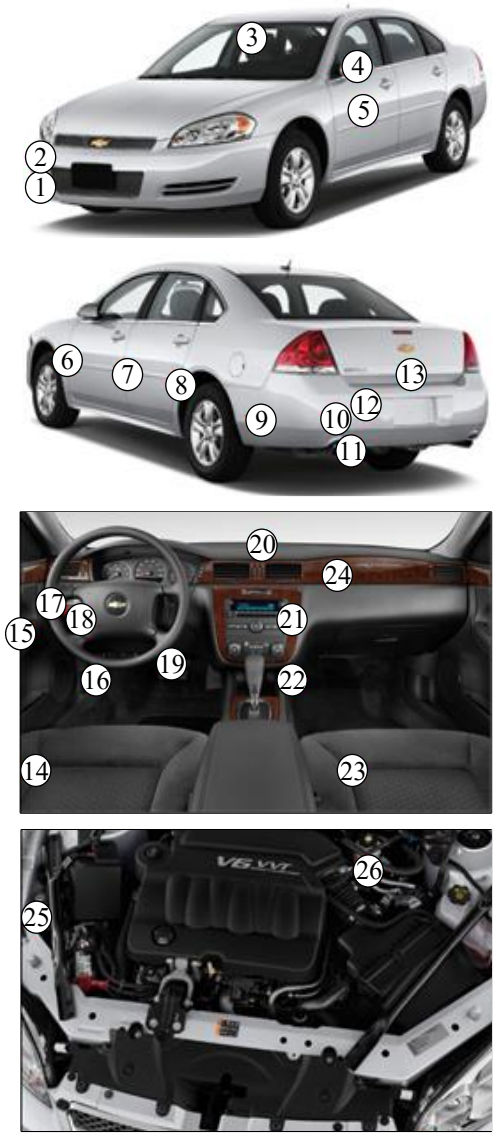

Figure 3.1 List and location of selected points of measurement (with potential sensor applications)

3.3 Experimental equipment and methods

3.3.1 Measurement platform description

Our measurement platform consisted of three accelerometers (MEAS 832M1, triaxial, piezoelectric, analog type) connected to a data acquisition (DAQ) module by 2 meters long PVC shielded cables. These accelerometers offer $>$ 6 kHz bandwidth and a $\pm$ 25 g's dynamic range. They are assembled on a ceramic support to improve vibration transmission and their low weight of only 3 grams also minimizes mass loading on the test structures. Working with an input supply voltage, V_{CC}, of 3 to 5 V, and consuming less than 25 µA, the sensors were powered via three AAA batteries or the 5 V output of the DAQ module. The nominal sensitivity (50 mV/g) and bias voltage ($V_{CC}/2$) of each accelerometer were adjusted and calibrated using a shaker and comparing with a reference accelerometer. The collected raw data was then converted in acceleration using MATLAB.

We manually soldered the shielded cables directly on the sensors, and a silicone paste was used to protect the connections. The voltage drop across the cable length once connected to the DAQ pinouts is minimal due to the sensors low current draw. Once assembled, the accelerometers broadband noise was measured and estimated at less than 1 mV (*i.e.*, approximately 0.02 g), which amounts to a minimum resolution of 0.063 g for a signal to noise ratio (SNR) of 10 dBs.

The DAQ system, a National Instrument NI-USB-6210 with 16 analog, 16 bits resolution inputs, was powered through a laptop and a USB cable. A LabVIEW application was used to collect and save the raw data at a sampling rate of 20 kHz, enough to cover the accelerometers bandwidth. This high sampling rate was also selected to properly observe the vibration peaks in the high frequency range, potentially caused by aerodynamic effects at higher vehicle speeds. Each record was limited to 40 seconds in length.

3.3.2 Experimental conditions

Before conducting our road tests, we validated the sensor mounting method to minimize its impact on the measurements. Although several fastening methods work for vibrations below 2 kHz, such as double-sided tapes, beeswax or magnetic mounts, they don't necessarily transfer higher frequency vibrations properly [208]. Screw-threaded stud or hard epoxy adhesives are usually recommended, but are less convenient for non permanent assembly. Therefore, we tested on a shaker and compared our sensors frequency response up to 1 kHz using either a strong,

0.1 mm thick doubled-sided tape or a super glue adhesive. We noticed only minor differences on the amplitudes and no effect on the frequencies, thus the tape was preferred for its convenience.

To reflect different driving conditions and observe several potential dynamics, three road types were selected near Université de Sherbrooke based on their speed limit: a highway (100 km/h), a boulevard (70 km/h) and a local road (50 km/h). For instance, we expected higher sound pressure and tire vibration orders while driving on the highway, because the vehicle travels at a mostly constant, but higher speed. Conversely, the other road types feature signalizations and traffic lights, which require the driver to frequently stop or start and introduces acceleration/deceleration phases that we hope to observe through shifting frequencies. The selected itineraries are depicted on Fig. 3.2

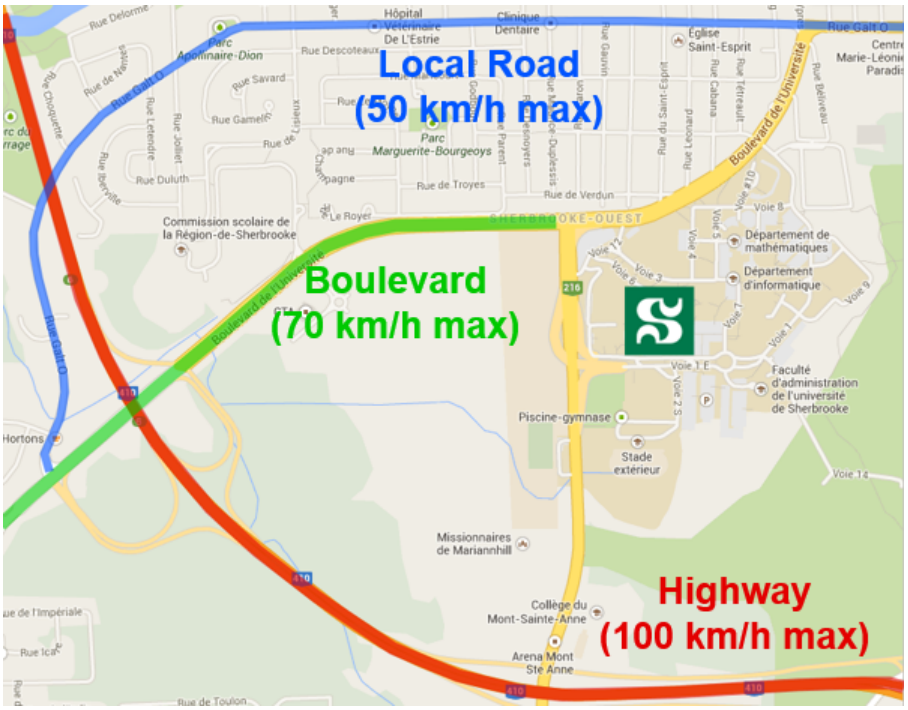

Figure 3.2 Map of the selected itineraries for testing.

3.4 Vibration data analysis methodology

3.4.1 Metrics used

Two metrics were used to assess the potential of car vibrations for MEMS energy harvesting: frequency and intensity (in terms of acceleration spectral density (ASD)). These metrics are needed to evaluate the design requirements of the harvesting device in terms of scale (micro or meso scale) and behavior. As discussed in chapter 2, higher frequencies (> 30 Hz) are more

compatible with small size resonant devices [121, 141], whereas lower frequencies are more suited for larger or non-resonant devices [141]. Moreover, a wide frequency spectrum or non stationary peaks may call for a broadband harvesting device. Meanwhile, the ASD level can provide the potential power with respect to the mass of the device, which also provides an order of magnitude on the harvester required size. The link between ASD values and expected power level is explained in the next section.

3.4.2 Source ASD level and harvester power relationship

To properly characterize the quality of the source and its potential for energy harvesting, we must first understand the relationship between the vibration characteristics and the inertial harvester power output. As described in section 2.4.1 of chapter 2, the power input to the harvester depends on the vibration characteristics, but also the device frequency response and its mass. Although the equations in chapter 2 were defined for harmonic excitations at steady state, they also extend to general stochastic vibrations as long as the device operates linearly [196]. In this case, the value of $|A|^2/2$ can be replaced by the acceleration spectral density, $S_a(f)$, expressed in $(m^2/s^4)Hz^{-1}$. Meanwhile, the electric power output spectrum is obtained from the product of the power input with the device efficiency, $\eta(f)$, as defined in equation 2.65. The average power input and electrical net power are then obtained through Parseval's theorem [3] such that

$$\bar{p}_{in} = \int_0^\infty \bar{P}_{in}(f)\mathrm{d}f, \tag{3.1}$$

$$\bar{p}_{el} = \int_0^\infty \bar{P}_{in}(f)\eta(f)\mathrm{d}f. \tag{3.2}$$

Based on the conclusions presented in section 2.8 and Eq. 2.118, the mass normalized power input, $\bar{p}^*_{in} = \bar{p}_{in}/M_{eq}$, of a linear device with a resonance frequency f_r will therefore be bounded by the simple relationship:

$$\bar{p}^*_{in} \leq S_a(f_r)/4. \tag{3.3}$$

Hence, the power input will be lower if the device bandwidth is significantly larger than the source peak bandwidth. We therefore analyze and use the results of our vibration measurements to define and evaluate potential designs tuned to a specific source. We finally assume that the

3. Single sided definition.

harvester response does not affect the source, which is reasonable if its mass remains small in comparison to the host structure or vibration sensor.

3.4.3 Vibration data treatment parameters

To streamline the presentation of the results, we translated each accelerometer axis to the general frame of reference of the car, shown on Fig. 3.3. However, we have not precisely measured the mounting surface angles and these are only general directions. The longitudinal axis is referred by the letter L, whereas T and V respectively refer to the transverse and vertical axes.

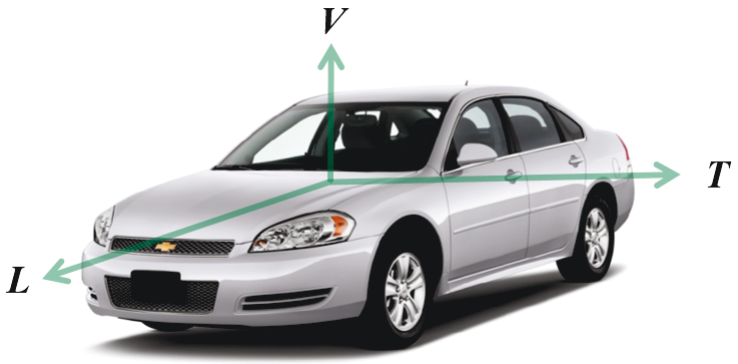

Figure 3.3 Schematic presentation of the frame of reference of the car.

After a preliminary analysis, we noticed that few ASD peaks are measured over 2 kHz and up to the Nyquist frequency of 10 kHz. Hence, the data was down sampled to 5 kHz to reduce processing time. Although significant power is observed in the frequencies below 5 Hz, which is probably due to the vehicle accelerations and suspension dynamics, it would be difficult for a MEMS inertial harvester to work in this frequency range. Therefore, we used a 5th order high pass elliptic filter (5 Hz pass frequency, 20 dB attenuation) in MATLAB to focus on the higher frequencies of interest. The data was then processed using a short-time Fourier transform algorithm (STFT) to get ASD spectrograms and observe variations of the vibrations characteristics during the recording period. A full record is buffered in segments that each contains 2^{14} data points, giving a frequency resolution of 0.3 Hz, and using Hanning windows with 67% overlap to get a 1.1 s time resolution.

Along with the short-time method, we also present the average spectrum for the entire data sample for each road type. Although it is less suited for assessing short impulses or phenomena where the frequency shifts over time, the average spectrum is appropriate to observe steady behaviors. We do so here by first using the Welch-method, in other words by averaging the spectrograms frames from a single run. This process is repeated for each run and we then compute another average with the multiple runs recorded. The variation between runs is observed

by holding the minimum and maximum values obtained at each frequency for all the runs. This gives us a signature for this location for a specific axis on a given road type, which can then be used to compare between road types. This scheme is repeated for all road type signatures to extract this axis location signature. This data analysis scheme is summarized in Fig. 3.4.

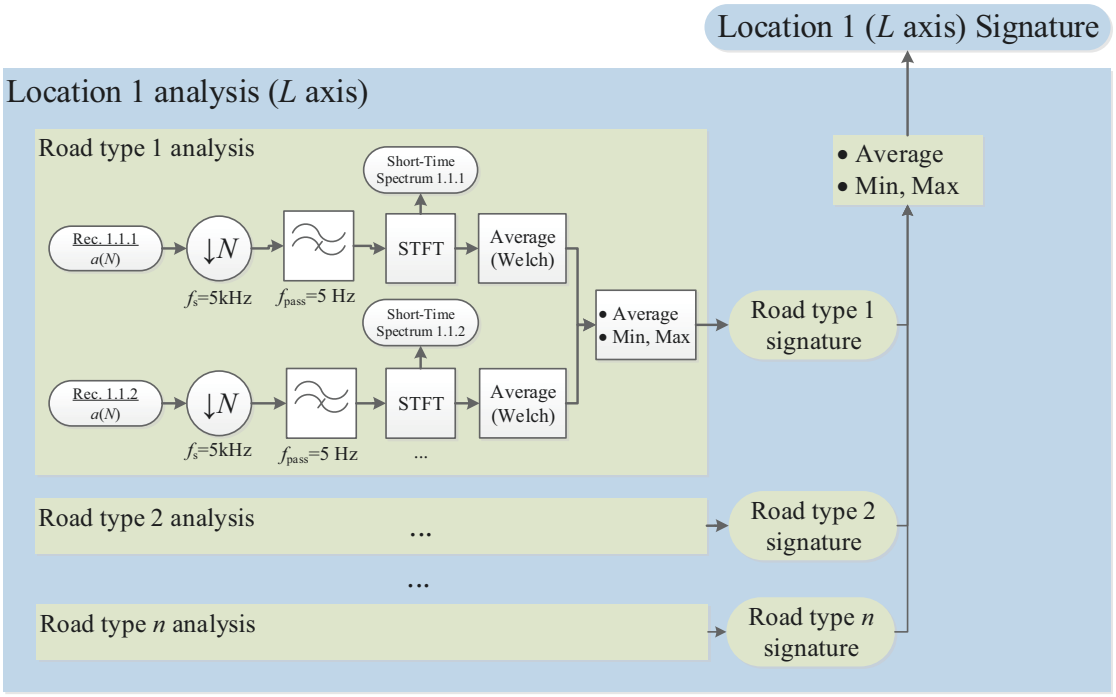

Figure 3.4 Data analysis scheme flowchart for a single axis.

3.5 Vibration data results

3.5.1 Assessment of the vibration characteristics on the rear bumper

Due to the amount of probing points, the results presented here are for a single sensor location to illustrate the methodology. Moreover, not all locations provided interesting data. The results from data captured on the rear bumper location (plastic structure) are presented in more details here because of the interesting dynamics observed. The actual sensor installation on the rear plastic bumper is presented in Fig. 3.5.

Figure 3.5 Accelerometer mounted on the rear plastic bumper

Short-time analysis

The spectrograms are presented for one run of each road type from a top-down view on Fig. 3.6. A logarithmic scaled color map is used to provide details on the ASD temporal variations. The most important frequency bands are observed around 48-50 Hz, 60-70 Hz and 115-140 Hz regardless of the road type. Significant power is found in the frequencies below 30 Hz, when the car is on the local road and the boulevard, although it is mostly random and broadband in nature. However, these perturbations are less significant on the highway, suggesting that they might be caused by the pavement conditions or related to the vehicle speed variations. Instead, two sharper peaks are now visible in this frequency range. One sharp peak is hovering between 12 and 13 Hz and a second one, less intense and wider, moves in the 23-28 Hz range. Although the former is mostly stable, the latter changes with the vehicle speed, suggesting it might be connected to an engine accessory. However, only small variations in terms of frequency are observed for many of the more intense peaks, but their magnitude vary during the recording period.

Average analysis: effect of road type

Figure 3.7 shows the run averaged ASDs for each road types. The solid line represents the average spectrum and the dotted lines are the minimum and maximum results held for all the runs. Several peaks are distinguishable around the same frequency bands as those identified in the previous spectrograms, but their magnitude again changes with the road and driving conditions. The local street and boulevard present similar frequency responses and magnitudes while the

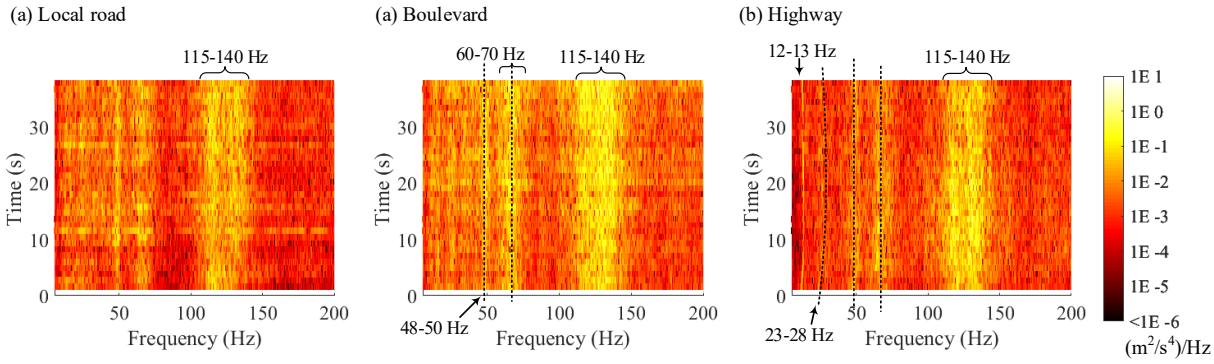

Figure 3.6 Top down view of the waterfall charts for the (a) local road, (b) boulevard and (c) highway driving conditions.

highway presents several differences. In the 20-80 Hz range, the ASD is significantly lower, while a sharper peak is visible around 12-13 Hz. However, this peak may be caused by an isolated event in one of the runs (such as the one displayed in Fig. 3.6), because it is not observed on the minimum value trace. Interestingly, the 115-140 Hz range is again consistent and shows acceleration densities in the same range of magnitude ($10^{-2} - 10^{-1}$ $(m^2/s^4)Hz^{-1}$) as the high power peaks in the lower frequency range. The 48-51 Hz and 65-70 Hz bands are also consistent from one run to another.

Average analysis: impact of measurement axis

Following the analysis for the longitudinal axis, we repeated the process for each axis and again averaged the results. This time, however, the average is done using all the captured data sets (4 on the local road and 3 for both the boulevard and the highway, for a total of 10 samples). The results are shown on Fig. 3.8. For frequencies below 40 Hz, the ASD along the V-axis is the highest (with values in the 10^{-2} to 10^{-1} $(m^2/s^4)Hz^{-1}$ range), but it drops rapidly to levels similar to or below the other axes as the frequency increases (10^{-2} to 10^{-5} $(m^2/s^4)Hz^{-1}$). In comparison, values along the L-axis remain over the 10^{-3} $(m^2/s^4)Hz^{-1}$ range at frequencies up to 140 Hz. Again, the minimum and maximum held values show some consistent peaks that however change in magnitude among the runs. This suggests that the shape of the ASD function on the bumper remains largely similar for each run, although it can change in average intensity. In other words, the bumper appears to have its own frequency response that can be more or less intense depending on the operating conditions.

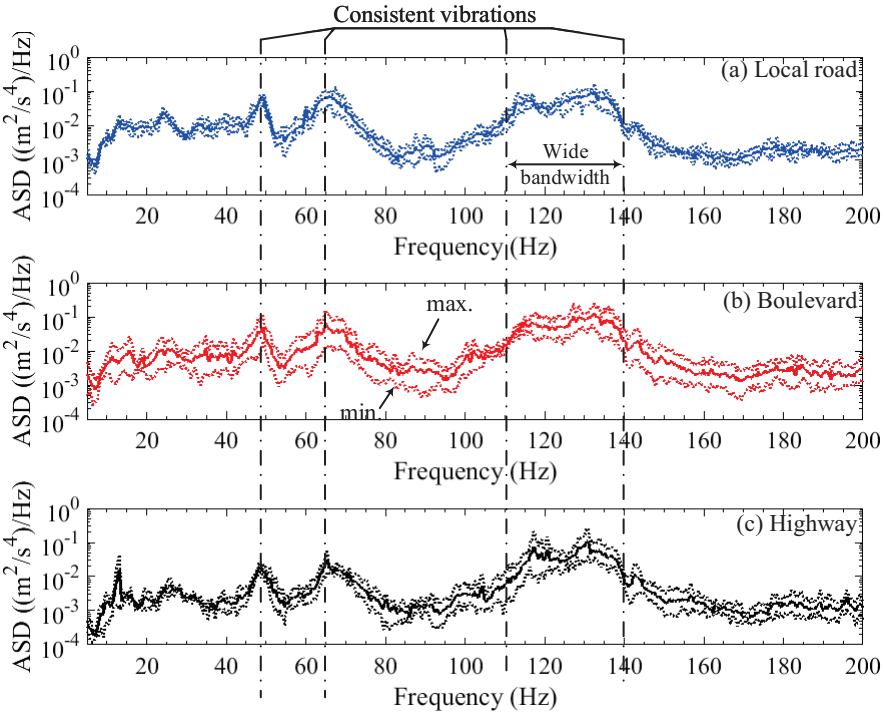

Figure 3.7 Averaged ASD recorded on the rear plastic bumper on the (a) local street, (b) boulevard and (c) highway.

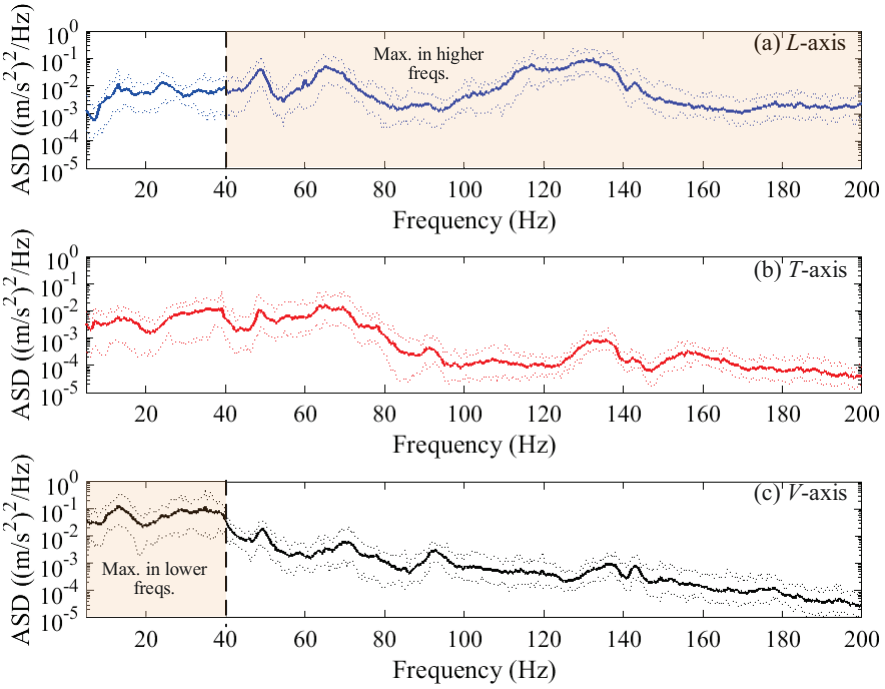

Figure 3.8 Averaged ASD recorded on the rear plastic bumper on the (a) longitudinal, (b) transverse and (c) vertical axes.

3.5.2 General automotive vibration characteristics

The same analysis techniques were applied for all of the measurement locations. Structural modal responses at frequencies over 500 Hz were detected in some parts of the vehicle, most notably on the metallic parts, such as the frame and chassis. The ASD magnitudes of those vibrations were however small and irregular among runs. In contrast with previously presented results, the spectrograms of several other locations showed numerous peaks which often shifted during a run. Those variations were observed as the speed of the vehicle changed. Hence, the behavior observed on the rear plastic bumper cannot be generalized to all the locations. Nevertheless, consistent and steady wideband peaks were also observed in other spectrograms (*e.g.*, below the brake fluid tank and near the trunk lid ajar sensor). Hence, we decided to analyze the run averaged ASDs of each measurement point to extract the most consistent vibration sources and assess their potential when used with a linear VEH device.

To eliminate as many weak sources as possible, peaks where the minimum spectrum values were below the 10^{-3} $(m^2/s^4)Hz^{-1}$ threshold were automatically discarded. Moreover, only peaks over 30 Hz were considered as viable sources for a MEMS VEH. Only 5 locations met both requirements and all potential vibration sources were below 150 Hz. Figure 3.9 presents the run averaged spectrum of these results and the list of locations that presented these consistent sources (with their respective axis of measurement). Table 3.1 collects the various peaks identified within this subset of data, with their characteristics and associated sensor application.

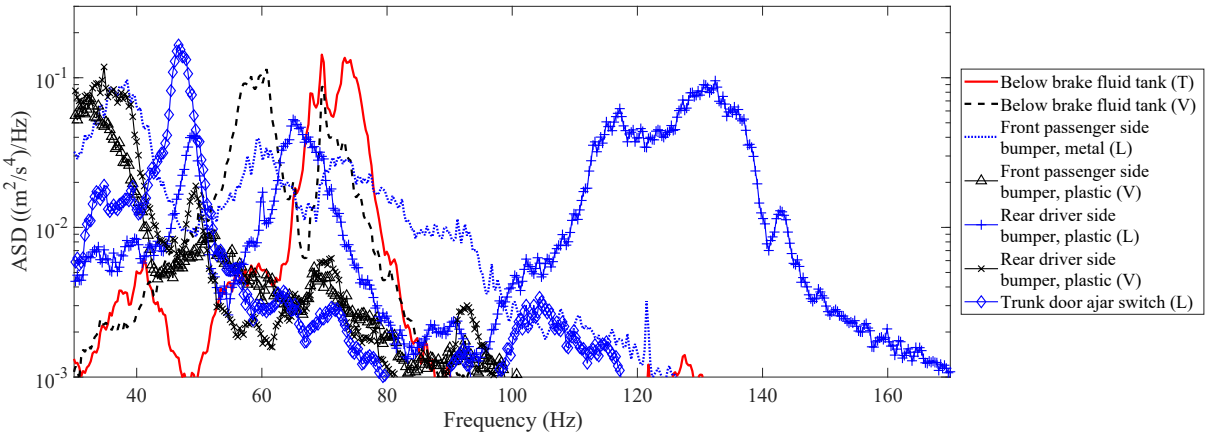

Figure 3.9 Averaged ASDs of the most consistent vibration peaks on the vehicle.

Table 3.1 Vibration peaks characterisitcs and related sensor applications.

#	Location	Sensor	Axis	Frequency (Hz)	ASD ($(m^2/s^4)Hz^{-1}$) Min	Mean	Max
1	Front passenger side bumper (metal)	Outdoor temp. (actual)	L	38.45	0.01	0.097	0.237
				59.2	0.002	0.039	0.13
2	Front passenger side bumper (plastic)	Outdoor temp. (potential)	V	32.65	0.014	0.072	0.382
10	Rear driver side bumper (plastic)	Park aid	L	49.13	0.001	0.041	0.114
				65.31	0.012	0.052	0.120
				117.2	0.011	0.062	0.209
				132.4	0.036	0.095	0.245
			V[a]	34.79	0.013	0.118	0.506
				49.44	0.004	0.019	0.036
13	Trunk door	Ajar switch	L	34.79	0.004	0.019	0.076
				46.69	0.037	0.165	0.375
26	Below brake fluid tank	Fluid level	T	69.58	0.011	0.143	0.700
				73.24	0.039	0.136	0.414
			V	60.73	0.014	0.114	0.544
				69.89	0.005	0.086	0.528

[a] Over threshold from 30 to 53 Hz

3.6 Discussion

Although analysis of the ASDs show that significant vibration energy is available on the car body, it is mostly located in a low and limited frequency range. This is an issue for MEMS VEH since they typically have resonant frequencies over 30 Hz. Moreover, most ASDs decrease rapidly with frequency, demonstrating the scarcity of high power density vibration sources in frequency ranges that are compatible with microfabricated devices. To get significant amount of power from these sources, large masses would be required, but this is counterproductive to the general goal of implementing MEMS energy harvesting devices in small wireless sensor nodes. Therefore, the overall limited harvestable power supports the decision to aim for low power and low duty cycle sensors (*e.g.*, sensors for maintenance monitoring or switches).

The spectrograms obtained on multiple locations also indicate that several vibration peaks shift in frequency while the vehicle is moving. However, these non-stationary vibrations are often surrounded by wideband noise, especially when the road condition is degraded. Conversely, the moving peaks are generally sharper when the vehicle is running on the highway, where we assume the road is in better conditions. Still, consistent harvestable frequencies can be measured on the car, but their intensity can fluctuate greatly, up to 10 dB, among runs. The spectral analysis of all the measurement points show that a limited frequency range, between 30 and 150 Hz, could be exploited in a consistent manner with a small scale linear VEH device, although those sources correspond to specific locations on the car, as indicated on Fig. 3.9. Moreover, the available vibrations are frequently wide-band. Therefore, as long as the source bandwidth is larger or equal to the device bandwidth, precise tuning of the harvester is not crucial. To complete this part of our assessment, we use the ASDs to evaluate potential harvester designs.

3.6.1 Performance of simulated energy harvester designs

We previously introduced the power bound for inertial harvester, stated in Eq. 3.3, to facilitate their design. In this section, we validate the methodology by comparing with actual power output estimates. In this example, we use the results presented in Fig. 3.9 and Table 3.1 for the rear plastic bumper (L-axis) to set design frequencies at the corresponding ASD peaks. The input power density should be in the same range regardless of the frequency, considering that all peaks have similar values. Bear in mind that this also applies to the other locations identified, which have mean ASDs ranging between 0.02 to 0.17 $(\mathrm{m}^2/\mathrm{s}^4)\mathrm{Hz}^{-1}$. We then assume all harvester designs have the same mechanical damping, $\zeta_\mathrm{m} = 0.002$ ($Q_\mathrm{m} = 250$), but may have varying electric damping, ζ_el, resulting in different harvesting efficiencies and device bandwidth. Finally, we compute the mass normalized electrical output power, $\bar{p}^*_\mathrm{el}$, by using two methods summarized in Fig. 3.10.

The first method uses spectral modulation and Parseval's theorem to extract the output power. To use this approach, however, the device bandwidth must be close to or larger than the spectral resolution of the average spectrum utilized for calculation. Otherwise, the ASD does not carry the details necessary to properly reproduce the response of a high Q device. We see from Table 3.2 that this condition is respected. In contrast, the second method uses Simulink to compute the harvesters response in the time domain using the raw acceleration time record as its input, which considers more accurately transient effects. The average power is then derived from the average of the simulated instantaneous power. We proceed in this manner for all the recorded runs and compute the average of these runs for each design. It is worth stressing that both methods are equivalent if the device is linear and the computation parameters are set properly (e.g., frequency resolution or sampling time versus the device damping factor). Both methods are therefore used mainly for validation. The parameters and results for each device are found in Table 3.2.

As expected, the average mass normalized power output of all the devices is in the same order of magnitude, although it fluctuates due to variations of the ASD. The power increases from design 1 to 4 because of the associated increase of the ASD value, despite the fact that the absolute bandwidth increases with f_r when Q_tot is kept constant ($\Delta f = f_\mathrm{r}/Q_\mathrm{tot}$). This occurs because the device bandwidth remains acceptable compared to the peak width. In contrast, design 5, which only differs from 4 by its increased electrical damping, produces more electric power because of its improved efficiency, despite a lower Q_tot. Because power distribution in this frequency range is relatively wideband, power absorption again remains similar. For comparison, the power output results are compared with the power bound stated in Eq. 3.3 by

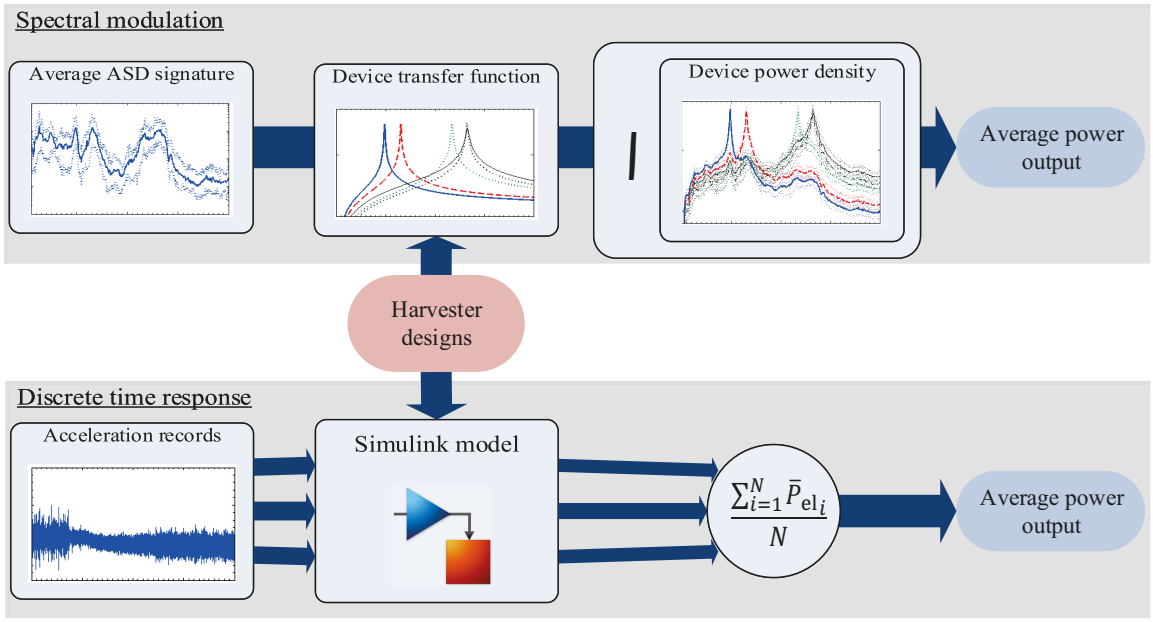

Figure 3.10 Schematic representation of the two methods used to evaluate the output power of the simulated harvesters.

also considering the conversion efficiency η. We see that the power values are close to those estimated using the simple relationship. However, the results tend to diverge when the device bandwidth increases. This is expected considering that the simple relationship only uses the peak of the ASD, whereas the exact output power accounts for variations or reduction of the ASD over the device bandwidth relatively to the peak value. Still, the overall approach is validated by these results.

Table 3.2 Results of the five simulated harvester designs

#	f_r (Hz)	ASD(f_r) ($(m^2/s^4)Hz^{-1}$)	ζ_{el}	$\eta(f_r)$ (%)	Q_{tot}	Δf (Hz)	$\bar{p}^*_{el}$ (µW/g) Modulation	Simulink	Bound
1	49	0.041	0.002	50	125	0.39	4.7	4.5	5.1
2	65.4	0.052				0.52	5.7	6.1	6.5
3	117.2	0.062				0.94	6.2	6.2	7.75
4	132.4	0.095				1.06	9.5	9.5	11.9
5	132.4	0.095	0.008	80	50	2.65	12.7	12.8	19

The simulation results show that sources with an ASD in the range of 5×10^{-2} $(m^2/s^4)Hz^{-1}$ could generate continuous power ranging in the 10s µW using a mass between 1 and 2 grams. For comparison, many state of the art silicon-based MEMS devices have masses in the range of 30 mg (1.3 mm^3) [62], which is more than an order of magnitude from what is required here.

Assuming silicon was kept for fabrication of the proof mass, and using a 500 µm thick wafer, its footprint would be in the range of 10 cm^2, which is impractical.

While non-linear harvesting schemes have not been considered here, it is not clear that they could drastically improve the power output and allow a significant reduction of the mass requirements based on the discussion in section 2.8.2 and the analyses in appendix A. In light of this, a more guaranteed option is to integrate higher density materials, such as gold or tungsten, to fabricate larger masses in a more compact volume. For example, using tungsten, which has a density that is approximately 8 times that of silicon, would allow a reduction of the mass footprint to approximatively 1 cm^2. Although still quite large for MEMS, it is more manageable.

3.7 Sensor applications

To complement this investigation and evaluate if a 10 µW target is realistic, we looked at the potential sensors identified in Table 3.1 to design a wireless node application. After consideration of the sensors available on the market, two appeared to be drastically less power consuming, namely the proximity detector and temperature sensor, and were therefore the focus of this study.

Although the power consumption profile of the node depends on the power draw from all its components during a measurement cycle, two other modules beside the sensor are typically the most demanding: the microcontroller unit (MCU) and the wireless transceiver (XCVR). Figure 3.11 presents a general architecture for a wireless node connected to an external energy harvester. Depending on the architecture, the power management circuit can be integrated directly to the node or separately with the power supply module. We used the second approach in this work to characterize the node separately from the power module.

3.7.1 Selected sensor components and expected consumptions

Table 3.3 presents the main specifications of suitable commercial components identified for a low power wireless node after review of the available options on the market. The ANTAP281M4IB RF transceiver, from Dynastream Innovations, is a module based on the nRF24AP2 system on chip family from Nordic Semiconductor. It uses the 2.4 GHz ANT protocol, which is among the lowest power consuming of its kind, and has an integrated antenna. As for the MCU, the Pic24F16KA102 from Microchip draws microamps of current in sleep mode, allowing for ultra-low power consumption between each measurements. It also has a Watch Dog Timer (WDT), flash memory, a 10-bits analog to digital converter (ADC) and supports both the Universal Asynchronous Receiver and Transmitter (UART) and Serial Peripheral Interface (SPI) protocols to communicate with the transceiver and sensor respectively. Although the selected

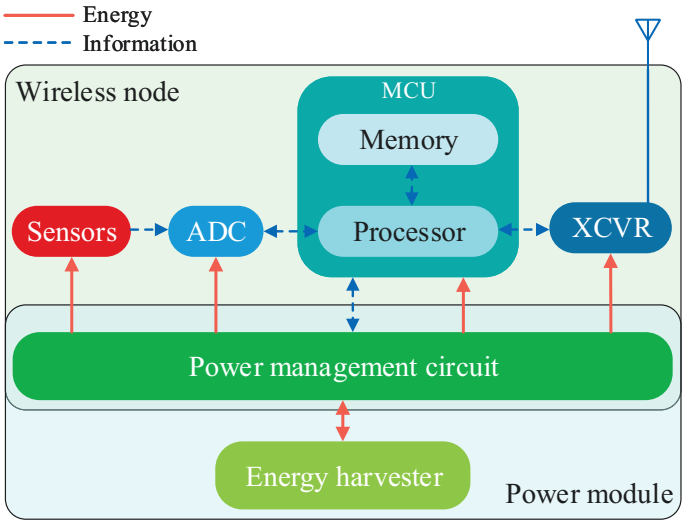

Figure 3.11 Schematic representation of a general wireless sensor node architecture.

MCU has an ADC, both sensors have this function integrated. The power evaluations in Table 3.3 are obtained considering a 3V supply for all components. Based on these numbers, we then evaluate the power consumption for a proposed operational sequence of the sensor node, which is described in Table 3.4 and depicted in Fig. 3.12(a).

Table 3.3 Off the shelf components specifications, partially taken from [191]

Function	Component	I_{active} (mA)	P_{active} (mW)	I_{sleep} (µA)	P_{sleep} (µW)	$t_{operation}$	t_{start}	Size (mm x mm)
XCVR	ANTAP281M4IB (Dynastream Innovations)	1[a]	3	0.5[b]	1.5	285 us	2 ms	20 x 20
MCU	Pic24F16KA102 (Microchip)	3.05[c]	9.15	0.87[d]	2.6	Config.	100 ms	6 x 6
Temp. sensor	TSYS 01 (Meas. Specialities)	1.4[e]	4.2	0.14	0.42	8.5 ms	21 ns	4 x 4
IR sensor	TMD2771 (TAOS)	0.175	0.525	2.5	7.5	2.72 ms	20 ns	4 x 2.4

[a] Average considering a RX-TX sampling rate of 17 seconds on UART port.
[b] In deep sleep mode. 2 µA in idle mode.
[c] Using 8MHz Fast RC Oscillator.
[d] WDT current
[e] Peak during conversion.

The average power consumption $\bar{P}$ is finally extrapolated as a function of the measurement interval $T_{tot} = \sum_{n=1}^{5} T_n$ in Fig. 3.12(b), based on Eq. 3.4.

Table 3.4 Operational sequence of the sensor node, partially taken from [191]

Phase	Actions	Active	Sleeping	Duration T (ms)		$\bar{P}$ (mW)	
				Temp.	IR	Temp.	IR
1	Wake-up MCU	MCU	Sensor + XCVR	100		9.15	
2	Wake-up sensor and meas.	MCU + sensor	XCVR	8.5	2.8	13.35	9.68
3	Sleep sensor + data process.	MCU	Sensor + XCVR	30		9.15	
4	Wake-up XCVR + transmit	MCU + XCVR	Sensor	2.3		12.5	
5	Sleep XCVR and MCU	None	All	T_{sleep}		0.005	0.012

$$\bar{P} = \frac{\sum_{n=1}^{5} P_n T_n}{T_{\text{tot}}} \tag{3.4}$$

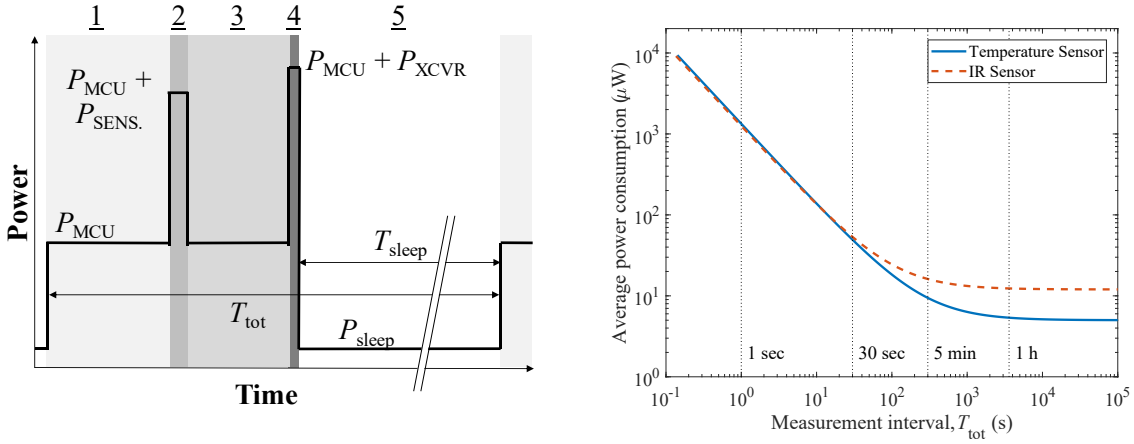

(a) Power consumption cycle over time

(b) Estimated power consumption with measurement interval T_{tot}.

Figure 3.12 Theoretical power consumption of the wireless nodes

In light of these estimations, we expect both sensors to work in the 10s of µW range by extending the measurement interval to 5 minutes, with little reduction achievable beyond this point. Quicker intervals would require reducing the power consumption during the active states. To confirm these estimates, we fabricated the temperature sensor and tested its performance experimentally. The results are presented in the next section.

3.7.2 Temperature sensor experimental results

The assembled temperature sensor node, pictured in Fig. 3.13, is 25 mm per 25 mm in size. Here, the sensor footprint is mostly driven by the size of the transceiver module soldered on the bottom face, but it could be reduced by using an external or flexible antenna.

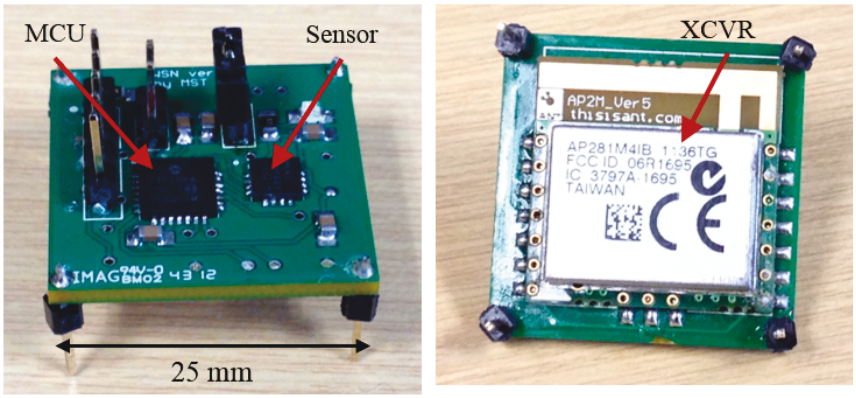

(a) (b)

Figure 3.13 Photographs of the assembled wireless temperature sensor node from (a) top view and (b) bottom view.

Although the sensor embedded program and the testing conditions have major effects on the power consumption, this discussion is out of the scope of this chapter. More details regarding these aspects are presented in [191]. Only the results obtained with optimal sensor configurations are presented and discussed here for the sake of brevity. Figure 3.14(a) presents a typical experimental current consumption profile obtained while the sensor is active ($T_{\text{on}} = \sum_{n=1}^{4} T_n$) and supplied with 3 V. During this time, the sensor sets its configuration, establishes a communication channel with the base station, takes a temperature reading, converts it digitally (using the temperature sensor integrated ADC) and finally transmits the data before going into sleep state. We estimate the active stage to last 110 ms and to consume approximately 7 mA on average, whereas the current in sleep state is estimated to 1.5 µA. In the depicted test, the period between measurements was set to 17 seconds, which gives an average current and power consumption of 47 µA and 140 µW respectively.

Based on these numbers, we again plot in Fig. 3.14(b) the expected power consumption as a function of the measurement interval and compare the results extrapolated from the experimental data with the theory. We observe the power trends are similar, although the theoretical result slightly underestimates the power consumption as the duty cycle increases. We believe this is due to additional overhead, which is unaccounted for in our theoretical estimates, such as energy consumption while the MCU communicates with the sensor. Several attempts are also necessary to establish the communication channel with the base station, as shown by Fig. 3.14(a). In reality, the current consumption is approximately twice the value we expected initially. Nevertheless, the theoretical predictions are in the same order of magnitude and are overall validated by these experiments, which confirms the feasibility of a low power node working on 10s of µW power budget.

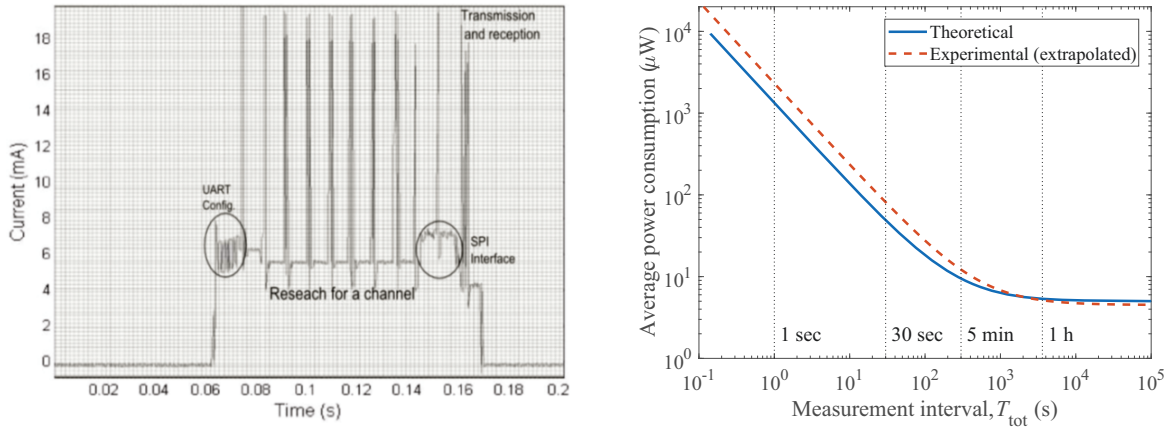

(a) Current consumption in active state. Source: [191]

(b) Comparison of the estimated power consumption with measurement interval T_{tot}.

Figure 3.14 Experimental power consumption of the temperature node

3.8 Conclusion

The present study focused on assessing the potential of energy harvesting applications using car vibration under typical driving conditions. To this end, we selected several measurement points based on two criteria, namely the location of actual or potential sensors and their criticality. A total of 20 locations were retained for this study. To reflect true operating conditions, the car was exposed to typical excitation on various road types. The data was then treated specifically to evaluate the harvestable power from those vibrations through an inertial resonant device. The vibration spectrum measured were correlated to the harvestable power from linear harvesters with known specifications. Based on the spectral analyses, most of the high power density vehicular vibrations measured were located below 200 Hz. While they often drifted in frequency during the recorded runs, several measured vibrations were consistent. Focusing on these sources, we conclude that a small range of design frequencies between 30 and 150 Hz could be exploited with a linear VEH device to produced expected power outputs in the range of 10 µW per gram of the proof mass. Complementary to this study, we have designed and tested a wireless temperature sensor. In optimal conditions, the sensor consumes 7 mA in its active states and 1.5 µA in sleeping state, which means that it is capable of operating on a 10 µW budget by setting a measurement interval of approximately 5 minutes. Although this result was obtained in ideal lab conditions and not on a vehicle environment, this demonstration supports our 10 µW target for the energy harvester. Real designs should be tested under these random vibrations to validate the design methodology and more tests should eventually be conducted on other car models and roads to get a more robust representation of typical car vibrations.

While this study mostly focused on linear harvester designs, non-linear harvesters could be an alternative approach. These devices are the focus of intensive research effort to improve the harvesters output under broadband vibrations. Although, the discussions in section 2.8.2 and appendix A do not suggest that the performances can be drastically improved with these designs nor that they would allow a significant reduction on the mass requirements, more studies should be realized before discarding them entirely. These considerations therefore motivate efforts to integrate higher density materials to improve the harvesters power density and hopefully provide more robust performances in real applications.

CHAPTER 4

Achieving high quality factor without vacuum packaging by high density proof mass integration in vibration energy harvesters

Foreword

Title: Achieving high quality factor without vacuum packaging by high density proof mass integration in vibration energy harvesters

Authors and affiliation:

A. Dompierre: Ph.D. student, Université de Sherbrooke, Faculté de génie, Département de génie mécanique

S. Vengallatore: Professor, McGill University, Faculty of Engineering, Departement of Mechanical Engineering

L. Fréchette: Professor, Université de Sherbrooke, Faculté de génie, Département de génie mécanique

Acceptation date: February 9th 2019
Acceptation status: accepted with corrections
Journal: *IEEE Journal of Microelectromechanical Systems*
Reference: [59]
Contribution to document: This article contributes to the thesis by describing and demonstrating an observed benefit of adding high density proof masses to cantilever beam resonant piezoelectric harvesters. The article also introduces general scaling laws and make a contribution because of the relatively straightforward models presented.
Note: Following the requested corrections by the members of the jury, the content of this article differs from the published version.

Abstract

This paper presents a simple approach to control fluidic damping, and thereby improve the mechanical Q factor at ambient pressure, of AlN-based piezoelectric resonant energy harvesters by using high density proof masses. Using models adapted from the literature, and accounting for the simultaneous transverse and rotational motion of the cantilever beam, scaling laws are extracted for the fluidic quality factor, Q_{f}, as a function of the fluid damping regime, either due to drag or squeeze film forces. Subsequently, we demonstrate the utility of the scaling laws by characterizing silicon-based devices and tungsten tip masses. By accounting for other damping sources and the device operating frequency, we achieve close to an order of magnitude improvement on Q_{f} with this strategy, going from 398 to 4193. Beside potential for footprint reductions and higher power outputs, these results suggest that high density proof mass integration can be an alternative to vacuum packaging for MEMS based vibration energy harvesting.

Keywords: Fluid damping, microcantilever, Q factor, vibration energy harvesting.

4.1 Introduction

Miniaturized wireless sensing nodes have evolved significantly over the last decade, with notable reduction in power consumption. Nevertheless, battery maintenance remains impractical and energy autonomy is still a critical problem [18, 20, 50, 180]. Among potential alternative energy sources, vibration energy harvesting (VEH) by means of inertial devices is emerging as a solution for some applications, including industrial, vehicular or structural health monitoring [212].

Previous work in this field has shown that energy losses due to fluidic damping can substantially reduce the efficiency and performance of MEMS-based VEH at ambient pressure [63]. The fluidic damping arises due to viscous dissipation caused by fluid-structure interactions [91] and squeeze film damping [63], depending on the details of the device architecture, packaging and dynamics.

The typical and most effective solution to this problem is to use a vacuum sealed package [4, 63]. This solution, however, increases the complexity of the package design and fabrication processes; introduces reliability and lifetime concerns due to outgassing and hermeticity; and increases the device footprint, especially in the case of packages fabricated by wafer bonding. The last-mentioned consideration can be problematic for VEHs that usually require a bulky mass as well as a large travel range ($\leqslant 1$ mm) to produce sufficient power.

These considerations motivate the search for alternate solutions for controlling fluidic damping without the use of vacuum packaging. One approach is to perforate the proof mass and thereby alter the fluid circulation [19], but this strategy reduces both the effective density of the proof mass and the VEH potential power output. In this work, we explore an alternative strategy based on the integration of high density proof masses.

Previous work has shown that high density materials improve the power density of VEH due to an increased sensitivity to input vibrations [57, 140]. Our recent work [50] highlighted an additional benefit: integrating high density proof mass can reduce the impact of fluidic damping on the mechanical quality factor [50]. This effect originates from the simple consideration that high density materials can store more energy in the same volume or as much energy in a smaller volume, whereas fluid losses effectively depend on the surface area.

Expanding on our initial analyses here, we first briefly present relevant models to evaluate the impact of a mass density variation on fluidic damping (with additional details presented in the appendixes). This effect is then demonstrated experimentally by characterization of the Q factor of aluminum nitride (AlN) based piezoelectric microcantilevers [41] with and without the addition of a tungsten proof mass. We finally discuss the general implications for the design and performances of VEH in ambient air.

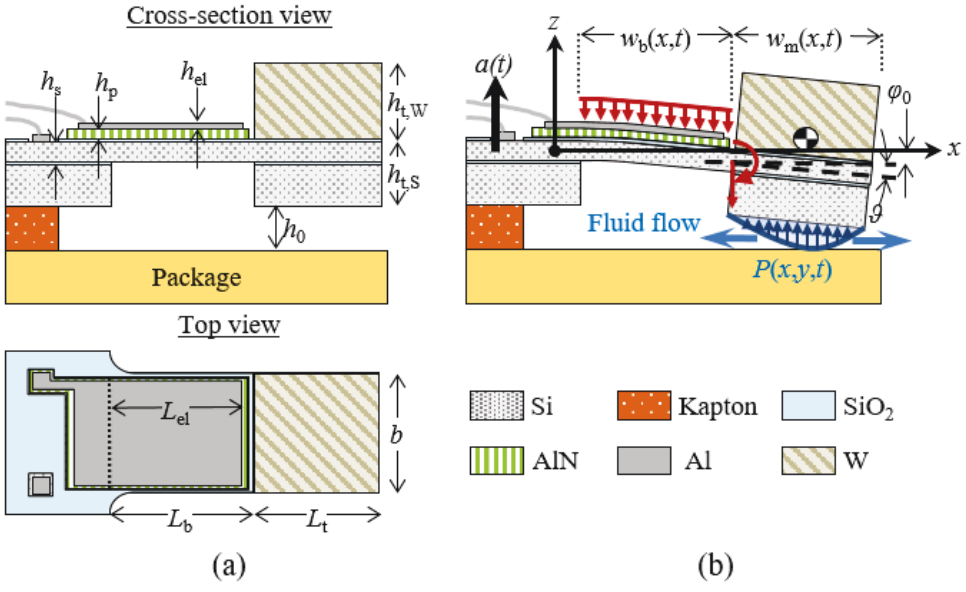

Figure 4.1 Diagram of the unstrained, packaged piezoelectric cantilevers with the dimensions (a) and deflected under the combined load with the squeeze film pressure in the gap (b).

4.2 Theoretical background

4.2.1 General assumptions and beam model definitions

The configuration of the packaged piezoelectric unimorph cantilevers studied in this work is depicted in Fig. 4.1. The variables ρ and h respectively denote material densities and thicknesses, where the subscripts s, p, el, and W respectively denote properties of the silicon substrate, piezoelectric layer, aluminum electrode, and tungsten mass. The additional subscripts t,S and t,W relate to thicknesses of the silicon and tungsten tip masses respectively, whereas L_t is the length of the proof mass, which has a total mass M_t. The beam of width b and length L_b is considered flat with the gap at rest, as illustrated in Fig. 4.1(a), and is subject to an harmonic base acceleration $a(t)$ with a radial frequency of oscillation ω. We further assume light linear viscous damping thus the structure response at the first vibration mode, noted $w(x,t)$, is real and separable in space x and time t such as [47],

$$w(x,t) = \hat{w}(x)\varphi(t) = \hat{w}(x)\varphi_0 \sin(\omega t + \psi), \tag{4.1}$$

where $\hat{w}(x)$ is the structure mode, normalized such that $\hat{w}(L_\mathrm{b}) = 1$, and $\varphi(t)$ is the time response containing both the amplitude φ_0 and phase ψ information. The normalized displacement profile of the full geometry $\hat{w}(x)$ is defined as a piecewise function,

$$\hat{w}(x) = \begin{cases} \hat{w}_\mathrm{b}(x) & 0 < x < L_\mathrm{b} \\ \hat{w}_\mathrm{m}(x) & L_\mathrm{b} < x < L_\mathrm{b} + L_\mathrm{t} \end{cases}, \tag{4.2}$$

where $\hat{w}_\mathrm{b}(x)$ is the beam deflection and $\hat{w}_\mathrm{m}(x)$ the displacement of the rigid mass. For simplicity, we use the Euler-Bernouilli beam theory and the first mode deformation is approximated to the static deflection of a cantilever subject to a combined inertial load. As described in appendix D.1, this load is the sum of the distributed beam inertia as well as a point force and a moment applied at the beam's tip due to the deported centroid of the proof mass. After normalization, the beam deflection shape from Eq. D.4 becomes:

$$\hat{w}_\mathrm{b}(x) = \frac{\left[6 + 12\lambda\left(\frac{L_\mathrm{t}}{L_\mathrm{b}} + \frac{1}{2}\left(\frac{L_\mathrm{t}}{L_\mathrm{b}}\right)^2\right)\right]\left(\frac{x}{L_\mathrm{b}}\right)^2 - 4\left(1 + \lambda\frac{L_\mathrm{t}}{L_\mathrm{b}}\right)\left(\frac{x}{L_\mathrm{b}}\right)^3 + \left(\frac{x}{L_\mathrm{b}}\right)^4}{3 + 8\lambda\frac{L_\mathrm{t}}{L_\mathrm{b}} + 6\lambda\left(\frac{L_\mathrm{t}}{L_\mathrm{b}}\right)^2}, \tag{4.3}$$

where λ is the ratio of the linear mass density of the proof mass to the beam,

$$\lambda = \left(\rho_s h_{t,S} + \rho_W h_{t,W}\right) / \left(\rho_s h_s + \rho_p h_p + \rho_{el} h_{el}\right). \tag{4.4}$$

The normalized mass displacement $\hat{w}_m(x)$ is then simply derived from the rigid body motion resulting from the beam tip rotation at the normalized angle $\hat{\vartheta}$ and its transverse displacement:

$$\hat{w}_m(x) = \left[1 + \left(\frac{x}{L_b} - 1\right)\hat{\vartheta}\right], \tag{4.5}$$

$$\hat{\vartheta} = L_b \frac{\mathrm{d}\hat{w}_b(L_b)}{\mathrm{d}x} = \frac{4 + 12\lambda\frac{L_t}{L_b} + 12\lambda\left(\frac{L_t}{L_b}\right)^2}{3 + 8\lambda\frac{L_t}{L_b} + 6\lambda\left(\frac{L_t}{L_b}\right)^2}. \tag{4.6}$$

We note that $\hat{\vartheta}$ is bounded between 4/3 for $L_t/L_b = 0$ and 2 for $L_t/L_b \to \infty$. Although the piezoelectric VEH literature mentions that the static deflection assumption should be used cautiously, because it may yield significant errors on the voltage and power estimates [70], we merely use this approach here to estimate the displacement profile and the gap function, which is all that is needed to evaluate damping.

The lumped stiffness K_m and mass M_{eq} are finally evaluated to find the structure's resonant frequency. The lumped stiffness K_m of the system is given by integrating the normalized strain energy over the beam length, which is expressed as:

$$\begin{aligned} K_m &= YI \int_0^{L_b} \left(\frac{d^2\hat{w}_b(x)}{\mathrm{d}x^2}\right)^2 \mathrm{d}x \\ &= \frac{YI}{L_b^3} \frac{\left\{\frac{144}{5} + \lambda\left[144\left(\frac{L_t}{L_b}\right) + (96 + 192\lambda)\left(\frac{L_t}{L_b}\right)^2 + 288\lambda\left(\frac{L_t}{L_b}\right)^3 + 144\lambda\left(\frac{L_t}{L_b}\right)^4\right]\right\}}{\left[3 + 8\lambda\left(\frac{L_t}{L_b}\right) + 6\lambda\left(\frac{L_t}{L_b}\right)^2\right]^2}, \end{aligned} \tag{4.7}$$

where YI is the flexural rigidity of the composite cantilever, defined by Eq. D.10 in appendix D.1. Equation 4.7 is validated by observing that K_m is constrained around three possible values. For $L_t/L_b = 0$, there is no tip mass and $K_m = 3.2YI/L_b^3$. When the mass is short, but thick or very dense ($L_t/L_b \ll 1, \lambda \gg 1$), the load is mainly applied at the tip and we find the classic solution $K_m = 3YI/L_b^3$. Finally, $K_m = 4YI/L_b^3$ for a long tip mass ($L_t/L_b \gg 1$), when the main loading term is the moment at the tip.

The lumped mass M_{eq} is rather computed by integrating the kinetic energy over the structure. More detail on the evaluation of M_{eq} are given in appendix D.2 and [207]. For a large tip mass,

the contribution of the beam is much smaller and can be neglected, which yields

$$M_{\mathrm{eq}} \approx M_{\mathrm{t}} \left[1 + \frac{L_{\mathrm{t}}}{L_{\mathrm{b}}} \hat{\vartheta} + \frac{r_{O'}^2}{L_{\mathrm{b}}^2} \hat{\vartheta}^2 \right]. \tag{4.8}$$

where $r_{O'}^2$ is the proof mass radius of gyration around the tip mass rotation axis O' and is given by Eq. D.19 in appendix D.2. For the considered geometries, the mass is much thicker than the beam ($h_{\mathrm{t}} \gg h_{\mathrm{s}}$) and the features are planar ($L_{\mathrm{t}} > h_{\mathrm{t}}$). Thus, we can approximate $r_{O'}^2 \approx L_{\mathrm{t}}^2/3$ and again simplify M_{eq} to:

$$M_{\mathrm{eq}} \approx M_{\mathrm{t}} \left[1 + \frac{L_{\mathrm{t}}}{L_{\mathrm{b}}} \hat{\vartheta} + \frac{L_{\mathrm{t}}^2}{3L_{\mathrm{b}}^2} \hat{\vartheta}^2 \right]. \tag{4.9}$$

Now that the basic structural model has been defined, the next section focuses on damping and defining the Q factor.

4.2.2 Damping and definition of the Q factors

For this work, we separate the damping force f_{D} in two separate components, namely intrinsic and fluidic damping, such that $f_{\mathrm{D}} = f_{\mathrm{D,int}} + f_{\mathrm{D,f}}$. Intrinsic damping may include boundary damping (due to elastic wave radiation, microsliding, and viscoelasticity at the anchors) and material damping (due to internal friction in the materials or thermoelastic effects) [101]. Intrinsic damping can therefore be determined experimentally in a vacuum chamber, by removing fluid structure interactions.

The device total quality factor, Q_{tot}, can be expressed as

$$Q_{\mathrm{tot}} = 2\pi U_{\mathrm{S}} / \left(U_{\mathrm{D,int}} + U_{\mathrm{D,f}} \right) = \left(Q_{\mathrm{int}}^{-1} + Q_{\mathrm{f}}^{-1} \right)^{-1} \tag{4.10}$$

where the stored energy U_{S} is simply the maximum kinetic energy at peak velocity,

$$U_{\mathrm{S}} = M_{\mathrm{eq}} \omega^2 \varphi_0^2 / 2, \tag{4.11}$$

whereas Q_{int} and Q_{f} are respectively the intrinsic and fluidic Q factors stemming from $U_{\mathrm{D,int}}$ and $U_{\mathrm{D,f}}$, the energy losses per cycle from each damping component. Although Q_{int} is determined experimentally, our objective is to also estimate Q_{f} analytically.

Fluidic damping arises from the fluid displacement and friction with the structure surfaces as it oscillates. Hence, $U_{\mathrm{D,f}}$ is obtained by integrating over the structure area and over one period the

product of the local fluid induced damping pressure $P(x,y,t)$ with the local velocity,

$$U_{\mathrm{D,f}} = \int_A \int_0^{2\pi/\omega} P(x,y,t)\hat{w}(x,y)\dot{\varphi}(t)\mathrm{d}t\mathrm{d}A = \pi\omega\varphi_0^2 C_{\mathrm{D,f}}. \tag{4.12}$$

with $C_{\mathrm{D,f}}$ the fluid drag coefficient. From Eqs. 4.10-4.12, Q_{f} finally simplifies to

$$Q_{\mathrm{f}} = \omega M_{\mathrm{eq}}/C_{\mathrm{D,f}}. \tag{4.13}$$

The following section reviews different fluid damping models to express $U_{\mathrm{D,f}}$ and highlight the impact of the tip mass characteristics on Q_{f}. However, based on Eq. 4.13, one can already appreciate that for a given frequency and mass geometry, Q_{f} will increase with the mass density considering that M_{eq} increases while $C_{\mathrm{D,f}}$ remains roughly unchanged.

4.3 Fluidic damping modeling

Several factors affect the interaction of the VEH with the surrounding fluid. One is the effect of gas rarefaction at lower ambient pressure, which causes slipping at solid and fluid boundaries [204]. The rarefaction level is characterized by the Knudsen number Kn, defined as the ratio of the gas molecular mean free path γ and a characteristic length L,

$$Kn = \gamma/L, \tag{4.14}$$

where γ is given by:

$$\gamma = \mu/P_{\mathrm{a}}\sqrt{\pi k_{\mathrm{b}} T_{\mathrm{a}}/(2m_{\mathrm{m}})}. \tag{4.15}$$

In Eq. 4.15, k_{b} is the Boltzmann constant in J/K and $m_{\mathrm{m}} = 4.81\mathrm{E}{-26}$ kg is air molecular mass, whereas T_{a} and P_{a} are respectively the fluid ambient temperature and pressure. For dry air, $\mu = 18.46\mathrm{E}-6$ Pa·s at room temperature T_{a}=295 K. The flow transitions to the free molecular regime, where independent gas molecules collide with the structure and the damping force obeys the kinetic theory of gases [23], when $Kn > 0.1$. The slip flow ($0.01 < Kn < 0.1$) and continuum ($Kn < 0.01$) regimes are instead described by the Navier-Stokes equations. Surfaces near the moving structure can also affect or bound fluid flow and notably cause squeeze film damping [19].

This section presents the basic equations and assumptions relating to each case, although we generally assume isothermal conditions, small transverse or angular displacements and consider air to be an ideal gas.

4.3.1 Effective viscosity

The fluid viscosity μ typically assumes no slip at the boundaries between the fluid and the solid walls, but it is not accurate in the slip flow regime. Gas rarefaction can be accounted for by replacing μ by an effective viscosity μ_{eff}:

$$\mu_{\text{eff}} = \mu / f(Kn), \tag{4.16}$$

where $f(Kn)$ is a function of the Knudsen number Kn, which corrects the flow rate based on the degree of slip at the boundaries. It is affected by numerous factors, including gas and solid properties, surface roughness, Reynolds number, fluid velocity profile and border effects [31, 32, 154, 155, 203]. Although several expressions have been derived to describe μ_{eff} [155], Eq. 4.17 from Veijola *et al.* [204] will be used in this work:

$$\mu_{L,\text{eff}} = \mu / \left(1 + 9.658 Kn^{1.159}\right), \tag{4.17}$$

where Kn is defined using the gap h_0. This approximation was derived specifically for squeeze film flow between smooth horizontal walls and narrow gaps (*i.e.*, Poiseuille flow), but we extend its use to extract general trends for any type of flow acknowledging this limitation. This expression also covers the transitional and molecular flow regimes ($Kn > 0.1$), although Q_{int} eventually dominates, which can make these regimes more difficult to observe properly.

4.3.2 Drag damping

Drag forces on an immersed body without surrounding walls is modeled based on Blom's work [23], which uses the Stokes flow assumption to consider a drag force proportional to the velocity. If inertia effects are neglected, the local differential pressure P due to drag is expressed as:

$$P(x,t) = \beta_{\text{D}} \hat{w}(x) \dot{\varphi}(t), \tag{4.18}$$

where β_{D} is the area normalized drag parameter. This assumption also implies limited impact on the drag coefficient from the structure shape. We hence use a similar approach as Kokubun *et al.* [109], which modeled the structure as a string of spheres vibrating independently of each other. We use the viscous drag parameter for an oscillating sphere of equivalent hydraulic diam-

eter D and normalize by the surface area, which yields [106]:

$$\beta_{\mathrm{D}} = 3\pi\mu_{\delta,\mathrm{eff}} D\left[1 + D/(2\delta)\right]/\left[b\left(L_{\mathrm{b}} + L_{\mathrm{t}}\right)\right], \tag{4.19}$$

$$D = 2\left[b\left(L_{\mathrm{b}} + L_{\mathrm{t}}\right)\right]/\left(b + L_{\mathrm{b}} + L_{\mathrm{t}}\right). \tag{4.20}$$

Here $\mu_{\delta,\mathrm{eff}}$ is defined using Kn_{δ}, the Knudsen number defined with respect to Stokes' boundary layer thickness δ. This length, which characterizes the depth of the fluid disturbance around the vibrating body, is expressed by:

$$\delta = \sqrt{2\mu/(\rho_{\mathrm{a}}\omega)}, \tag{4.21}$$

where ρ_{a} is the density of the ambient fluid. From the ideal gas assumption:

$$\rho_{\mathrm{a}} = m_{\mathrm{m}} P_{\mathrm{a}}/(k_{\mathrm{b}} T_{\mathrm{a}}) \tag{4.22}$$

Finally, from Eq. 4.12,

$$C_{\mathrm{D,f,drag}} = bL_{\mathrm{t}}\beta_{\mathrm{D}}\left[\frac{\hat{\vartheta}^2}{3}\left(\frac{L_{\mathrm{t}}}{L_{\mathrm{b}}}\right)^2 + \hat{\vartheta}\left(\frac{L_{\mathrm{t}}}{L_{\mathrm{b}}}\right) + 1 + \int_0^{L_{\mathrm{b}}} \hat{w}_{\mathrm{b}}^2(x)\mathrm{d}x/L_{\mathrm{t}}\right], \tag{4.23}$$

and therefore, from Eq. 4.13, $Q_{\mathrm{f,drag}}$ can be expressed by

$$Q_{\mathrm{f,drag}} = \omega M_{\mathrm{eq}} \Bigg/ \left\{bL_{\mathrm{t}}\beta_{\mathrm{D}}\left[\frac{\hat{\vartheta}^2}{3}\left(\frac{L_{\mathrm{t}}}{L_{\mathrm{b}}}\right)^2 + \hat{\vartheta}\left(\frac{L_{\mathrm{t}}}{L_{\mathrm{b}}}\right) + 1 + \int_0^{L_{\mathrm{b}}} \hat{w}_{\mathrm{b}}^2(x)\mathrm{d}x/L_{\mathrm{t}}\right]\right\}. \tag{4.24}$$

Upon simplification for cases where most of the drag is caused by the mass, $Q_{\mathrm{f,drag}}$ will scale as:

$$Q_{\mathrm{f,drag}} \approx \omega\rho_{\mathrm{t}} h_{\mathrm{t}}\left(b + L_{\mathrm{b}} + L_{\mathrm{t}}\right)/\left[6\pi\mu_{\delta,\mathrm{eff}}\left(1 + D/(2\delta)\right)\right]. \tag{4.25}$$

4.3.3 Squeeze film damping

Squeeze film damping occurs when the gap h_0 between the mass and the package, as shown in Fig. 4.1, is small enough to restrict fluid flow. As a result, a differential pressure profile $P(x,y,t)$ builds up along the gap with respect to the ambient pressure P_{a}, whereas it is uniform across the gap. We can expect this to happen when $h_0 \ll L_{\mathrm{t}}$, b or δ.

Assuming it is the case, and based on our general assumptions, the Navier-Stokes equations can be simplified to the linearized Reynolds equation. We then use the Green function approach presented by Darling *et al.* [43] to evaluate the fluid force resulting from a 2D squeeze film

flow. The required development for this study is presented in appendix D.3, where we also assume ideal venting at the edges ($P = 0$) and a squeeze number $\ll 1$, therefore neglecting compressibility and fluid inertia effects.

The fluid drag coefficient due to squeeze film $C_{\mathrm{D,f,squeeze}}$ is derived from Eq. 4.12 by using the pressure terms (Eqs. D.35-D.40), the energy losses per cycle (Eq. D.41) and mass displacement (Eq. 4.5). After integrating relatively to time and simplifying Eq. D.42 to a single term expansion, we get:

$$C_{\mathrm{D,f,squeeze}} = \frac{768}{\pi^6} \frac{\mu_{\mathrm{eff,h_0}}\left(bL_{\mathrm{t}}\right)}{h_0^3\left(L_{\mathrm{t}}^{-2}+b^{-2}\right)} \left(1+\frac{L_{\mathrm{t}}}{L_{\mathrm{b}}}\frac{\hat{\vartheta}}{2}\right)^2. \tag{4.26}$$

A simplified general trend for $Q_{\mathrm{f,squeeze}}$ is finally obtained using M_{eq} from Eq. 4.9 and $C_{\mathrm{D,f,squeeze}}$ from Eq. 4.26 in Eq. 4.13:

$$Q_{\mathrm{f,squeeze}} \approx \frac{\pi^6}{768} \frac{\omega\left(\rho_{\mathrm{t}} h_{\mathrm{t}}\right) h_0}{\mu_{h0,\mathrm{eff}}} \left[\frac{h_0^2}{\left(L_{\mathrm{t}}^{-2}+b^{-2}\right)^{-1}}\right] \frac{\left[1+\frac{L_{\mathrm{t}}}{L_{\mathrm{b}}}\hat{\vartheta}+\left(\frac{L_{\mathrm{t}}}{L_{\mathrm{b}}}\right)^2\frac{\hat{\vartheta}^2}{3}\right]}{\left(1+\frac{L_{\mathrm{t}}}{L_{\mathrm{b}}}\frac{\hat{\vartheta}}{2}\right)^2}. \tag{4.27}$$

4.4 Experimental methods

4.4.1 Fabrication process and mass fixation method

The piezoelectric devices, schematized in the cross section of Fig. 4.1(a), were fabricated via MEMSCAP's PiezoMUMPs™process [41]. This process uses n-type SOI wafers as the starting substrates with a backside oxide on the handle layer. The 10 µm thick device layer acts as the beam support material and is also phosphorous doped to serve as the bottom electrode. A 200 nm thick thermal oxide is then grown and patterned by RIE, followed by deposition of a 0.5 µm thick piezoelectric AlN layer by reactive sputtering. The piezoelectric layer is then patterned by wet etching and a 20 nm thick Cr and 1 µm thick Al metal stack is deposited to define the top electrode by lift-off. The beam geometry is machined by DRIE through the device layer and stopped at the 1 µm thick buried oxide layer. To reduce stress concentration at the anchors, each beam features fillets of 225 µm in radius. After application of a protective polyimide layer on the top side, the wafer is reversed for the final backside definition of the Si proof mass. The patterns are first etched in the thermal oxide by RIE, followed by a silicon DRIE through the

400 µm thick handle layer. The cantilever beams are released by wet etching of the buried oxide and dry plasma etching of the protection layer.

The dies are then packaged and wire bonded to 28 gold plated leads ceramic DIP packages. Polyimide spacers are used to create clearance for the mass displacement and the EPO-TEK EK2000 two-part silver epoxy is used to fix the dies to the spacers and the package. A close-up view of the packaged MEMS die is shown on Fig. 4.2(a). The packaged devices are then placed in a socket soldered on a prototyping board for dynamic characterization, as shown on Fig. 4.2(b). After their initial characterization, the devices are modified by adding a tungsten mass on top of the silicon mass. The bonding alignment is done manually under a binocular microscope using a vacuum needle to manipulate the bulk tungsten mass and a multistage positioner to move the chip. The EPOTEK 301-2 epoxy is used to attach the mass due to its low viscosity and low curing temperature of 120 °C.

The nominal dimensions of the devices used in our experiments and models, as labelled in Fig. 4.1(a), are found in Table 4.1. These designs were chosen to observe the effect of the gap (D2 vs. N2, D6 vs. N6) as well as the effect of the beam length and the resonant frequency (D2 vs. D6, N2 vs. N6). The addition of the tungsten proof mass is moreover denoted by the symbol $'$ (*e.g.*, D2 vs. D2$'$). Additional theoretical designs, which are only modeled and discussed later on, are also included for reference in Table 4.1 and are denoted with the symbol $''$.

Table 4.1 Nominal dimensions of the devices

Dim.	D2	D2′	D2″	D6	D6′	D6″	N2	N2′	N2″	N6	N6′	N6″
$h_{t,W}$ (µm)	0	550		0	550		0	550		0	550	
L_b (mm)	1.5			0.5			1.5			0.5		
L_t (mm)	1		0.14	1		0.211	1		0.125	1		0.199
b (mm)	1											
h_s (µm)	10											
h_p (µm)	0.5											
h_{el} (µm)	1											
$h_{t,S}$ (µm)	410											

4.4.2 Experimental setup and damping characterization procedure

The electromagnetic shaker setup shown in Fig. 4.2(b) is used to excite the cantilevers at their resonant frequency until the steady state is reached. The shaker is then turned off to measure the decaying cantilever response. The device displacement is indirectly measured through its piezoelectric open circuit voltage. Due to the high impedance of the piezoelectric devices (1-10 MΩ), a LF356N operational amplifier with an input impedance of 10 TΩ is used as a voltage follower

to prevent current circulation and electrical effects from affecting the measurement [57]. For each testing conditions, four data sets are recorded using a Rigol DS1072U oscilloscope in long memory mode. The damped angular frequency ω_d, which for $Q > 10$ is $\approx \omega_n$ [46], is first determined from the signal's autocorrelation function. The Q factors are then computed using the logarithmic decrement method with a nonlinear least square curve fitting algorithm on the envelope of the measured data. This methodology reduces errors due to noise in the output signal at low amplitude of vibrations. The devices are tested on the shaker with low input acceleration to avoid nonlinearities (notably spring hardening and nonlinear fluid drag). The measurements and the fits are very consistent across all experiments, as shown by a typical record and its associated fit on Fig. 4.2(c). The inset, which shows a zoomed in view, demonstrates the quality of the fit over several periods.

For each device, a first set of records is done with the silicon proof mass in vacuum to eliminate most of the fluid-structure interaction. The Edward's T-Station 75 turbopumping station provides a minimal pressure of P_a=5E-4 mbar based on the value measured by a WRG-S-NW25 wide range active pressure gauge. As shown on Fig. 4.3, the Q factor is capped to a limit value under a certain pressure threshold, which we assume is a good assessment of the intrinsic damping factor Q_{int} of the fabricated structures and the clamping scheme. The leak rate of the chamber is then controlled with a needle valve to perform measurements at increased pressures and evaluate Q_{tot} when both intrinsic and fluidic damping are in effect. We therefore extract the fluidic component Q_f using Eq. 4.10 and by assuming the pressure has no significant effect on the intrinsic damping.

The next step consists in bonding a tungsten mass on top of the silicon mass and repeating the Q factor measurement methodology; hence any variation of Q_{int} due to the bonding process or device manipulation can be evaluated and accounted for while the effect of the added mass on Q_f is measured.

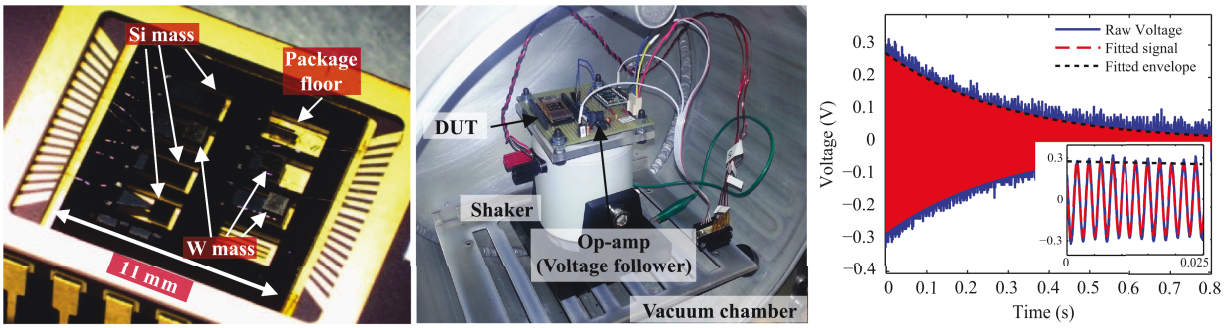

(a) (b) (c)

Figure 4.2 Pictures of the experimental setup showing a zoomed in view of a mounted PiezoMUMPs die featuring several designs with and without a tungsten tip mass (a), the shaker inside the vacuum chamber with the test devices on (b) and a typical voltage ring down record with its envelope and curve fit (c).

4.5 Results and discussion

4.5.1 Experimental demonstration

Beam model validation

Table 4.2 presents the material properties used in the models to evaluate the dynamic response of the cantilevers. Table 4.3 shows that the frequencies obtained from the simplified analytical beam model are generally in agreement with the experiments, although the error reaches up to 20% in some cases. To validate the approach, we also compared the results with a COMSOL finite element 3D model, which showed errors consistently below 4%. The model generally underestimates the resonant frequency, which could be due to several factors. One of them could be errors on the dimensions, but also errors on the material properties, none of which were measured directly. The model also does not account for the beam shear stress and the additional axial stress caused by the mass offset in the vertical direction. Contrary to the model, the tungsten tip mass is also not perfectly aligned with the silicon mass underneath. Nonetheless, these results are satisfactory, considering the simplifications applied.

Table 4.2 Material properties used in the model

ρ_s (kg/m^3)	ρ_w (kg/m^3)	ρ_p (kg/m^3)	ρ_{el} (kg/m^3)	Y_s (GPa)	Y_p (GPa)	Y_{el} (GPa)
2330	19300	3260	2712	130	345	69

Table 4.3 Experimental and modeled resonant frequencies

		D2	D2′	D2″	D6	D6′	D6″	N2	N2′	N2″	N6	N6′	N6″
ω_n (Hz)	Mod.	399	114	433	1120	313	1222	399	114	461	1120	313	1272
	FEM	410	117	445	1164	325	1254	410	117	474	1164	325	1304
	Exp.	431	119	-	1221	389	-	461	139	-	1271	338	-
% $\text{Error}_{\text{FEM}}$		2.7	2.6	2.7	3.8	3.8	2.6	2.7	2.6	2.7	3.8	3.7	2.5
% $\text{Error}_{\text{Exp}}$		7.5	4.2		8.3	19.5		13.4	18.0		11.9	7.3	

Quality factor results

The influence of pressure due to gas rarefaction on the fluidic damping is demonstrated in Fig. 4.3, showing a typical drop of the Q factor with P_a in the experimental results. Analysis of Fig. 4.3(a) first shows strong squeeze-film damping, as the Q factor tends to reach a stable lower plateau in the higher-pressure range. A similar behavior is also seen on Fig. 4.3(b), although Q_{tot} frequently drops further when the pressure approaches 1 bar. Such a drop is not typical for squeeze film damping, but results from the drag force on the other surfaces of the mass. Analytical estimates of Q_{tot} are also presented for comparison. They are obtained by combining all the damping components, namely the intrinsic damping measured experimentally, the squeeze film damping, but also the drag damping from Eq. 4.24. The results of the squeeze film flow model are obtained from a series expansion limited to the first 10 terms (max $m,n = 10$) whereas Q_{int} is derived from the mean value measured experimentally in vacuum. Moreover, the frequency used in the fluidic model is the experimentally measured frequency for the tested designs to minimize errors.

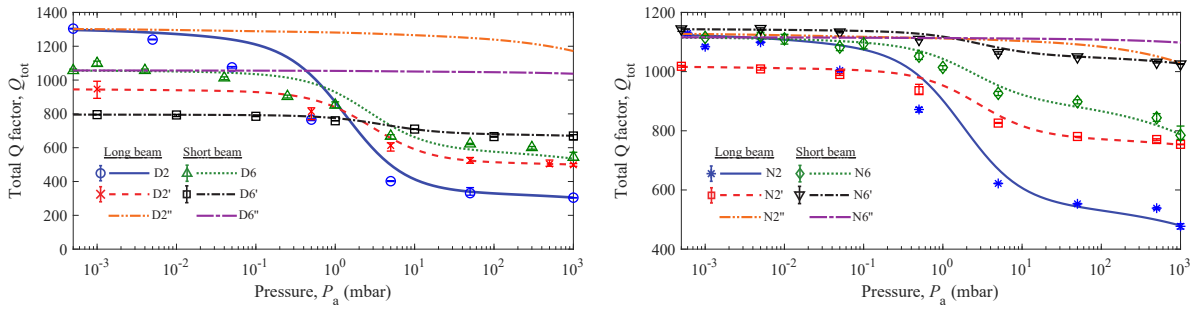

(a) Small gaps (b) Large gaps

Figure 4.3 Total quality factor Q_{tot} variation with the ambient pressure P_a for 2 dies, one mounted with a smaller gap (a) and the other with a larger gap (b). The data points (markers) are compared with the model (lines) as well as with additional modeling scenarios denoted by $''$.

Due to the model sensitivity to h_0 and the poor precision on its measurement, this parameter was fitted using the Q-factor measured experimentally at ambient pressure. The fitted gap values are noted in Table 4.4, which also compiles the Q factors measured in vacuum, Q_{int}, with those

measured at atmospheric pressure, Q_{tot}. The values of Q_f are then extracted from Eq. 4.10. The ratio between Q_f calculated from drag and squeeze film ($\Upsilon \ll 1$ when drag is dominant) is also included to show that drag is potentially significant for some of the designs tested. As expected, it is apparent when the gap is larger, such as for device N6.

Table 4.4 Measured Q factors for all designs

	D2	D2′	D6	D6′	N2	N2′	N6	N6′
Q_{int}[a]	1304	947	1057	796	1129	1018	1116	1144
Q_{tot}[b]	305	499	531	669	477	754	785	1026
Q_f	398	1055	1067	4193	826	2907	2647	9947
h_0 (μm)	109	98	107	102	144	134	165	154
Υ	6.8	16	4	7.6	3.0	5.9	0.98	2.3

[a]measured value in vacuum

[b]measured value at atmospheric pressure

Intrinsic damping

Interestingly, only small variations of Q_{int} are observed upon addition of the tungsten mass for device N2 and N6. This was observed on several other devices, but degradation of Q_{int} could not always be avoided. For example, a significant increase of the intrinsic losses for devices D2 and D6 was measured. Although we cannot identify the cause for the increased damping, the bonding process or the package mounting procedure may have led to an increase in clamping losses. Even though the resonant frequencies of N2′ (139.3 Hz) and N6 (1271 Hz) almost span over one decade, their Q_{int} values are in the same range. This therefore suggests that intrinsic damping is weakly dependent on frequency, which is expected for hysteretic damping linked to internal friction [46].

Fluidic damping extraction, mass density, device frequency and size effects

We consistently observe a notable increase of Q_{tot} at atmospheric pressure when the tungsten mass is bonded, regardless of the device frequency or gap. By accounting for the measured Q_{int}, we derived Q_f from Eq. 4.10 in Table 4.4. To gain additional insight on the potential damping sources, we compare the different damping contributions (Q^{-1}) for all the designs in Fig. 4.4. For any given design, Q_f^{-1} consistently drops by a factor ranging from 2.5 to 4.5 by adding the tungsten mass. These levels are expected based on Eq. 4.25 and Eq. 4.27 if we consider the simultaneous increase of the linear mass density (x 11.4) and the frequency drop (x 0.3). When the frequency and gap are kept in the same range, the drop of Q_f^{-1} is even more pronounced. Indeed, by comparing D2/N2, which have a silicon mass, with D6′/N6′, which have

an additional tungsten mass, **we note that Q_f^{-1} decreases by an order of magnitude while the device footprint is also reduced by 40%**. For the sake of comparison, we also considered additional modelling scenarios, referred to as D2″, D6″, N2″, and N6″, with shorter W+Si masses to conserve the frequency relatively to the bigger Si mass of the baseline designs. An improvement of Q_f is again predicted, effectively because the equivalent mass is similar but in a smaller volume, which reduces the fluid induced forces. Moreover, damping due to squeeze film is greatly reduced and drag generally dominates in these designs. If we instead compare designs D6′ with D2″ (or N6′ with N2″), which have drastically different mass and beam dimensions, but both integrate tungsten and similar operating frequencies, the improvement is less drastic. Although the smaller mass footprint again reduces damping from squeeze film, the effect of drag increases overall.

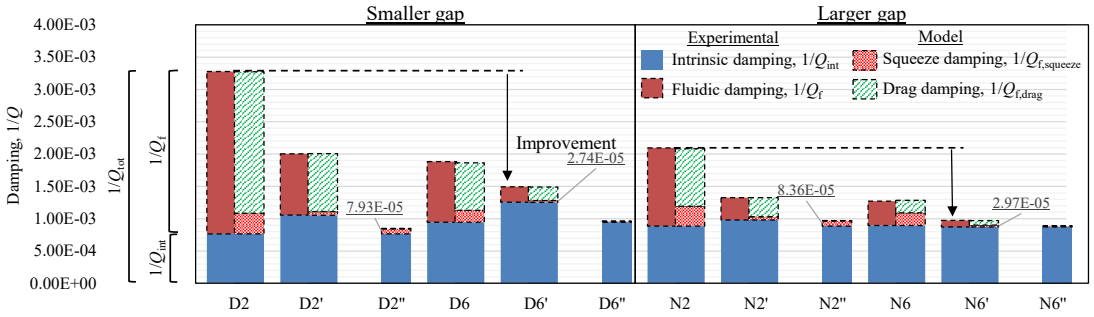

Figure 4.4 Comparison of Q_{int}^{-1} and Q_f^{-1} to Q_{tot}^{-1} at ambient pressure for all designs. The experimental results (solid) are compared with the model (textured), which for reference are decomposed in terms of drag and squeeze film damping components. For modeled designs, Q_{int}^{-1} is based on the experimentally measured values for the silicon mass design. An order of magnitude reduction on Q_{tot}^{-1} for two set of devices with comparable frequencies is observed, namely for D2/D6′ and N2/N6′. D2/N2 feature a long beam and a Si mass whereas D6′/N6′ have a short beam with an added W mass.

Discussion on modeling errors

Most of the discrepancies observed on Q_f between model and experiments are likely due to the relative simplicity of the model, but could also be caused by errors in the dimensions. For one, the real gap may not be as flat as assumed. For example, it is possible that the dies are not laying perfectly flat in the device package. Moreover, the addition of the W proof mass introduces a static load simply due to gravity; for the longer beams, the resulting static deflection can be almost 10 µm. Both considerations can significantly affect the gap value, which is why this value was fitted with the model. Equation 4.17 appears to consistently overestimate the effect of gas rarefaction in our experiments below 1 mbar. An hypothesis for this observation is that

Eq. 4.17 is obtained using several assumptions, namely that both surfaces are identical and smooth, and that the ratio h_0/L_t is small (<0.01). However, these assumptions do not apply to our case: our surfaces are made from different materials, with the base being a rough gold surface, and the h_0/L_t is significantly larger. Furthermore, the Stokes flow assumption typically requires a Reynolds number $Re \ll 1$, which is flawed in our case. By considering the size and maximum tip displacement of our devices, we estimate Re to rather be in the range of 1-1000. Although still in the laminar regime, inertial effects are not negligible. Nevertheless, the model consistently predicts the increase of Q_{tot} at ambient pressure upon addition of the tungsten proof mass and appears to capture adequately the combined effect of transverse and torsional motion of the mass. It is therefore reasonable to use it to make generalized observations.

4.5.2 Extending the effects of mass characteristics, frequency and pressure on viscous damping based on model

Equations 4.25 and 4.27 highlight the interest of high density materials, as they both scale linearly with this parameter. An improvement up to a factor of $\rho_W/\rho_{Si} = 8.3$ is expected if tungsten is used instead of silicon to fabricate masses of similar sizes for the same VEH operating frequency. While this results in a much heavier proof mass, which requires a redesign of the beam, another option is to scale down the mass volume. This second approach improves the device quality factor by instead reducing the drag coefficient. It is however less clear which dimensions should be prioritized and the extent of the potential improvement. As observed experimentally, reducing the pressure, P_a, clearly has a positive effect on Q_f, regardless of the damping model. However, the trend versus P_a differs for each model, which may partly explain the small drop observed close to ambient pressure on Fig. 4.3(b).

Viscous damping from drag

The presence of h_t and the peripheral dimensions in the numerator of Eq. 4.25 shows potential adverse effects from the size reduction on Q_f. This is mainly because Stokes' drag scales with the peripheral length comparatively to the stored energy in the mass, which scales with its volume. In this regime, there is no benefit from reducing the mass thickness, hence, any reduction in size should be applied to the lateral dimensions. Nonetheless, the influence of the oscillatory boundary layer, δ, is also important.

MEMS VEHs typically operate near ambient frequencies of 10-1000 Hz, therefore $\delta \approx 100$ µm - 1 mm in air at atmospheric pressure. Hence, for large VEH, such as those fabricated by Elfrink *et al.* [63], the reduction in drag will be more important than for harvesters with dimensions $\ll \delta$.

Assuming $D \gg \delta$, the improvement is still expected to follow ρ_W/ρ_{Si}, whereas for $D \ll \delta$, it will instead scale as $(\rho_W/\rho_{Si})^{1/2}$. However, the effect of drag on the beam may become significant again as the mass is shrunk in size. Finally, because $\delta \propto \rho_a^{-1/2} \propto P_a^{-1/2}$, P_a can have an immediate effect on damping if $D \gg \delta$, even in the continuum regime ($0 < Kn \leqslant 0.01$).

Viscous damping from squeeze film

Just as in the case of drag damping, the first term of the squeeze film expression (Eq. 4.27) states that Q_f improves proportionally with the proof mass thickness if the frequency is kept constant. However, it might be advantageous to reduce the mass thickness to increase the gap h_0 if the packaging space is constrained. The second term, which varies to the square of the gap to mass side lengths ratio, also shows significant potential for improvement by reducing the mass planar dimensions. The last term mainly depends on L_t/L_b and stems from the effect of the mass tilting. It has a marginal impact if the geometry is adjusted to conserve the frequency and gap ratio, going from 1 for $L_t/L_b \ll 1$ and up to 4/3 when $L_t \gg L_b$; each value respectively describing the case of pure linear or rotation motion of the proof mass. Although the tip mass/beam length ratio has a significant impact on M_{eq}, its effect on Q_f is an overall limited 33% improvement at best. It is however not clear which dimensions to rescale first due to these numerous factors.

The fluid mainly flows along the shortest planar dimension, which therefore has the most impact on Q_f. If a constant tip mass area and a constant frequency are assumed, a square mass results in a minimum Q_f. Although this geometry is frequently used [4, 63], Eq. 4.27 suggests this is far from optimal. Nevertheless, it is often not practical to scale down only one dimension, thus why openings are usually etched through the mass to reduce the effective flow length [19]. This approach works well for surface micromachined devices, but is harder to implement in bulk micromachining, which is often preferred to make harvesters with large masses. Thick proof masses also require larger channels, which inconveniently reduce their effective density. Using materials with higher densities to reduce significantly the mass area therefore represent an interesting option in this regard. Finally, P_a only affects the effective viscosity, μ_{eff}, thus its impact on the damping coefficient only becomes noticeable in the slip flow regime ($Kn > 0.1$), contrary to drag.

Effect of the gap and mixed regime

The assumptions of squeeze film become less accurate as h_0/L_t increases, because the forces acting on the sidewalls and the top surface of the mass (caused by drag) become comparable to the force on the bottom (squeeze film). Even though the surface extension approach proposed by Veijola *et al.*in [203] could reduce errors stemming from border effects, it can still result in

errors from 10% to more than 40%, depending on the h_0/L_t ratio and the dominant motion type (linear or rotation). Moreover, this approach does not seem to capture the behavior of the other forces with respect to Pa, especially in the continuum regime. Judging from both model trends, which are shown on Fig. 4.5, the variation of the bottom force with P_a differ significantly from drag. Hence, the drag damping model presented in section III.B may eventually become more appropriate as h_0/L_t increases. Here, we have simply added squeeze film damping and drag damping in parallel to try to capture the effect of additional drag at larger gaps. Although this is an oversimplification (it does not account for fluid flow interactions between the bottom borders with the other surfaces), this approach seems to provide satisfactory results.

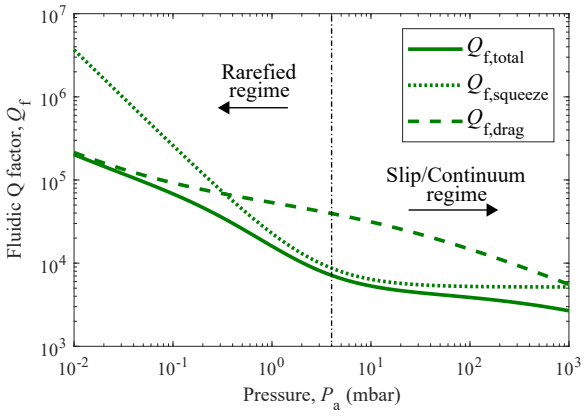

Figure 4.5 Comparison of simulated Q_f from the drag model (dashed line) and squeeze film model (dotted line) with pressure P_a. Drag does not follow the same trend as squeeze film with pressure, which can impact significantly Q_f in the continuum regime. Curves plotted for design N6 with $h_0 = 165$ µm.

We finally plot in Fig. 4.6 the anticipated Q_f at ambient pressure with respect to h_0 for 3 device designs. The figure evidently shows how Q_f improves by increasing the gap, but also demonstrates the limit of this approach passed a certain gap value. By again comparing D2″ with D6′, we observe the negative effect of reducing the mass volume instead of redesigning the beam if the gap is large enough. Therefore, drag effectively imposes the upper bound on Q_f as the mass shrinks or as the gap increases. Nevertheless, these results demonstrate how the added mass greatly improves Q_f overall, even allowing values up to 10^4 to be reached at ambient pressure with smaller gaps.

We previously identified the dominant fluid damping type by computing the ratio of the quality factor stemming from drag (Eq. 4.25) over squeeze film flow (Eq. 4.27). We propose to use this value as a metric to estimate when downsizing the mass footprint or increasing the gap has a diminished impact on Q_f. To simplify the expression, we assume the effect of tilt on Q_f is small compared to the other factors and most of the drag is exerted on the mass, a reasonable

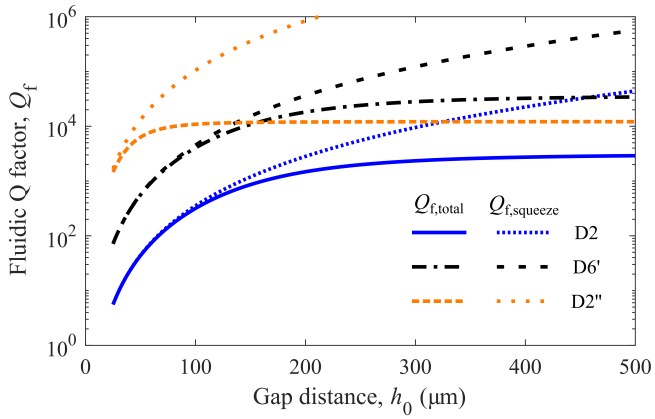

Figure 4.6 Comparison of simulated Q_f at various gap distance h_0 for designs operating at similar frequencies. The analytical result for the combined fluid damping are compared to the squeeze film damping to illustrate how increasing the gap eventually provides no additional benefit.

assumption if $L_t/L_b \geq 0.5$. This metric is given by

$$\Upsilon = \left(\frac{128}{\pi^7}\right)\left(\frac{\mu_{h0,\text{eff}}}{\mu_{\delta,\text{eff}}}\right)\left\{\frac{(b+L_b+L_t)\left(b^{-2}+L_t^{-2}\right)^{-1}}{h_0^3\left[1+D/(2\delta)\right]}\right\}. \tag{4.28}$$

and effectively states that squeeze film is dominant (*i.e.*, significant gain from reducing the mass foot print can be made) if $\Upsilon \gg 10$, whereas drag is dominant if $\Upsilon \ll 0.1$.

4.5.3 Implications for VEH

These results successfully demonstrate the benefits of integrating a tungsten mass to simultaneously reduce the footprint and improve the quality factor in ambient air. The implications for VEH are numerous.

Because the power output of the VEH is proportional to its effective mass and considering the final device footprint, Fig. 4.4 suggests that it is preferable to shorten the beam to tune the frequency instead of scaling down the proof mass, unless the gap is very small $(h_0/L \ll 0.01)$.

In some cases, our results show that $Q_f \gg Q_{int}$, thus vacuum packaging would only provide marginal benefits in these scenarios. Alternatively, if the material, anchoring and structural losses were reduced, Q_{tot} at ambient air could be improved further, perhaps up to 10^4. Although the potential improvements on the mechanical Q factor are then limited to an order of magnitude at best if this is realized, it is worth discussing other limiting factors.

First, the Q factor cannot be increased indefinitely. Higher Qs require more traveling range for the mass, especially at low operating frequencies, but also imply large stresses on the structures. Both may become limiting due to space constraints and fundamental limits on the materials [58, 141].

Furthermore, mechanical damping could become very small comparatively to electrical damping, Q_{el}^{-1}, from energy harvesting [57]. For example, the damping capacity of piezoelectric AlN devices have been reported to yield Q_{el} ranging around 600-1200 [102]. Efficient harvesting is possible when $Q_{\mathrm{el}} \leq Q_{\mathrm{f}}, Q_{\mathrm{int}}$, with the optimal power output for a narrowband vibration source achieved if Q_{el} is equal to the mechanical Q [57]. Both conditions become easier to achieve at ambient pressure with a higher density mass.

Finally, the sensitivity of VEHs to input vibration increases with the mass density, but their power output and power density also scale with the mechanical Q factor. By combining both effects, the power density at ambient pressure could improve by nearly 60 times by replacing Si with W.

4.6 Conclusion

We have shown analytically and experimentally the impact of the tip mass characteristics on the fluidic damping and device Q factor. Simplified analytical models were first introduced to describe the beam deflection and fluid damping behaviour, as well as to extract scaling laws on Q_{f}. Verified with experimental results, we demonstrate that, for a fixed operation frequency, Q_{f} can be generally improved by increasing the linear mass density. As anticipated, the behaviour of the damping force changes based on the device geometric parameters, mainly the gap to mass planar dimensions' ratio. If the gap is large compared to the mass planar dimensions, most of the damping will be due to drag and downsizing the mass has a negative impact on Q_{f}. In the case of squeeze film damping however, a reduction of the mass footprint can rapidly bring substantial improvement.

The integration of a high density material to replace silicon, such as tungsten, consistently increases the total Q factor. By accounting for the frequency changes, Q_{f} typically increases by close to an order of magnitude. In effect, $Q_{\mathrm{f}} \gg Q_{\mathrm{int}}$ was observed in some cases, thus further improvement of Q_{tot} was limited by the structural intrinsic losses rather than by fluid losses. Therefore, this approach could make vacuum packaging unnecessary for VEH. At the same time, it could also effectively boost their power output and power density by more than an order of magnitude, potentially up to 60 times compared to Si based designs. This method hence appears promising to meet the power needs for a growing range of wireless sensors envisioned for the

Internet of Things, while also offering a path towards size and cost reduction for MEMS-based VEH.

CHAPTER 5

A wafer-level process for bulk tungsten integration in MEMS vibration energy harvesters and inertial sensors

This chapter presents the development of an original fabrication process to integrate thick, high density proof masses made from 500 µm thick tungsten (W) substrates with silicon-based devices in a wafer-level MEMS batch process. The proposed approach integrates W masses on the functional wafers via wafer bonding and are patterned in a 2-step wet chemical milling process. The concept is demonstrated through the realization of several short-loops. First, by fabricating cantilevers in a silicon-based substrate on which W masses are integrated by adhesive bonding. The feasibility of the metal milling method is demonstrated for wafer-level mass patterning and a novel temporary carrier bonding scheme is also developed to accommodate for the important topologies created. The initial prototype, an out of plane silicon resonator, is tested and shows a resonant frequency of 87 Hz and a Q-factor of 267. We then show that the W wet etching method is compatible with many common cleanroom materials, but can still cause integration issues with others.

Hence, in parallel of these advancements, a process to fabricate AlN-based piezoelectric devices is developed on silicon on insulator (SOI) wafers. Here also, short-loops are designed to validate the compatibility of the materials with the W wet etching solution. Due to some of the compatibility concerns identified, protective layers are incorporated in the flow and those are shown to be effective in protecting the piezoelectric layer. However, contradictory results are observed with respect to the capping layer strategy adopted to protect the contact pads.

Although all the fabrication blocks are not integrated seamlessly yet, this work shows the potential for doing so. Nevertheless, piezoelectric vibration energy harvesters integrating high density proof masses are fabricated through a die-level bonding scheme to demonstrate the potential of this technology. The approach developed here is used to improve the sensitivity of vibration energy harvester driven by low frequency ambient vibrations, but it could also enable an array of potential applications for highly sensitive inertial sensors.

5.1 Introduction

Silicon based inertial devices like MEMS accelerometers and gyroscopes are now widely adopted in consumer electronic products. They however have limited performances compared to macro scale devices at low g accelerations and low frequencies, especially in terms of background noise and resolution. This limits their market penetration in some applications, such as seismology, human activity monitoring, asset tracking and structural health monitoring [129, 157]. In addition, MEMS vibration energy harvesters are considered as an emergent solution to power the Internet of Things (IoT) and wireless sensor networks [144], but they must be relatively large to produce enough power at this time. In both applications, the limitations are partly due to the small size of MEMS and the low material density of their silicon proof masses.

Indeed, the sensitivity and minimal resolution of inertial MEMS depends on several factors including the transducer and read out circuit design, but also the size of the mass. Larger bulk micromachined silicon based devices are an explored solution [90], but their large footprint on the wafer leads to increased costs per unit.

An alternate solution is to integrate materials with a density larger than silicon ($\rho_{Si} = 2.33$ g/cm^3) to produce the proof mass. Among common metals, gold has the highest density ($\rho_{Au} = 19.3$ g/cm^3) and can be readily electrodeposited. Recent work for instance used this approach to produce both springs and proof masses in a post-CMOS process [218]. Gold is however expensive and has a large mismatch in coefficient of thermal expansion compared to silicon (CTE=14 vs. 3). Tungsten, which has the second highest density ($\rho_W = 19.25$ g/cm^3 = 8.3 x ρ_{Si}), offers a better CTE match (CTE=4) and is more cost effective. It is also compatible with MEMS and CMOS microelectronic processes. For these reasons, it is a more attractive option, although thick layers cannot be electroplated.

Polymer pastes filled with W nanoparticles have been used to make screen printed masses, but their actual density is about 50% of bulk W [192, 225]. This density is slightly higher but comparable to nickel and copper ($\rho_{Ni/Cu} = 8.9$ g/cm^3), which can both be electroplated. Tungsten can also be integrated using thin film deposition, such as metal organic chemical vapor deposition (MOCVD), but this may limit the thickness of the masses. This approach was in fact developped by Analog Devices [77] and they obtained structures of about 4 µm thick. This constraint can be circumvented by using a silicon mold structured with thin pillars or etched wells, which are then filled with W by conformal MOCVD. This technology was demonstrated by Sandia Labs, which have produced masses of about 20 µm thick [73]. Analog Devices have also recently filed a patent based on the same principle in which they report composite masses having up to 7 times the density of standard silicon with thicknesses up to 50 µm [224]. Although the

resulting masses are thicker and approach the bulk density of W, it is still far from what can be achieved by bulk silicon microfabrication. Producing thicker masses that preserve an effective density close to bulk W using this approach is still challenging due to the high aspect ratios necessary, even using deep reactive ion etching (DRIE). Integration by bonding of bulk W masses was also proposed by Aktakka *et al*. for the fabrication of high power density vibration energy harvesters [6]. However, the masses are pre-patterned by electro discharge machining (EDM) and aligned individually at the die level by pick and place, which could be ineffective in terms of costs.

In this work, we propose a wafer-level process to integrate thick, bulk W proof masses made from thick metallic substrates. Defined by 2-steps chemical wet etching, they are integrated by wafer bonding on a silicon based device wafer which contains the functional layers and spring structures of the MEMS device. The first part of this chapter hence presents the general process flow proposition. The concept is then validated by demonstrating each fabrication blocks through various short-loops. A fabricated cantilever beam prototype device is initially tested by measuring its quality factor and resonant frequency. Active piezoelectric devices are finally fabricated and presented in the last section. Although out of plane devices were fabricated here, the developed process flow could theoretically produce in plane transducers as well.

5.2 Proposed fabrication process flow

Figures 5.1 and 5.2 summarize the 4 main steps of the proposed process flow, which are separated as follow: (A) W and (B) device wafers preparation, (C) wafer bonding and (D) the final mass and cantilever definition. Two process variations are illustrated here, but they only differ by their wafer bonding approach, as one uses an adhesive, whereas the other uses an eutectic tin-gold interface. The overall wafer-level integration scheme remains the same. This section briefly presents each step. Issues related to specific process nodes are then discussed in section 5.3. A detailed presentation of the processing parameters and the mask layouts used for all fabrication steps is available in appendix E.

5.2.1 Tungsten wafer preparation

Tungsten wafer characteristics and cleaning

The masses are produced from 100 mm diameter, 500 µm thick W substrates (99% purity, polycrystalline) purchased from American Elements Inc [7]. As observed on Fig. 5.3, they did not exhibit visible porosity, but the initial supplier polish produced a rather rough surface with an

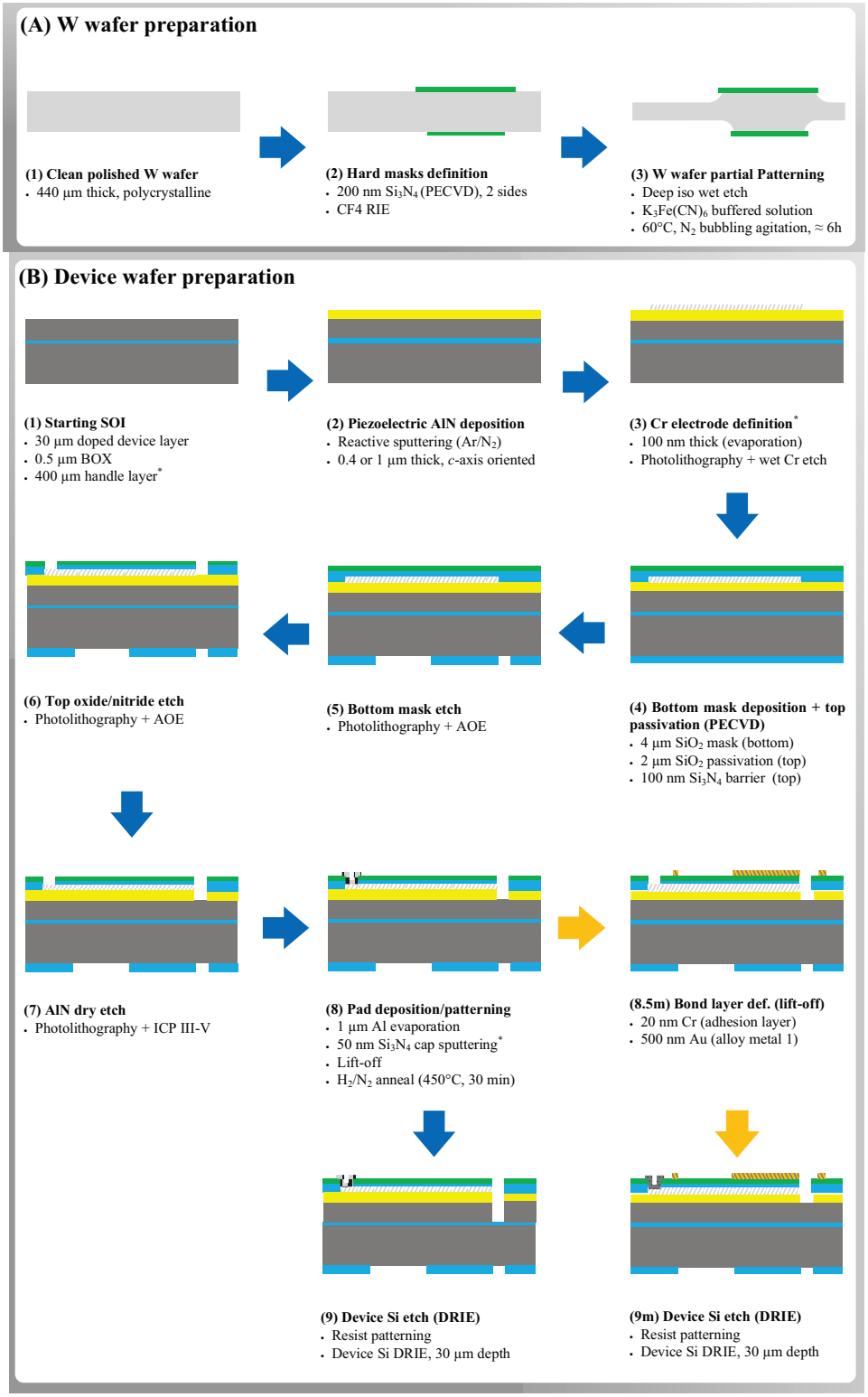

Figure 5.1 Bulk W integration process flow overview part 1: wafers pre-bonding preparations.

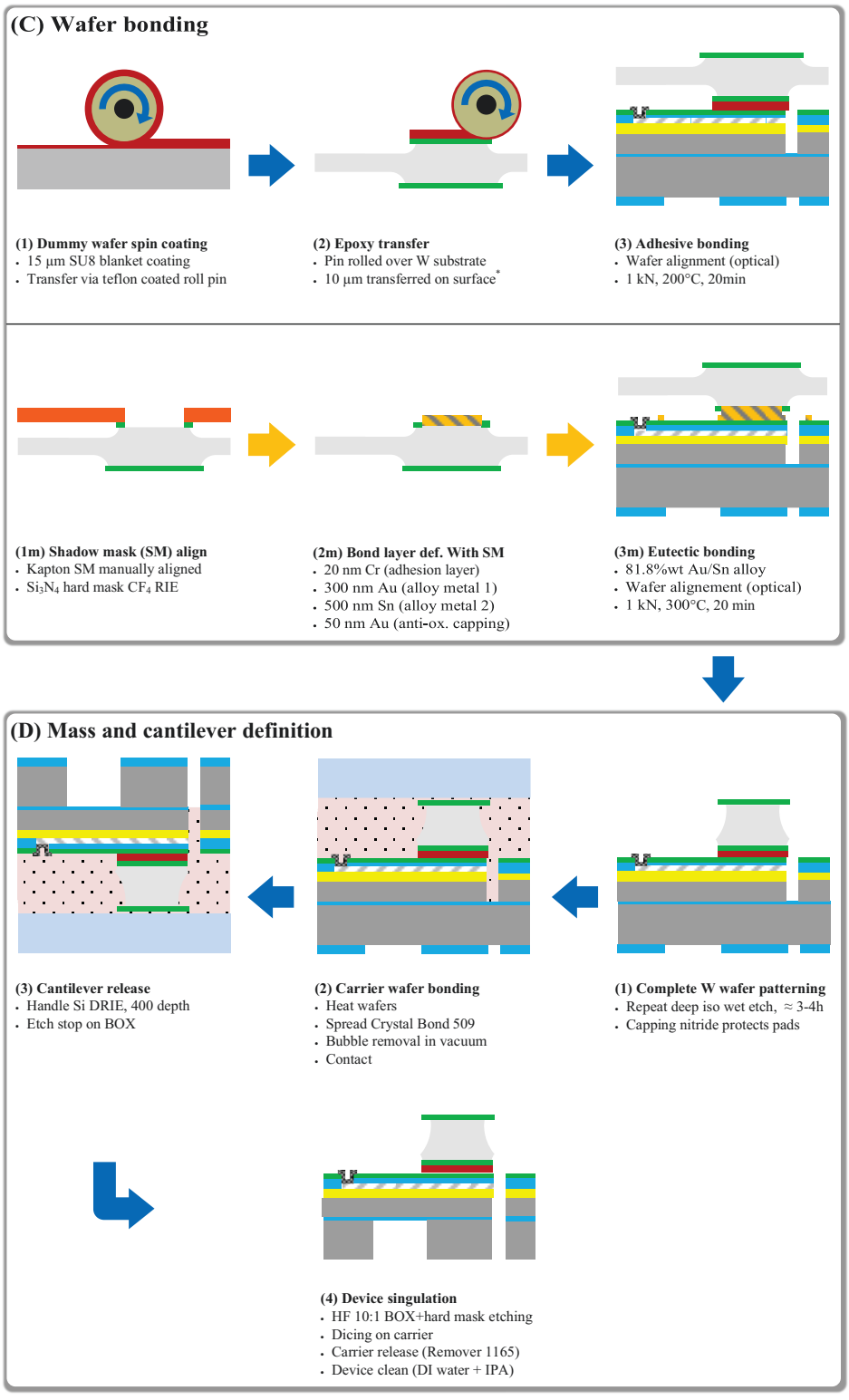

Figure 5.2 Bulk W integration process flow overview part 2: wafer bonding and device release. Although two wafer bonding approaches are presented, the mass and cantilever definition step remains the same for both.

RMS roughness R_q in the range of 0.2 µm. An additional polishing step using water based silica slurries was subsequently realized by Valley Design Corp [202] to improve the surface topology and get a mirror finish on both sides. After this second polish, the final thickness was 440 µm and, as shown on Fig. 5.4, a very smooth surface was obtained with a typical $R_q < 4$ nm, as measured by AFM. The surface observed by SEM also showed densely packed grains, but with minor porosity, as seen from the occasional voids on the surface. Although not critical for adhesive bonding, low roughness is needed to use solid phase bonding technologies, such as thermocompressive or direct (fusion) bonding. The wafer bow was also measured on a Dektak stylus profilometer and varied significantly among wafers, going from 40 µm to 300 µm. Such variability is assumed to be caused by the polycrystalline wafer fabrication and polishing process, which is not standard. For comparison, the bow of 100 mm Si wafer is typically less than 30 µm.

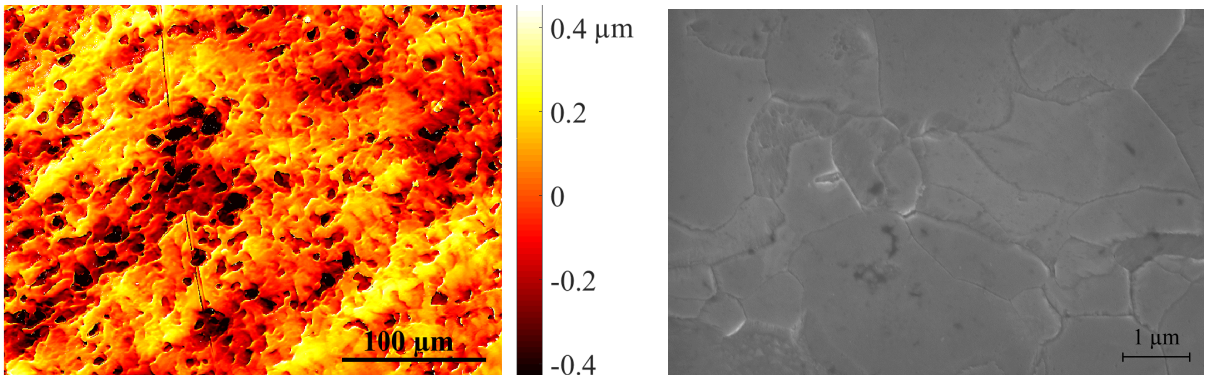

(a) Topology scan, 20 X magnification, $R_q = 0.16$ µm (b) SEM image, 14k X magnification.

Figure 5.3 Initial W substrate surface finish.

Before further processing, the metal wafers are cleaned using standard acetone/IPA and a gentle wipe scrub followed by a prolonged Remover 1165 bath heated at 70°C. The wafers are finally water rinsed until hydrophilic surfaces are observed.

Hard masks definition

A 200 nm silicon nitride layer is deposited on both sides of the W wafer by plasma enhanced chemical vapor deposition (PECVD) to produce masking layers for the subsequent wet etch. The hard masks are then patterned by first defining a photoresist mask by photolithography and etching the nitride layer with a CF_4 based RIE.

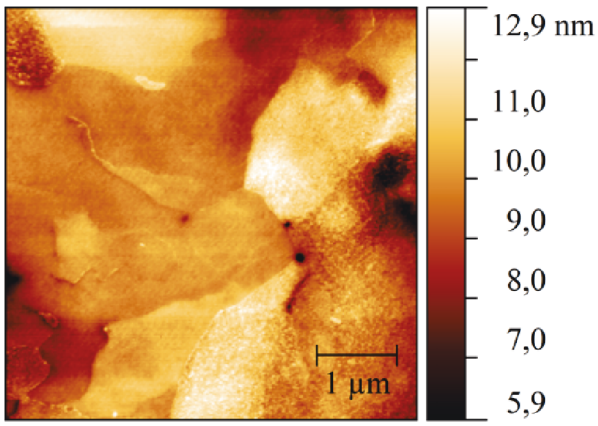

(a) AFM scan of a polished W substrate. R_q=1.09 nm, with a 13.4 nm maximum height variation measured on this sample.

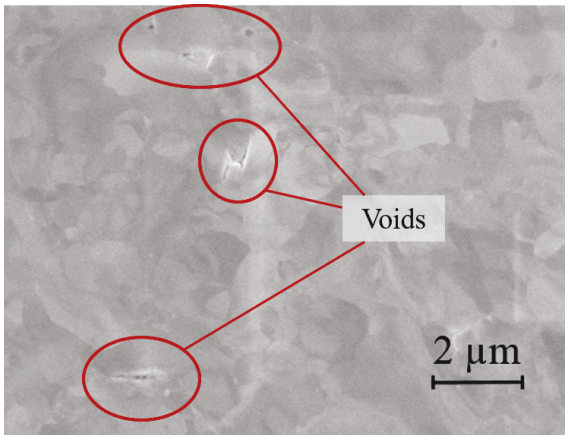

(b) SEM image of a W substrate after polishing, showing a densely packed surface with minimal porosity.

Figure 5.4 Polished W substrate surface finish

First wet deep isotropic tungsten etching

A prolonged deep isotropic wet etching step on both sides of the W substrate is then realized to begin the partial definition of the masses and thinning of the metallic substrate using a buffered potassium ferricyanide based W etchant[1]. Composed of KOH-KH_2PO_4-$K_3Fe(CN)_6$, the solution removes W by basic oxidation of the surface according to the following chemichal reactions [45, 184]:

$$K_3Fe(CN)_6 + H_2O \longrightarrow 3\,K^+ + Fe(CN)_6{}^{3-} + OH^- + H^+ \tag{5.1}$$

$$W + 6\,Fe(CN)_6{}^{3-} + 8\,OH^- \longrightarrow WO_4{}^{2-} + 6\,Fe(CN)_6{}^{4-} + 4\,H_2O. \tag{5.2}$$

Practically, W reacts with dissolved ferricyanide $Fe(CN)_6{}^{3-}$ to form soluble tungstate $WO_4{}^{2-}$ and ferrocyanide $Fe(CN)_6{}^{4-}$ in water, as described by Eq. 5.1. Potassium phosphate KH_2PO_4 is used to buffer the solution to maintain a near neutral pH and ensure compatibility with photoresists.

To increase the etch rate and improve uniformity, the solution is stirred using nitrogen bubbling. A custom etch vessel, shown in Fig. 5.5, is used here to minimize the required etchant volume and agitate the solution on both sides. The substrate is inspected and flipped at regular intervals (varying from 20 to 60 minutes). The vessel is immersed in a water bath heated up to 85°C, but the solution temperature is slightly lower due to the nitrogen flow and usually closer to 60°C.

1. supplied by Sigma Aldrich or Transene

At this temperature, the measured etch rate is approximately 0.5 to 0.6 µm/min across the wafer, thus a cumulative etch time of approximately 6 hours is expected to thin it down to roughly 100 µm at this stage.

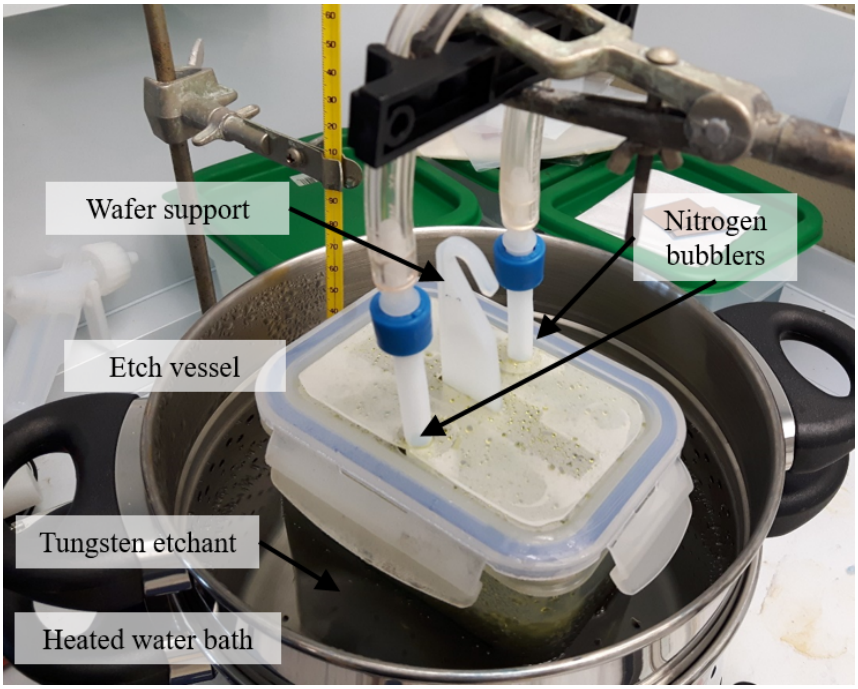

Figure 5.5 Photograph of the custom W wet etching setup

5.2.2 Device wafer preparation

In parallel, the device wafer is prepared ahead of the bonding step to form functional layers and spring structures.

Initial substrate characteristics, piezo layer deposition and wafer recoring

SOI wafers are used for fabrication of the functional MEMS structures with a piezoelectric layer. The initial substrates, supplied by Okmetic, consists of 200 mm SOI wafers made from fusion bonded silicon wafers. The device layer is 30 µm thick and made of <100> oriented P+ boron doped silicon (0.014-0.020 Ohm-cm), whereas the buried oxide (BOX) is 500 nm thick. The handle silicon layer has the same electrical properties as the device layer, but is 675 µm thick.

Three wafers were processed at C2MI by Teledyne Dalsa in Bromont for deposition of the active piezoelectric layer. C-axis oriented aluminum nitride (AlN) is synthesized by RF reactive sputtering directly on the device silicon layer. Two wafers had 1 µm thick deposited (referred as *high stress AlN*), whereas the third had 400 nm deposited (*low stress AlN*).

The wafers were cut-down into smaller 100 mm and 3 inches wafers using a LPKF Protolaser U3 to allow processing on 3IT equipments. The surfaces were protected beforehand with 100 nm PECVD SiO_2 and 1.2 µm thick photoresist layers on both sides. A gentle edge polish was then executed by hand using fiber optic grade polishing paper to smooth the wafer edges and minimize risks of fracture. The wafers were subsequently cleaned in standard solvent and the surface oxide was stripped using concentrated HF to lift any remaining particles from the surface. Cleaning was finally completed by immersion in a piranha solution. To prevent attack from the developer on the AlN (see section 5.3.4), a thin PECVD oxide of 100 nm is regrown on top of the piezoelectric layer.

Top electrodes definition

The top electrodes are made from 100 nm thick chromium deposited by evaporation. We initially used a lift-off approach, but it left large amounts of flakes on the surface after rinsing and drying and instead opted to wet etch the electrodes afterward.

Wafer thinning

The initial wafers were 705 µm thick. Although a DRIE in this depth range could probably be achieved to release the cantilevers near the end of the process, we decided against it to reduce risks, because etches of such depth have not been done by the 3IT staff. The handle layer was therefore thinned to 400 µm by grinding and polishing, which was done externally by Aptek Industries [13]. The wafers were then cleaned in a standard SC1 solution and water rinsed before further clean room processing.

Top passivation and bottom hard mask definition

A 2 µm oxide layer is deposited on top of the metallic electrodes for surface passivation and protection. Additionnaly, this oxide could be planarized and thinned down to reduce the surface topology if a cap wafer was to be bonded over the MEMS structures. A 100 nm silicon nitride layer is then deposited over the oxide to prevent diffusion if a metallic layer is used for wafer bonding (e.g., Cu for thermocompressive bonding or Au for eutectic bonding). Depending on the metal stack used, it can also improve adhesion (with Ti for instance). A 4 µm thick SiO_2 layer is also deposited on the backside to form an oxide hard mask for the subsequent backside DRIE step.

These dielectric layers are finally etched using a CF_4 based recipe in the Advanced Oxide Etch (AOE) Inductive Coupled Plasma (ICP) tool. The top patterns define the beam contours and

open windows for the contact pads. The bottom patterns define the beam overhang length and the silicon proof mass. To prevent damaging the underlying AlN layer in the next photolithography step, the top etch is stopped before reaching the AlN to keep some residual oxide.

Aluminum nitride etching

Another lithography is realized to define the beam contours and open a window for the bottom contact through the AlN layer. The residual oxide is first dry etched using a CF_4 based RIE, whereas the AlN is then completely etched down to the device Si using the ICP III-V etching tool with a BCl_3 based recipe.

Aluminum pad integration

To allow electrical connection by wire bonding, bond pads are then patterned by lift-off to make contacts on the device layer Si (bottom) and on the Cr electrode (top). Before the pad deposition, a CF_4 based RIE is again realized to remove any residual oxide over the contact areas. The bond pads stack is then made from a 1 µm thick aluminum layer deposited by evaporation, which is topped by capping layer. This layer is added to protect the pads from prolonged exposition to the W etchant later in the process. Here Fig. 5.1 shows a 50 nm Si_3N_4 layer is used (deposited by sputtering without breaking vacuum after the Al deposition), but several cap layers were investigated (see section 5.3.5). Finally, the wafer are annealed for 30 minutes at 450°C in forming gas ambient to form ohmic contacts by controlled diffusion of Al in the device Si layer.

Metalic bonding layer deposition

If metallic bond layers are used, they are deposited just before the device layer silicon etching. A thick negative photoresist layer is used for the metal lift-off due to the topologies present on the wafer surface. Here, deposition of a 500 nm Au layer over 20 nm Cr adhesion layer by evaporation is proposed to realize part of a tin-gold eutectic bonding interface.

Device layer silicon etching

The last photolithography step is finally realized by spin coating a 6 µm thick photoresist (AZ9245) on the wafer front side. The spring patterns are then defined in the device layer by DRIE down to the BOX layer. Any traces of metals (Au, Cr, Al) are wet etched before entering the ASE-STS tool to prevent contaminations.

5.2.3 Wafer bonding

This step is where the significant process variations occur. This section presents details regarding each of the methods proposed.

Adhesive bonding

Adhesive bonding is a flexible and convenient approach due to its low requirements on surface roughness and low thermal budget. A roller based resist transfer method, adapted from [220], can be used to apply the resist on the patterned substrate, which features significant topologies at this point. To realized this transfer, a 15 µm thick SU-8 layer is first spun on a silicon support wafer, with no subsequent baking step or prescribed dwell time. A Teflon coated rolling pin is then rolled on the support wafer and immediately rolled over the W wafer to transfer part of the resist.

Finally, the silicon and W wafers are optically aligned[2] and transferred in the bonding tool. After pumping the air from the bonding chamber, a force of 1 kN is applied and the chucks are heated to 200°C for 20 min to complete the bond.

Eutectic bonding

An alternate approach using Au-Sn eutectic bonding can provide a more robust bonding interface. The notable topologies present on the wafer surfaces again prevent the use of spin coating and a shadow mask is necessary here. The size of the mask openings are reduced by an offset of 250 µm to allow for misalignment errors, considering that this step needs to be done manually under the microscope. By doing so, risks of melt overflowing at the edges during bonding are also minimized.

Once the shadow mask is solidly attached to the wafer, the Si_3N_4 hard mask is first stripped using the same CF_4 based RIE recipe as before in order to deposit the thin metal layers directly on the metallic substrate for maximum adhesion. A Cr/Au/Sn/Au metallic stack, with respective layer thicknesses of 20, 300, 500 and 50 nm, is then deposited by evaporation. The Cr layer is again used for adhesion, whereas the 300 nm Au and 500 nm Sn layers are part of the bonding alloy. A 50 nm thick Au capping layer is deposited last to prevent Sn oxidation and allow for a flux less eutectic bonding process [197]. By also considering the 500 nm Au layer on the device wafer, the full bonding stack gold composition is expected to be close to 81.8 %wt, thus forming a slightly Au rich eutectic alloy.

2. Optical alignment is mandatory because W blocks infrared light.

As for adhesive bonding, the silicon and W wafers must be optically aligned before bonding under vacuum ambient. A 1 kN force is applied while the chucks are heated up to 300°C [197] and this plateau is maintained for 20 minutes before cooling down.

5.2.4 Mass and cantilever definition

Tungsten mass release

To complete the patterning and release of the masses, the assembled wafer stack is re-immersed in the W etchant in the same conditions as before. During this step, only the top of the W substrate is exposed and etched. Assuming a similar etch rate of 0.5 µm/min, an estimated immersion time of 3h20 is expected to etch through the wafer, with additional over etching planned to adjust the knife edges and compensate for potential etch anisotropy. During the over etch phase, the device wafer is exposed to the W etch solution, but most of the layers are covered and protected by a Si_3N_4 layer, a SiO_2 layer or both. Although some side etch occurs, its impact is minimal due to the large size of the device features. Once the etch is completed, the assembly is rinsed thoroughly in water to remove residual etchant and other surface residues.

Cantilever release and dicing

The cantilevered structures are finally released by a backside DRIE. A temporary carrier scheme is however necessary to accommodate the thick W masses on the front side. The wafer stack is then inserted in the ASE-STS tool to proceed with the backside silicon DRIE. Before being sent for dicing, the temporary assembly is immersed in diluted HF to etch the BOX layer to complete the beam release. The oxide hard mask is also removed in the same acid bath to reveal clear patterns etched on the backside at the beginning of the process. These motifs are used to facilitate devices dicing on the DISCO diamond saw blade. The separated dies are finally released from the carrier by immersion in a warm acetone or Remover 1165 bath. The necessary time for release can vary from a couple of hours to 3 days, depending on the device dimensions and distance between openings in the wafer. The dies are finally cleaned by immersion in DI water, followed by IPA and are lastly dried in ambient air.

5.3 General process results, divergences and discussion

Due to logistical and time constraints, the integration of some fabrication nodes could not be validated in the complete process described in section 5.2. Nevertheless, most of the fabrication blocks were demonstrated by separate short-loops to demonstrate their feasibility and intercom-

patibility. In this section, we present results obtained and issues raised during the realization of these short-loops.

5.3.1 Tungsten masses wafer-level integration short-loop

Integration of W at the wafer-level, using wafer bonding with subsequent cantilever release by DRIE on a temporary carrier, was demonstrated on a pre-patterned silicon wafer instead of active piezoelectric SOI wafers. In this short-loop, the W wafer preparation block was similar, although with a different masking scheme, whereas the device wafer preparation block is much simpler, essentially consisting of just a top etch in a silicon wafer (to later produce a 50 µm thick silicon beam). Adhesive bonding of the W wafers and the following mass and cantilever release were however realized mostly as described in Fig. 5.2.

Issues during 1st isotropic etch

As previously mentioned in section 5.2.1, the objective of the first W etch step is to thin down the wafer to approximately 100 µm. This target was defined to extend the immersion time of the double sided etch as much as possible. This is desired to reduce the required post-bond etching time and thus the overall process time, while still allowing for robust handling of the mass wafer. Moreover, it reduces the exposure time of the active wafer to the etching solution, which can be damaging to the contact pads and piezoelectric layer. For a 440 µm thick wafer, this can be achieved by a double sided etch of approximately 6h.

Initially, a 100 nm Si_3N_4 layer over 1 µm of SiO_2 was deposited on the top side of 2 W wafers, whereas a 15 µm thick KMPR photoresist mask was instead patterned on the backside to produce a temporary mask. Etching for 6h was however not possible with this scheme, because the resist mask peeled after 2h20 minutes of cumulated immersion. Figure 5.7(a) shows a partially defined W wafer up to this point, with the SiO_2/Si_3N_4 mask facing up. Those wafers were then bonded on silicon wafers using the roller based approach presented in section 5.2.3.

Validation of adhesive wafer bonding

The adhesive bonding block presented in Fig. 5.2, which uses a roller transfer method, was then used to integrate the W mass wafer on the silicon wafer. The thickness of the film transferred from the dummy wafer on the patterned W substrate was approximately 10 µm, although the applied resist film was not smooth and very nonuniform. Nevertheless, the presence of voids at this stage is not a problem, because they mostly disappear when the adhesive flows and spread during the bonding process, as shown by the test glass/silicon bonding interface presented in

Fig. 5.6 . Although adhesive spillage is a potential issue here, especially for larger bonded surfaces such as ours, this parameter can be controlled by implementing bake recipe before bonding to reduce the film solvent content [179]. However, this optimization was not realized for this feasibility demonstration.

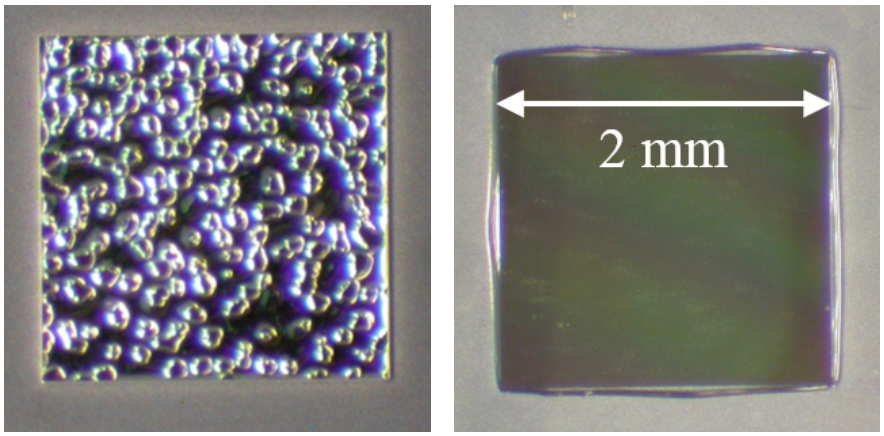

(a) SU-8 film after roller transfer (b) SU-8 film after bonding

Figure 5.6 SU-8 bonding layer before and after bonding

The wafers were then optically aligned using the EVG620 aligner available at McGill University, which is compatible with the bonding jig assembly of the EVG501 bonding tool. The bow of the bonded wafer stack was then measured at around 160 µm, with the bottom silicon being in tensile stress. For comparison, a 300 µm bow was initially measured on the W wafer.

2nd isotropic etch

To complete the patterning and release of the masses, the assembly was re-immersed in the W etchant. After 2h40 min, partial milling through the W substrate was achieved, as shown on Fig. 5.7(b). The hard mask was however partially attacked, suggesting a degraded selectivity following the bonding step. Etching was continued for another 3.5 hours to remove all the metal in the desired areas and 2h of over etch was used to adjust the mass geometry. The top surface was therefore exposed to the solution for close to 10.5 hours in total. Figure 5.7(c) shows fully released bonded W masses on the silicon wafer after this step, also demonstrating the compatibility of the adhesive bonding approach with the chemistry used.

Validation of the cantilever release

Following the masses release, the assembly was processed according to part (D) of the flow presented in Fig. 5.2. To bond the wafer on the temporary carrier, thick films of Crystal Bond 509 are applied on a double side polished fused silica wafer and on top of the W masses/silicon

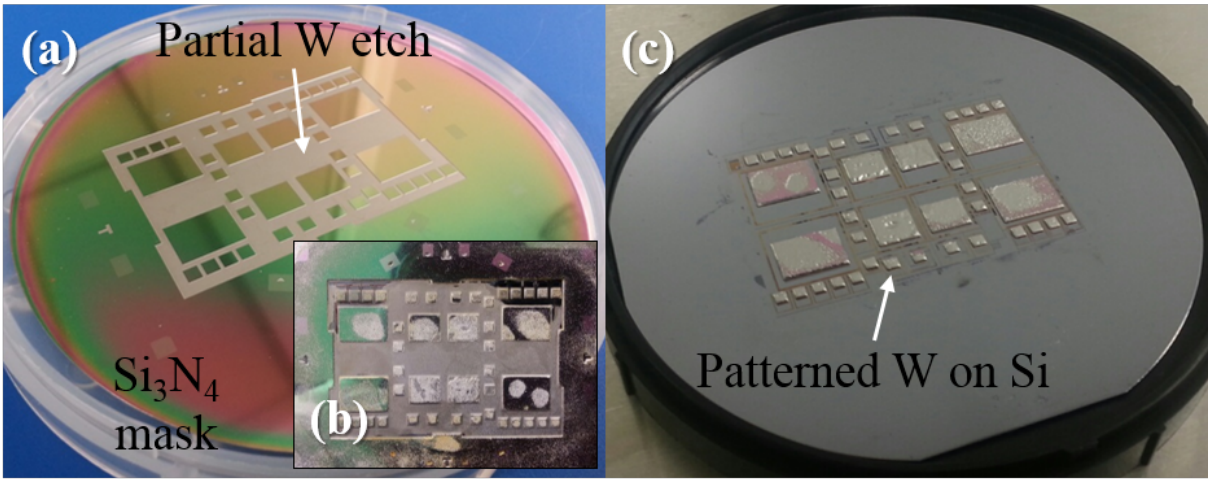

Figure 5.7 Partially etched W wafer after 1st immersion. The top hard mask remains in good conditions (a). Partially milled W wafer after 2nd immersion. The hard mask shows signs of damages (b). Fully released W masses on Si. The outer part of the W wafer was not bonded and purposely removed for easier handling.

wafer. This clear adhesive flows at 120°C and is soluble in solvents (*e.g.*, acetone or Remover 1165). It is therefore easy to remove and compatible with additional lithography steps if needed. After coating both wafers, the crystal bond films are heated, put in vacuum to remove bubbles or voids and finally put in contact to complete the temporary bond. Excess adhesive on the edges is then simply removed by scrubbing this area with a solvent soaked wipe or by full immersion in solvent for a short time, followed by rinsing in water. The result of this procedure is presented in Fig. 5.8. Because the carrier wafer and adhesive are clear, it is also possible to define a resist mask by photolithography using a front to back alignment, which was done in this short-loop. In the flow proposed in Fig. 5.2, an oxide mask is used instead to avoid this step altogether.

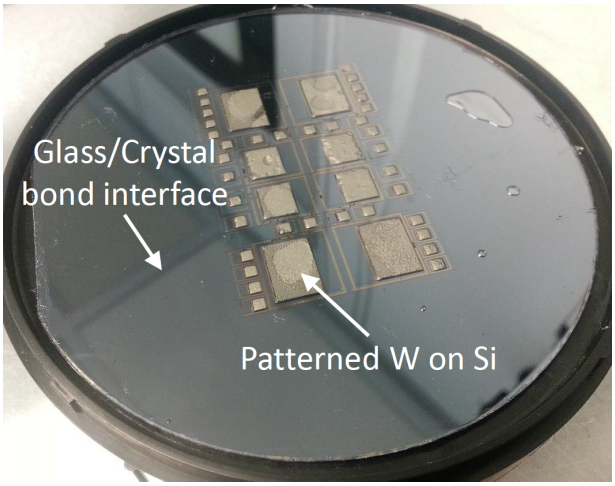

Figure 5.8 Photograph of a wafer with bonded masses on a glass carrier

The stack was then inserted in the DRIE tool to etch the silicon mass and produce the thin beams by etching the substrate down to the openings previously etched on the front side. Despite the thickness of the stack and the thick Crystal Bond layer, the etching tool helium leak up rate remained low and the recipe responded according to expectations. This suggests that the impact of the wafer mounting scheme was minimal, at least for our large etching patterns. After the DRIE was completed, the bonded stack was used for dicing. The dies were finally released by immersion in a warm Remover 1165 bath and rinsed in DI water, followed by IPA. Figure 5.9 shows a die fabricated by this short-loop, with a foot print of 1.74 cm^2. This first short-loop demonstrated that our masking scheme needed improvements and a revised approach is presented in section 5.3.2. The mechanical response of this prototype was also characterized to validate the structure integrity.

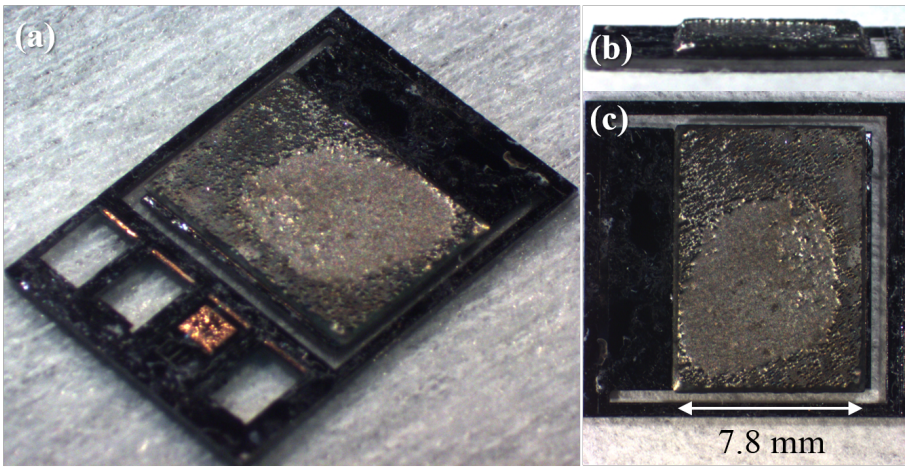

Figure 5.9 Photographs of a fabricated prototype device with wafer-level integrated W mass. A perspective view of the full die (a), as well as a side (b) and top view (c) of the cantilever with a thick W mass is presented.

Characterization of the mechanical prototype

The initial mechanical prototype presented in Fig. 5.9 was characterized dynamically to validate the mechanical robustness of the microfabricated structures. The die was glued to a carrier board and mounted on a shaker to evaluate its Q-factor and its resonant frequency. The experimental setup shown on Fig. 5.10(a) consists of an electromagnetic shaker and a laser probe. The device is brought into resonance by the shaker and once the steady-state is reached, the shaker is turned off and the decaying laser probe signal is used to evaluate the Q-factor by the logarithmic decrement method. A non-linear curve fitting algorithm was finally used to extract the value of Q. A typical probe signal with the decaying envelop fit is shown on Fig. 5.10(b). The device was tested under low vibration amplitude to avoid signal distortion due to mass tilting. A resonant

frequency $f_n = 87.2$ Hz and $Q = 267$ were estimated for the device tested based on the average of 5 data sets.

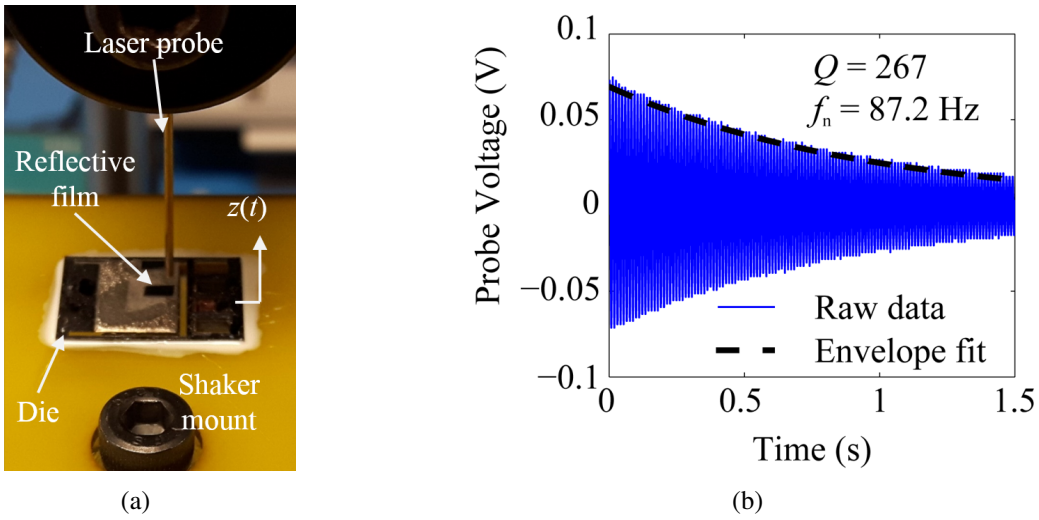

(a) (b)

Figure 5.10 Experimental setup for Q-factor measurement (a) and example of recorded data and fitted signal envelope (b).

5.3.2 Revised hard mask and characterization of the two step etching times

Because the first prolonged etch could not be fully realized on our first set of W wafers due to resist delamination, a second set was prepared with a double hard mask instead, as presented in the process flow of Fig. 5.1. We also assumed that stress induced defects in the bi-layer structure could be responsible for causing failure of the hard mask after long immersion (due to mismatch between the thin top nitride and the thick underlying oxide). Hence, a 200 nm nitride mask was instead deposited directly on W in our second run.

Although this layer demonstrated adequate masking capability during the first step, which lasted approximately 6 hours, it still exhibited similar defects that are visible on Fig. 5.11. Defects also appeared to be more severe on areas where scratches or increased roughness were visible, suggesting the quality of the layer might be worsened by surface roughness. After this initial processing step, the etch depth was approximately 204 µm on the top side and 160 µm on the bottom side, resulting in a thickness of approximately 40 µm in the thinnest part of the wafer. The wafer was therefore slightly over etched, but still thick enough to allow safe handling.

To streamline the validation of the second etch step, the W wafer was then simply mounted on a dicing tape to simulate the effect of a single side exposure due to bonding. The wafer was completely etched through after 2 hours and 15 minutes and an over etch of 1h was applied. Figure 5.12 shows the etch progression with the dicing tape on and demonstrate good integrity of

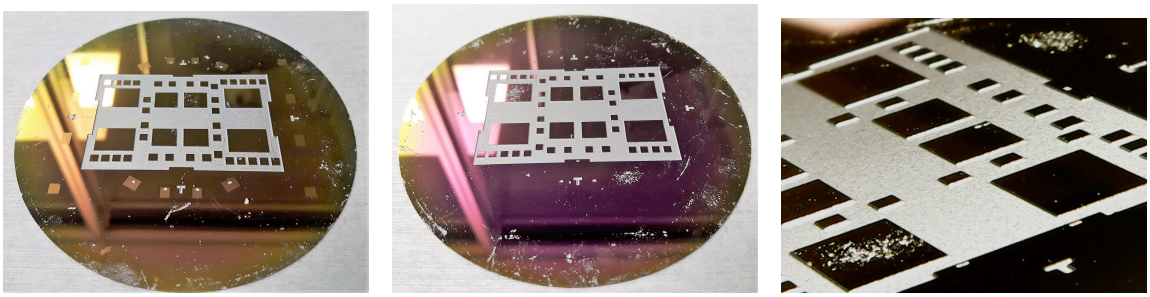

(a) (b) (c)

Figure 5.11 Top (a) and bottom (b)-(c) surfaces of a W wafer after etching for 6h

the top hard mask after a total exposure time of approximately 9h15 minutes. Figure 5.13 meanwhile shows a SEM picture of one of the smaller mass, demonstrating a somewhat symmetric etch profile with approximately 75 µm of knife edge on each side. The mass has a maximum width of 2 mm, which is the exact target dimension and also the width of the smaller beams on the device wafers, hence validating the etching recipe.

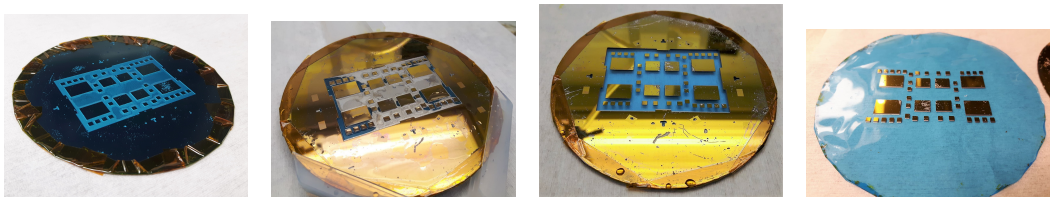

(a) (b) (c) (d)

Figure 5.12 Tungsten etching progression for substrate mounted on dicing tape. Dicing tape mounting (a), partial etching (b), completed etch (c) and after de-taping the surrounding frame (d).

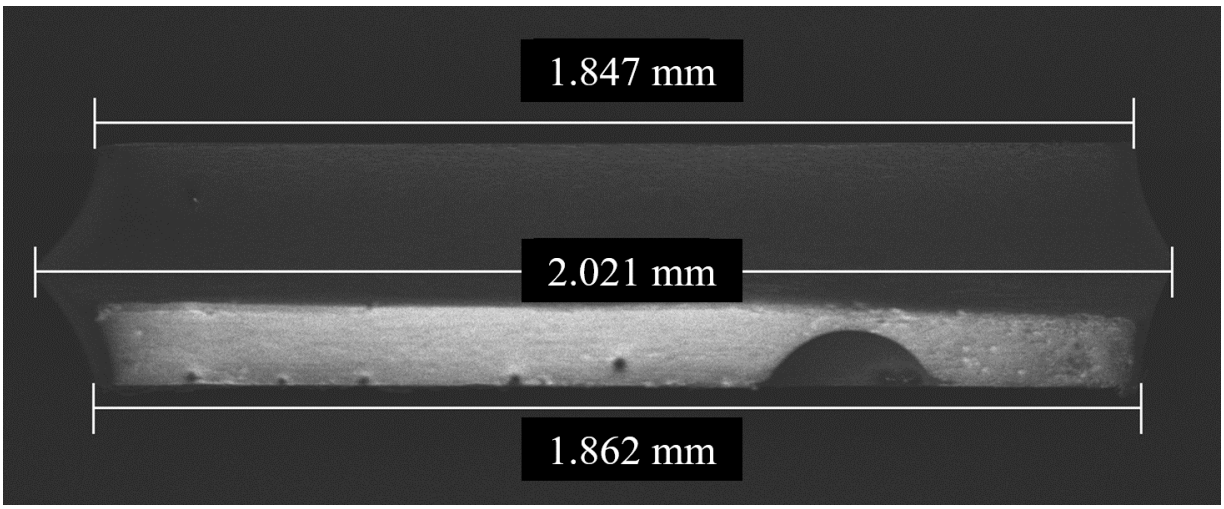

Figure 5.13 Side view of one of the smaller etched W mass.

Concluding remarks on masking scheme and etching profiles

Overall, the issue of the mask integrity was not fully solved, but our experiments suggest the etchant is able to diffuse through the mask layer via grain boundaries, pin holes or other film defects to initiate under etching of the substrate. This seems plausible based on Fig. 5.14(a), which shows an optical photograph of a typical mask defect. Once defects are initiated, the mask is progressively weakened and fails as they grow bigger (as depicted in Fig. 5.14(b-c)). The patterns observed on the hard mask after the second etching stage (after bonding, see section 5.3.1) also indicate that scratches initiated by friction or ionic contamination from contacts with the bonding tool may promote formation of these defects. More experiments would however be needed to validate either of these assumptions. Although all the hard masks tended to present numerous defects after prolonged exposure to the W etchant, they were sufficiently functional to demonstrate the concept and several improvements could be investigated. For example, multiple layers of PECVD deposited SiO_2 or Si_3N_4 could be grown sequentially to form layered hard masks which more effectively hinder diffusion by having uncorrelated, randomly positioned defects. Alternatively, LPCVD deposited layers would probably provide better quality films which are less prone to formation of pin holes.

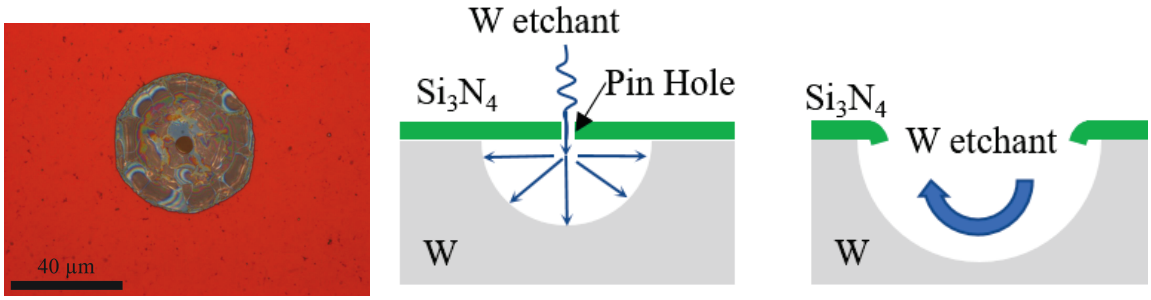

(a) Photograph of a pin hole defect (b) Defect initiation (c) Mask collapsing

Figure 5.14 Depiction of mask failure mechanism

In addition, the mass side etch profile varied greatly between experiments, as depicted on Fig. 5.15. This was expected, considering the isotropic wet etching approach used here is greatly affected by the agitation conditions, bath temperature and the overall etchant usage. It was therefore very challenging to identify optimal conditions to obtain straight sidewalls, but such an optimization would be possible in future work. The last two experiments nevertheless provided adequate geometries for integration on the device wafers.

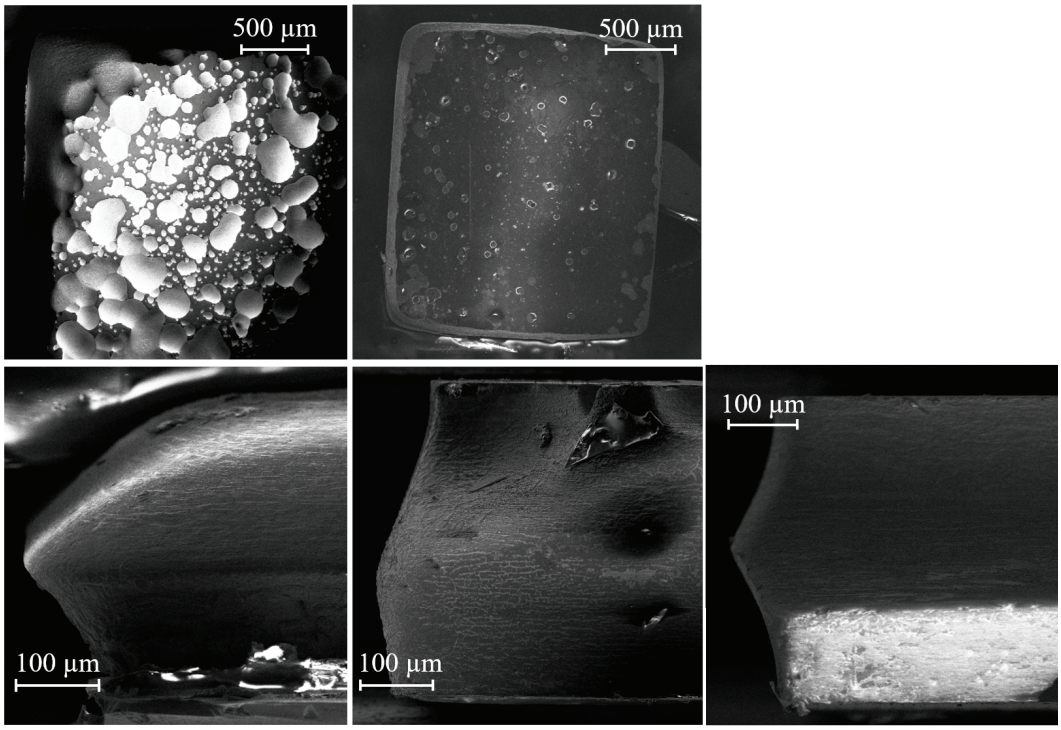

(a) First experiment (b) Second experiment (c) Third experiment

Figure 5.15 Etched W masses side wall profiles for the different experiments. Images for columns (a) and (b) are obtained from two separate experiments done in the first short-loop. Image in column (c) is obtained in the revised masking scheme experiment.

5.3.3 Tungsten etchant properties

Etching selectivity

To address integration concerns, we also characterized the effect of the etchant on other materials, namely Si, SU-8, Cu, Al, Au, Sn, TiN, Cr, SiO_2, Si_3N_4 and AlN. All materials were deposited on blanket silicon coupons and immersed for at least 30 minutes in an agitated and heated etching bath maintained to approximately 60°C. The etch rate was then estimated by measuring the difference in thickness before and after exposure to the solution. We used two methods to do so: 1) measuring the step between an exposed and a masked area using a Dektak stylus profilometer or 2) by measuring the film thickness before and after with an ellipsometer.

Si and cured SU-8 were not etched at all. Additionally, the solution did not significantly etch Cr (sputtered) or PECVD deposited SiO_2 and Si_3N_4, although a slight increase of the surface roughness was observed on these last two. This could be linked to the formation of pin holes, as previously observed on our hard masks during the prolonged etching of the W substrates. Meanwhile, Cu turned to a dark brown color and its thickness had increased, suggesting oxidation of the surface. A 150 nm thick Al layer (sputtered) was also etched by the solution in about 15 min. The solution similarly attacked AlN, which showed a roughened surface and reduction in thickness of approximately 200 nm after 30 minutes. Although these etch rates are significantly lower than for the target metal, providing at least 50:1 selectivity, it remains problematic due to the prolonged immersion required in the process. This is why we added Si_3N_4 on top of the Al contact pads, as described in section 5.2.2, and additional protection layers on the AlN. Finally, other metals, such as Au (evaporated), Sn (electroless plated on copper) and TiN (sputtered), were also tested, but did not exhibit signs of attack by the solution. A summary of these observations is presented in Table 5.1.

Etchant degradation

As the W etchant solution is consumed and saturated by tungstate formation, it goes from a clear orange/amber tinted coloration to an opaque dark green. The etching rate is also reduced by half if consumed solution is reused on a second wafer, whereas precipitate formation and sludge redeposition on the wafer surface becomes more noticeable.

According to [44], this occurs because the solution's pH drops as OH^- and $Fe(CN)_6{}^{3-}$ ions are consumed and no reactants are added to compensate. When the pH drops below a certain value, the W in solution as $WO_4{}^{2-}$ also starts to polymerize and form insoluble tungstate byproducts, which can stick to the wafer and slow the etching process by effectively masking the surface. In

Table 5.1 Etch rates of W etch for several common clean room materials at 60°C.

Material	**Etch rate** (nm/min)	**Comments**
W	≈ 500	Sensitive to agitation (mass transport limited)
Cu	$\uparrow$ thickness	Copper oxide formation
Sn	-	No visible etch (tested on electroless plated)
Al	≈ 10	50:1 selectivity to W
AlN	≈ 7	75:1 selectivity to W, generates roughness
Au	-	No visible etch
Cr	-	Slight roughness increase
TiN	-	No visible etch after 1h
Si	-	No visible etch
SiO_2	≤ 0.1	Slight roughness increase, long immersion forms pin holes
Si_3N_4	≤ 0.1	Slight roughness increase, long immersion forms pin holes
SU-8 (uncured)	Not meas.	Dissolves in solution
SU-8 (cured)	-	No visible etch
KMPR	-	Not etched, but peels off after long immersion

addition, hydroxide attacks ferrocyanide to form ferrous hydroxide $Fe(OH)_2$, which, by subsequent oxidation with air, can form an insoluble $Fe(OH)_3$ gel [44] that may also inhibit etching.

To prevent these issues, the etchant could be recycled by reversing the ferrocyanide back to ferricyanide using an ozone (O_3) treatment, as suggested in [44]. The pH of the solution can also be controlled by adding phosphoric acid (H_3PO_4) to compensate for the addition of KOH [45]. Although we have not tried the ozone treatment, small quantities of H_2O_2 were added to depleted etchant based on the assumption that it could have similar effects. Partial restoration of the etching rate was effectively observed, but more studies would be necessary to propose a proper dosage and evaluate the effect on other materials.

5.3.4 Effect of the developer on AlN layers

We realized an experiment to evaluate the effect of the developer on the evolution of the surface roughness. Figure 5.16 illustrates SEM and AFM images of unprotected AlN surfaces after different time of immersion in the MIF319 resist developer. Although the initial surface is very smooth, with an $R_q = 1.1$ nm, the roughness is effectively doubled after only 10 s of immersion in the developer and is more than 50 times worse after 2 minutes. Hence, protection of the piezoelectric layer was critical to preserve surface quality. In fact, some samples were also used to evaluate the overall etch rate of the developer and these showed that AlN can be rapidly wet etched. For instance, it took less than 7 minutes to remove most of the 400 nm thick AlN layer and a bit more for the 1 µm thick samples.

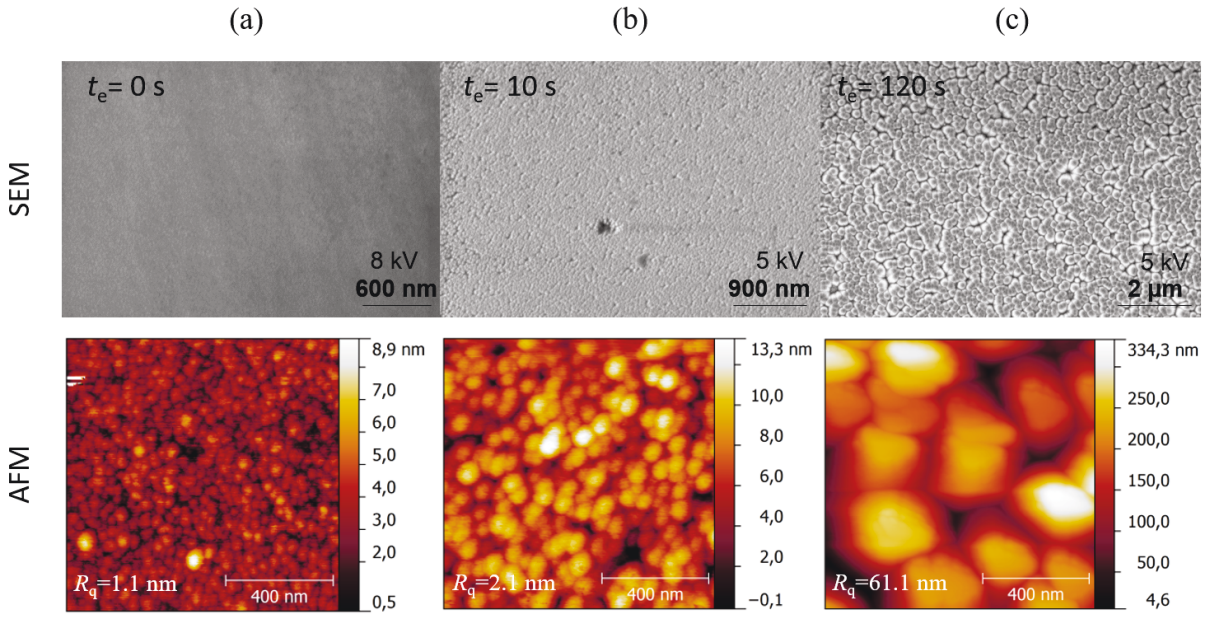

Figure 5.16 Effect of MIF319 developer exposure time t_e on AlN shown by SEM and AFM. (a) After oxide removal by BOE, no exposure, (b) after $t_e = 10$ s, the surface is quickly roughened as the AlN is etched and (c) after $t_e = 2$ min, large crystallite columns are visible.

5.3.5 Compatibility of the tungsten etchant with device wafers

In the process flow proposed in Fig. 5.2, the device wafers can be exposed to the W etchant for considerable time during completion of the mass patterning by overetch (step D-1). However, the results presented in Table 5.1 denote that both Al and AlN are sensitive to this chemical. We therefore validated the feasibility of this process step by conducting two set of experiments. The first experiment was designed to find and implement a suitable protection for the aluminum pads that also allows wire bonding afterwards, whereas the second experiment was realized to verify the effectiveness of the protection layers over the AlN and validate the pad protection strategy on actual device wafers. The results of both experiments are presented in this section.

Pad protection evaluation short-loop

For this experiment, we tested 6 different metalization stacks, summarized with the results in Table 5.2. All metals were deposited on the same substrate, which was also used for fabrication of the device wafers (*i.e.*, doped silicon device layer on an SOI wafer), and were patterned using a lift-off process. All stacks were then annealed at 450°C in forming gas ambient for 3 hours.

Figure 5.17 shows all the various stacks directly after patterning, whereas Fig. 5.18 is after annealing. We can clearly notice that, although samples A, B and C appear mostly unaffected,

Table 5.2 Metal stack tested for protection to W etchant and summarized results

Stack ID	Seed layer (Thickness)	Cap layer (Thickness)	Ohmic Contact?	Etched?	Wire bond-able?	Comments
A		None	Yes	Yes	N/A	Fully etched
B		SiO_2 (100 nm)	Yes	No	Yes	No apparent changes
C	Al (1 µm)	Si_3N_4 (50 nm)	Yes	No	Yes	No apparent changes
D		Si (100 nm)	Yes	Yes	N/A	Rough post anneal, post etch
E		Ni (100 nm)	Yes	Yes	N/A	Rough post anneal, post etch
F	Ti (100 nm)	TiN (50 nm) + Au (500 nm)	Yes	No	Yes	Bad adhesion/bond if unalloyed

samples D, E and F all show notable differences. Sample D, which was capped using a thin silicon layer, shows increased surface roughness, probably due to alloying with the underlying aluminum. Meanwhile, the nickel cap layer (sample E) is much darker, which is not readily explainable, but points toward a degradation of the stack. Lastly, sample F, with gold pads, shows an irregular appearance on specific pads, which suggests formation of an eutectic SiAu alloy due to interdiffusion through the Ti/TiN underlying layers. Gold on other pads simply delaminated due to improper adhesion with the TiN barrier. At this point, all stacks were tested on a probe station and showed minimal resistance (< 1 Ohm on a 4 points probe measurement), despite some of them having a 100 nm thick dielectric cap layer. It is safe to assume that the probe needles can pierce through these layers due to the thick and soft Al layer beneath. Hence, from an electrical standpoint, all stacks were somewhat viable.

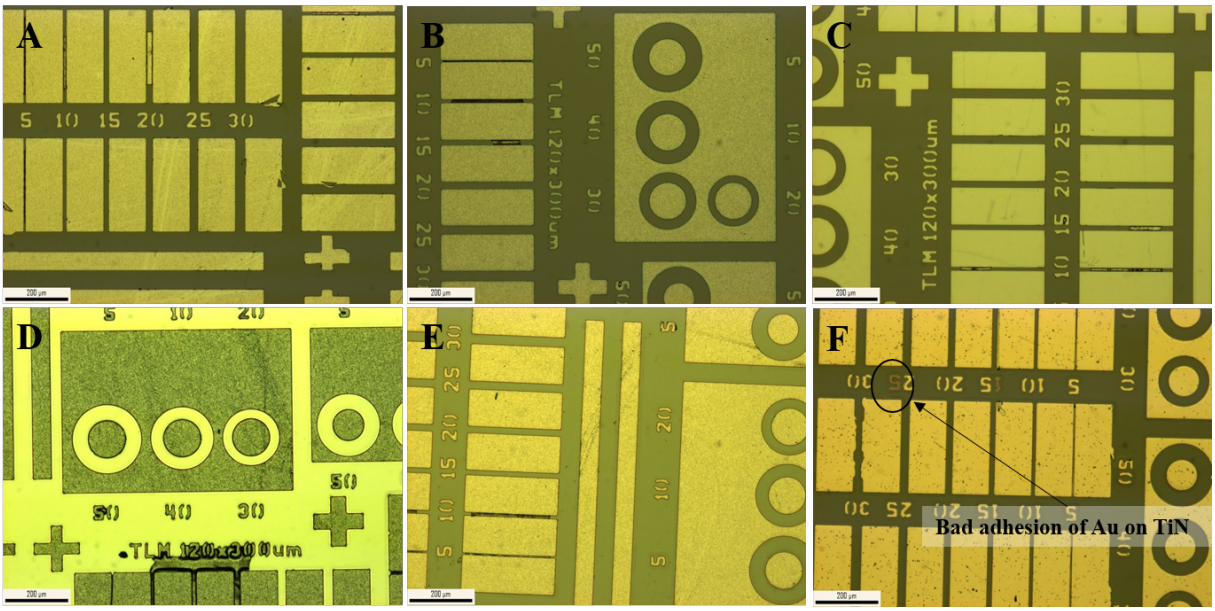

Figure 5.17 Test metallization before annealing. Sample F already shows sign of bad adhesion of Au over TiN.

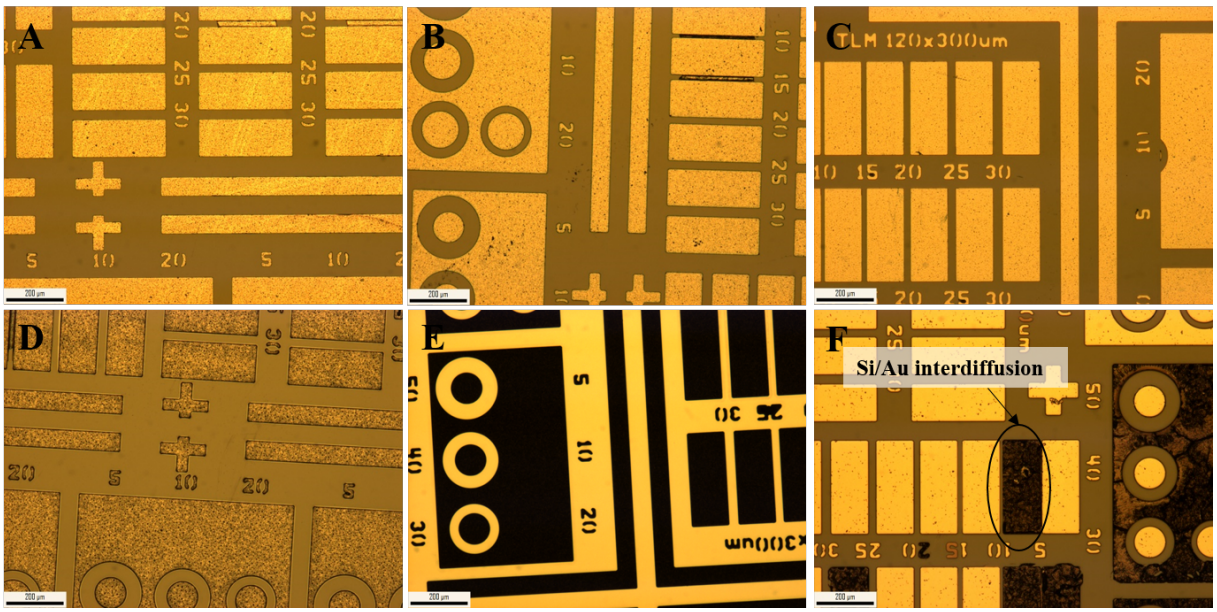

Figure 5.18 Test metallization after annealing. Samples A, B and C show little change, whereas sample D, E and F have all been visibly affected.

The samples were then immersed in the W etchant for a total of 65 minutes using the same methodology as in section 5.3.3. Figure 5.19 first shows that the aluminum pads were mostly etched away, as expected. Although samples D and E show metal remaining, they were still partially etched and showed severe surface roughness, which is an issue for wire bonding. Sample F appears barely affected, although many pads were again delaminated under the mechanical effect of fluid agitation. This bad adhesion therefore prevents wire bonding. Lastly, both samples B and C maintained pristine conditions, showing that the SiO_2 and Si_3N_4 cap layers were effective to protect the aluminum pads in this experiment.

Finally, stacks B, C and F were tested to verify their compatibility with wire bonding. Surprisingly, they all allowed formation of wire bonds which are mechanically robust and electrically conductive (in the case of sample F, this only worked on regions were SiAu interdiffusion had occured). We assume that for sample B and C, the thick and soft aluminum pads allow for enough deformation to break the thin brittle dielectric film as the wedge bond tool is pressed on the surface. Under the action of ultrasonic energy, clean metal is then exposed and is soldered, creating the wired connection. It is therefore not mandatory to remove the protective cap layer after releasing the masses, although it can still be done rather easily by doing a blanket CF4-based RIE.

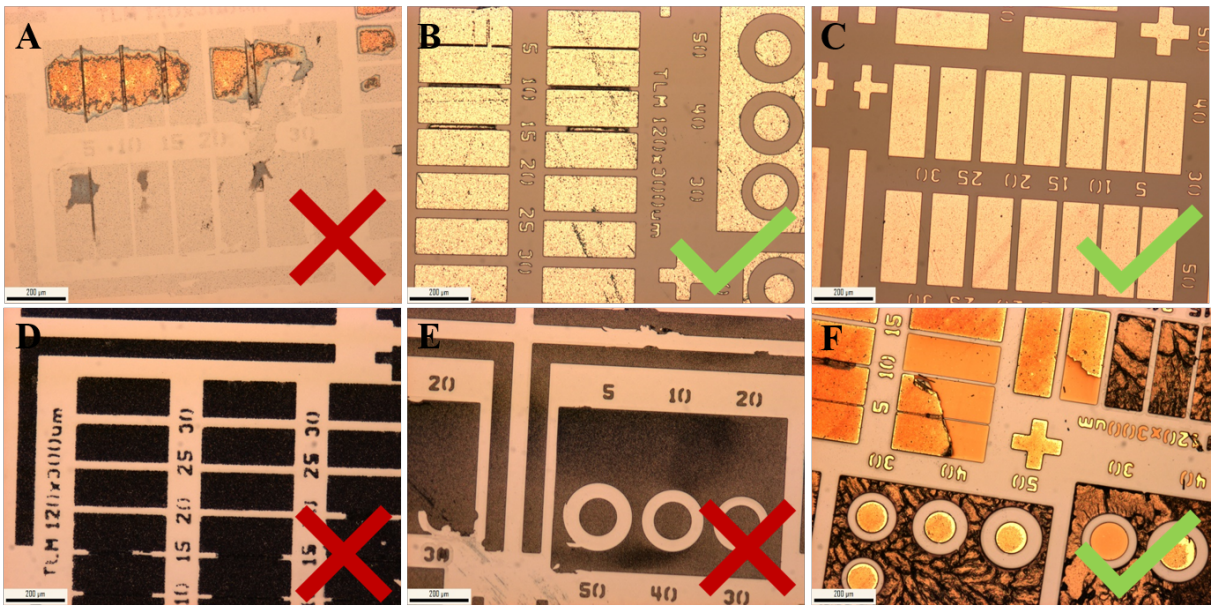

Figure 5.19 Test metallization after exposure to the etching solution. Samples A, D and E were etched to varying degrees, whereas samples B, C and F maintained their post-anneal appearance.

Verification on AlN wafers

Beside the electrical contacts, the active piezoelectric layer must also be protected from the W etching solution. Based on our previous knowledge, we expected that the 100 nm Cr electrode, 2 µm SiO_2 passivation layer and 100 nm Si_3N_4 diffusion barrier would be more than enough to prevent damage to the AlN layer. The impact of side etch was also expected to be minimal, considering the $\approx$ 7 nm/min etch rate reported in Table 5.1 (4.2 µm after 10h). An active wafer was therefore immersed for 90 minutes in an heated etching solution brought to 60°C to confirm the effectiveness of the protection. As depicted in Fig. 5.20, visual inspection of the wafer before and after exposure to the solution showed no noticeable damage to the piezoelectric layers. However, the pads were etched significantly, which was not expected based on the results from the metalization short-loop. The reasons for the pads degradation is unclear at this point, since both samples had the same layer thicknesses and saw the same annealing treatment. A 100 nm SiO_2 capping layer also showed potential and should therefore be considered as an alternative in future fabrication runs.

5.3.6 Fabrication of piezoelectric devices

Fabrication of fully functional piezoelectric devices (without the high density proof mass integrated at the wafer level) was also completed. This process essentially uses all the fabrication

(a) Before immersion (b) After immersion (c) Close up on etched pad

Figure 5.20 Visual inspection of the device wafer after immersion in the warm W etchant for 90 minutes. The device appears intact, except for the pads that are mostly gone.

steps presented in block (B), presented in Fig. 5.1, and skips the wafer bonding to go directly to the cantilever definition block (D), presented in Fig. 5.2. Because silicon is etched through and DRIE stopped on the BOX layer, a temporary carrier is still necessary, but requires much less adhesive due to the absence of thick W masses. Figure 5.21 depicts completed harvesters after dicing. The larger dies, with multiple harvesters on them, are slightly smaller than a quarter, whereas an individual small harvester is roughly 4.5 mm long by 3 mm wide.

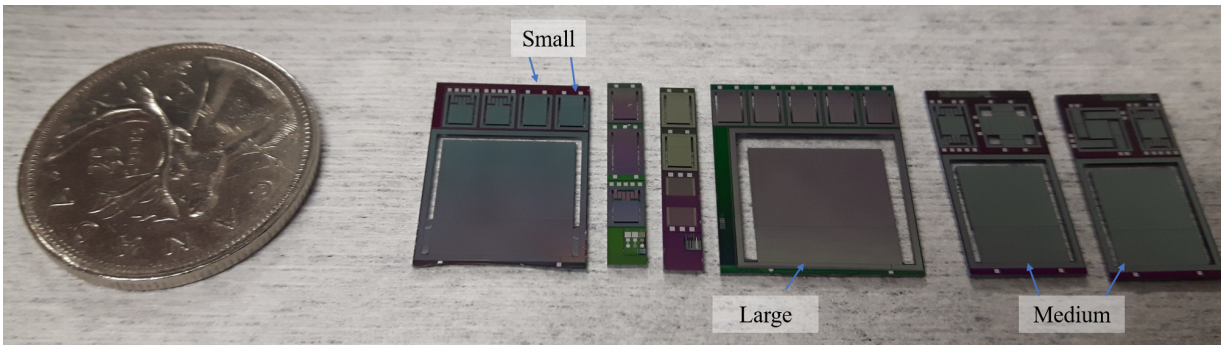

Figure 5.21 Photograph of diced piezoelectric harvesters.

Device assembly and die level integration of tungsten masses

Fabricated dies are glued on custom PCBs with an embedded flex cable output, allowing for dynamic and electrical testing on the test bench. Traces on the PCBs are designed to minimize noise and parasitic capacitance when connected to an external decoupling circuit. Holes are first machined into the PCBs by laser machining to allow the displacement of the masses. Each die

is then secured on the PCB using an epoxy resin which is cured at 125°C for 1h. The devices are subsequently connected by wire bonding onto the PCB.

Because of the issues reported in this section, W could not be integrated at the wafer level on the active device wafers. Tungsten based devices were therefore instead fabricated using the methodology presented in chapter 4, by bonding the masses at the die level. A photograph of several fully assembled dies laying side by side is presented in Fig. 5.22, showing some devices with and without a W mass.

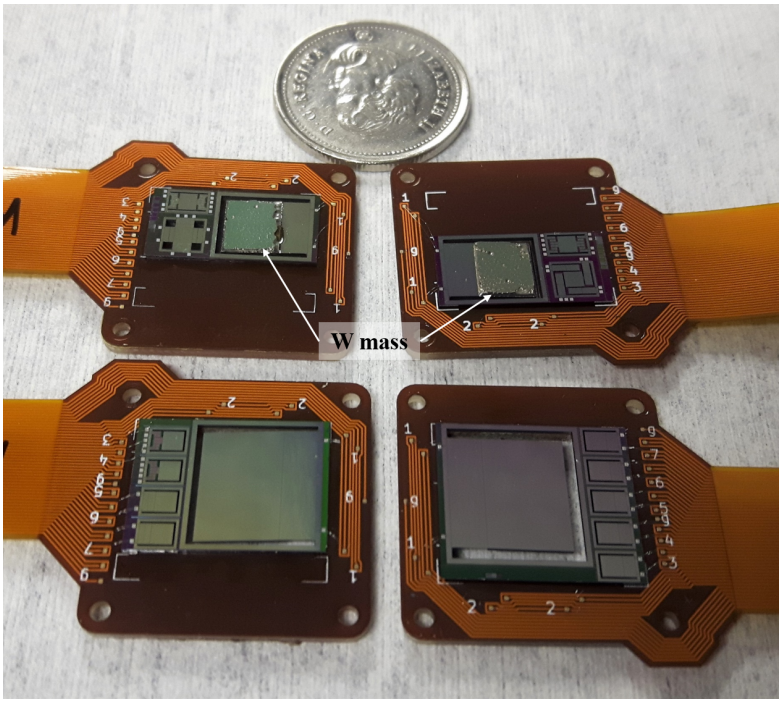

Figure 5.22 Picture of assembled harvesters. Two harvesters are shown with a bonded W proof mass.

Devices specifications

Various designs were fabricated, such as nonlinear and ultra low frequency devices incorporating meandering structures, but a subset of five different configurations are considered for further characterization in chapter 6. They are described in Table 5.3 by their respective dimensions. In total, three configurations with only the silicon mass (noted Si) and two including an additional high density W proof mass (noted W) are tested. In both cases, the same cantilever beam designs are used and here labeled as small (S), medium (M) and large (L). Theses 8 test devices are identified by their respective device ID and reported in Table 5.3.

Table 5.3 Tested designs nominal dimensions

Config. **Device ID**	**SiL** **G6**	**SiM** **I3, J3**	**SiS** **G5, E3**	**WM** **I3′, J3′**	**WS** **E3′**
Beam width (mm)	11	7	2	7	2
Beam length (mm)	3.2	3.23	1	3.23	1
Si beam thickness (µm)	30				
AlN thickness (µm)	1				
SiO_2 protection thickness (µm)	0.1				
Cr electrode thickness (µm)	0.1				
SiO_2 passivation thickness (µm)	2				
Si_3N_4 thickness (µm)	0.1				
Mass width (mm)	11	7	2	7	2
Mass length (mm)	7.8	6	2	6	2
Si mass thickness (µm)	430				
W mass thickness (µm)	0		440		

5.4 Conclusion

This chapter presented a process to integrate high density W proof masses in MEMS piezoelectric inertial devices at the wafer level. The heterogeneous integration scheme proposed here, which combines wet chemical etching of a high density metallic substrate with wafer bonding on a silicon-based substrate, leverage the strength of both materials to fabricate dense masses and high quality springs, which can provide low damping, high stress resistance and high sensitivity. A temporary carrier bonding approach allowing backside etching of wafers with severe front side topologies was also developed to this end.

Wafer level integration of W was demonstrated in a piezo-less version of this process, which produced a device with a 1.74 cm^2 footprint, a low resonant frequency of 87.2 Hz and a Q-factor of 267 in ambient air. Although this process was validated for fabrication of an out of plane transducer, it could also produce in plane transducers by changing the mask designs. The inter-compatibility of the remaining fabrication blocks was then evaluated with separate short-loops. Fully functional piezoelectric devices were fabricated and their fabrication process was shown to be, for the most part, compatible with the approach presented. The protective layers put on the piezoelectric AlN were effective to prevent damage from the W etching solution, but some integration issues remain with regard to the aluminum contact pads. Although an initial short-loop showed that they could resist to prolonged exposure to the etchant if protected with a 50 nm thick Si_3N_4 capping layer, this result was unfortunately not replicated on a device wafer. Still, other pad integration strategies showed potential in the initial short-loop and these could be tested to clarify their viability on actual device wafers in future fabrication runs.

Still, the use of wet chemical milling is challenging in terms of dimensions control and limits the minimum feature sizes to values close to the mass wafer thickness. Nevertheless, these concerns are mitigated by the fact that the mass in MEMS harvesters and inertial sensors is typically the biggest component. A dry etching approach could alleviate these concerns and is a path to consider for future developments, especially considering that the feasibility of high aspect ratio dry etching of W has already been demonstrated [190] .

Although adhesive and eutectic wafer bonding were proposed here, our process could also be adapted with other intermediate layer bonding methods, such as thermocompressive bonding. Future work should therefore focus on developing and integrating the remaining processing blocks, but also improving the process robustness, dimensional control, as well as exploring compatibility with a wider array of materials. A packaging strategies should also be developed to protect the device from the environment or displacement overload. It is worth pursuing these efforts, as adopting W wafers instead of silicon to fabricate the proof masses shows great potential to reduce the die size or improve sensitivity. In both cases, the magnitude of the impact is almost an order of magnitude, which can directly affect cost and open market opportunities.

CHAPTER 6

Piezoelectric harvesters characterization and benchmarking

This chapter presents the characterization of piezoelectric vibration energy harvesters fabricated using the process developed in chapter 5. We first describe the test equipment and methodology used. A sample of dynamic characterization results from a subset of test devices is then presented and analyzed to explain their performances. We finally complete this work by comparing these test designs with previously published prototypes. The results demonstrate that by adding tungsten in the harvester design, the normalized power density can be improved by more than an order of magnitude, as predicted. Consequently, these devices have some of the best normalized power density figure of merit reported to date, which is possible by leveraging both an increased sensitivity to vibration brought by the larger induced force and by taking advantage of the high mechanical Q factor of AlN. Tested in ambient air, their mechanical Q factor is even improved in some cases by the addition of the tungsten proof mass, as observed in chapter 4.

6.1 Device characterization methodology

This section presents the overall methodology used to characterize the devices fabricated. We first describe the test hardware, general setup, and then present the test methodology and data analysis approach used to extract results.

6.1.1 Test setup description

The prototypes are characterized dynamically on an electromagnetic shaker (KCF Technologies ES020) by supplying a base acceleration and measuring the resulting piezoelectric voltage. Figure 6.1 presents a schematic representation of the full test setup, consisting of the following components:

- a Crystal Instrument Spider-81B vibration controller module. It is used to control the shaker dynamics in closed-loop through its analog output and record both the acceleration and piezoelectric voltage signals via 2 configurable analog inputs;

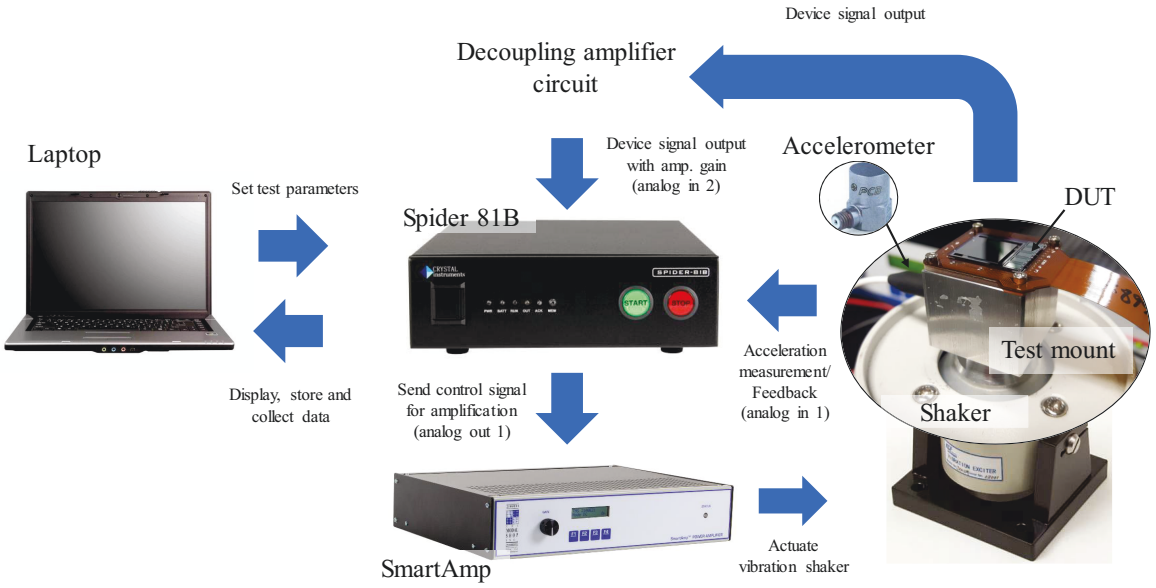

Figure 6.1 Schematic representation of the device characterization setup

- a PCB-Piezotronics 352C33 piezoelectric accelerometer, which provides feedback on the input vibration applied to the device under test (DUT). This signal is measured through input channel 1 of the Spider-81B;
- a 100 W power amplifier (The Modal Shop SmartAmp 2100E21-100), which amplifies the control signal and supplies the actuating current to the shaker;
- a custom designed pre-amplification decoupling circuit. With its high input impedance, this circuit minimizes the impact of the electrical measurements on the DUT before going to the Spider-81B's input channel 2.

Finally, the Spider-81B vibration controller module connects through an Ethernet cable to a laptop installed with Crystal Instruments' Time Waveform Replication control software. This tool is used to configure each test and collect data during and after each run.

6.1.2 Test procedure and data treatment

Pretest and test profiles

Each test run begins with a pretest, which consists of replicating a predefined wide band random signal on the shaker to characterize its frequency response function (FRF) and adjust the control gain with respect to frequency accordingly. In other words, the results of the pretest are used to produce a control signal that replicates as faithfully as possible the provided test profile. All

profiles are generated numerically, using Crystal Instruments' Waveform Editor, and consist of forward frequency sine sweeps which vary slowly at a constant amplitude. This standard approach can be used to rapidly measure the FRF of the DUT with a high resolution in frequency, under the condition that the sweeping rate is maintained sufficiently low to excite the system in a quasi-static manner (*i.e.*, allow the device transient response to subside in order to mostly record the steady-state response) [78]. As mentioned in section 6.1.1, the accelerometer output (channel 1) and piezoelectric voltage (channel 2) are both measured and recorded by the Spider-81B controller.

Result extraction algorithm

The raw data is then extracted and processed in MATLAB using the algorithm pictured in Fig. 6.2. The raw time signals are first buffered and segmented to evaluate the variation of their RMS value over time. Knowing the frequency of the input sweep signal as a function of time,

$$\omega(t) = (\omega_2 - \omega_1)\, t/t_{\text{total}} + \omega_1, \tag{6.1}$$

where ω_1, ω_2 and t_{total} are respectively the start radial frequency, end radial frequency and total sweep time, we then convert the time values to frequencies. Although the ideal acceleration input signal should be flat, the measured acceleration often fluctuates close the the resonant frequency (as seen on the acceleration raw data signal displayed on Fig. 6.2). This is especially pronounced when the DUT has a large mass and a high Q factor. This occurs because the DUT dynamics at resonance affect the shaker response in a narrow frequency range, which cannot be entirely compensated by the vibration controller due to limits on the frequency resolution achieved during the pretest. To compensate for this, we compute the ratio between both RMS values to accurately derive the voltage FRF. Alternatively, a pre-test based on a swept sine control signal would allow the controller to capture the more intricate shaker dynamics near the DUT resonance frequency and improve the flatness of the acceleration input. This approach, however, requires an additional software license key, which we currently do not have.

Types of test runs

We conduct two types of test for each device. We first use a constant acceleration level and measure the voltage output with different resistances connected to the DUT to find the optimal load. In the second round of tests, the resistance is kept constant while the device is excited at different vibration amplitudes. Results for both tests are presented in the next section. It is also

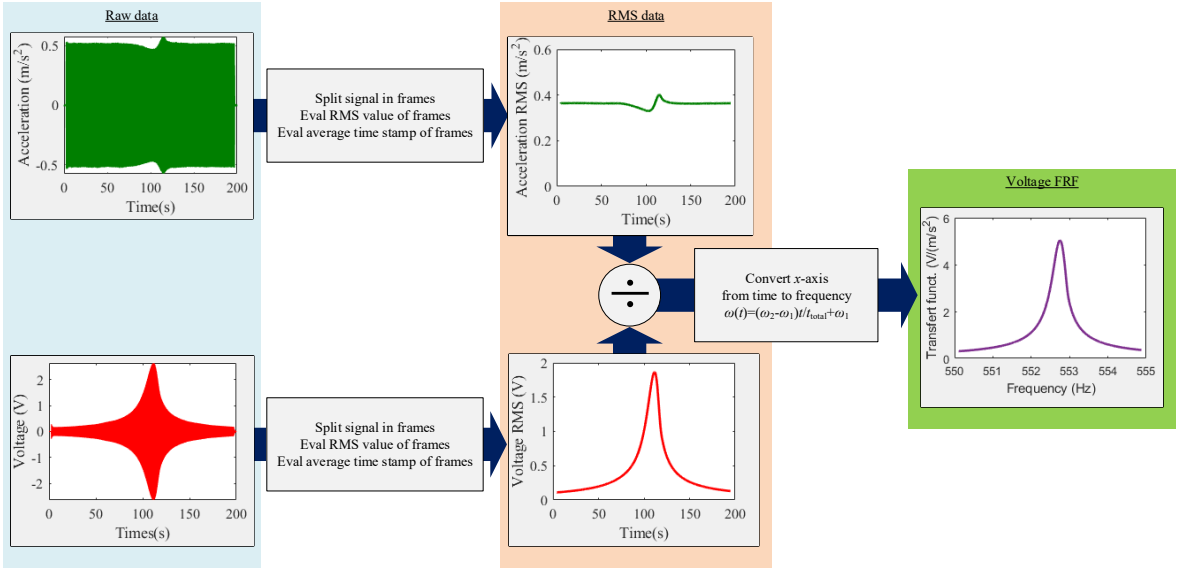

Figure 6.2 Schematic representation of the data analysis methodology

worth mentioning that, similarly to the methodology presented in chapter 4, all tungsten based devices are initially tested with the silicon mass only for purpose of comparison.

6.2 Experimental results

This section presents the processed results and begins with the test done by varying the resistance. Results are plotted in the form of FRFs, with the voltage FRFs displayed as the ratio of the RMS voltage over the RMS acceleration (in V/(m/s^2)), whereas the power FRFs are instead presented as the ratio of the average electrical power over the squared acceleration amplitude (in µW/(m/s^2)^2). The peaks of the power FRFs for each resistance are then considered to show voltage and average power changes with the load. The second part of this section presents the impact of the input acceleration on the RMS voltage and average power outputs for all the devices tested. To complete this chapter, a global summary of the test results is laid out and they are finally compared with the state of art.

6.2.1 Voltage and power FRF variations with the resistance

Due to significant differences between designs, different acceleration levels and frequency ranges are used during testing. The acceleration input is also not always flat over the full duration of a run (due to strong interactions between the DUT and the shaker at resonance). The FRF approach is therefore used to compensate for both factors. In the FRF plots displayed here, the lines follow the data points and spaced out markers are added to differentiate between test conditions. To be concise, results for only 2 devices are reported here, namely E3 and E3′, but readers can consult the results related to other test devices in appendix F.1. These prototypes were selected specifically to highlight how the integration of the tungsten proof mass increases the performances of the device in numerous ways. Their voltage and average power FRFs are compared in Fig. 6.3 and 6.4 respectively. The nominal acceleration used with E3 was 5 m/s^2, whereas E3′ was tested using 0.5 m/s^2.

Figure 6.3 first shows the peak voltage frequency slightly increases with the connected load for both devices, as expected for piezoelectric resonators. By adding tungsten, E3 resonant frequency's drops from approximately 1352 Hz to 553 Hz, while the peak of its open circuit RMS voltage FRF increases by about 18 times, going from 0.45 V/(m/s^2) to 8.5 V/(m/s^2). Meanwhile, Fig. 6.4(a) shows the optimal load for E3 is close to 750 kΩ , whereas Fig. 6.4(b) shows E3′ instead has two optimal loads, one at 250 kΩ and another at 2.5 MΩ. Here again, the peak average power FRF increases significantly after integration of the tungsten mass, rising by more than 50 times. Although the reduction of the frequency and the increased mass both play a part, they don't completely explain these gains.

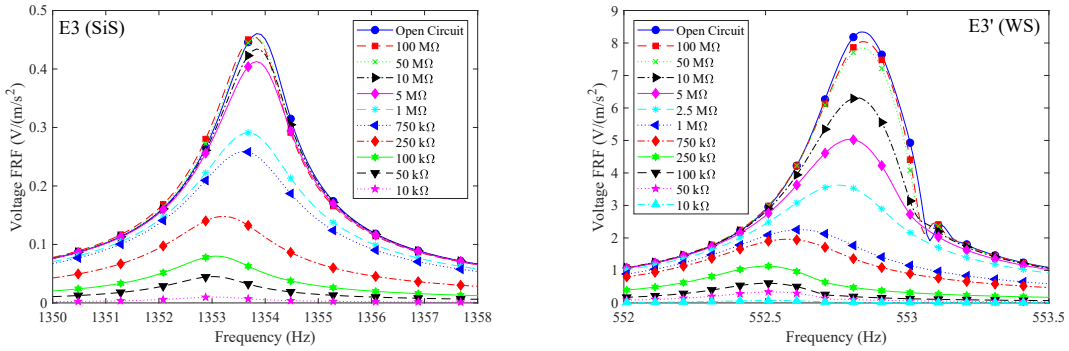

(a) (b)

Figure 6.3 Voltage FRFs comparison for device E3 (a) and E3′ (b) versus the connected resistance.

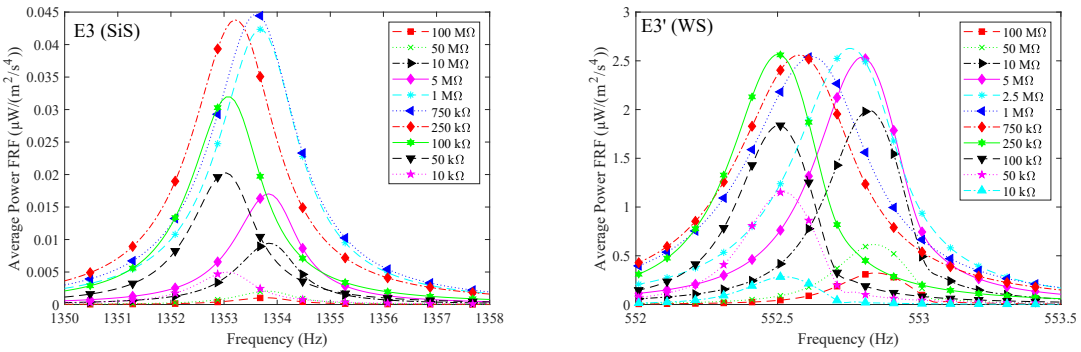

(a) (b)

Figure 6.4 Average power FRFs comparison for device E3 (a) and E3′ (b) versus the connected resistance.

Peak outputs versus load

As explained in chapter 2, two optimal loads are observed when the electrical damping, ζ_{el}, is strong enough to surpass the mechanical damping, ζ_m. Hence, the fact that two peaks are visible for device E3′ can only be explained if ζ_m has diminished relatively to E3, assuming the tungsten mass had no effect on the piezoelectric coupling. This was demonstrated and discussed in great details in chapter 4 and is also visible on Fig. 6.5, which compares the peak RMS voltage and average power FRFs versus the load for both devices. These results again highlight how device E3 operates in a suboptimal condition, whereas E3′ exhibits the two optimal loads typical of devices that meet the critical coupling criteria.

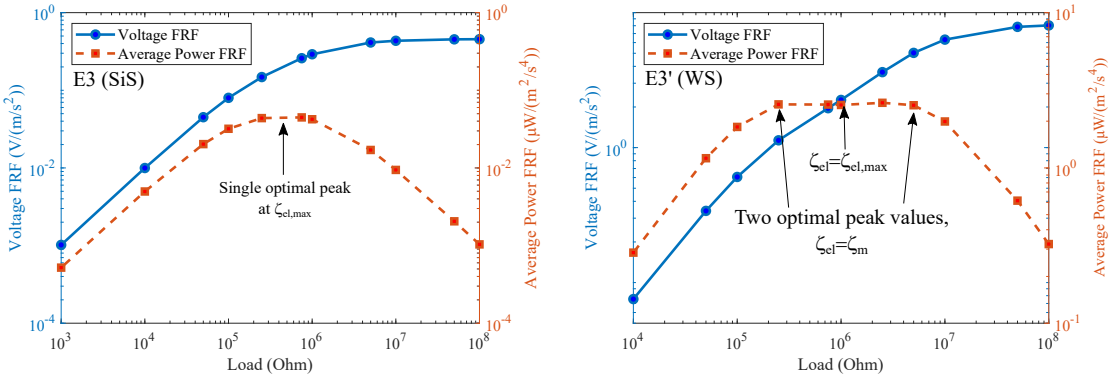

Figure 6.5 Comparison of peak outputs versus the connected resistance for devices E3 (a) and E3′ (b). Device E3′ now has two optimal loads, demonstrating an improved Q factor due to the addition of tungsten.

Figure 6.6, which plots the peak frequency f_r and estimated total Q factor [1] versus the connected load for both devices, also support this observation. The coupling factor κ^2 is estimated to ≈ 0.0012 for both devices, based on their peak frequency shifts, which confirms the tungsten mass had no substantial impact on the piezoelectric coupling. Meanwhile, the Q factor in the short circuit and open circuit testing conditions has almost doubled between device E3 and E3′, whereas the dip of the Q factor with the 1 MΩ load is more pronounced for E3′. The resonator figures of merit $\kappa^2 Q_m$ for E3 and E3′ are hence estimated to 1.3 and 2.4 respectively. Both observations again support that Q_m has improved after adding the tungsten mass.

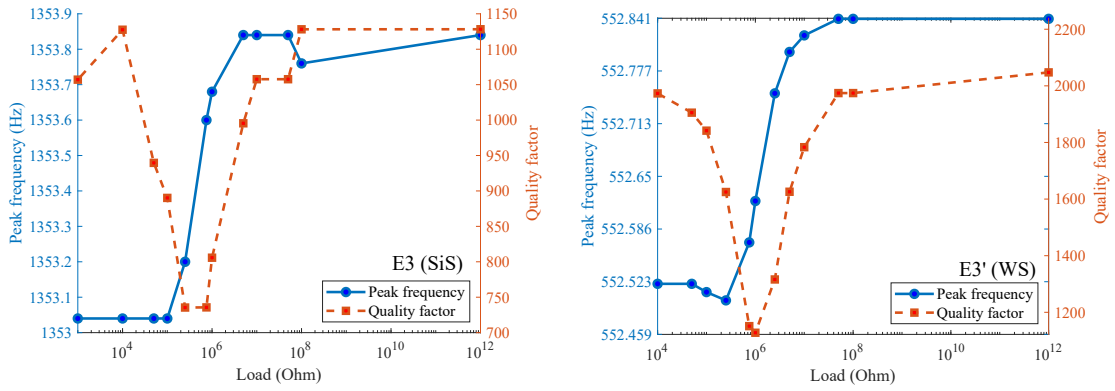

Figure 6.6 Comparison of the peak frequency and total Q factor variations with the load between device E3 (a) and E3′ (b).

1. Calculated from $Q = f_r/\delta f$, where δf is the full width at half maximum (FWHM)

Because both devices were tested using different amplitudes of vibration, it is possible non linear damping could explain this behavior, as more damping is typically observed when larger amplitudes are used (due to structural effects or increased fluid damping at larger amplitude of motion). However, we show in the next section that it is not observed for this specific case.

6.2.2 Voltage and power output variations with input acceleration

Figure 6.7 presents the voltage and power outputs of all the harvesters versus the input acceleration, providing an overview of their overall relative performance. These results correspond to the RMS voltage and average power recorded at the peak of each device response with a matched impedance load. The corresponding resistances are reported in Table 6.1 and the raw results of all related experiments are presented in appendix F.2.

Table 6.1 Optimal resistance for all tested devices

Config. **Device ID**	**SiL** **G6**	**SiM** **I3, J3**	**SiS** **G5, E3**	**WM** **I3′, J3′**	**WS** **E3′**
R_{optimal} (MΩ)	0.25	0.5	0.5	1	1

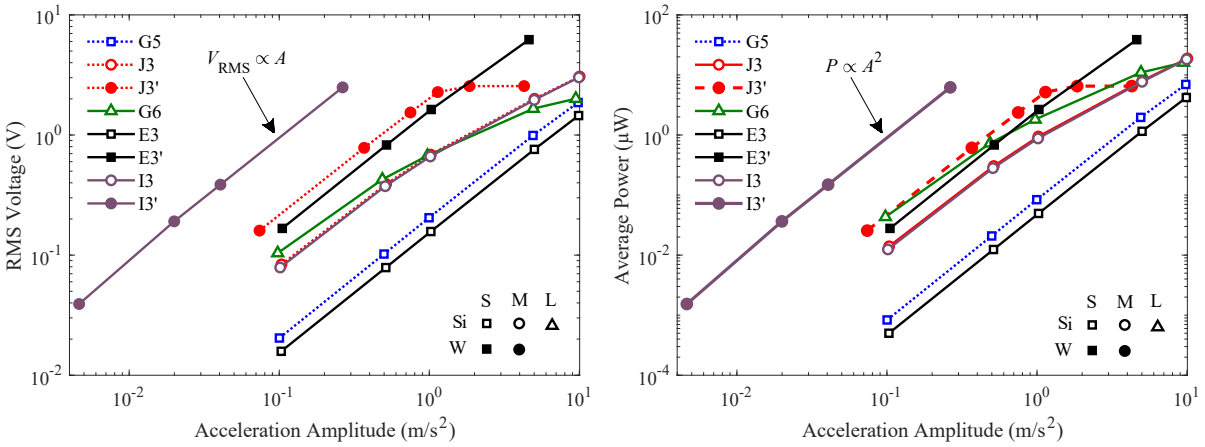

(a) (b)

Figure 6.7 Harvesters' RMS voltage (a) and average power output (b) versus the input acceleration amplitude. All data points correspond to the peak of the transfer function and are obtained with an optimal resistance for each device.

Nonlinear damping

In Fig. 6.7, devices afflicted by nonlinear damping present a reduction of slope as the input acceleration increases. It is not the case for devices E3 and E3′. In the low acceleration range (< 1 m/s^2), voltage and power increase with the same rate for most of the devices tested. In

agreement with the model presented in chapter 2, voltage varies linearly with the acceleration and consequently the power output increases with the square of this value. However, the slope diminishes at higher amplitudes, starting around 1 m/s^2, for large and medium sized devices, such as G6, I3, I3′ and J3. The drop, however, is less pronounced for I3, I3′ and J3 than for G6. In fact, the nonlinear damping effects on G6, the biggest design reported here, are such that G6 produces less power than J3/I3 from similar acceleration amplitudes. Squeeze film effects are probably responsible, considering that G6's footprint is approximately twice that of J3/I3, whereas the gap with the accelerometer located underneath is the same (and estimated to 1.7 mm, the PCB thickness).

Influence of the tungsten mass bonding

Figure 6.7 highlights once more how adding tungsten greatly enhances performance, with the most notable examples demonstrated by the change from I3 to I3′ and E3 to E3′. For instance, this modification allows I3′ to produce >1 μW from a level of vibration as low as 0.1 m/s^2 at 50 Hz. In both cases, the power output is increased by a factor greater than 30 (although the reduced frequency also contributes). By comparison, the improvement is lesser between devices J3 and J3′. In this case, significant increase of the mechanical damping was observed, originating from spilled epoxy on the beam during bonding of the tungsten mass.

Other observations

It is worth mentioning that devices I3 and J3 have roughly the same response, which, although expected considering they have the same nominal design, demonstrates results repeatability. However, G5 and E3 also have the same nomimal design relatively to one another, but G5 appears to have slightly better performances. The origin of this difference remains to be determined, but could be due to a superior Q factor for G5. In the case of J3′, the voltage and power outputs rapidly saturate at 1 m/s^2. This occurs because at this point the mass displacement is restrained and hits the accelerometer located underneath. Also worth of mention is the maximum power output of ≈ 39 μW measured for device E3′, which was obtained using an amplitude of vibration of 5 m/s^2, as it was recorded just before mechanical failure (shown by the graph discontinuity in Fig F.14).

Overall, these results are encouraging, but proper benchmarking, which accounts for the contribution of the devices overall size and the vibration source characteristics, is still needed to assess the performance and compare with the state of the art.

6.2.3 Results summary

To evaluate the general level of performance of all prototypes tested relative to one another, we compute the normalized power density figure of merit P_ρ (previously defined in section 2.4.2) for one selected test run of each. This analysis is presented in Fig. 6.8 as a function of the frequency ratio (*i.e.*, for each curve the frequency axis is normalized by its respective device resonant frequency), with the test parameters associated to each peak reported in Table 6.2.

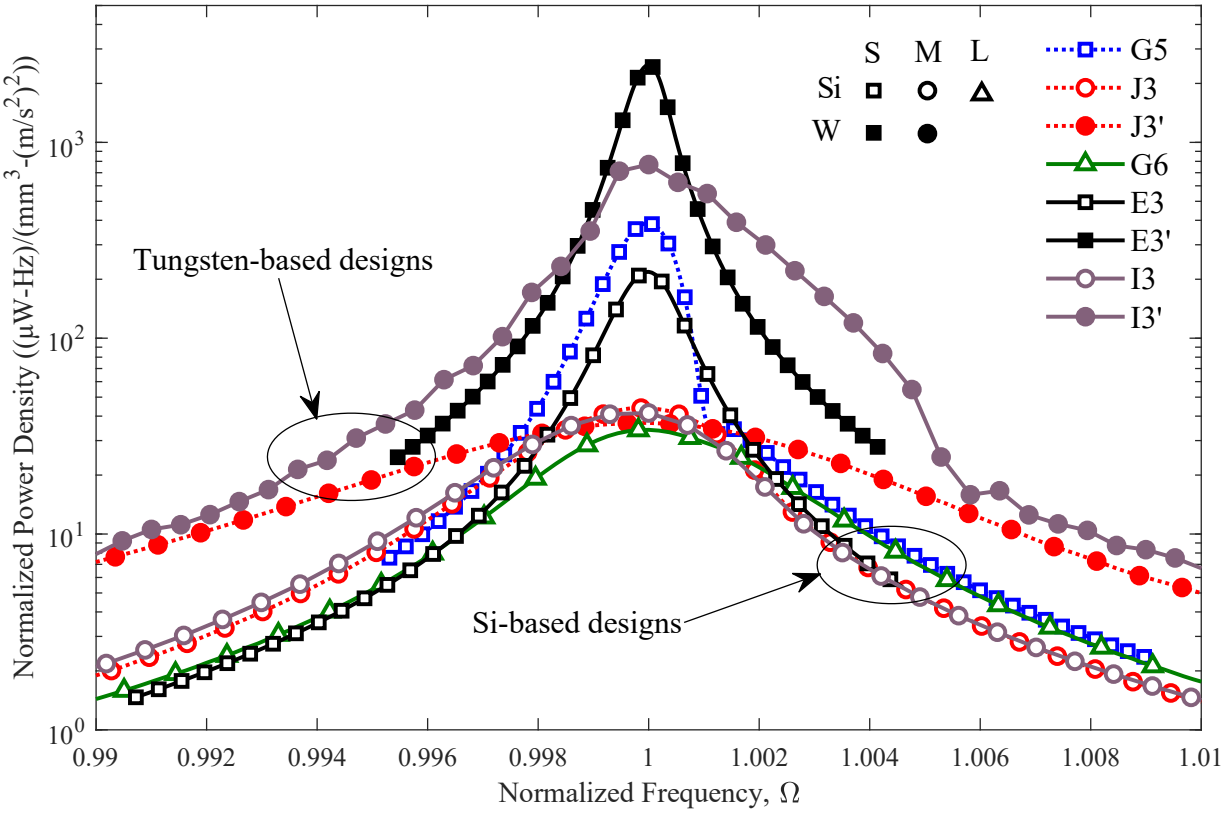

Figure 6.8 Comparison of the normalized power density, P_ρ, for all test devices. The frequency axis is normalized by the peak frequency.

General harvesters parameters

Table 6.2 includes estimates for the mechanical and total Q factors, Q_m and Q_{tot}, obtained from the FWHMs, as well as estimates for the piezoelectric coupling factor, κ^2, obtained from the frequency shift between the short and open circuit conditions. In general, κ^2 remains in the range of 0.001 for all test devices, which is consistent with the fact that this value depends mostly on the materials Young's modulus, layer thicknesses and electrode coverage (and identical for all). Meanwhile, the mechanical Q factor varies greatly, going from 100 to up to 2000, depending on the design. The general trend, however, is that smaller, higher frequency harvesters have better

Table 6.2 Test devices parameters and benchmarking

	Config.	**SiL**	**SiM**		**SiS**		**WM**		**WS**
	Device ID	**G6**	**I3**	**J3**	**G5**	**E3**	**I3′**	**J3′**	**E3′**
Design	Vol_{b} (mm^3)	1.172	0.753		0.067		0.753		0.067
	Vol_{M} (mm^3)	36.894	18.06		1.72		36.54		3.48
	Mass (mg)	86	42		4		357		34
Test cond.	f (Hz)	107.4	146.04	146	1347	1353	50.39	51.8	552.6
	A (m/s^2)	0.972	1.02	1.02	4.91	5.02	0.04	0.749	0.52
	A^2/ω (m^2/s^3)	0.0014	0.00113	0.00113	0.00285	0.00296	5.05E-06	0.00172	0.0000779
Outputs	V_{RMS} (V)	0.67	0.662	0.69	0.992	0.76	0.386	1.54	0.826
	$\bar{P}_{\mathrm{el}}$ (µW)	1.81	0.877	0.94	1.97	1.15	0.149	2.37	0.68
Performance	Q_{m}[a]	225	260	250	900	1100	700	120	2000
	Q_{tot}[b]	210	240	240	770	710	470	110	1100
	Bandwidth[b] (Hz)	0.52	0.61	0.62	1.76	1.92	0.11	0.48	0.5
	κ^{2}[c]	0.0015	0.0014	0.0011	0.00095	0.0012	0.0014[d]	0.0011[d]	0.0012
	$\kappa^2 Q_{\mathrm{m}}$	0.3	0.4	0.3	0.9	1.3	1	0.1	2.4
FOM	$\bar{P}_{\mathrm{el}}/Vol$ (µW/mm^3)	0.048	0.0466	0.05	1.1	0.64	0.004	0.064	0.192
	P_ρ $\left(\frac{\mu\mathrm{W\,s^{-1}}}{\mathrm{mm^3(m/s^2)^2}}\right)$	34	41.1	44.1	387	217	791	36.9	2462
	$\eta_{\max}$ (%)	14	15	12	30	40	33	6.2	55
	ξ	0.54	0.56	0.63	1.5	0.71	0.93	0.26	1

[a]Estimated from the FWHM in short and open circuit conditions

[b]Estimated from the FWHM in matched impedance condition

[c]Estimated from the frequency shift between short and open circuit

[d]Taken from Si device value due to low resolution at lower frequency values

Q_m that ranges close to 1000, whereas larger, low frequency ones are limited to values closer to 250. It remains unclear if these lower values are caused by structural anchoring losses, by fluid damping effects (like squeeze film) or both. The Q factor improvement seen from I3′ suggests fluid damping is at least part of the root causes. Tests under vacuum environment would allow to evaluate the contribution of anchoring losses. It is also worth noting that devices with the same nominal design have similar resonant frequencies, attesting for the uniformity of fabrication brought by the SOI wafer that provides tight dimensional control on the beam thickness.

Performance enhancement evaluation from adding tungsten

The improvements for devices E3′ and I3′ are quite significant, as they respectively end up with the first and second highest FOMs after adding a tungsten mass. In both cases, the normalized power density FOM is improved by more than an order of magnitude compared to the original silicon designs. As explained in section 6.2.1, the high values for E3′ and I3′ originate from the combined effect of the higher mass density and slight improvement of their mechanical Q factor after adding the tungsten mass.

Performance degradation from J3 to J3′

However, Fig. 6.8 also shows the extent of device J3′ poor performance due to epoxy spillage on the beam. The reduction of the device Q factor is such that most of the benefit brought by the mass density increase is canceled at the peak. Still, it is worth pointing that the FOM remains generally higher out of resonance due to the increased force applied. More generally, a higher density proof mass is beneficial for wide band performances, because it increases the normalized power density over the whole spectrum, whereas changing Q_m only affects frequencies in the vicinity of the peak.

Haverster effectiveness analysis

The harvesting effectiveness, ξ, is also evaluated and reported in Table 6.2. Although the majority of the devices have $\xi \leq 1$ and respect the electrical power limit based on the inertial coupling limit presented in section 2.4.1, device G5 shows some discrepancies in the results by having $\xi = 1.5$. One hypothesis it that the measurement of Q_m could be inaccurate and underestimated. For large Q_m, the frequency sweep rate must be reduced to accommodate a longer oscillation settling time. Thus, if the sine sweep is ran too rapidly, the full amplification effect is not properly picked up. This is supported by the dips observed on this device FRFs, plotted in Fig. 6.8 and Fig. F.1, which is a display of the ringing effect resulting from the system responding at two close but different frequencies at the same time (the transient response at the resonant frequency

and the harmonic response from the source excitation) [78]. A similar effect is observed for device I3' and makes the assessment of Q_m potentially inaccurate for this prototype as well. Its non-symmetric response curve when subject to the forward frequency sweep also suggests it has a slightly non-linear response.

Overall, these results are nevertheless consistent with the theory and demonstrate that several prototypes can provide µW level of power at small vibration levels. In the next section, these results are compared to the state of the art previously reported in section 2.9.

6.3 Comparison to state of the art

The normalized power density metric is again used to compare the test devices relatively to the prototypes previously reported in section 2.9. The results of this analysis are presented by the bar chart of Fig. 6.9, whereas Fig. 6.10 plots this metric versus the reported frequency of operation, essentially updating Fig. 2.17 with our results. Both figures show the test devices produced in this work fare comparably or better.

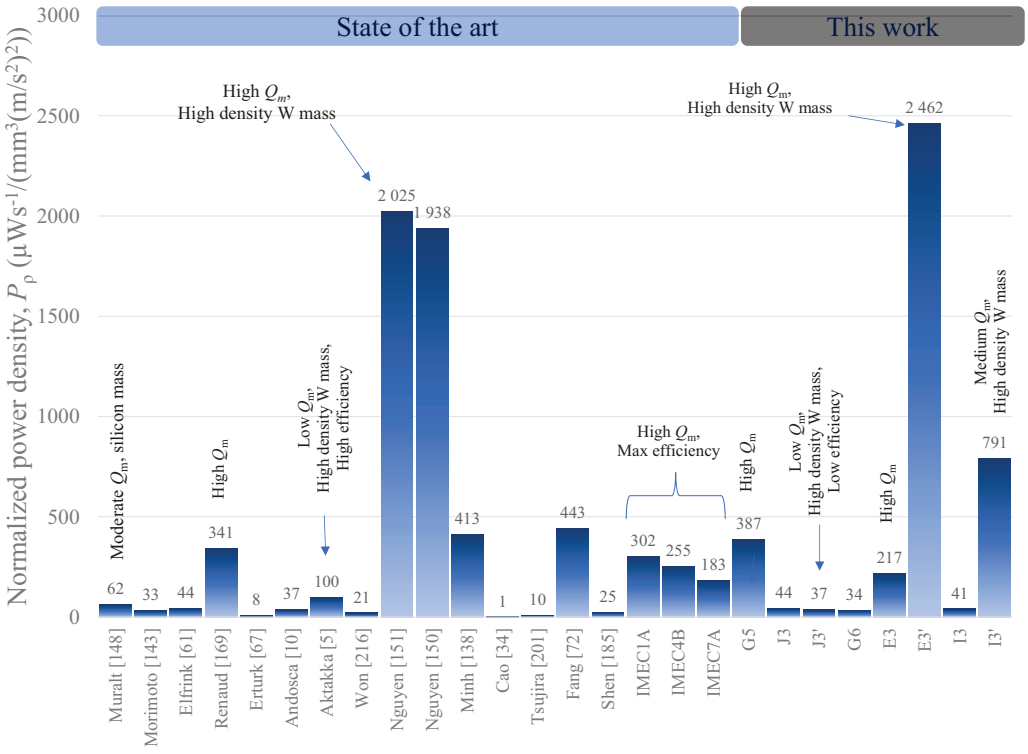

Figure 6.9 Comparison of our devices' normalized power density FOM to the state of the art. Devices E3′ and I3′ fare well relatively to others previously reported due to their moderate to high mechanical Q factor and high mass density.

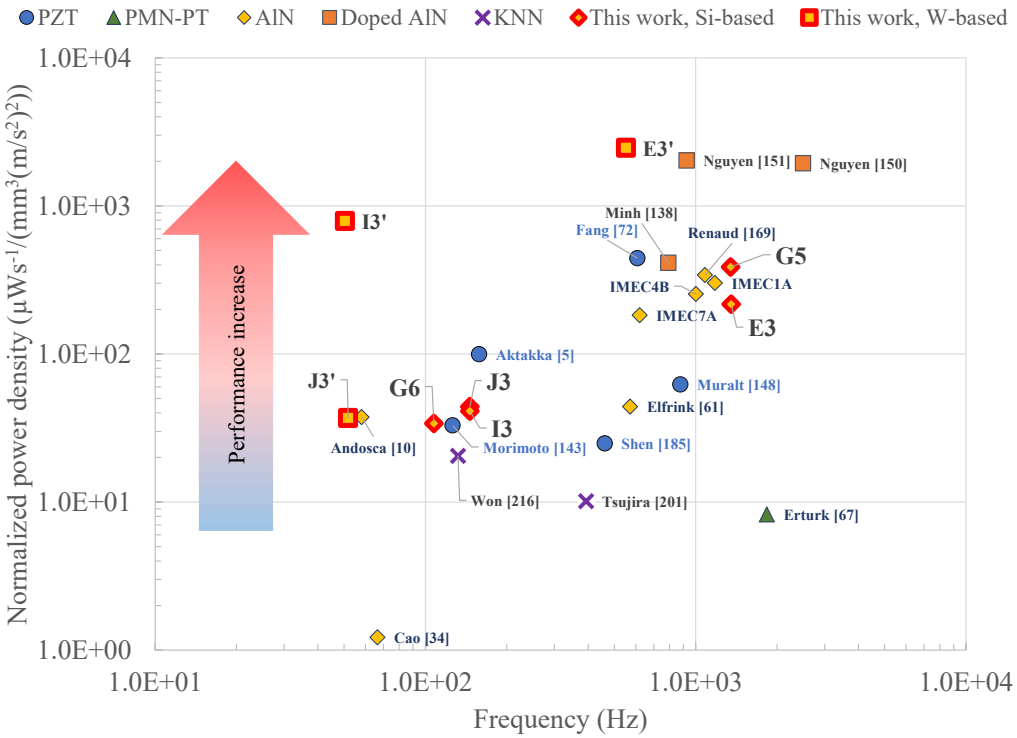

Figure 6.10 Comparison of the normalized power density versus frequency for our devices with the state of the art. Devices E3′ and I3′ again show good performance relatively to previously reported designs. For low frequency operation, I3′ shows the best performance reported to date.

Our small silicon based devices, namely G5 and E3, perform similarly to those produced by IMEC. They share high mechanical Q factors over 1000, although IMEC's design have better coupling (they also operate at maximum efficiency). The lower Qs (≤ 300) of the medium and larger sized silicon devices (J3, G6, I3) prevent those from reaching the same level of performance. We believe fluid damping is limiting the performances here.

For J3′, the FOM barely changes and is in fact slightly worse despite the addition of the high density proof mass. Again, this is due to additional damping introduced after the tungsten mass bonding procedure. By comparison, I3′, which is essentially the same design as J3′, behaves quite differently and benefits significantly from the addition of the tungsten mass. In fact, its FOM surpasses all other devices reported in this frequency range and ranks among the bests overall.

Both figures again highlight the addition of tungsten can significantly increase the devices FOM and general performance by allowing the harvesters to produce much more power from low level vibrations for a given volume of material. Still, most test devices do not have an optimal coupling factor, as many don't exhibit the two optimal resistances typically observed in this situation. Only E3′ respects this condition, thus even better performances could be expected by improving coupling, either through geometric optimization or by material enhancement.

In the first case, the simplest solution would be to reduce the thickness of the non-piezoelectric layers (*e.g.*, SiO_2 or Si) to increase the piezoelectric material thickness fraction. Here, the 30 µm silicon thickness was not guided by a design choice, but was rather limited by the price and availability of stock SOI wafers. The second option would require more work to characterize the material properties. However, at this time, direct comparisons can be made with IMEC's designs, because they use the same material, deposition technique and even similar thickness ratios. Based on the data reported in Table 2.8, their devices' coupling is 3 to 4 times better than ours, which suggests that the coupling properties of the piezoelectric material has room for improvement.

High normalized power density FOMs are achieved here despite inferior coupling properties compared to other similar devices reported in the literature. For instance, the devices of Nguyen *et al.* [150, 151] and Minh *et al.* [138] use doped AlN. However, based on the results observed in this work, it is clear that the high value of the FOM reported in [151] is mostly due to the use of the tungsten mass. Still, improving coupling remains desirable overall, because it can provide better wide band performances (as shown in Fig. 2.3) and efficiency. Alternatively, these test devices would also benefit from non-linear harvesting circuits.

6.4 Conclusion

In this chapter, the performance of prototypes fabricated using the process introduced in chapter 5 have been tested and evaluated experimentally. The eight designs tested had overall volumes ranging from 1.8 to 38 mm^3 and resonant frequencies between 51 and 1350 Hz. All were tested dynamically using forward frequency sine sweep base acceleration excitations and put through two types of scenario, namely constant acceleration-variable resistance and constant resistance-variable acceleration runs. The data collected allowed for a comprehensive characterization of the devices response versus the input excitation and the resistive load. The best designs can produce $> 1\mu W$ on average from acceleration sources as low as 0.1 m/s^2 at their resonant frequency.

The results presented here confirm that by using AlN and silicon MEMS structures, combined with high density tungsten masses, it is possible to reach high performance levels by simultaneously leveraging a high Q factor and a higher sensitivity to input vibrations. This strategy allows reaching normalized power densities in excess of 2 $mWs^{-1}/(mm^3(m/s^2)^2)$, which is more than what has been reported for other published harvesters to date. Our devices performance are notable because they have been achieved in ambient air and without using high coupling materials, such as PMN-PT or doped AlN. These results therefore support the efforts to develop highly sensitive and low loss vibration energy harvesters to power wireless sensors.

CHAPITRE 7

Conclusion (français)

7.1 Sommaire

Cette thèse a présenté les différents travaux effectués pour concevoir, fabriquer et développer des générateurs vibratoires piézoélectriques pour l'alimentation de capteurs autonomes ultra faible puissance. Dans le chapitre 1, nous avons tout d'abord discuté des motivations principales derrière le développement de capteurs sans-fil autonomes, du pourquoi l'enjeux de la suffisance en énergie est critique et de comment les technologies de récupération d'énergie pourraient apporter une solution à ce problème. Un court résumé des travaux antérieurs, portant spécifiquement sur la récupération d'énergie à partir des vibrations, a été présenté pour exposer l'état de la recherche actuelle et les questions qui demeurent ouvertes dans ce domaine. Plus spécifiquement, il a été discuté que les véritables limites de cette technologie devaient être clarifiées pour pouvoir proposer des outils de comparaison et d'étalonnage des différents dispositifs. Par ailleurs, il a été souligné que des caractéristiques réalistes concernant les vibrations disponibles et le budget énergétique requis devaient être établies pour guider la conception de prototypes. Finalement, un besoin pour des dispositifs plus sensibles, permettant d'améliorer la densité de puissance, a été identifié, ce qui demandait des nouvelles approches de fabrication. Les objectifs de cette thèse ont donc été formulés pour s'attaquer à ces aspects et les travaux réalisés en ce sens ont été présentés dans les chapitres suivant.

Le chapitre 2 s'attaquait tout d'abord aux limites générales de la récupération d'énergie vibratoire. Le but était donc d'établir des méthodes rigoureuses pour la comparaison des dispositifs, indépendamment de leur taille ou des vibrations utilisées. Les travaux précédents pertinents ont été référés, mais aussi complétés par nos propres analyses pour bâtir un cadre de travail exhaustif. Des aspects tels que la réponse dynamique du dispositif, son architecture, les matériaux utilisés, le circuit connecté, les caractéristiques des vibrations et la géométrie du dispositif ont tous été analysés pour dresser un portrait complet des facteurs limitant. Au final, des indicateurs de performance ont été proposés et un compte rendu de l'état de l'art actuel a été fait en comparant tout près d'une vingtaine de dispositifs répertoriés dans la littérature. Malgré qu'il ne s'agit pas du seul facteur, nous en sommes arrivé à la conclusion que le facteur limitant principal est d'abord et avant tout l'apport d'énergie au dispositif.

À la lumière de cette conclusion, nous avons jugé nécessaire de caractériser une source de vibration typique pour être en mesure de mieux évaluer des spécifications réalistes pour un récupérateur d'énergie. Pour ce faire, nous avons réalisé au chapitre 3 une étude de cas portant sur les vibrations présentes sur une automobile afin d'évaluer leur potentiel pour alimenter un capteur sans fil à partir de la récupération d'énergie vibratoire. Tout d'abord, un recensement des capteurs présents dans les véhicules automobiles modernes a été fait, suivi d'une évaluation de leur compatibilité avec la récupération d'énergie vibratoire. De part les risques associés à cette technologie, nous avons jugé que la criticité et le taux de transmission des données des capteurs devaient être utilisés comme critères de base pour choisir une application potentielle. Par la suite, nous avons présenté les méthodes de mesure et d'analyse des données employées pour évaluer le potentiel énergétique d'emplacements spécifiques sur un véhicule. Nos résultats ont démontré que l'énergie des vibrations accessible pour un dispositif MEMS est principalement contrainte dans une plage de fréquence entre 30 et 200 Hz, avec des densités spectrales d'accélération de l'ordre de 0.1 $(m^2/s^4)Hz^{-1}$ ou moins. Fait intéressant, certains emplacements démontraient des spectres d'énergie répétables à large bande, ce qui suggérait que l'ajustement de la fréquence de résonance n'est potentiellement pas essentiel pour ces cas. En se basant sur ces résultats et une cible de puissance de 10 µW, nous avons néanmoins conclu qu'il serait difficile d'alimenter un capteur sans-fil de cette façon avec un dispositif MEMS, d'autant plus si on se limite à des dispositifs en silicium seulement. En effet, une masse de 1 gramme a été identifiée comme étant nécessaire pour attendre la cible de puissance, ce qui a motivé l'intégration du tungstène pour améliorer la densité de presque un ordre de grandeur.

Bien que les bénéfices de l'usage du tungstène pour augmenter la force inertielle, donc la puissance potentielle, soient évidents, nous avons aussi démontré au chapitre 4 qu'il existe d'autres avantages, notamment en ce qui concerne l'impact de l'air et donc l'opération du dispositif à pression ambiante. Nous avons démontré analytiquement et expérimentalement qu'en utilisant du tungstène pour produire des masses de haute densité, l'impact de l'amortissement fluidique sur le générateur est réduit d'environ un ordre de grandeur. Dans certains cas, cela pourrait être suffisant pour permettre de simplifier la mise en boîtier en éliminant, par exemple, les contraintes sur la pression nécessaire à l'intérieur, le besoin d'herméticité à long terme ou l'usage de matériaux absorbant le dégazage.

Au chapitre 5, nous avons proposé et présenté un procédé de fabrication original pour intégrer des masses de tungstène à l'échelle de la tranche. Ce procédé utilise des méthodes de collage de tranches et de gravure chimique du métal pour joindre et définir des masses sismiques volumineuses à partir d'une tranche de métal sur des dispositifs résonants à base de silicium et d'AlN. Malgré que tous les blocs de fabrication n'aient pas pu être intégrés d'un bout à l'autre dans

un seul procédé, ces blocs ont tout de même été validés séparément. D'autres expériences ont également été réalisées pour démontrer la faisabilité et l'inter-compatibilité des blocs entre eux. L'intégration de masses épaisses de tungstène à l'échelle de la tranche a notamment été démontré par collage sur des micropoutres de silicium. Par la suite, cette boucle courte a été validée en testant la réponse dynamique de l'assemblage, notamment en mesurant la fréquence de résonance et le facteur de qualité. En parallèle, un procédé permettant de fabriquer des générateurs piézoélectriques à base d'AlN a été développé et sa compatibilité avec l'approche d'intégration du tungstène a été vérifié séparément. Néanmoins, pour fabriquer des dispositifs représentatifs du procédé intégré proposé et démontrer leur potentiel expérimentalement, des masses de tungstène ont été ajoutées aux générateurs piézoélectriques fabriqués en utilisant un collage au niveau de la puce.

Finalement, le chapitre 6 a présenté les résultats expérimentaux et l'évaluation des performances de 8 prototypes. L'équipement et les méthodes de tests ont tout d'abord été expliqués en détail. Les réponses en fréquence pour la tension et la puissance produites ont ensuite été présentées pour divers scénarios de test, notamment en variant la charge électrique et l'accélération fournie, pour couvrir un large éventail de conditions d'opération. Ces résultats ont mis en lumière qu'en combinant le haut facteur de qualité mécanique de l'AlN et la densité élevée du tungstène, il est possible d'atteindre des niveaux de performance élevés. Deux designs en particulier ont démontré des résultats impressionnants et produisaient > 1 µW à partir de vibrations d'intensité aussi faible que 0.1-1 m/s^2. La performance de tous les dispositifs testés a été évaluée et comparée à l'état de l'art en utilisant la méthode de comparaison introduite au chapitre 2. En terme de densité de puissance normalisée, nos 2 meilleurs designs atteignent des figures de mérite près de 0.8 et 2.5 mWs^{-1}/(mm^3(m/s^2)^2), se classant parmi les meilleurs résultats rapportés à ce jour dans la littérature.

7.2 Contributions

Cette section présente les principales contributions issues de ce projet de recherche au domaine de la récupération d'énergie vibratoire.

7.2.1 Révision complète des limites de la récupération d'énergie vibratoire et proposition d'un cadre comparatif

Ce travail propose une analyse exhaustive des nombreuses limites se rapportant à la récupération d'énergie vibratoire à partir de matériaux piézoélectriques. Bien que nombre de chercheurs ont proposés plusieurs méthodes pour comparer les dispositifs à partir de divers indicateurs, notre

contribution ici est principalement d'en avoir fait une révision complète. Nous avons analysé leur pertinence selon le contexte et avons proposés de nouvelles approches complémentaires sur plusieurs niveaux. Par conséquent, ce travail représente le cadre de travail le plus complet à ce sujet, car il inclus l'impact des dimensions du dispositif, de l'architecture, du design du transducteur, des propriétés des matériaux et de la topologie du circuit utilisé. Ces travaux de recherche ont été publiés en partie dans plusieurs formats, notamment 2 chapitres de livre et un article de conférence.

- A. Dompierre, S. Vengallatore, and L. G. Fréchette, "Theoretical and practical limits of power density for piezoelectric vibration energy harvesters," in *Proceedings of PowerMEMS 2011, Seoul, South Korea*. KAIST, 2011
- A. Dompierre, S. Vengallatore, and L. Fréchette, "Power density limits and benchmarking of resonant piezoelectric vibration energy harvesters," in *Novel Advances in Microsystems Technologies and Their Applications*. CRC Press, 2013, pp. 293–333
- A. Dompierre, S. Vengallatore, and L. G. Fréchette, "Piezoelectric vibration energy harvesters : Modeling, design, limits and benchmarking," in *Energy Harvesting with Functional Materials*, M. Bhaskaran, S. Srira, and K. Iniewski, Eds. CRC Press, 2013, ch. 9, pp. 215–264

7.2.2 Méthodologie pour évaluer les sources et les applications de récupération d'énergie vibratoire

Cette thèse propose également une méthodologie originale pour évaluer le potentiel de certaines applications de capteur sans-fil. Notre approche couvre l'identification qualitative des applications les plus compatibles, ainsi que l'évaluation quantitative de la puissance disponible à partir d'une source ambiante. Pour cette thèse, les vibrations automobiles ont été considérées, mais la méthode est transposable pour tout type d'environnement. Ce travail a aussi mis en lumière que la densité du silicium est généralement insuffisante pour produire des dispositifs fonctionnels dans un volume compact, démontrant le besoin pour l'intégration de masses à plus forte densité. Ce travail a été présenté dans le cadre d'une présentation orale à l'ASME 2013 IMECE.

- A. Dompierre, M. Traore, and L. Fréchette, "Measurements of car vibrations under real-life driving conditions and assessment of energy harvesting for wireless sensor nodes," in *ASME 2013 International Mechanical Engineering Congress and Exposition*, American Society of Mechanical Engineers. American Society of American Engineers, 2013, pp. V014T15A023–V014T15A023

7.2.3 Bénéfices additionnels de l'intégration de masses à haute densité

Nous avons démontré que l'usage du tungstène au lieu du silicium pour produire des masses de grande densité dans les générateurs MEMS permet de réduire l'effet de l'amortissement fluidique par un ordre de grandeur. Bien que reposant sur des considérations physiques très simples, c'est la première démonstration expérimentale de ce bénéfice important. Ceci ouvre des possibilités nouvelles pour la conception de boîtier faible coût et ne nécessitant pas de vide. Cette contribution a été présentée pour la première fois à la conférence PowerMEMS 2016 à Paris et a été acceptée pour publication dans le *Journal of Microelectromechanical Systems* de l'IEEE.

- A. Dompierre and L. Fréchette, "Improvement of vibration energy harvesters mechanical Q-factor through high density proof mass integration," in *Journal of Physics : Conference Series*, vol. 773, IOP Publishing. Institute of Physics, 2016, p. 012095
- A. Dompierre, S. Vengallatore, and L. G. Fréchette, "Achieving high quality factor without vacuum packaging by high density proof mass integration in vibration energy harvesters," *Journal of Microelectromechanical Systems*, in press

7.2.4 Procédé de microfabrication original

Un procédé de fabrication original qui intègre du tungstène au niveau de la tranche a été proposé pour les MEMS inertiels. Dans cette thèse, nous avons démontré son potentiel pour produire des récupérateurs d'énergie vibratoire MEMS ayant une forte densité de puissance, mais cette technologie pourrait être bénéfique pour les capteurs inertiels en général. Le fruit de ce travail a mené au dépôt d'une demande de brevet international (PCT en instance) et une partie des travaux réalisés a été présentée à la conférence internationale Transducers 2017 à Kaohsiung, Taiwan.

- A. Dompierre and L. G. Fréchette, "A wafer-level process for bulk tungsten integration in MEMS vibration energy harvesters and inertial sensors," in *Solid-State Sensors, Actuators and Microsystems (TRANSDUCERS), 2017 19th International Conference on*, IEEE. IEEE, 2017, pp. 2127–2130
- A. Dompierre and L. Fréchette, "Inertial devices with wafer-level integration of higher density proof masses and method of manufacturing," PCT Patent WO2 018 227 308, 2018

7.3 Travaux futurs

Amélioration du procédé, approches alternatives et développements additionnels Nous n'avons pas été en mesure d'intégrer tous les blocs de fabrication pour démontrer d'un bout à l'autre le procédé proposé au chapitre 5. Du travail additionnel est donc nécessaire pour compléter ces efforts. De plus, plusieurs blocs pourraient être améliorés ou changés pour rendre le procédé plus manufacturable ou précis relativement aux dimensions critiques. Par exemple, une approche de gravure sèche profonde du tungstène pourrait être développée pour améliorer le contrôle sur les dimensions des masses et leur verticalité. Une autre approche qui pourrait être envisagée serait de croître les couches fonctionnelles directement sur un substrat métallique au lieu d'utiliser des approches de collage. En fait, plusieurs procédés du genre ont été considérés au cours de ce projet (plusieurs se retrouvant dans le brevet déposé), mais ils ne pouvaient pas être explorés davantage par manque de temps et de ressources.

De plus, le procédé de fabrication actuel a permis de produire des dispositifs fonctionnels, mais ils n'ont pas un boîtier robuste pour les protéger des risques externes ou d'une surcharge dynamique. Ainsi, plus de travail est requis pour concevoir et développer une approche de mise en boîtier qui est compatible avec l'intégration au niveau de la tranche des masses de tungstène. Cela est d'autant plus pertinent si le but est un jour de commercialiser des dispositifs fonctionnels.

Tester des générateurs avec des circuits appropriés et un capteur dans un environnement réel Bien que des vibrations réelles ont été considérées au chapitre 3, aucun générateur n'a été testé dans des conditions réelles ou avec les signaux enregistrés. Dans le future, il serait intéressant de tester un générateur mis en boîtier sur le terrain pour le tester dans ces divers environnements. Le chapitre 3 a aussi brièvement présenté un capteur de température sans-fil, mais il n'était pas alimenté par un récupérateur d'énergie vibratoire. Ici encore, une étape intéressante serait d'interfacer ce capteur avec un générateur vibratoire MEMS grâce à un circuit de gestion de puissance approprié, le tout dans le but de développer un noeud de capteur pouvant se recharger de lui même à partir des vibrations.

Optimisation des dispositifs et usage du procédé de fabrication pour développer des capteurs inertiels sensibles et faible puissance Cette thèse portait sur les applications de récupération d'énergie vibratoire. Par contre, le nouveau procédé proposé au chapitre 5 représente également une plate-forme intéressante pour développer divers capteurs MEMS inertiels très sensibles, comme des accéléromètres ou des gyroscopes pour détecter de faibles niveaux d'accélération. De plus, l'intégration de matériaux piézoélectriques dans ces dispositifs pour-

rait également permettre de réduire leur consommation d'énergie, ce qui, tel que mentionné en introduction, est critique pour des applications IoT.

Évaluation de la durée de vie en fatigue et de la dégradation causée par les contraintes Pour cette thèse, la durée des tests réalisées s'est limitée à quelques heures, le temps de caractériser les prototypes fabriqués. Par contre, les générateurs déployés dans des produits réels devraient fonctionner plusieurs années. À ce jour, peu d'études ont été réalisées pour évaluer expérimentalement la dégradation des performances au fil du temps des générateurs MEMS. Par conséquent, il serait pertinent de mener davantage d'études à ce sujet pour observer et évaluer la fiabilité des générateurs à base d'AlN.

Explorer le potentiel des dynamiques instables Bien que cette thèse s'est principalement concentrée sur les systèmes stables linéaires afin d'identifier leurs limites fondamentales, il vaudrait la peine d'explorer d'autres systèmes dynamiques qui comportent des instabilités. Il serait entre autre intéressant d'évaluer si le fait d'exploiter ces instabilités permettrait d'augmenter l'apport en énergie au dispositif de récupération d'énergie (autrement dit, voir s'il y a une amélioration importante du couplage mécanique avec la source), ce qui pourrait aussi augmenter la génération d'énergie. Par exemple, les effets du flottement aéroélastique pourraient être exploités pour développer de nouveaux types de micro-éoliennes. La récupération d'énergie pourraient aussi être intégrée dans des systèmes de transmission sujets à des effets non-linéaires de frottement par à-coups (*stick-slip*), soit pour détecter ou supprimer ce phénomène.

CHAPTER 8

Conclusion (english)

8.1 Summary

This thesis presented various efforts to design, fabricate and develop piezoelectric vibration powered generators for ultralow power autonomous sensor applications. In chapter 1, we presented the general motivation for the development of wireless autonomous sensors, why the issue of long term energy sufficiency was critical, and how energy harvesting technologies could potentially address this challenge. A short summary of previous work, with a specific focus on vibration energy harvesting, was presented to highlight the state of current research and the questions still open in this field. Notably, we found that the actual limits of this technology still needed to be clarified to propose irrevocable tool for benchmarking. Moreover, realistic vibration characteristics and power budget needed to be established to guide the design of prototypes. Lastly, we expressed the need for more sensitive devices to improve the power density, which requires new fabrication approaches. All those aspects were addressed throughout the following chapters of this thesis.

Chapter 2 first laid out the general limits of vibration harvesting. The goal was to establish rigorous methods for device comparison, regardless of the device size or vibration source. We referred to previous results obtained by numerous authors and complemented their work using our own framework. Aspects such as the device dynamic response, architecture, material properties, connected circuit, the vibration characteristics and device geometry were all investigated to draw a comprehensive portrait of all the limiting factors. In the end, a general review of the current state of the art was presented, and a list of benchmarking metrics were also proposed. Although not the only factor, we came to the general conclusion that vibration energy harvesting is, first and foremost, fundamentally restricted by the energy input.

In light of this conclusion, we decided that characterization of a typical vibration source was necessary to better asses realistic harvester specifications. To do so, we conducted a case study based around car vibrations and their potential for supplying energy to wireless sensors using vibration harvesting in chapter 3. First, a survey of sensors present in modern consumer cars was presented, as well as an assessment of their compatibility with vibration energy harvesting. Due to the risk related to this technology, it was proposed that the criticality and rate of data transmission of the sensors be considered as the fundamental criteria to select potential applica-

tions. We then presented a vibration measurement and data analysis methodology to assess the harvesting potential on specific locations of the vehicle. Our results showed that vibration energy accessible to a MEMS based device was mostly restricted to a 30-200 Hz frequency range, with acceleration densities of 0.1 $(m^2/s^4)Hz^{-1}$ or less. Interestingly, some locations exhibited consistent, wideband peaks, suggesting frequency tuning may not be essential in these cases. Based on these results and a 10 µW target, we nevertheless concluded that it would be challenging to supply wireless power using vibration with a MEMS device. This is especially true if silicon based devices were used, because a 1 gram mass was identified as a basic requirement to achieve our power target. For this reason, approaches to integrate tungsten in these devices were considered.

Although the benefit of using tungsten to increase the inertial force, and therefore the potential power output, is evident, we also showed in chapter 4 how this integration can benefit in other areas, namely in terms of packaging and the device response at atmospheric pressure. We showed analytically and experimentally that by using tungsten to produce the masses, the impact of the fluid damping on the harvester is reduced by up to one order of magnitude. In some cases, this could be enough to allow simplification of the package by reducing constraints on the pressure inside and eliminate the need for long term hermetticity or use of getter materials to absorb outgassed species.

In chapter 5, we proposed and presented an original fabrication process to integrate tungsten proof masses at the wafer-level. This process uses wafer bonding and metal chemical etching to bond and pattern bulk metallic proof masses made from a bulk tungsten wafer with silicon/AlN based resonant harvesters. Although all the fabrication blocks could not be fully integrated in a single process, they were still validated individually and additional experiments were realized to demonstrate the feasibility. Integration at the wafer-level of bulk tungsten masses on microfabricated silicon cantilevers was demonstrated and this short-loop was validated by measuring the quality factor and the resonant frequency of the passive prototype. In parallel, a process to produce AlN-based piezoelectric harvesters was developed and its compatibility with the aforementioned tungsten integration scheme was verified separately. To fabricate devices representative of the proposed fully integrated process and demonstrate its potential experimentally, tungsten masses were added to the fabricated piezoelectric devices using a die-level approach.

Finally, chapter 6 presented experimental results and performance evaluations for eight prototypes produced. The test equipment and methodology were first explained in detail. Voltage and power frequency response functions were then presented for numerous testing scenarios where the connected resistive load and input accelerations are varied to capture a broad range of operating conditions. These results highlighted that the combination of AlN's high mechanical

quality factor and the high density of tungsten enable high level of performance. Two designs in particular showed impressive results and produced > 1 µW from levels of acceleration as low as 0.1-1 m/s^2. The performance of all test devices were then evaluated and compared to the state of the art using the benchmarking methodology introduced in chapter 2. In terms of normalized power density, our 2 best designs achieved FOMs close to 0.8 and 2.5 mWs^{-1}/(mm^3(m/s^2)^2), which rank among the best results reported in the literature.

8.2 Contributions

This section presents the numerous contributions of this research project to the field of vibration energy harvesting.

8.2.1 Comprehensive review of vibration harvesting limits and benchmarking framework

This work has proposed an extensive analyses of the numerous fundamental limits of piezoelectric vibration energy harvesting. Although previous researchers have proposed several methods to compare devices based on different metrics, our contribution here is to review them, analyze their relevancy and propose complementary metrics. This work therefore proposes what we think is the most comprehensive framework for device comparison, because it includes the impact of the device dimensions, architecture, transducer design, material properties and circuit topology. Part of this research has been published in several forms, namely 2 book chapters and a conference paper.

- A. Dompierre, S. Vengallatore, and L. G. Fréchette, "Theoretical and practical limits of power density for piezoelectric vibration energy harvesters," in *Proceedings of PowerMEMS 2011, Seoul, South Korea*. KAIST, 2011
- A. Dompierre, S. Vengallatore, and L. Fréchette, "Power density limits and benchmarking of resonant piezoelectric vibration energy harvesters," in *Novel Advances in Microsystems Technologies and Their Applications*. CRC Press, 2013, pp. 293–333
- A. Dompierre, S. Vengallatore, and L. G. Fréchette, "Piezoelectric vibration energy harvesters: Modeling, design, limits and benchmarking," in *Energy Harvesting with Functional Materials*, M. Bhaskaran, S. Srira, and K. Iniewski, Eds. CRC Press, 2013, ch. 9, pp. 215–264

8.2.2 Methodology for source and application assessment with vibration harvesting

This thesis also proposed an original methodology to assess potential wireless sensor applications. Our approach covers the qualitative identification of the most suited applications, as well as quantitative evaluations for the potential power output from ambient sources. For this thesis, vehicle vibrations were considered, but the methodology can be transposed to any type of environment. This work also highlighted that silicon mass density is generally insufficient to realize most applications in a compact volume and thus brought to light the need for high density proof mass integration. This work was previously presented in an oral presentation at the ASME 2013 IMECE.

- A. Dompierre, M. Traore, and L. Fréchette, "Measurements of car vibrations under real-life driving conditions and assessment of energy harvesting for wireless sensor nodes," in *ASME 2013 International Mechanical Engineering Congress and Exposition*, American Society of Mechanical Engineers. American Society of American Engineers, 2013, pp. V014T15A023–V014T15A023

8.2.3 Additional benefits of high density proof mass integration

We have demonstrated that using tungsten instead of silicon to produce high density proof masses in MEMS harvester can reduce the effect of fluidic damping on the performance by up to an order of magnitude. Although based on simple physics, this is the first demonstration of this significant benefit, which may open up new possibilities for low cost, vacuum-less packaging approaches. This contribution was presented for the first time at the PowerMEMS 2016 conference in Paris and was submitted for publication in the IEEE Journal of Microelectromechanical Systems.

- A. Dompierre and L. Fréchette, "Improvement of vibration energy harvesters mechanical Q-factor through high density proof mass integration," in *Journal of Physics: Conference Series*, vol. 773, IOP Publishing. Institute of Physics, 2016, p. 012095
- A. Dompierre, S. Vengallatore, and L. G. Fréchette, "Achieving high quality factor without vacuum packaging by high density proof mass integration in vibration energy harvesters," *Journal of Microelectromechanical Systems*, in press

8.2.4 Novel microfabrication process flow

An original microfabrication process flow was proposed to integrate tungsten at the wafer level for inertial MEMS. In this thesis, we demonstrate the potential of this process to produce high power density MEMS vibration energy harvesters, but the technology could benefit inertial sensors in general. The outcome of this work has lead to the filing of an international patent (PCT pending) and part of it was also previously presented at the Transducers 2017 international conference, in Kaohsiung, Taiwan.

- A. Dompierre and L. G. Fréchette, "A wafer-level process for bulk tungsten integration in MEMS vibration energy harvesters and inertial sensors," in *Solid-State Sensors, Actuators and Microsystems (TRANSDUCERS), 2017 19th International Conference on*, IEEE. IEEE, 2017, pp. 2127–2130
- A. Dompierre and L. Fréchette, "Inertial devices with wafer-level integration of higher density proof masses and method of manufacturing," PCT Patent WO2 018 227 308, 2018

8.3 Future research avenues

Fabrication process improvements, alternatives and additional development We could not fully integrate all the blocks of the fabrication process proposed in chapter 5 in one seamless flow. Thus, additional work is required to complete this effort. Moreover, many blocks could be improved or changed to improve manufacturability or the precision on the dimensions. For example, a dry etching approach could be developed to improve the dimensional control and verticality of the mass side walls. Another approach could be to grow the functional layers directly on the metallic substrate instead of using wafer bonding. Many alternate process concepts were considered for this project (several of them are presented in our patent filing), but they could not be explored due to lack of time or resources.

In addition, the current fabrication process produced functional devices, but they still lack a robust package to protect them from external damages or vibration overloads. Hence, more work is required to design and propose a packaging approach that is compatible with the wafer-level integration of tungsten masses, especially if one goal is to someday commercialize functional devices.

Test matching of harvester with harvesting circuit and sensor applications in real vibration environment Although real vibrations have been considered in chapter 3, actual harvesters have not been tested in real conditions or with recorded data. In the future, it would be interesting

to bring packaged harvesters on the field and test them in various environments. Chapter 3 also briefly presented a wireless temperature node, but it was not powered by a vibration harvester. An interesting next step would be to interface this wireless temperature sensor with a MEMS harvester through an appropriate harvesting circuit to develop a complete self-charging wireless node.

Optimized design for low power inertial sensors using new process flow. This thesis focused on vibration energy harvesting applications. However, the novel process flow proposed in chapter 5 could also be an interesting platform to develop various types of highly sensitive inertial MEMS sensors, such as low g accelerometers or gyroscopes. Moreover, the integration of piezoelectric materials in these devices may also allow to reduce their power consumption, which is critical for future IoT applications.

Evaluation of fatigue and stress degradation For this thesis, the scope of our tests has been limited to only a couple of hours. However, harvesters in real applications will have to last several years. At this point few studies have been realized to experimentally evaluate the degradation in performance over time of MEMS based harvesters. Therefore, it would be interesting to conduct additional studies of AlN degradation and fatigue to assess the reliability of piezoelectric generators using this material.

Explore instable dynamics Although this thesis has focused on harvesting energy from stable systems and identified their fundamental limits, it would be worth exploring other dynamical systems which feature instabilities. Leveraging these instabilities could potentially increase the input of energy (*i.e.*, improved source coupling) and as a result significantly boost the energy harvesting capacities. For example, aerodynamic flutter could be exploited to develop new kinds of highly effective wind turbines. Energy harvesting could also be integrated in transmission systems to detect and even limit the effect of various stick-slip mechanisms.

APPENDIX A

Broadband energy harvesting

Energy harvesters have mainly been modeled and characterized using sinusoidal excitations. In reality, the ambient energy is more or less spread across the frequency spectrum and its distribution affects the power output of the harvester in several ways. For monochromatic sources, it is known that increasing the total quality factor of the harvester increases its power output, but the bandwidth also becomes very small. The power output is therefore very sensitive to frequency perturbation of the vibration source and it may deteriorate by orders of magnitude. In other words, the linear system may lack robustness and its small bandwidth does not allow harvesting energy localized outside of its effective range. As briefly discussed in 2.8.2, several approaches have been investigated to address these performance issues. They are mostly based on the use of nonlinear oscillators to broaden the functional frequency range of energy harvesters.

In this appendix, different types of oscillator are briefly presented and reviewed. An analysis of their response to different types of excitation is then presented. Nonresonant architecture are also analyzed using a simplified approach to evaluate their potential for broadband harvesting. Based on these results, a comparative analysis discussing the pros and cons of each approach closes this chapter.

A.1 Oscillator types

A.1.1 Linear oscillator

The linear oscillator is represented by the classic mass-spring-dashpot system. The equation of motion for the electro mechanically coupled piezoelectric system was given in section 2.3, from Eq. 2.6, but we rewrite it here using the oscillator displacement φ:

$$M_{\text{eq}}\ddot{\varphi}(t) + C_{\text{m}}\dot{\varphi}(t) + K_{\text{m}}\varphi(t) + \theta v(t) = f_{\text{in}}. \tag{A.1}$$

The electrical equation (Eq. 2.7) remains unchanged,

$$\theta\dot{\varphi}(t) + C_{\text{p}}\dot{v}(t) + \frac{v(t)}{R_{\text{eq}}} = 0. \tag{A.2}$$

This system was presented in plenty of details in section 2.3.

A.1.2 Duffing oscillator

The Duffing oscillator is a non-linear second-order system which is frequently used to model nonlinear springs that don't obey Hook's law. Its motion equation is given by the Duffing equation, which, modified for our piezoelectric system, is generally represented by equation A.3,

$$M_{\text{eq}}\ddot{\varphi}(t) + C_{\text{m}}\dot{\varphi}(t) + K_1\varphi(t) + K_3\varphi^3(t) + \theta v(t) = f_{\text{in}}. \tag{A.3}$$

The coefficients K_1 and K_3 are respectively attached to the linear and cubic nonlinear terms of the restoring force $f_{\text{R}} = K_1\varphi + K_3\varphi^3$. The behavior of the oscillator can change drastically based on the respective sign of these terms and the level of potential energy stored in the oscillator (here given by the integral $\int f_{\text{R}}\text{d}\varphi$). Table A.1 and Fig. A.1 presents a summary of the physical interpretation of each case, with examples of typical configurations where such behavior can be observed. It is worth pointing that in the case where $K_1 > 0$ and φ is small, the oscillator essentially behaves like a linear oscillator. The majority of passive non-linear designs proposed in the literature are based on these configurations.

Table A.1 Summary of different types of Duffing oscillator.

Parameters	$K_1 > 0$	$K_1 < 0$
	Stiffening spring	**Bistable system**
$K_3 > 0$	• stretched clamped-clampled membrane/beam under large amplitude	• buckled beam • beam tip attracted or repulsed by magnets
	Softening spring	
$K_3 < 0$	• electrostatic attraction between the moving mass and the fixed wall • large oscillation of a clamped-free beam	**Unstable system**

When $K_1 > 0$, the spring is said to be hardening if $K_3 > 0$ or softening if $K_3 < 0$. For the softening case, the range of validity of the equation is limited in amplitude, since the solution eventually becomes unstable. In practice, other non-linear effects, such as damping, typically limit the amplitude. When $K_1 < 0$, only the case where $K_3 > 0$ leads to stable solutions. This system is bistable due to the presence of a local maximum and two minimums that form two potential wells in the potential energy function. The response of the bistable system is strongly dependent on the level of energy input, because it can oscillate around either one or both of these stable positions.

A.1.3 Piecewise oscillator

The piecewise oscillator introduces a non-linear component by changing the slope (or even the shape) of the restoring force past a given amplitude. These oscillators are commonly used to model systems in which components make intermittent contact during a cycle, such as cantilever

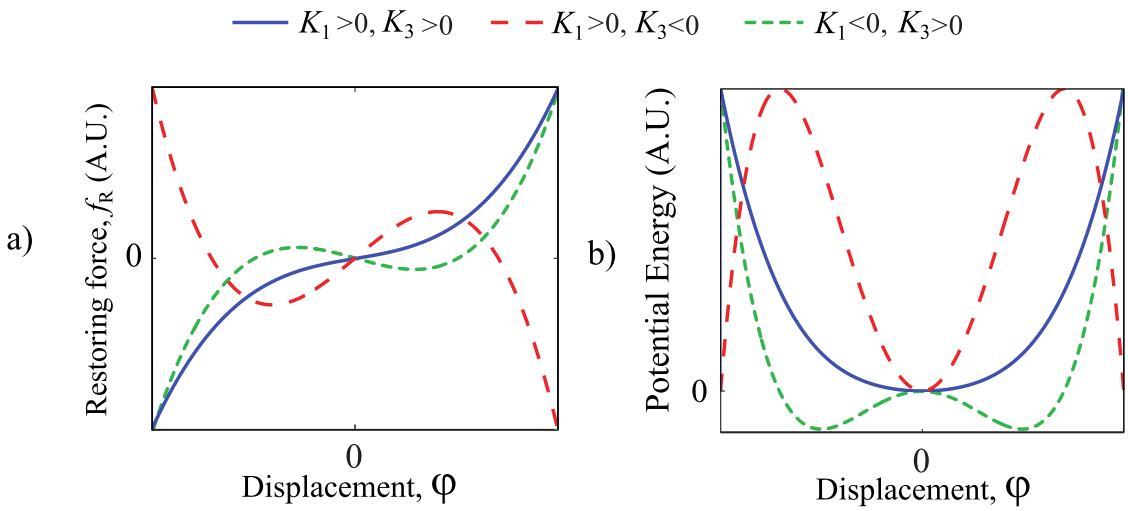

Figure A.1 Restoring force function (a) and potential energy function (b) for different types of Duffing oscillators.

beams hitting stoppers for instance. In this model, the restoring force slope increases with the stoppers stiffness and in the limit case of hard stopper surfaces, the system is an impact oscillator where the change of slope approaches infinity. Additionally, losses due to inelastic impact or incurred by the stopper may also be considered. Figure A.2 illustrates the restoring force and potential energy functions for a system with stoppers positioned symmetrically on both sides with the same linear stiffness, K_s.

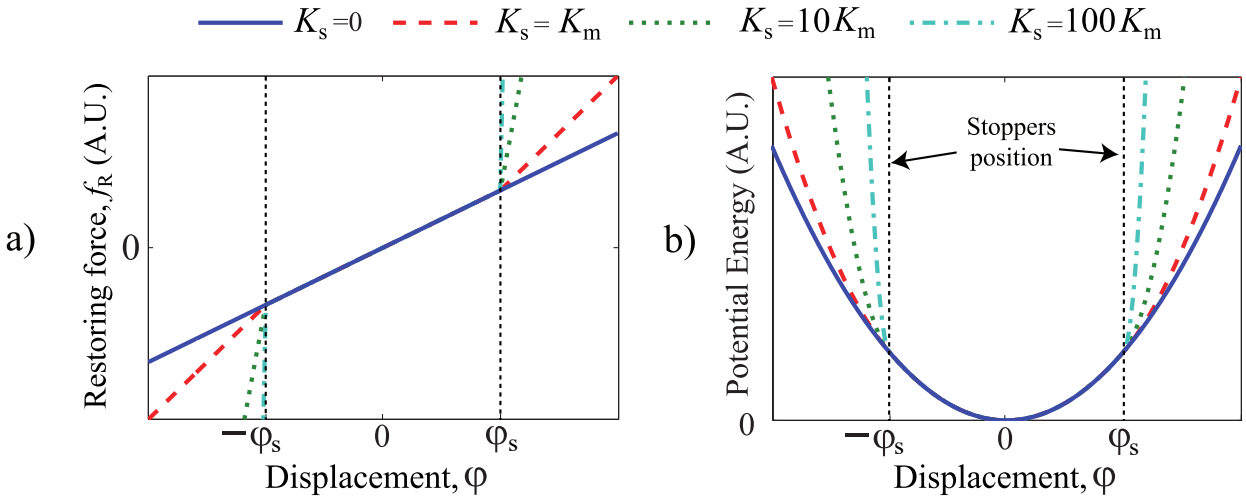

Figure A.2 Restoring force function (a) and potential energy function (b) for different piecewise oscillator. The stoppers are positioned at $\pm\varphi_s$ and have a linear behavior.

The equation of motion, assuming no loss is introduced by the impacts with the symmetrical stoppers, is given by Eq. A.4

$$M_{\mathrm{eq}}\ddot{\varphi}(t)+C_{\mathrm{m}}\dot{\varphi}(t)+f_{\mathrm{R}}(t)+\theta v(t)=f_{\mathrm{in}}, \tag{A.4}$$

where $f_R(t)$ is here defined as

$$f_{\mathrm{R}}(t)=\begin{cases} K_{\mathrm{m}}\varphi(t)+K_{\mathrm{s}}\left(\varphi(t)+\varphi_{\mathrm{s}}\right) & \text{if } \varphi\leq-\varphi_{\mathrm{s}} \\ K_{\mathrm{m}}\varphi(t) & \text{if } -\varphi_{\mathrm{s}}<\varphi<\varphi_{\mathrm{s}} \\ K_{\mathrm{m}}\varphi(t)+K_{\mathrm{s}}\left(\varphi(t)-\varphi_{\mathrm{s}}\right) & \text{if } \varphi\geq\varphi_{\mathrm{s}}, \end{cases} \tag{A.5}$$

and φ_{s} are the positions of the stoppers.

A.1.4 Parametric oscillator

The parametric oscillator is driven by the time variation of its energy storing parameters (*i.e.*, its mass or stiffness for a mechanical oscillator). A classical example is the swing set, where the moment of inertia of the system changes as the person moves at a given frequency to drive the oscillations. Parametric oscillation may also occur when the applied force leads to time varying modification of its stiffness, such as in the case of a vertically excited pendulum or a cantilevered beam with a time varying load along its longitudinal axis [28, 97, 98]. This type of oscillation has also been observed in elliptical and circular membranes [96]. Mathematically, a parametric oscillator with an axial loading term is represented by:

$$\ddot{\varphi}(t)+2\zeta_{\mathrm{m}}\omega_n\dot{\varphi}(t)+\left[\omega_n^2+2\varepsilon\cos(\omega t)\right]\varphi(t)=0,$$

where ε is the amplitude of the parametric excitation. Although this excitation is typically orthogonal to the oscillation axis, it is not necessarily exclusive to this direction. In this case, the right hand side of the motion equation would be different to 0.

Parametric resonance modes can be accessed when the driving frequency approaches values close to $\omega=2\omega_n/n$ (with n a positive integer representing the order of the parametric resonance mode), and ε is over a given activation threshold. When these conditions are met, the oscillator becomes unstable and even very small perturbations in the perpendicular direction to the parametric excitation are sufficient to start parametric resonance. The activation thresholds can be reduced by minimizing damping, which allows to observe several parametric modes [96].

A.1.5 Van der Pol oscillator and other limit cycle oscillators

The Van der Pol oscillator exhibit a specific kind of nonlinear damping. Its dynamic is governed by a second order differential equation of the form

$$\ddot{\varphi}(t)-\varepsilon\left(1-\varphi^2(t)\right)\dot{\varphi}(t)+\varphi(t)=0,$$

where $\varepsilon > 0$ is a system parameter. At low amplitudes, this oscillator has negative damping which becomes positive for larger amplitudes of oscillation ($\varphi^2(t) > 1$). In effect, this make the system unstable close to $\varphi = 0$, but eventually stable due to the increasing non-linear damping at larger amplitudes. This type of oscillation is frequently referred to as Limit Cycle Oscillation (LCO). The Van der Pol oscillator is typically found in electrical circuits involving operational amplification with positive feedback loops. However, there are some examples of mechanical systems, such as oscillations induced by aeroelastic flutter (the cause of the famous failure of the Tacoma bridge) or stick-slip friction. More recently, another type of LCO has been demonstrated in microscale mechanical resonators. A spontaneous oscillations was induced by adding a piezoresistive actuator driven by a DC current [161, 167]. The actuator effectively acts as a thermal energy pump which can boost the amplitude of oscillations. Although this mechanism could be applied to an inertial device to boost its sensitivity to vibrations, the power consumption and inefficiency of actuation makes it unattractive for vibration energy harvesting. To provide added value, thermal actuation would have to be introduced with zero additional energy cost.

A.2 Forced oscillation responses

This section looks at the frequency response and output power of the different types of oscillator for several typical excitation situations, namely monochromatic, broadband white noise and limited band white noise excitations. A representation of the single sided power spectral density of each acceleration source is presented in Fig. A.3. A colored noise resulting from a second order system is also depicted.

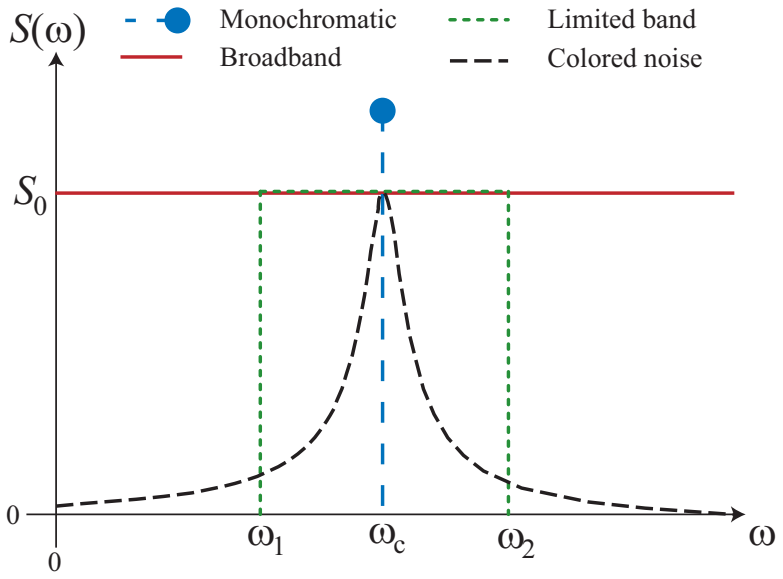

Figure A.3 Power spectral density (PSD) of different types of excitation

The monochromatic excitation is the typical sinusoidal input and represents an extreme case of narrow band process. It is commonly produced by unbalanced rotating machinery for example. The other extreme is the broadband white noise source, which has an infinite bandwidth. Although it doesn't exist in reality, the broadband white noise source is adequate when the source bandwidth is much larger than the dynamic system's bandwidth. The limited band white noise is

more representative of realistic sources where the excitation is mostly random. White noises can be produced by uncorrelated impacts and shocks for instance. Finally, the colored noise is another finite bandwidth source, although the term loosely applies to any sources where the energy is concentrated around dominant frequencies. For example, a colored noise can be generated by subjecting a second order system to a white noise, hence "coloring" the broadband noise based on the second order system characteristics.

A.2.1 Response to monochromatic excitation

The response to a single harmonic excitation is presented here for the Duffing and piecewise nonlinear oscillators. Please refer to section 2.3 for the case of the linear oscillator. The forcing term for a monochromatic base acceleration excitation is of the form

$$f_{\text{in}}(t) = M_{\text{eq}}|A|\sin(\omega_{\text{c}}t),$$

with $|A|$ the amplitude of the base acceleration and ω_{c} the frequency of the source (center frequency). In term of power spectral density [1], it can be defined as an extreme case of a narrow band process with zero bandwidth, which is expressed by

$$S(\omega) = \frac{|A|^2}{2}\delta(\omega - \omega_{\text{c}}),$$

where $\delta(\omega - \omega_{\text{c}})$ is the delta-dirac function applied at the source frequency ω_{c}. Note that for the remainder of this section, the source frequency will however be referred by an arbitrary frequency ω for simplicity.

Duffing oscillator

An approximate analytical solution for the steady-state response of the Duffing oscillator can be obtained using the harmonic balance method. In this approach, we consider that the response of the nonlinear coupled vibration problem can be expressed as converging sums of N harmonics. This method is presented in [193] for the specific case of nonlinear energy harvesters and a full mathematical development is also presented in appendix B.1. This development shows that the effect of the piezoelectric force can still be viewed as a combination of an electrical stiffness, K_{el}, and electrical damping C_{el}, and follows the same equation as in the linear case. The implicit expression of the squared amplitude of the displacement, φ_0^2, is given as,

$$\varphi_0^2 = \frac{M_{\text{eq}}^2|A|^2}{\left[K_1 + K_3\left(\frac{3}{4}\varphi_0^2 + 3b_0^2\right) + K_{\text{el}} - \omega^2 M_{\text{eq}}\right]^2 + \omega^2\left(C_{\text{m}} + C_{\text{el}}\right)^2}, \tag{A.6}$$

with the amplitude term found on both sides of the equation. Contrary to the linear system, it is not possible to normalize the amplitude by the input force to scale the response accordingly.

1. Single sided convention

The impact of the non-linearity becomes more pronounced with the increase of the input force and it directly affects the dynamic behavior of the oscillator. To obtain a closed form solution, the terms must be reorganized to find the roots of a polynomial equation of φ_0 of the 6th order with coefficients functions of the frequency. In addition, there are two solutions for b_0 (see equation B.14), with one that also depends on the amplitude.

$$b_0 = 0 \tag{A.7}$$

$$b_0 = \sqrt{-\left(\frac{K_1}{K_3} + \frac{3}{2}\varphi_0^2\right)} \tag{A.8}$$

The first solution is valid for all types of Duffing oscillator. In the bistable case however, it corresponds to the local maximum of the potential energy function. This solution is unstable if the amplitude of oscillation is small and applies only for large oscillations that steadily cross over from one well to the other. This behavior is called interwell oscillations. The second solution gives a real positive value only if $K_1 < 0$ and $\varphi_0^2 < -\frac{2}{3}\frac{K_1}{K_3}$. Thus, it is only applicable to the bistable oscillator and it corresponds to the level of oscillation under which the mass is trapped in a single potential well. In other words, it marks the transition from intrawell to interwell motion.

For the case of the stiffening and softening systems, $b_0^2 = 0$ and the polynomial equation is

$$\varphi_0^6\left(\frac{9}{16}K_3^2\right) + \varphi_0^4\left[\frac{3}{2}K_3\left(K_1 + K_{\text{el}} - \omega^2\right)\right] + \varphi_0^2\left[\left(K_1 + K_{\text{el}} - \omega^2 M_{\text{eq}}\right)^2 + \omega^2 M_{\text{eq}}\left(C_{\text{m}} + C_{\text{el}}\right)^2\right] - M_{\text{eq}}^2|A|^2 = 0. \tag{A.9}$$

Equation A.9 therefore leads to six possible solutions, but only those which are real are meaningful. Figure A.4 shows the multiple potential solution as a hysteretic behavior in the frequency response function. In the stiffening case, a frequency increasing chirp signal attracts the oscillator towards the high amplitude state, but the amplitude drops abruptly past a certain frequency. This occurs because the resonant frequency shifts in the same direction as the shift of frequency of the source excitation when the oscillator enters resonance. However, the system remains in the low amplitude state for a decreasing frequency chirp signal since the shifts are now in opposite directions. A sudden jump to the higher energy state may occur as the oscillator gets closer to resonance, but only if the input force amplitude is large enough to introduce a saddle point. Meanwhile, the response for the softening spring follows the opposite trends. Hence, these two states correspond to two of the real solutions and the third real solution, which is unstable, corresponds to a transient state between the high energy and low energy state.

For the case of the bistable system, it was shown that b_0^2 can take one of two values depending on the level of φ_0^2. The impact of this term is therefore critical to analyze the behavior of the

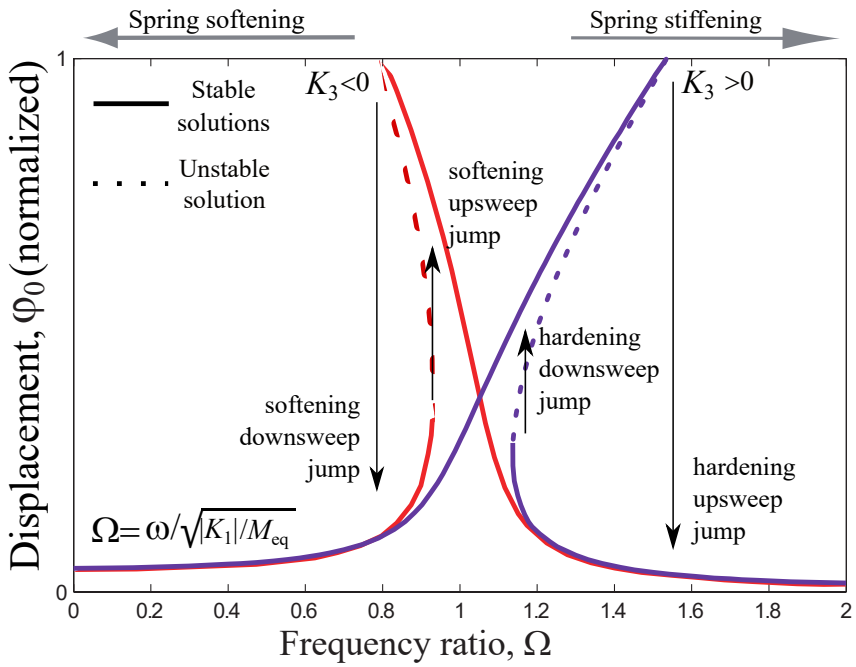

Figure A.4 Approximate frequency response functions for monostable oscillators with a stiffening or softening spring. Each curved is normalized by its maximum value.

system. For low level excitations, the response is around one of two stable positions. Replacing b_0^2 by its corresponding value from equation A.8, equation A.6 becomes

$$\varphi_0^2 = \frac{M_{eq}^2 |A|^2}{\left[-2K_1 - \frac{15}{4}K_3\varphi_0^2 + K_{el} - \omega^2 M_{eq}\right]^2 + \omega^2 \left(C_m + C_{el}\right)^2}. \tag{A.10}$$

Expression A.10 reveals that inside the potential well, the oscillator has a softening behavior due to the negative sign in front of the nonlinear stiffness term. Rearranging the terms, the polynomial equation is now instead

$$\varphi_0^6 \left(\frac{225}{16}K_3^2\right) - \varphi_0^4 \left[\frac{15}{2}K_3\left(-2K_1 + K_{el} - \omega^2 M_{eq}\right)\right] + \varphi_0^2 \left[\left(-2K_1 + K_{el} - \omega^2 M_{eq}\right)^2 + \omega^2 (C_m + C_{el})^2\right] - M_{eq}^2 |A|^2 = 0. \tag{A.11}$$

An increase of the excitation eventually leads to transitions between the wells. At a moderate energy level, these transitions occur on an intermittent basis and cause transient interwell oscillations as well as chaotic behavior. This behavior is not well represented by this model.

For even larger energy levels, interwell oscillations become periodic and part of the steady state response of the system. The motion of the oscillator is maintained in a large orbit and the oscil-

lations are centered around $b_0 = 0$. In this case, the solution is again provided by equation A.9 but keep in mind that K_1 now has a negative value. Additionally, this solution is valid only at the condition that φ_0^2 is over the interwell oscillation threshold of $-\frac{2}{3}\frac{K_1}{K_3}$. In the high orbit regime, the oscillator rather has a hardening behavior.

Figure A.5 presents a typical frequency response function for a bistable system which exhibits a transition from the low orbit to the high orbit oscillation regime. The response shows 3 unstable solutions (the red, cyan and green dashed curves). For a forward frequency sweep, the oscillator suddenly goes from the low orbit solution (solid orange curve) to the high orbit solution (solid blue curve) as the frequency ratio increases. The oscillator then exhibits an hardening behavior in the high orbit regime. Over a given frequency, the oscillator suddenly drops back to the low orbit regime. For a backward frequency sweep, the oscillator rather has a softening behavior (shown by the pink dotted curve) as the frequency ratio approaches 1. When the amplitude increases close to resonance and becomes greater than the interwell transition threshold, the oscillator enters the high orbit regime.

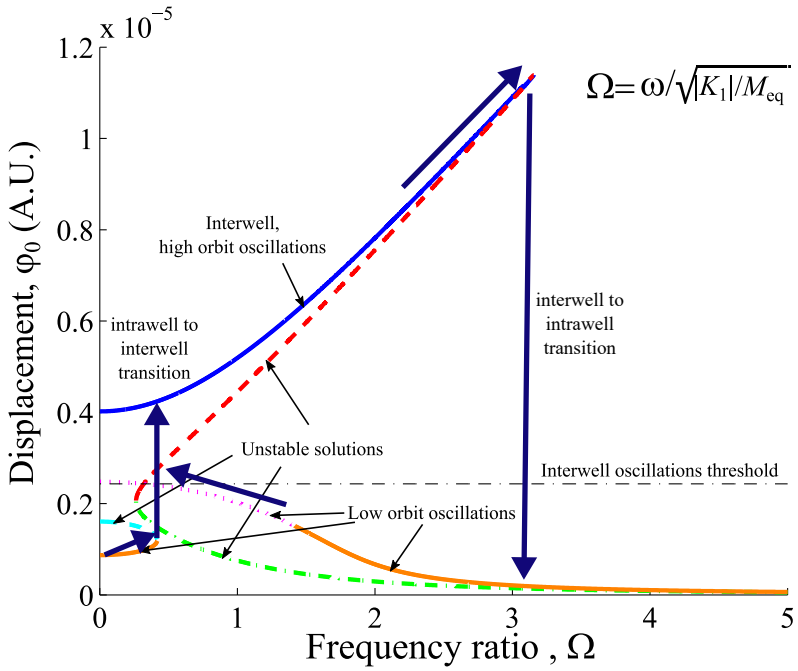

Figure A.5 Approximate frequency response functions for a bistable oscillator exhibiting large orbit transition.

Piecewise oscillator

An approximative analytical solution for the piecewise oscillator is similarly obtained via the equivalent linearization method. The basis for this approach is to replace the nonlinear restoring force by an equivalent linear force that minimizes the error. By the end, an equivalent stiffness term, $\bar{K}$, is found. The full development for this approach is presented in appendix B.2.2. The analysis is based on several assumptions, namely that the deformation of bodies upon impact is negligible and that all collisions are elastic (no energy loss). Furthermore, it is assumed that

the stoppers have a negligible mass compared to their stiffness and the oscillator mass. The equivalent stiffness, $\bar{K}$, is given by

$$\bar{K} = \begin{cases} K_\mathrm{m} & \text{if } \frac{\varphi_0}{\varphi_\mathrm{s}} < 1 \\ K_\mathrm{m} + K_\mathrm{s}\left\{1 - \frac{2}{\pi}\left[\left(\frac{\varphi_0}{\varphi_\mathrm{s}}\right)^{-1}\sqrt{1-\left(\frac{\varphi_\mathrm{s}}{\varphi_0}\right)^{-2}} + \arcsin\left(\frac{\varphi_\mathrm{s}}{\varphi_0}\right)^{-1}\right]\right\} & \text{if } \frac{\varphi_0}{\varphi_\mathrm{s}}^{-1} \geq 1 \end{cases}. \tag{A.12}$$

Equation A.12 is plotted on figure A.6 and shows the effective stiffness is that of the linear system (K_m) for amplitude to gap ratio $\varphi_0/\varphi_\mathrm{s} < 1$, whereas it tends toward $K_\mathrm{m} + K_\mathrm{s}$ as the ratio increases. This is an intuitively sound result considering that at this point both springs are acting simultaneously for most of the traveling distance.

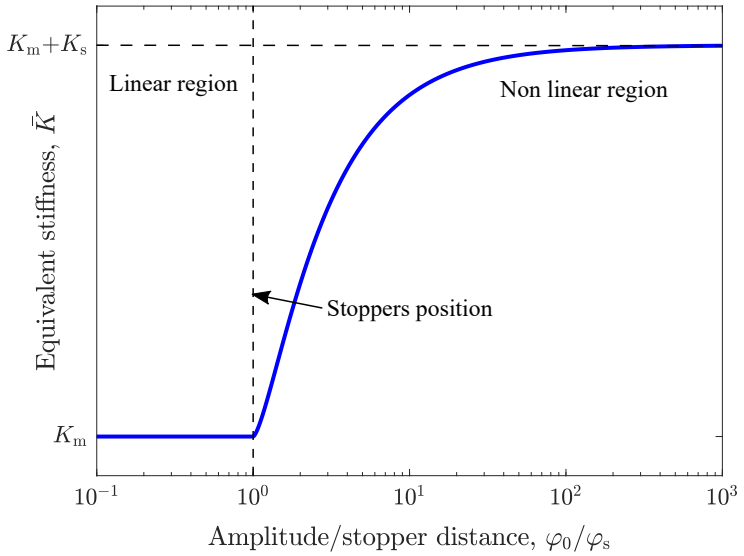

Figure A.6 Equivalent linear spring constant for a symmetrical piecewise oscillator as a function of the amplitude to gap ratio. As the amplitude grows, the stiffness of the system increases and tends to $K_\mathrm{m} + K_\mathrm{s}$.

Therefore, when the amplitude remains below φ_s, the solution is that of the linear oscillator, but for larger amplitudes, the effective spring constant is used into the frequency response function and yields

$$\varphi_0^2 = \frac{M_\mathrm{eq}^2 |A|^2}{\left[\bar{K} + K_\mathrm{el} - \omega^2\right]^2 + \omega^2 \left(C_\mathrm{m} + C_\mathrm{el}\right)^2}. \tag{A.13}$$

This implicit nonlinear equation can be solved numerically and, of all the possible roots, only the real positive values are valid solutions. Figure A.7 illustrates the typical spring stiffening behavior of a symmetric piecewise oscillator. As for the Duffing stiffening case, the natural frequency shifts towards higher frequencies when the excitation frequency is gradually increased, although the transition is more abrupt here. The magnitude of this shift, hence the achievable

bandwidth, is function of both the stoppers stiffness (as shown on Fig. A.7), but also the ratio of the applied force (due to its relationship to the resulting displacement) to the stoppers distance φ_s. As a result, the response of a system with rigid stoppers can significantly broaden the bandwidth. In this case however, the stable and unstable solutions become closer to one another, which suggests that the system stability can become sensitive to input force amplitude variations. Similarly, bandwidth broadening also occurs by reducing the stoppers distance, as this also produces an increased equivalent stiffness. Although the addition of stoppers can improve the device bandwidth, it comes at the expense of a limited maximum output power since the oscillation amplitudes are restricted. In this case, increasing the electrical damping could also improve the power output, but it would also reduce the bandwidth broadening effect originating from the nonlinear spring term.

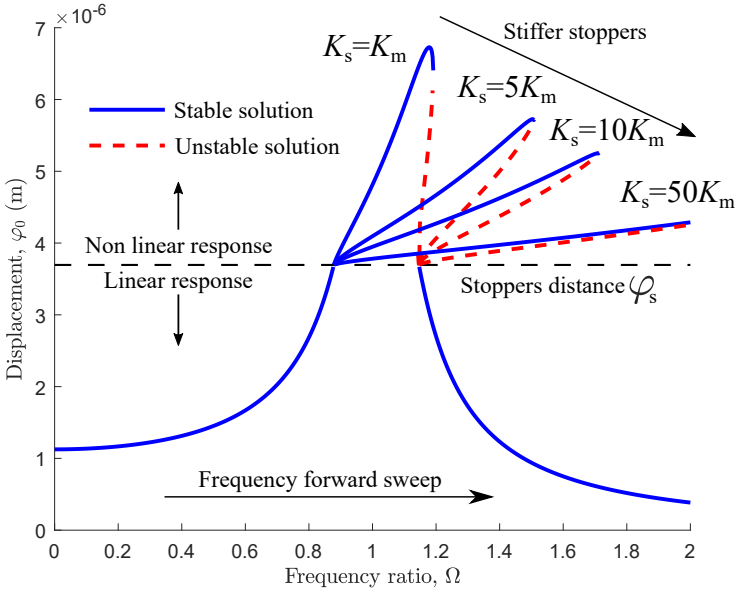

Figure A.7 Typical frequency responses for piecewise oscillators. On this figure, the stoppers positions are fixed and set to half the amplitude of the linear oscillator. Several stopper stiffnesses are shown, demonstrating the effect of this parameter on the frequency broadening behavior.

A.2.2 Response to broadband Gaussian white noise excitation

The forcing term is now assumed to be stationary, ergodic, random and broadband; it is represented by a Gaussian white noise process with zero mean and an autocorrelation function given by [104]:

$$\langle f_{in}(t) f_{in}(t+\tau)\rangle = M_{eq}^2 \langle a(t)a(t+\tau)\rangle = M_{eq}^2 \frac{S_0}{2}\delta(\tau), \tag{A.14}$$

where $\langle\rangle$ denotes an ensemble average (or expected value) over a long sampling time T, such that for any quantity x,

$$\langle x \rangle = \lim_{T \to \infty} \frac{1}{T} \int_0^T x(t) dt. \tag{A.15}$$

Meanwhile, $\delta(\tau)$ is the dirac delta function at a time lag τ and S_0 is the single sided power spectral density of the base acceleration $a(t)$ (expressed in $(\mathrm{m}^2/\mathrm{s}^4)\mathrm{Hz}^{-1}$). As shown on Fig. A.3, the single sided power spectral density of this source acceleration in the frequency domain is flat across the full spectrum and is therefore written as

$$S_{\mathrm{a}}(\omega) = S_0. \tag{A.16}$$

Stochastic calculus is generally used to evaluate the behavior of randomly excited systems. Their response are thus described statistically in terms of probability density functions (PDF), mean values, variances and covariances. The PDF provides the relative likelihood of one or more random variables (*e.g.*, the oscillator's displacement φ, velocity $\dot{\varphi}$ or voltage v) to fall on a given value. This representation will be used in this section to compare the response of the different systems. However, it is worth first discussing a general conclusion with respect to oscillators subject to broadband white noise.

General note on oscillators subject to white noise

Langley [113, 114] made the general demonstration that the power absorbed by any oscillator with a nonlinear restoring term and with multiple degrees of freedom is bounded by its total mass and the source noise power. The demonstration is briefly presented here for the SDOF system with electromechanical coupling. The equation of motion for such a system can be expressed as

$$M_{\mathrm{eq}} \ddot{\varphi} + g(\varphi, \dot{\varphi}, v) = -M_{\mathrm{eq}} a, \tag{A.17}$$

where $g(\varphi, \dot{\varphi}, v)$ is a general term which encompasses the restoring, damping and electromechanical forces, whereas a is the random vibration source. Multiplying Eq. A.17 by the mass velocity $\dot{\varphi}$ and taking the expected value yields the average absorbed power,

$$\langle P_{\mathrm{in}} \rangle = -\langle M_{\mathrm{eq}} a \dot{\varphi} \rangle = \langle M_{\mathrm{eq}} \ddot{\varphi} \dot{\varphi} \rangle + \langle \dot{\varphi} g(\varphi, \dot{\varphi}, v) \rangle. \tag{A.18}$$

As discussed in section 2.4, the input power is the upper bound on the harvestable power. The first term on the right hand side is equivalent to

$$\langle M_{\mathrm{eq}} \ddot{\varphi} \dot{\varphi} \rangle = \langle \frac{\mathrm{d}}{\mathrm{d}t} \left(\frac{1}{2} M_{\mathrm{eq}} \dot{\varphi}^2 \right) \rangle, \tag{A.19}$$

which is the average kinetic energy variation rate of the system and is zero for the stationary response. Therefore, Eq. A.18 simplifies to

$$\langle P_{\text{in}} \rangle = -\langle M_{\text{eq}} a \dot{\varphi} \rangle = \langle \dot{\varphi} g(\varphi, \dot{\varphi}, v) \rangle. \tag{A.20}$$

Moreover, direct time integration of the equation of motion A.17 yields,

$$\int_{-\infty}^{t} M_{\text{eq}} \ddot{\varphi}(\tau) \mathrm{d}\tau = M_{\text{eq}} \dot{\varphi}(t) = -\int_{-\infty}^{t} M_{\text{eq}} a(\tau) \mathrm{d}\tau - \int_{-\infty}^{t} g(\tau) \mathrm{d}\tau, \tag{A.21}$$

with g here explicitly expressed as a function of time. From A.20 and A.21, the absorbed power expression can now be developed as

$$\langle P_{\text{in}} \rangle = -\langle M_{\text{eq}} \dot{\varphi}(t) a(t) \rangle = \int_{-\infty}^{t} \langle M_{\text{eq}} a(\tau) a(t) \rangle \mathrm{d}\tau + \int_{-\infty}^{t} \langle g(\tau) a(t) \rangle \mathrm{d}\tau. \tag{A.22}$$

The first term of the right hand side represents the noise power, which is constant for a stationary process based on Eq. A.14. Meanwhile the second term is the expected value of the cross-correlation between the vibration input and the induced system response. This term is zero for random vibration, because future source events at time t are uncorrelated to the device past or present response at time τ. Hence, Eq. A.22 further simplifies to

$$\langle P_{\text{in}} \rangle = \frac{S_0 M_{\text{eq}}}{2} \int_{-\infty}^{t} \delta(t - \tau) \mathrm{d}\tau = \frac{S_0 M_{\text{eq}}}{4}, \tag{A.23}$$

which is the upper bound on the available power from white noise. Regardless of this result, it remains relevant to evaluate the systems' response statistics to get insight on their general behavior.

Linear oscillator

To find the statistics of the linear system, we first rearrange Eqs. A.1 and A.2 to express the time domain equations in the matricial state-space form as

$$\dot{\mathbf{X}} = \mathbf{A}\mathbf{X} + \mathbf{G}. \tag{A.24}$$

Here $\mathbf{X}$ is the state vector,

$$\mathbf{X} = \begin{Bmatrix} \varphi \\ \dot{\varphi} \\ v \end{Bmatrix} = \begin{Bmatrix} X_1 \\ X_2 \\ X_3 \end{Bmatrix}, \tag{A.25}$$

where X_1, X_2 and X_3 are used here to follow probability conventions to represent random variables using uppercase symbols. Meanwhile, $\mathbf{A}$ and $\mathbf{G}$ are the matrices containing the linear system parameters,

$$\mathbf{A} = \begin{bmatrix} 0 & 1 & 0 \\ -\omega_n^2 & -2\zeta_{\mathrm{m}}\omega_n & \frac{\theta}{M_{\mathrm{eq}}} \\ 0 & -\frac{\theta}{C_{\mathrm{p}}} & -\frac{1}{C_{\mathrm{p}}R_{\mathrm{eq}}} \end{bmatrix} \tag{A.26}$$

$$\mathbf{G}(t) = \begin{Bmatrix} 0 \\ \frac{f_{\mathrm{in}}(t)}{M_{\mathrm{eq}}} \\ 0 \end{Bmatrix}. \tag{A.27}$$

We now also define the vector $\tilde{\mathbf{x}}$ to express the potential observed values (or realizations) of the states X_1, X_2, X_3,

$$\tilde{\mathbf{x}} = \begin{Bmatrix} x_1 \\ x_2 \\ x_3 \end{Bmatrix}. \tag{A.28}$$

For the case of a stationary Gaussian white noise vibration, the covariance matrix, $\mathbf{C} = \langle \mathbf{X}\mathbf{X}^{\mathrm{T}} \rangle$, does not vary with time and satisfies the following matrix Lyapunov equation [113],

$$\mathbf{A}\mathbf{C} + \mathbf{C}\mathbf{A}^{\mathbf{T}} = -\mathbf{G}\mathbf{G}^{\mathrm{T}} = \begin{bmatrix} 0 & 0 & 0 \\ 0 & \frac{S_0}{2} & 0 \\ 0 & 0 & 0 \end{bmatrix}, \tag{A.29}$$

with

$$\mathbf{C} = \begin{bmatrix} \langle x_1^2 \rangle & \langle x_1 x_2 \rangle & \langle x_1 x_3 \rangle \\ \langle x_1 x_2 \rangle & \langle x_2^2 \rangle & \langle x_2 x_3 \rangle \\ \langle x_1 x_3 \rangle & \langle x_2 x_3 \rangle & \langle x_3^2 \rangle \end{bmatrix}. \tag{A.30}$$

The terms of this matrix are evaluated analytically. After substitution of the terms by their non dimensional forms (Eqs. 2.19, 2.20 and 2.22), the variances $\langle x_1^2 \rangle$, $\langle x_2^2 \rangle$ and $\langle x_3^2 \rangle$ are expressed as

$$\langle x_1^2 \rangle = \left(\frac{S_0}{4\omega_n^3} \right) \frac{1 + 2\alpha\zeta_{\mathrm{m}} + \alpha^2}{\kappa^2\alpha + 2\zeta_{\mathrm{m}} + 4\zeta_{\mathrm{m}}^2\alpha + 2\zeta_{\mathrm{m}}\alpha^2(1+\kappa^2)} \tag{A.31}$$

$$\langle x_2^2 \rangle = \left(\frac{S_0}{4\omega_n} \right) \frac{1 + 2\alpha\zeta_{\mathrm{m}} + \alpha^2 + \alpha^2\kappa^2}{\kappa^2\alpha + 2\zeta_{\mathrm{m}} + 4\zeta_{\mathrm{m}}^2\alpha + 2\zeta_{\mathrm{m}}\alpha^2(1+\kappa^2)} \tag{A.32}$$

$$\langle x_3^2 \rangle = \left(\frac{S_0\theta^2}{4\omega_n^3 C_{\mathrm{p}}^2} \right) \frac{\alpha^2}{\kappa^2\alpha + 2\zeta_{\mathrm{m}} + 4\zeta_{\mathrm{m}}^2\alpha + 2\zeta_{\mathrm{m}}\alpha^2(1+\kappa^2)} \tag{A.33}$$

with the covariances given as

$$\langle x_1 x_2 \rangle = 0 \tag{A.34}$$

$$\langle x_1 x_3 \rangle = -\left(\frac{S_0\theta}{4\omega_n^3 C_\mathrm{p}}\right)\frac{\alpha^2}{\kappa^2\alpha + 2\zeta_\mathrm{m} + 4\zeta_\mathrm{m}^2\alpha + 2\zeta_\mathrm{m}\alpha^2(1+\kappa^2)} \tag{A.35}$$

$$\langle x_2 x_3 \rangle = -\left(\frac{S_0\theta}{4\omega_n^2 C_\mathrm{p}}\right)\frac{\alpha}{\kappa^2\alpha + 2\zeta_\mathrm{m} + 4\zeta_\mathrm{m}^2\alpha + 2\zeta_\mathrm{m}\alpha^2(1+\kappa^2)} \tag{A.36}$$

Without surprise, $\langle x_1 x_3 \rangle$ and $\langle x_2 x_3 \rangle$ have non zero values, expressing coupling of the voltage with the displacement and velocity, as observed in the monochromatic case. The probability density function (PDF) of a linear system subject to Gaussian white noise is also a Gaussian distribution. For a multivariate normal PDF with zero means values,

$$PDF_{X_1X_2X_3}(\tilde{\mathbf{x}}) = A_0 \exp\left(-\frac{\chi^2}{2}\right), \tag{A.37}$$

where A_0 is a normalization constant (used so that the integral of the PDF will give an overall probability of 1) and χ^2 is a scalar calculated from the product

$$\chi^2 = \tilde{\mathbf{x}}^T \mathbf{C}^{-1} \tilde{\mathbf{x}}. \tag{A.38}$$

The value of χ^2 is given by

$$\chi^2 = C_{11}x_1^2 + C_{22}x_2^2 + C_{33}x_3^2 + C_{12}x_1x_2 + C_{13}x_1x_3 + C_{23}x_2x_3 \tag{A.39}$$

where

$$C_{11} = \frac{2\omega_n^3\left(2\zeta_\mathrm{m} + \alpha + \alpha\kappa^2\right)}{S_0} \tag{A.40}$$

$$C_{22} = \frac{2\omega_n\left(1 + 2\zeta_\mathrm{m}\alpha\right)}{S_0\alpha} \tag{A.41}$$

$$C_{33} = \frac{2C_\mathrm{p}^2\omega_n^3}{S_0\theta^2}\frac{\left(1 + 2\zeta_\mathrm{m}\alpha + \alpha^2\right)\left(1 + 2\zeta_\mathrm{m}\alpha + \alpha^2 + \alpha^2\kappa^2\right)}{\alpha^3} \tag{A.42}$$

$$C_{12} = \frac{4\omega_n^2}{S_0} \tag{A.43}$$

$$C_{13} = \frac{4C_\mathrm{p}\omega_n^3\left(1 + 2\zeta_\mathrm{m}\alpha + \alpha^2 + \alpha^2\kappa^2\right)}{S_0\theta\alpha} \tag{A.44}$$

$$C_{23} = \frac{4C_\mathrm{p}\omega_n^2\left(1 + 2\zeta_\mathrm{m}\alpha + \alpha^2\right)}{S_0\theta\alpha^2}. \tag{A.45}$$

Based on Eqs. A.40 to A.45, the states are not orthogonal (*i.e.*, not independent) since C_{12}, C_{13}, C_{23} and the covariances are not zero. In this case,

$$PDF_{X_1X_2X_3}(x_1,x_2,x_3) \neq PDF_{X_1}(x_1)PDF_{X_2}(x_2)PDF_{X_3}(x_3) \tag{A.46}$$

Computing the correlation coefficients thus gives

$$r_{x_1x_2} = \frac{\langle x_1x_2\rangle}{\sqrt{\langle x_1^2\rangle\langle x_2^2\rangle}} = 0, \tag{A.47}$$

$$r_{x_1x_3} = \frac{\langle x_1x_3\rangle}{\sqrt{\langle x_1^2\rangle\langle x_3^2\rangle}} = \frac{\alpha}{\sqrt{\alpha^2+2\zeta_m\alpha+1}}, \tag{A.48}$$

$$r_{x_2x_3} = \frac{\langle x_2x_3\rangle}{\sqrt{\langle x_2^2\rangle\langle x_3^2\rangle}} = \frac{1}{\sqrt{\alpha^2+\alpha^2\kappa^2+2\zeta_m\alpha+1}}. \tag{A.49}$$

Equation A.47 suggests the displacement and velocity are not correlated, because it is always zero. This result rests on the fact that these states are orthogonal. However, Eqs.A.48 and A.49 demonstrate that the voltage is correlated to the other states. The degree of correlation depends on the electric load, like in the case of the monochromatic excitation, as shown on Fig. A.8.

For an open circuit ($\alpha \to \infty$), $r^2_{x_1x_3} = 1$ and $r^2_{x_2x_3} = 0$, which means that the voltage has a direct linear relationship to the displacement. Inversely, a short-circuit ($\alpha \to 0$) gives $r^2_{x_1x_3} = 0$, whereas $r^2_{x_2x_3} = 1$. The voltage now instead has a direct linear correlation to the velocity. Both results are consistent with what is observed for the monochromatic case. However, it remains unclear if the voltage can still be seen as a linear combination of components for other intermediate electrical loading scenarios. We therefore compute the multiple correlation coefficient, given as

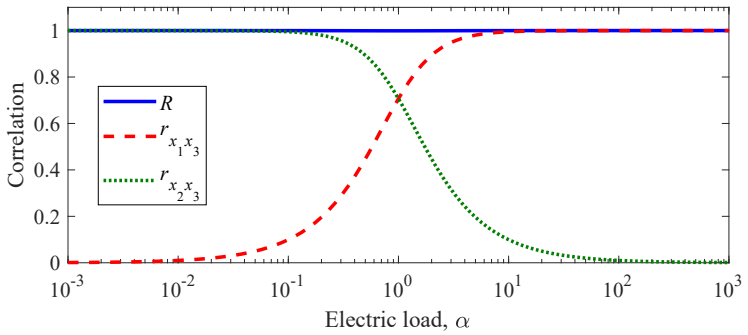

Figure A.8 Variation of the correlation coefficients between the displacement X_1, velocity X_2 and voltage states X_3 with respect to the electric load α. Here, $\kappa^2 = 0.0001$ and $\zeta_m = 0.001$.

$$R^2 = \frac{r_{x_1x_3}^2 + r_{x_2x_3}^2}{1 - r_{x_1x_2}^2}, \tag{A.50}$$

to verify this assumption. Although Eq. A.50 has a minimal value for $\alpha \to 1$, which varies with the mechanical damping ζ_m and coupling κ^2, Fig. A.8 shows that the correlation coefficient remains very close to 1 at any load α. Hence, the voltage can be simultaneously correlated to both the displacement and the velocity, which again reflects what was previously found for the harmonic excitation. Based on this result, it appears again possible to represent the effect of piezoelectric coupling with equivalent stiffness and damping terms.

To evaluate these terms, we start by computing the joint marginal probability density function $PDF_{X_1X_2}$,

$$PDF_{X_1X_2} = \int_{-\infty}^{\infty} PDF_{X_1X_2X_3} \mathrm{d}x_3, \tag{A.51}$$

$$= A_0^* \exp\left[-\frac{1}{2}\left(C_{11}^* x_1^2 + C_{22}^* x_2^2 + C_{12}^* x_1 x_2\right)\right], \tag{A.52}$$

where

$$A_0^* = A_0 \sqrt{\frac{2\pi}{C_{33}}}, \tag{A.53}$$

$$C_{11}^* = C_{11} - \frac{C_{13}^2}{4C_{33}}, \tag{A.54}$$

$$C_{22}^* = C_{22} - \frac{C_{23}^2}{4C_{33}}, \tag{A.55}$$

$$C_{12}^* = C_{12} - \frac{C_{13}C_{23}}{2C_{33}}. \tag{A.56}$$

The coefficients C_{11}^*, C_{22}^* and C_{12}^* can be expressed explicitly as

$$C_{11}^* = \frac{2\omega_n^3}{S_0} \frac{2\zeta_\mathrm{m} + 2\alpha^2\zeta_\mathrm{m} + 4\alpha\zeta_\mathrm{m}^2 + \alpha\kappa^2 + 2\alpha^2\kappa^2\zeta_\mathrm{m}}{\alpha^2 + 1 + 2\zeta_\mathrm{m}\alpha}, \tag{A.57}$$

$$C_{22}^* = \frac{2\omega_n}{S_0} \frac{2\zeta_\mathrm{m} + 2\alpha^2\zeta_\mathrm{m} + 4\alpha\zeta_\mathrm{m}^2 + \alpha\kappa^2 + 2\alpha^2\kappa^2\zeta_\mathrm{m}}{2\alpha\zeta_\mathrm{m} + \alpha^2\kappa^2 + \alpha^2 + 1},$$

$$= \frac{\omega_n}{S_0}\left[2\zeta_\mathrm{m} + \frac{\alpha\kappa^2}{2\alpha\zeta_\mathrm{m} + \alpha^2\kappa^2 + \alpha^2 + 1}\right]. \tag{A.58}$$

$$C_{12}^* = 0 \tag{A.59}$$

Note that C_{12}^* yields zero, again expressing that X_1 and X_2 are orthogonal states. Rearranging Eq. A.52, we can now express the PDF of the coupled linear system by again using equivalent electrical stiffness $\Delta\Omega_{\text{el}}^2$ and damping ζ_{el} terms.

$$\begin{aligned} PDF_{X_1X_2}(x_1,x_2) &= A_0^* \exp\left(-\frac{C_{22}^*}{2}\left(\frac{C_{11}^*}{C_{22}^*}x_1^2 + x_2^2\right)\right) \\ &= A_0^* \exp\left\{-\frac{2\omega_n}{S_0}\left(\zeta_{\text{m}}+\zeta_{\text{el}}\right)\left[\omega_n^2\left(1+\Delta\Omega_{\text{el}}^2\right)x_1^2 + x_2^2\right]\right\}, \end{aligned} \tag{A.60}$$

where

$$\Delta\Omega_{\text{el}}^2 = \frac{\alpha^2\kappa^2}{1+\alpha^2+2\zeta_{\text{m}}\alpha}, \tag{A.61}$$

$$\zeta_{\text{el}} = \frac{\alpha\kappa^2}{2\left(1+\alpha^2+\alpha^2\kappa^2+2\zeta_{\text{m}}\alpha\right)}. \tag{A.62}$$

The power output of the harvester is next obtained from $\bar{P}_{\text{el}} = \langle x_3^2\rangle / R_{\text{eq}}$, which based on Eq. A.33 gives

$$\bar{P}_{\text{el}} = \left(\frac{M_{\text{eq}}S_0}{4}\right)\frac{\kappa^2\alpha}{\kappa^2\alpha+2\zeta_{\text{m}}+4\zeta_{\text{m}}^2\alpha+2\zeta_{\text{m}}\alpha^2(1+\kappa^2)}. \tag{A.63}$$

The optimal electrical power, obtained for $\alpha = 1/\sqrt{1+\kappa^2}$, is given by

$$\bar{P}_{\text{el}}|_{\max} = \left(\frac{M_{\text{eq}}S_0}{4}\right)\frac{\kappa^2}{\kappa^2+4\zeta_{\text{m}}\sqrt{1+\kappa^2}+4\zeta_{\text{m}}^2} \tag{A.64}$$

Similarly, the mechanical power dissipated by the system can be obtained by $\bar{P}_{\text{m}} = C_{\text{m}}\langle x_2^2\rangle$, which based on Eq. A.32 gives

$$\bar{P}_{\text{m}} = \left(\frac{M_{\text{eq}}S_0}{4}\right)\frac{2\zeta_{\text{m}}\left(1+2\zeta_{\text{m}}\alpha+\alpha^2+\alpha^2\kappa^2\right)}{\kappa^2\alpha+2\zeta_{\text{m}}+4\zeta_{\text{m}}^2\alpha+2\zeta_{\text{m}}\alpha^2(1+\kappa^2)}. \tag{A.65}$$

Both power expressions are finally validated by computing the total power absorbed by the system, $\bar{P}_{\text{in}} = \bar{P}_{\text{m}} + \bar{P}_{\text{el}}$,

$$\begin{aligned}\bar{P}_{\text{in}} &= \left(\frac{M_{\text{eq}}S_0}{4}\right)\frac{\kappa^2\alpha+2\zeta_{\text{m}}+4\zeta_{\text{m}}^2\alpha+2\zeta_{\text{m}}\alpha^2(1+\kappa^2)}{\kappa^2\alpha+2\zeta_{\text{m}}+4\zeta_{\text{m}}^2\alpha+2\zeta_{\text{m}}\alpha^2(1+\kappa^2)},\\ &= \frac{M_{\text{eq}}S_0}{4}.\end{aligned} \tag{A.66}$$

Equation A.66 is consistent with the previous result presented by Eq. A.23, which demonstrated that the total power absorbed by any oscillator (linear or not) subject to white noise is only function of the power of the noise and the mass of the oscillator. As a result, the electrical power output only depends on the electrical efficiency of the system, η,

$$\eta = \frac{\bar{P}_{\text{el}}}{\bar{P}_{\text{in}}} = \frac{\kappa^2\alpha}{\kappa^2\alpha+2\zeta_{\text{m}}+4\zeta_{\text{m}}^2\alpha+2\zeta_{\text{m}}\alpha^2(1+\kappa^2)} = \frac{\zeta_{\text{el}}}{\zeta_{\text{m}}+\zeta_{\text{el}}}. \tag{A.67}$$

However, if we also consider size constraints and account for the mass travel, it is worth evaluating the ratio $\bar{P}_{\text{el}}/\langle x_1^2\rangle$,

$$\frac{\bar{P}_{\text{el}}}{\langle x_1^2\rangle} = \omega_n^3 M_{\text{eq}}\frac{\kappa^2\alpha}{1+\alpha^2+2\alpha\zeta_{\text{m}}}. \tag{A.68}$$

Equation A.68 is optimized for $\alpha = 1$, increases with the coupling factor κ^2 as well as the natural frequency ω_n (*i.e.*, stiffness), but decreases with the mechanical damping. In other words, for a given mass M_{eq}, noise power density S_0 and damping factor ζ_{m}, devices operating at higher frequencies can produce the same amount of power in a more compact volume when the source is wide band.

Nonlinear oscillators

The steady-state response of the mechanical Duffing and piecewise oscillators can be obtained analytically using the Fokker-Planck-Kolmogorov (FPK) equations. An exact analytical solution exists for these systems for which the nonlinearity is in the conservative term only [36]. The solution is given in the form of the joint probability density function of the displacement X_1 and velocity X_2,

$$PDF_{X_1,X_2}(x_1,x_2) = A_0\exp\left(\frac{-2C_{\text{m}}}{S_0M_{\text{eq}}^2}E_{\text{mech}}\right), \tag{A.69}$$

where E_{mech} is the total mechanical energy of the oscillator and is given by

$$E_{\text{mech}} = \int_0^{x_1} f_{\text{R}}(X_1)\text{d}X_1 + \frac{1}{2}M_{\text{eq}}x_2^2. \tag{A.70}$$

In Eq. A.70, $f_{\mathrm{R}}(X_1)$ is the nonlinear restoring force, which is function of the displacement $X_1 \equiv \varphi$ (for reference, this function can be found in Eq. A.3 for the Duffing systems, whereas it is provided by Eq. A.5 for the piecewise oscillator). It is worth noting that the states remain orthogonal regardless of the system considered. Figure A.9 presents contour plots of the PDFs for these different nonlinear oscillators compared to the linear system. Each contour marks an isoprobability level. From Eq. A.69, we can also infer that each contour relates to a constant stored energy level E_{mech}. Since E_{mech} is also constant at steady state when oscillators are subject to an harmonic excitation, these contours also relate to the phase portrait, which we discuss later in section A.3.1.

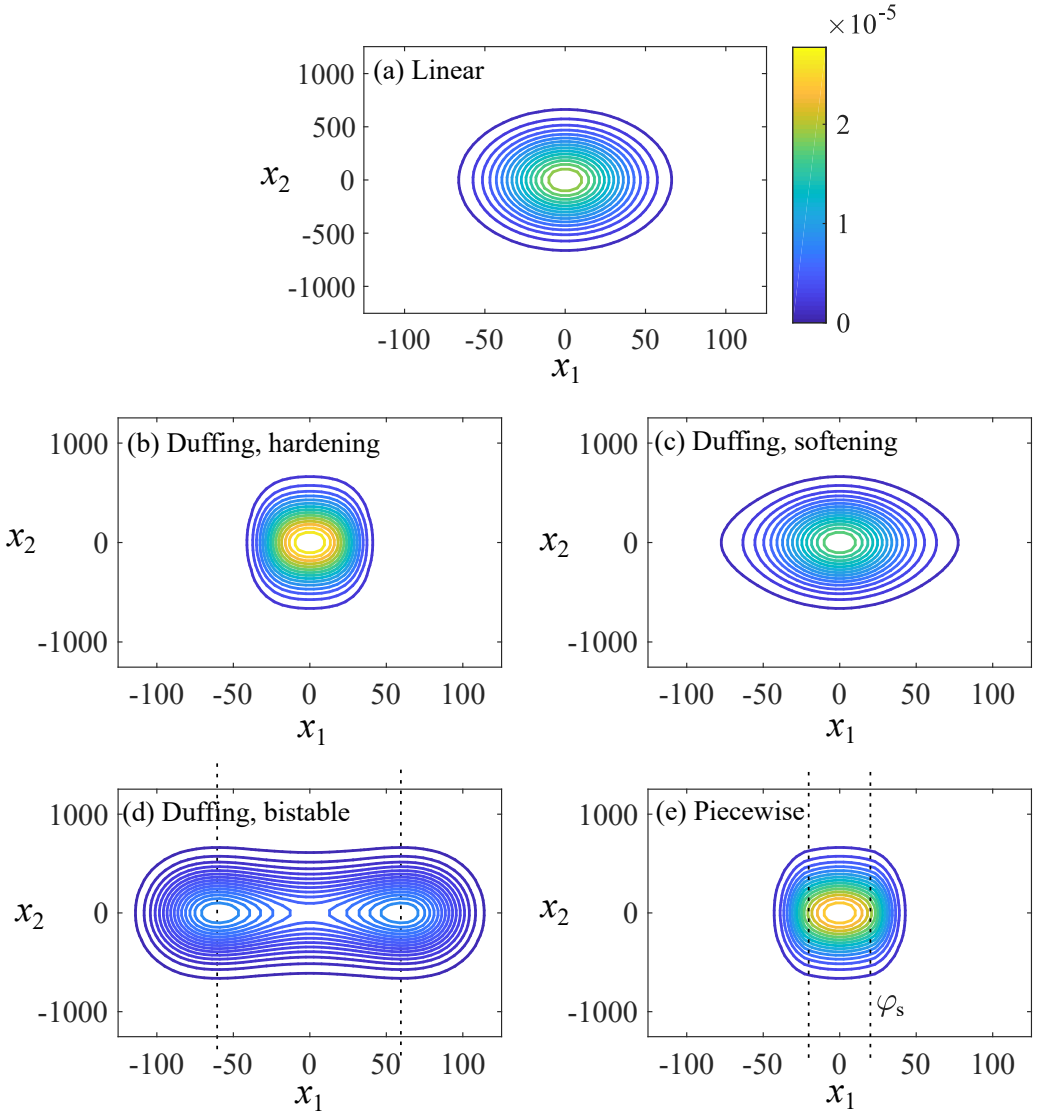

Figure A.9 PDF for different types of oscillator: (a) linear, (b) hardening spring, (c) softening spring, (d) bistable, (e) piecewise. The contours represent isoprobability levels.

The PDF of the linear system is a 2D Gaussian surface which presents elliptic orbits. For nonlinear systems, the distribution along x_1 is no longer Gaussian, although the distribution remains

normal and unchanged with respect to x_2. Therefore the non linearity has no impact on the absorbed or dissipated power compared to the linear system, since $\langle x_2^2 \rangle$ has not changed. However, the apparent frequency of oscillation of the system is very different and can be evaluated using Rice formula [165],

$$\frac{\langle \dot{x}^2 \rangle}{\langle x^2 \rangle} = \omega_{\text{eq}}^2. \tag{A.71}$$

A complete development for the nonlinear coupled system is out of the scope of this section, but we already know based on our previous developments for the linear coupled system that similar results are to be expected. Moreover, the power limit defined by Eq. A.23 still applies regardless of the system nonlinearities [113, 114]. Hence, there is no room for improving the power absorption capability from a broadband stationary noise by using these nonlinearities. Any observed increase in electrical power output is therefore caused by an improved electrical efficiency.

A.2.3 Response to band-limited white noise excitation

In this section, the forcing term is assumed to be a stationary, random, but band-limited noise; it is represented by a Gaussian white noise process with zero mean and the autocorrelation function:

$$\langle f_{\text{in}}(t) f_{\text{in}}(t+\tau) \rangle = \frac{S_0}{\pi \tau} (\sin \omega_2 \tau - \sin \omega_1 \tau). \tag{A.72}$$

Here, ω_1 and ω_2 designate the lower and upper frequencies of the band limited noise. As shown on figure A.3, the single sided power spectral density of this source acceleration is flat across the specified frequency band and is zero elsewhere. Therefore, its power spectral density can be written as

$$S_{\text{a}}(\omega) = \begin{cases} S_0 & \text{for } \omega_1 \leq \omega \leq \omega_2 \\ 0 & \text{for } \omega < \omega_1 \text{ and } \omega > \omega_2 \end{cases}. \tag{A.73}$$

In this section, we evaluate the power output of the coupled linear oscillator subject to this type of excitation. The nonlinear cases are not presented.

Linear oscillator

An exact analytical solution for the coupled oscillator is difficult to obtain because it would require the integration of a high order rational equation. We've seen however that its behavior is close to that of the mechanical linear oscillator. The following analysis will first focus on the equations for the uncoupled case and it will then be compared with numerical results for the electromechanically coupled oscillator.

The power dissipated by the mechanical oscillator is provided by $C_{\mathrm{m}}\langle \dot{x}^2 \rangle$ and from the Wiener-Khintchine theorem [164],

$$\bar{P}_{\mathrm{in}} = C_{\mathrm{m}} \int_0^{\infty} \omega^2 |\varphi(\omega)|^2 \mathrm{d}\omega. \tag{A.74}$$

Hence for the band limited white noise,

$$\bar{P}_{\mathrm{in}} = C_{\mathrm{m}} \int_{\omega_1}^{\omega_2} \omega^2 |\varphi(\omega)|^2 \mathrm{d}\omega. \tag{A.75}$$

Computing the indefinite integral of $\bar{P}_{\mathrm{in}}$ from the tables in [160],

$$\bar{P}_{\mathrm{in}} = \frac{M_{\mathrm{eq}} S_0}{4} \left[J(\Omega_2, \zeta_{\mathrm{m}}) - J(\Omega_1, \zeta_{\mathrm{m}}) \right], \tag{A.76}$$

where S_0 again expresses the single sided power spectral density in units of $(\mathrm{m}^2/\mathrm{s}^4)\mathrm{Hz}^{-1}$), whereas $\Omega = \omega/\omega_n$ is the frequency ratio and

$$J(\Omega, \zeta_{\mathrm{m}}) = \frac{1}{\pi} \arctan\left(\frac{2\zeta_{\mathrm{m}}\Omega}{1-\Omega^2} \right) - \frac{\zeta_{\mathrm{m}}}{2\pi\sqrt{1-\zeta_{\mathrm{m}}^2}} \ln\left[\frac{1+\Omega^2+2\sqrt{1-\zeta_{\mathrm{m}}^2}\Omega}{1+\Omega^2-2\sqrt{1-\zeta_{\mathrm{m}}^2}\Omega} \right]. \tag{A.77}$$

We can recognize the first term of Eq. A.76 as the power absorbed by a white noise. Meanwhile, $[J(\Omega_2, \zeta_{\mathrm{m}}) - J(\Omega_1, \zeta_{\mathrm{m}})]$ is a term ≤ 1 correcting for the fact that the noise is band limited between Ω_1 and Ω_2. Plotting this function in Fig. A.10 reveals that most of the energy variations occur close to the natural frequency, at $\Omega = 1$, and the rate of these variations depends on the damping factor ζ_{m}. Hence, for a fixed value of the source bandwidth $\Delta\Omega = \Omega_2 - \Omega_1$, J tends toward a value of 1 for smaller values of ζ_{m}

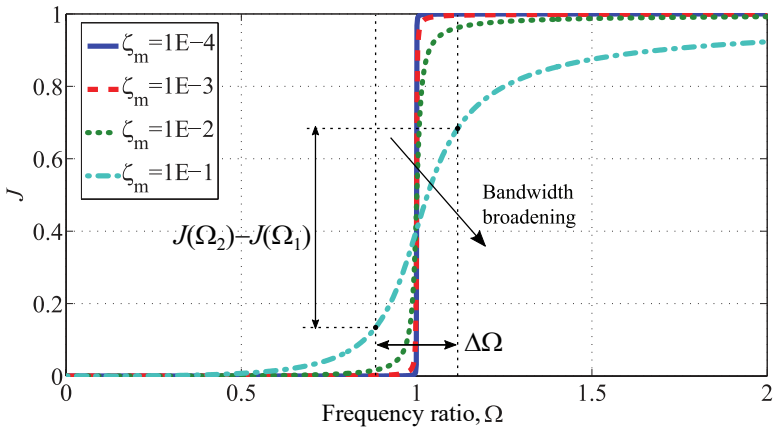

Figure A.10 Correction factor J on the band limited white noise power input with the frequency ratio Ω and mechanical damping ζ_{m}.

Figure A.11 is a log-log plot of the normalized absorbed power by the oscillator (compared to a white noise) as a function of the oscillator damping ζ_m and the noise bandwidth $\Delta\Omega$ with a noise centered at $\Omega = 1$. The isolines shown are parallel and correspond to specific ratios of $\frac{\Delta\Omega}{\zeta_m}$. Notice that the 50% valued isoline follows $\frac{\Delta\Omega}{\zeta_m} = 2$, which is the half-power bandwidth of a linear oscillator by definition, and it drops to 30% for $\frac{\Delta\Omega}{\zeta_m} = 1$. Therefore, the absorbed power is strictly function of the oscillator to source bandwidth ratio. Moreover, this graphic can be used to evaluate if the limited band noise can be approximated by a broadband white noise (95% absorbed power for $\frac{\Delta\Omega}{\zeta_m} \approx 10$), a monochromatic noise (5% absorbed power for $\frac{\Delta\Omega}{\zeta_m} \approx 0.15$) or something in between. Figure A.11 also applies to the electromechanical oscillator, except that ζ now is the total damping and the central frequency can be slightly shifted due to the electrical stiffness.

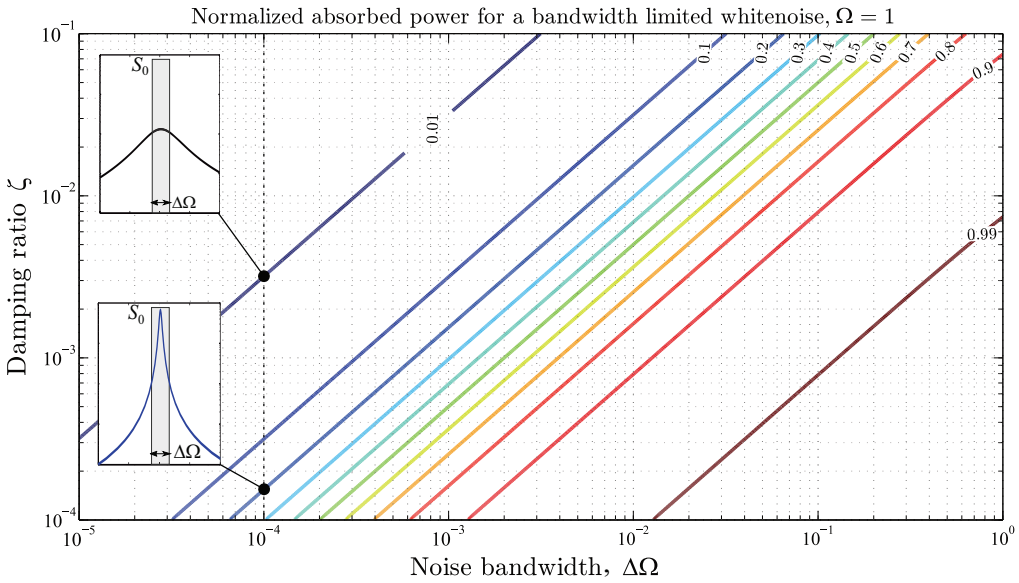

Figure A.11 Normalized absorbed power by a linear oscillator subject to band limited white noise centered at $\Omega = 1$.

For constant noise power S_0 and bandwidth $\Delta\Omega$, the coupled oscillator absorbs less power than the uncoupled one due to the response broadening from the electrical damping. However, the electrical power output increases up to a certain point due to the improved harvesting efficiency. Figure 2.15 plots the electrical power output (displayed as isocontours) normalized by the absorbed power from a white noise. For low bandwidths, we find that the optimal power is obtained when $\zeta_{el} \approx \zeta_m$, which corresponds to the monochromatic case. On the other hand, the electrical damping should be increased to take advantage of the improved harvesting efficiency when the source bandwidth increases significantly relatively to the device bandwidth. The optimal power output is essentially obtained from the ideal trade off between the efficiency and the absorbed power. Figure 2.15 shows that the trade off transition occurs between $1 \leq \frac{\Delta\Omega}{\zeta_m} \leq 10$. The optimal damping ratio then increases steadily with $\sqrt{\Delta\Omega}$. An approximate solution is derived graphically, assuming a solution of the form

$$\zeta_{\text{el}}|_{\text{opt}} \approx \zeta_{\text{m}} \left(\frac{2}{\sqrt{\Xi}} \sqrt{\frac{\Delta\Omega}{\zeta_{\text{m}}} + \Xi} - 1 \right), \tag{A.78}$$

where $\Xi = 5.2$ is a constant obtained by a least mean square fit.

A.3 Nonresonant architectures

As rapidly discussed in section 2.8.2, several nonresonant architectures have also been proposed over the years. Notable exemples include Renaud's free mass, impact based generator [170], Galchev's Parametric Frequency Increased Generator (PFIG) [75, 76], or Hosseinloo's latch based principle [84]. Each are respectively illustrated in Fig. A.12, A.13 and A.14. Other authors have also proposed numerous scrape-through/upconverting devices [85, 122], which essentially operate similarly to Renaud's concept, although the mass is sometimes attached to its own spring.

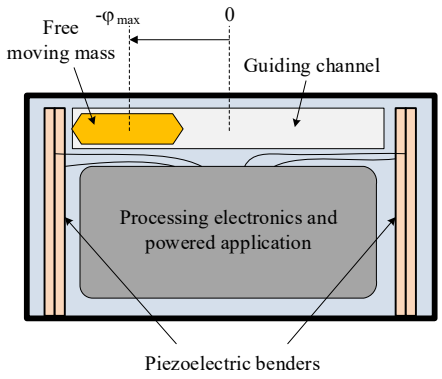

Figure A.12 Illustration of an free moving mass, impact based PFIG, adapted from Renaud *et al*. [170]

In this section, we first present useful tools to allow for general comparison of these architectures with other harvesters. These tools are first applied to define an ideal harvesting cycle and then to the linear oscillator to demonstrate their usage. We then present simplified models and equations for the impact and latch based architectures to extract their performance limits. Finally, we compare both of these nonresonant architectures to the ideal harvesting cycle and the linear oscillator.

A.3.1 Force-displacement and phase plane diagrams

The first important tool is the force-displacement diagram (or $f_{\text{in}} - \varphi$ diagram), which is equivalent to the pressure-volume diagram used to compare thermodynamic cycles. It is used to evaluate the ability of the architecture to harness power with respect to fundamental limits, such as mass, acceleration and space. By computing the area inside the cycle drawn on the $f_{\text{in}} - \varphi$ diagram and then dividing by the period, we can estimate the maximum absorbed power for

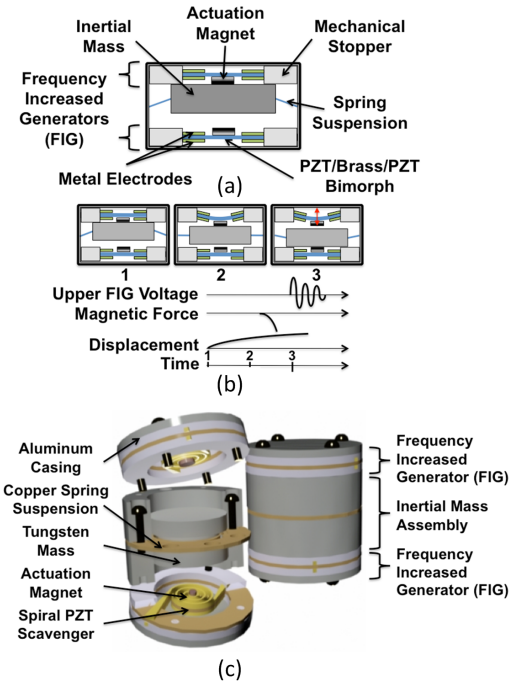

Figure A.13 Illustration of a PFIG based on passive magnetic latching mechanisms.(a) PFIG architecture cross section, (b) decomposition of the device operating stages, (c) an exploded view of the device. Adapted from Galchev *et al.* [75]

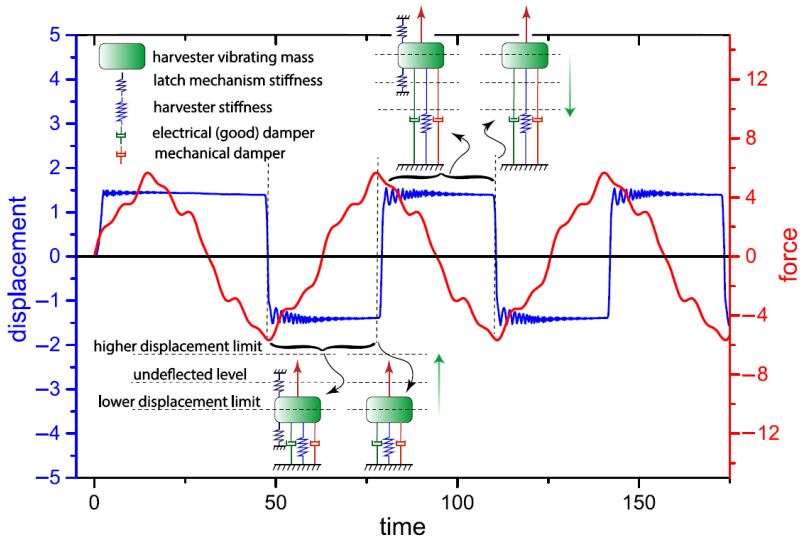

Figure A.14 Active latch assisted harvester principle. In this architecture, the latch mechanism release is synchronized with each force peak events. Source: [84]

specified bounds and thus the potential power harvesting capabilities, knowing that the link between these two values is the harvesting efficiency.

As illustrated on Fig. A.15(a), the ideal thermodynamic cycle draws a rectangular shape on the $f_{\text{in}} - \varphi$ diagram. For an allowed travel range of $2\varphi_{\max}$ and an arbitrary periodic input force that reaches a peak value of $f_{\text{in,max}}$ with a frequency $\omega = 2\pi/T$, the maximum average power thus cannot be greater than

$$\bar{P}_{\text{in,max}} = 4\varphi_{\max} f_{\text{in,max}}/T = \frac{2}{\pi}\omega\varphi_{\max} f_{\text{in,max}}. \tag{A.79}$$

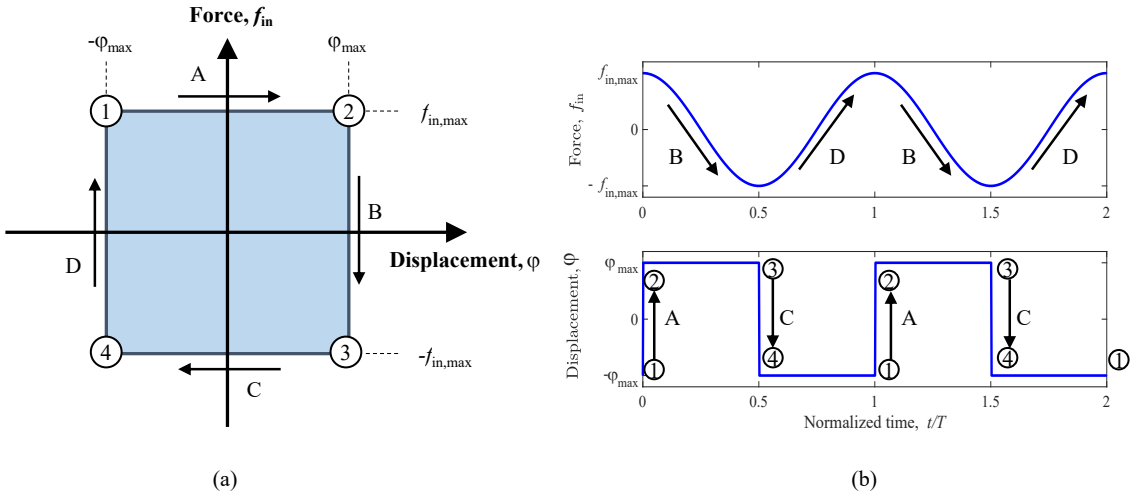

Figure A.15 Ideal harvester power cycle (a)$f_{\text{in}} - \varphi$ diagram and (b) associated force-displacement waveforms over 2 periods for an harmonic input force.

If the system is driven by an inertial harmonic force $f_{\text{in}}(t) = M_{\text{eq}}a(t)$, the ideal displacement waveform describes a square wave synchronized with each passing force peaks, as shown on Fig. A.15(b). Equation A.79 then becomes

$$\bar{P}_{\text{in,max}} = \frac{2}{\pi}M_{\text{eq}}\omega\varphi_{\max}|A|. \tag{A.80}$$

Another interesting tool is the phase plane diagram, which plots the position on the horizontal axis versus the velocity on the vertical axis. The shape of the phase portrait typically provides additional information on the nature of the system and often allows comparison between very different dynamics that may not be obvious otherwise. For the ideal cycle, the phase portrait has the same shape as the $f_{\text{in}} - \varphi$ diagram and is also rectangular. For reference, the linear harmonic oscillator phase portrait is characterized by an ellipse/circle. It is also worth noting the similarity of the phase portrait and the PDF contour plots presented in Fig. A.9(a). For the non-linear oscillators presented earlier, the contours presented in Fig. A.9(b)-(e) also give an idea of their respective phase portraits. As we will soon demonstrate, nonresonant systems behave differently and therefore draw different phase plane patterns.

A.3.2 Linear oscillator

The displacement of a linear harmonic oscillator driven at its resonance frequency produces a sinus waveform exactly out of phase with the driving force; the resulting $f_{\text{in}} - \varphi$ diagram is an ellipse (or circle if rescaled), as depicted on Fig. A.16.

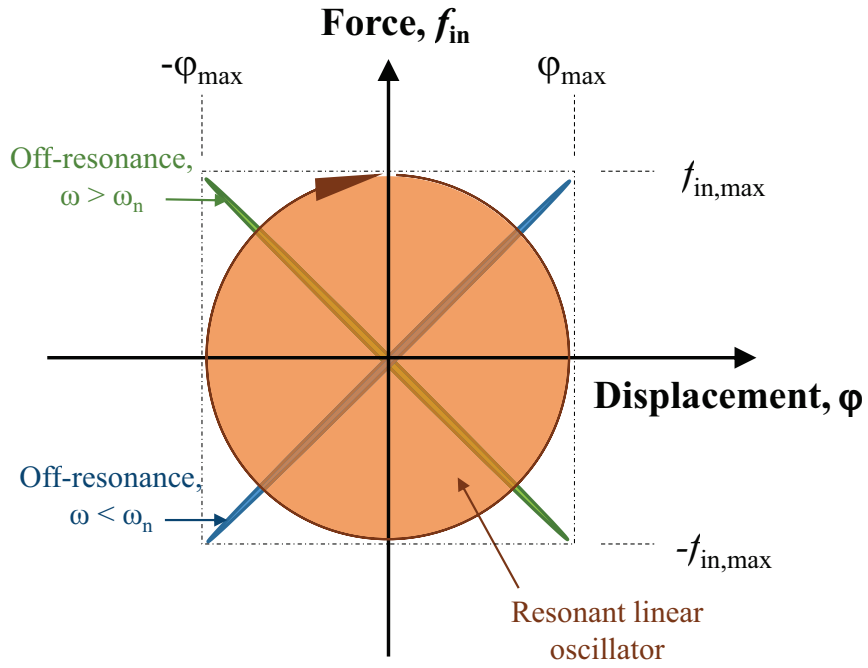

Figure A.16 Linear oscillator $f_{\text{in}} - \varphi$ diagram. At resonance, the diagram draws a circle, whereas narrow tilted ellipses are described for an off-resonance oscillator. The maximum displacement in all cases has been normalized by its max value for clarity.

Assuming the same frequency, maximum force and maximum displacement as for the ideal cycle, we obtain

$$\bar{P}_{\text{in,lin}} = \pi \varphi_{\text{max}} f_{\text{in,max}} / T = \frac{\omega \varphi_{\text{max}} M_{\text{eq}} |A|}{2}. \tag{A.81}$$

This result can be obtained geometrically, but is also consistent with what we obtain from the product of the mass velocity and force RMS values. It is the same results as provided by Eq. 2.61. By comparing Eqs. A.80 and A.81, and noting that the linear oscillator cycle draws a circle inscribed inside the square that represents the ideal cycle, we observe $\bar{P}_{\text{in,lin}}$ only differs by a ratio of $\pi/4$ (0.785) compared to $\bar{P}_{\text{in,max}}$. Hence, the linear oscillator is quite effective, although it must operate at resonance and with the right amplitude.

If the driving frequency is off resonance, and damping is small, the $f_{\text{in}} - \varphi$ diagram will morph toward a tilted ellipse and eventually take the shape of a line. In this case, the oscillator displacement is also much smaller. But even if it was not the case, the enclosed area in the $f_{\text{in}} - \varphi$ diagram would still be drastically reduced, because it would describe an overall conservative system which dissipates marginal power.

If damping is the dominant force in the linear system, the $f_{in} - \varphi$ diagram will describe a circular pattern, regardless of the frequency, but the amplitude will be smaller than for a weakly damped resonance mode. As briefly discussed in section 2.8.2, this is not an issue if the magnitude of the vibration source displacement is close to or superior to the space available. For this situation, the challenge is rather to provide enough damping.

A.3.3 Impact based harvester

Let's now consider an impact based harvester consisting of a free mass sliding along a channel, such as Renaud's device depicted in Fig. A.12. In this system, the mass is not physically attached to any springs; the springs are rather used as stoppers to collect the stored kinetic energy upon impact. Ideally, friction along the guiding channel is minimal to allow the mass to reach as much velocity upon impact with the stoppers. By doing so, the maximum amount of kinetic energy is transferred to the stopper and can be harvested in a perfectly inelastic collision. If the channel is too long, the inertial force will work against the mass and slow it down before impact and in the worst case, there is simply no impact. If instead the channel is too short, the mass will collide with the end stops without reaching its full velocity.

We now assume the harvester is driven by an harmonic acceleration $a(t)$. In this scenario, the mass starts at one of the end stopper and moves as soon as the force starts to push in the opposite stopper direction. The mass then hits the stopper and stays there until the sign of the force changes for the process to repeat itself in the opposite direction. This occurs twice by period, thus we can simply evaluate the energy captured over half a period and double the result to estimate the amount of power that can be harvested with this scheme. The initial conditions are given by

$$\varphi(0) = -\varphi_{max}, \tag{A.82}$$
$$\dot{\varphi}(0) = 0, \tag{A.83}$$
$$\ddot{\varphi}(0) = 0, \tag{A.84}$$
$$a(0) = 0, \tag{A.85}$$

and the relevant dynamic equations are given by

$$f_{in}(t) = M_{eq} a(t) = M_{eq} \omega^2 Y_0 \sin(\omega t), \tag{A.86}$$
$$\ddot{\varphi}(t) = a(t), \tag{A.87}$$
$$\dot{\varphi}(t) = \int_0^t a(t)dt = \omega Y_0 \left(1 - \cos(\omega t)\right), \tag{A.88}$$
$$\varphi(t) = \int_0^t \dot{\varphi} dt = Y_0 \left(\omega t - \sin(\omega t)\right) - \varphi_{max}. \tag{A.89}$$

The displacement in the channel that maximizes kinetic energy upon impact is given at half a period,

$$\varphi(\pi/\omega) = \varphi_{\max} = \pi Y_0 - \varphi_{\max}, \tag{A.90}$$

$$\varphi_{\max} = \frac{\pi Y_0}{2}, \tag{A.91}$$

and the average power over one full period is therefore given by

$$\bar{P}_{\text{in,impact}} = \frac{2}{\pi} M_{\text{eq}} \omega^3 Y_0^2 = \frac{4}{\pi^2} \omega \varphi_{\max} f_{\text{in,max}}. \tag{A.92}$$

If we compare Eq. A.92 with the ideal cycle (Eq. A.80), we find a ratio of $2/\pi$ (0.636). We can however evaluate the power numerically for a shorter channel and find an optimal ratio of ≈ 0.92 if $\varphi_{\max} \approx Y_0/2$.

Figure A.17 illustrates typical waveforms for such an architecture driven by an harmonic oscillation $a(t)$ over 5 consecutive periods, assuming the channel allows a maximum mass travel $2\varphi_{\max} = \pi Y_0$. Meanwhile, Fig. A.18 depicts the corresponding phase portrait and $f_{\text{in}} - \varphi$ diagram of the system. As we can see, both are distinctive and differ from those of the ideal cycle or the harmonic oscillator.

A.3.4 Latch based harvester

The latch based harvester has many similarities with the impact based architecture. For example, it can also operate by using a mass traveling along a guiding channel, although here the mass latches to the ends stopper (which are again springs) and is released only until the peak of the force occurs. This principle therefore requires some kind of feedback and control mechanism to ensure adequate timing for the release. At this point, the mass is free to move, gaining momentum towards the opposite stopper, where all its kinetic energy can be harvested after latching to the other side. Again, the physics are similar to the impact based harvester and friction along the channel should also be minimized. Here, however, the length of the channel must be smaller than Y_0, otherwise the mass will not be able to latch on the other end stop. Even for $\varphi_{\max} > Y_0/2$, the inertial force will work against the mass to slow its impact (*i.e.*, the input power is negative over a part of the cycle). For this system, most initial conditions remain the same as for the impact based harvester, minus the initial acceleration $a(0)$, which is at peak value $a(0) = \omega^2 Y_0$ here instead. The relevant dynamic equations for this system over half a period are given by

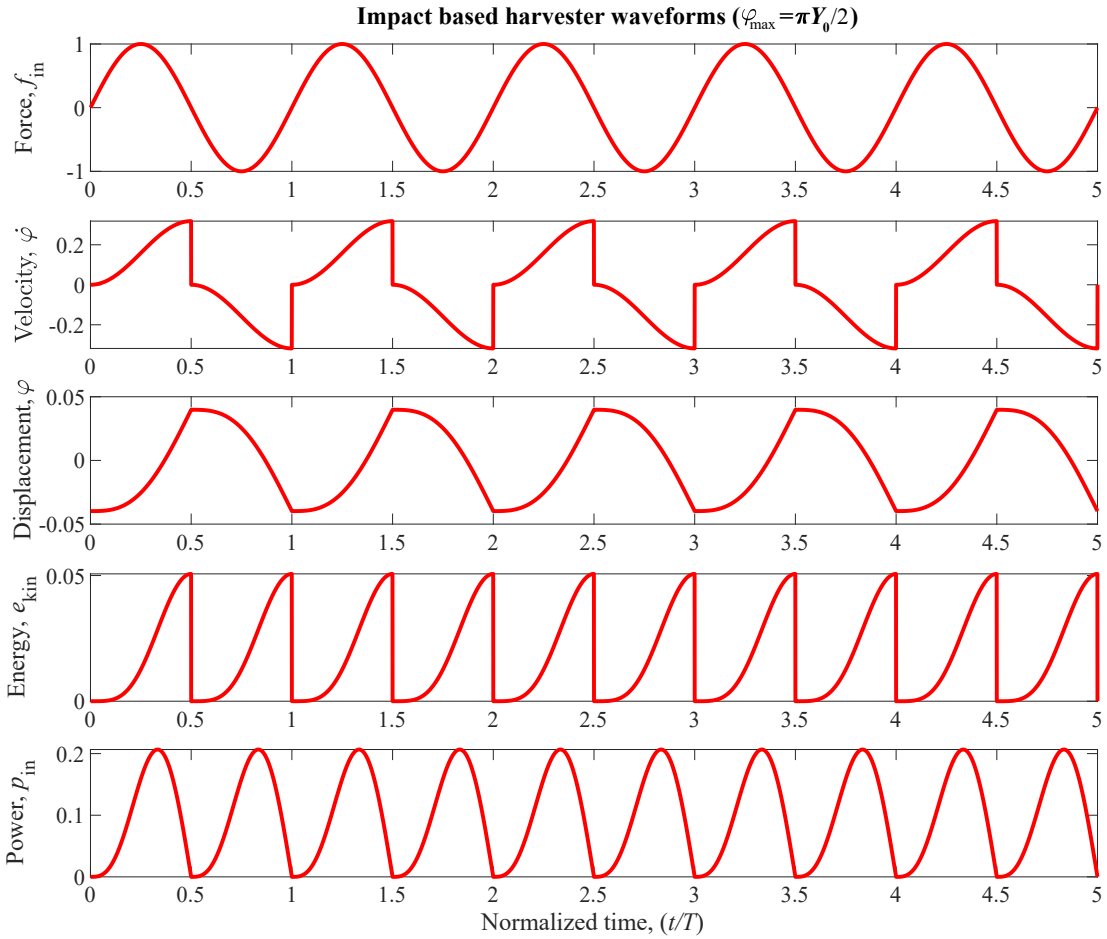

Figure A.17 Impact based harvester waveforms. $\varphi_{\max} = \pi Y_0/2$

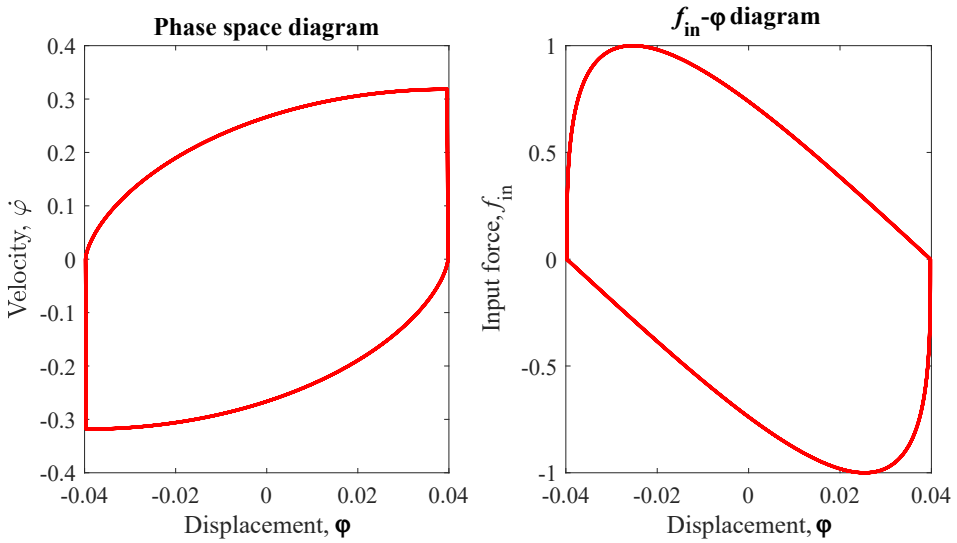

Figure A.18 Impact based harvester phase space and $f_{\text{in}} - \varphi$ diagrams. $\varphi_{\max} = \pi Y_0/2$

$$f_{\text{in}}(t) = M_{\text{eq}} a(t) = M_{\text{eq}} \omega^2 Y_0 \cos(\omega t), \tag{A.93}$$

$$\dot{\varphi}(t) = \int_0^t a(t)dt = \omega Y_0 \sin(\omega t), \tag{A.94}$$

$$\varphi(t) = \int_0^t \dot{\varphi}(t) = -Y_0 \cos(\omega t) + Y_0 - \varphi_{\max}. \tag{A.95}$$

Computing the necessary travel time to latch on the opposite stopper gives

$$t_{\text{latch}} = \arccos\left[1 - \frac{2\varphi_{\max}}{Y_0}\right] / \omega, \tag{A.96}$$

which then results in the following power expression

$$\bar{P}_{\text{in,latch}} = \frac{\omega}{\pi} \int_0^{t_{\text{latch}}} \left(M_{\text{eq}} \omega^2 Y_0 \cos(\omega t)\right) \dot{\varphi}(t) dt, \tag{A.97}$$

$$= \frac{M_{\text{eq}} \omega^3 Y_0^2}{2\pi} \sin^2(\omega t_{\text{latch}}), \tag{A.98}$$

which finally simplifies to

$$\bar{P}_{\text{in,latch}} = \frac{2}{\pi} M_{\text{eq}} \varphi_{\max}^2 \omega^3 \left(\frac{Y_0}{\varphi_{\max}} - 1\right). \tag{A.99}$$

Figure A.19 illustrates the typical waveforms for this architecture, here assuming $\varphi_{\max} = Y_0/2$, while Fig. A.20 depicts the phase space and $f_{\text{in}} - \varphi$ diagrams. It is however worth pointing out that for $Y_0 \gg \varphi_{\max}$, the $f_{\text{in}} - \varphi$ diagram and time wave forms approach that of the ideal cycle depicted in Fig. A.15. We demonstrate this mathematically by computing the ratio of Eqs. A.99 over A.80, which gives $(1 - \varphi_{\max}/Y_0)$ and shows that this architecture is most effective at capturing energy under tight geometric constraints.

A.3.5 Conclusion on nonresonant architectures

Figure A.21 compares both nonresonant architechtures analyzed here to the linear oscillators (assuming it is optimized for all given space constraints) to provide a general perspective on their potential. In Fig. A.21(a), the input power is normalized by $Y_0^2 \omega^3 M_{\text{eq}}$, whereas in Fig. A.21(b) the input power is normalized by the maximum input power of an ideal cycle (*i.e.*, the architecture effectiveness relatively to the ideal cycle).

Based on these analyses, we can see that the latch-based architecture is optimal for $W_{\max}/Y_0 \leq 0.19$, whereas the impact based architecture outperforms it for $W_{\max}/Y_0 > 0.19$. Then, a sufficiently damped, tuned linear device can be better than both if $W_{\max}/Y_0 > 1.18$. This again demonstrates that nonresonant architectures are suited for applications where the available mass

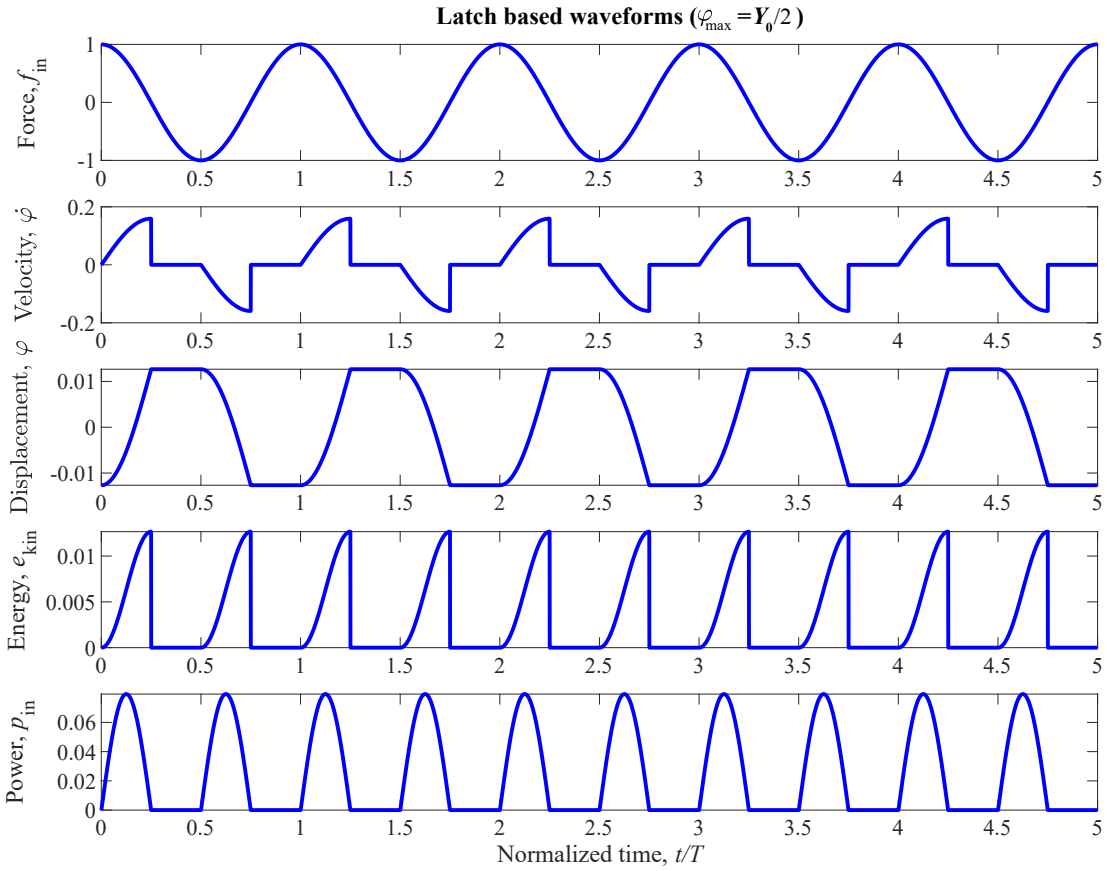

Figure A.19 Latch based harvester waveforms, assuming $\varphi_{\max} = Y_0/2$.

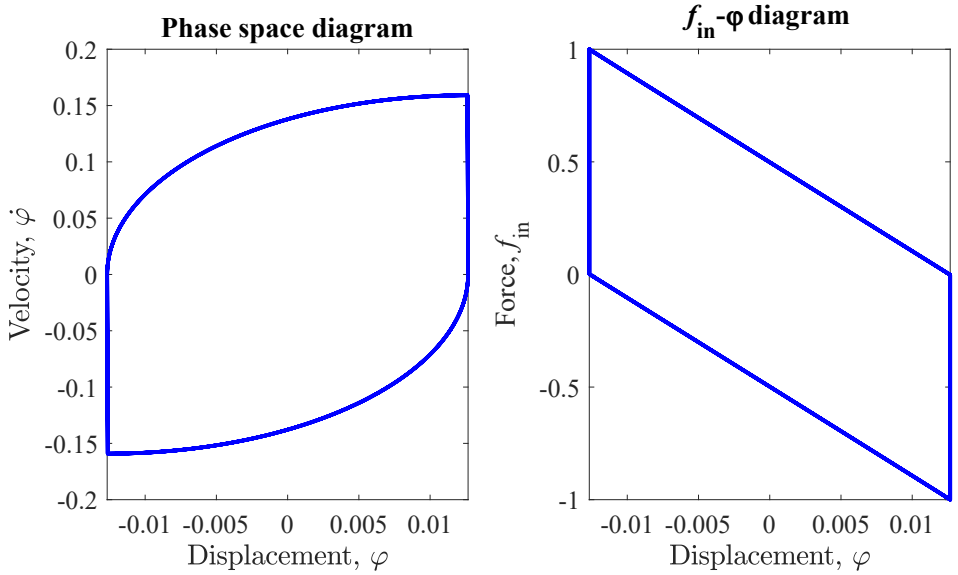

Figure A.20 Latch based harvester phase space and $f_{\text{in}} - \varphi$ diagrams. $\varphi_{\max} = Y_0/2$.

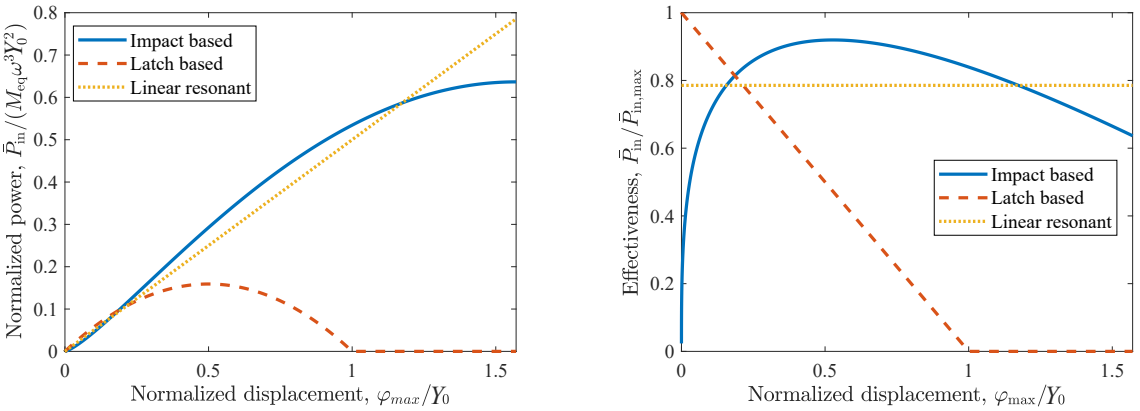

(a) Power trend for the nonresonant architectures (b) Effectiveness trend for the nonresonant architectures

Figure A.21 Power and effectiveness trend for the nonresonant architectures. The linear oscillator is compared here, assuming resonance for all $\varphi_{\max}/Y_0$ ratios or a dominant damping force.

travel range is close to or smaller than the source vibration displacement (human motion for example). In those instances, a resonant device does not make sense because it would require damping levels that are difficult to achieve to suppress the mass displacement.

Although perfectly inelastic collisions are assumed for these analyses, thus considering the energy can be harvested instantly and neglecting the stoppers dynamics, it is sufficient to provide significant insight on the fundamental limits of these configurations. Practically, it entails that the stoppers dynamics must be much faster than the source. For example, in the case of Renaud's impact based design, the piezoelectric benders have a natural frequency that is significantly higher than the vibration source. This is advantageous, because the ring down time can be fast, even if the beams are not critically damped, and the energy can be harvested more efficiently by maximizing the electrical damping. However, losses during impacts and while the free mass is moving must be minimized.

These architectures can operate over a range of frequencies, but only as long as:

1. the source displacement Y_0 remains significant compared to the device travel range $2\varphi_{\max}$;
2. the harvesting mechanisms (*e.g.*, piezoelectric stoppers) have ring down times that are fast enough to harvest most of the energy before the next contact with the mass.

In other words, the wide band harvesting capabilities of these architectures is mainly function of the ratio between the device size and the vibration source displacement. For a given source displacement, smaller devices offer a broader frequency range of operation, but Fig. A.21 also illustrates how they generate less power. Hence, nonresonant architectures are still affected by a trade-off between the maximum power output and the functional bandwidth, similar to what exists for linear resonant devices.

The overall approach used here can be extended to any harvester architecture, regardless of its operating principle or transduction mechanism, and is an effective method to compare their

performances under prescribed displacement constraints. It would therefore be of significant interest to also include nonlinear oscillators in this framework to provide a unified theory for all types of harvesters.

APPENDIX B

Linearization methods

This appendix presents two linearization methods used for solving many of the nonlinear system equations presented in appendix A. First, the harmonic balance method is presented and used to solve the Duffing oscillator equations. Then, the equivalent linearization approach is presented for the monostable Duffing oscillator (for validation) as well as for the piecewise oscillator.

B.1 Harmonic balance method

The harmonic balance method can provide an approximate analytical solution for the steady-state response of the Duffing oscillator. In this approach, we consider that the response of the nonlinear coupled vibration problem can be expressed as converging sums of N harmonics, such as in equations B.1 and B.2.

$$\varphi(t) = \sum_{n=0}^{N} a_n \sin(n\omega t) + b_n \cos(n\omega t) = b_0 + \sum_{n=1}^{N} a_n \sin(n\omega t) + b_n \cos(n\omega t), \tag{B.1}$$

$$v(t) = \sum_{n=1}^{N} \hat{a}_n \sin(n\omega t) + \hat{b}_n \cos(n\omega t). \tag{B.2}$$

The coefficients a_n, b_n are attached to the displacement response, whereas $\hat{a}_n$, $\hat{b}_n$ provide the voltage response. The presence of b_0 in equation B.1 is to account for the possible stable positions in the bistable case, which can be different than 0. Such a term in the voltage equation is not included because we know that the response of the equivalent RC circuit does not have a DC component at the steady state.

The time derivatives of these expressions are given by

$$\dot{\varphi}(t) = \dot{b}_0 + \sum_{n=1}^{N} (\dot{a}_n - n\omega b_n) \sin(n\omega t) + \left(\dot{b}_n + n\omega a_n\right) \cos(n\omega t), \tag{B.3}$$

$$\ddot{\varphi}(t) = \ddot{b}_0 + \sum_{n=1}^{N} \left(\ddot{a}_n - 2n\omega\dot{b}_n - n^2\omega^2 a_n\right) \sin(n\omega t) + \left(\ddot{b}_n + 2n\omega\dot{a}_n - n^2\omega^2 b_n\right) \cos(n\omega t), \tag{B.4}$$

$$\dot{v}(t) = \sum_{n=1}^{N} \left(\dot{\hat{a}}_n - n\omega\hat{b}_n\right) \sin(n\omega t) + \left(\dot{\hat{b}}_n + n\omega\hat{a}_n\right) \cos(n\omega t). \tag{B.5}$$

Although the a_n, b_n, $\hat{a}_n$ and $\hat{b}_n$ coefficients could also be functions of time, we assume here that they vary very slowly. Moreover, we are interested in the steady-state response, therefore their time derivatives are neglected. The cubic term can be expanded as

$$\varphi^3(t) = \sum_{n,i,j=0}^{N} [a_n \sin(n\omega t) + b_n \cos(n\omega t)] [a_i \sin(i\omega t) + b_i \cos(i\omega t)] \\ [a_k \sin(k\omega t) + b_k \cos(k\omega t)] \quad \text{(B.6)}$$

and the following product-to-sum trigonometric identities are used to express the equation in the harmonic form:

$$\cos(\Psi)\cos(\psi) = \frac{\cos(\Psi-\psi)+\cos(\Psi+\psi)}{2}, \quad \text{(B.7)}$$

$$\sin(\Psi)\sin(\psi) = \frac{\cos(\Psi-\psi)-\cos(\Psi+\psi)}{2}, \quad \text{(B.8)}$$

$$\sin(\Psi)\cos(\psi) = \frac{\sin(\Psi+\psi)+\sin(\Psi-\psi)}{2}, \quad \text{(B.9)}$$

$$\cos(\Psi)\sin(\psi) = \frac{\sin(\Psi+\psi)-\sin(\Psi-\psi)}{2}. \quad \text{(B.10)}$$

After manipulation, equation B.6 becomes

$$\begin{aligned}\varphi^3(t) = \sum_{n,i,j=0}^{N} & \frac{1}{4}\sin((n+i+j)\omega t)\left[-a_n a_i a_j + b_n b_i a_j + a_n b_i b_j + b_n a_i b_j\right] + \\ & \frac{1}{4}\sin((n+i-j)\omega t)\left[a_n a_i a_j - b_n b_i a_j + a_n b_i b_j + b_n a_i b_j\right] + \\ & \frac{1}{4}\sin((n-i+j)\omega t)\left[a_n a_i a_j + b_n b_i a_j + a_n b_i b_j - b_n a_i b_j\right] + \\ & \frac{1}{4}\sin((n-i-j)\omega t)\left[-a_n a_i a_j - b_n b_i a_j + a_n b_i b_j - b_n a_i b_j\right] + \\ & \frac{1}{4}\cos((n+i+j)\omega t)\left[-a_n b_i a_j - b_n a_i a_j - a_n a_i b_j + b_n b_i b_j\right] + \\ & \frac{1}{4}\cos((n+i-j)\omega t)\left[a_n b_i a_j + b_n a_i a_j - a_n a_i b_j + b_n b_i b_j\right] + \\ & \frac{1}{4}\cos((n-i+j)\omega t)\left[-a_n b_i a_j + b_n a_i a_j + a_n a_i b_j + b_n b_i b_j\right] + \\ & \frac{1}{4}\cos((n-i-j)\omega t)\left[a_n b_i a_j - b_n a_i a_j + a_n a_i b_j + b_n b_i b_j\right]. \quad \text{(B.11)}\end{aligned}$$

To get a simplified analytical solution, we limit the Fourier series development to the first order ($N = 1$), which yields

$$\varphi^3(t) = b_0\left[b_0^2 + \frac{3}{2}\left(a_1^2 + b_1^2\right)\right] + \left[\frac{3}{4}\left(a_1^2 + b_1^2\right) + 3b_0^2\right]\left[a_1\sin(\omega t) + b_1\cos(\omega t)\right] + \left[3b_0a_1b_1\right]\sin(2\omega t) + \frac{3}{2}b_0\left[-a_1^2 + b_1^2\right]\cos(2\omega t) + \frac{a_1}{4}\left[-a_1^2 + 3b_1^2\right]\sin(3\omega t) + \frac{b_1}{4}\left[-3a_1^2 + b_1^2\right]\cos(3\omega t). \quad \text{(B.12)}$$

Despite the first order simplification, the nonlinear cubic term introduces second and third harmonics. We however assume these terms to be small and they are dropped according to our initial assumption.

Now noting that $r_n^2 = a_n^2 + b_n^2$ is the squared amplitude of the n^{th} harmonic, we can write

$$\varphi^3(t) \approx b_0\left[b_0^2 + \frac{3}{2}r_1^2\right] + \left[\frac{3}{4}r_1^2 + 3b_0^2\right]\left[a_1\sin(\omega t) + b_1\cos(\omega t)\right]. \quad \text{(B.13)}$$

The next step requires replacing the assumed solutions, as well as the derivatives and cubic term in the differential equations (Eqs. A.3 and A.2) with their values from equations B.1, B.2, B.3, B.4, B.5 and B.13. The process of harmonic balancing is now achieved by separating the constant, cosinus and sinus terms, which yields a 5 unknowns, 5 equations system.

$$K_1b_0 + K_3b_0\left(b_0^2 + \frac{3}{2}r_1^2\right) = 0 \quad \text{(B.14)}$$

$$-\omega^2M_{\text{eq}}a_1 - C_{\text{m}}\omega b_1 + K_1a_1 + K_3a_1\left(3b_0^2 + \frac{3}{4}r_1^2\right) - \theta\hat{a}_1 = 0 \quad \text{(B.15)}$$

$$-\omega^2M_{\text{eq}}b_1 + C_{\text{m}}\omega a_1 + K_1b_1 + K_3b_1\left(3b_0^2 + \frac{3}{4}r_1^2\right) - \theta\hat{b}_1 - M_{\text{eq}}|A| = 0 \quad \text{(B.16)}$$

$$-\theta\omega b_1 - C_{\text{p}}\omega\hat{b}_1 + \frac{\hat{a}_1}{R_{\text{eq}}} = 0 \quad \text{(B.17)}$$

$$\theta\omega a_1 + C_{\text{p}}\omega\hat{a}_1 + \frac{\hat{b}_1}{R_{\text{eq}}} = 0 \quad \text{(B.18)}$$

The voltage equations B.17 and B.18 are linear and can easily be rearranged to be expressed exclusively as explicit function of the displacement,

$$\hat{a}_1 = \theta\omega R_{\text{eq}} \frac{\left(b_1 - \omega R_{\text{eq}} C_{\text{p}} a_1\right)}{1 + \omega^2 R_{\text{eq}}^2 C_{\text{p}}^2}, \tag{B.19}$$

$$\hat{b}_1 = -\theta\omega R_{\text{eq}} \frac{\left(a_1 + \omega R_{\text{eq}} C_{\text{p}} b_1\right)}{1 + \omega^2 R_{\text{eq}}^2 C_{\text{p}}^2}. \tag{B.20}$$

Then, by squaring and adding both Eqs. B.19 andB.20, we obtain the squared value of the voltage amplitude, $\hat{r}_1^2 = \hat{a}_1^2 + \hat{b}_1^2$, which can be expressed as a function of the square of the oscillator amplitude r_1^2 after simplification,

$$\hat{r}_1^2 = \frac{\theta^2\omega^2 R_{\text{eq}}^2}{1 + \omega^2 R_{\text{eq}}^2 C_{\text{p}}^2} r_1^2. \tag{B.21}$$

It is worth pointing out the equivalence of Eq. B.21 with the solution for the linear oscillator, which can be verified by evaluating the square of the magnitude of the voltage phasor in Eq. 2.9 (*i.e.*, $\hat{r}_1^2 = |V|^2$, $r_1^2 = \varphi_0^2 \equiv |W|^2$). It is therefore safe to state that the electrical force can still be expressed as a summation of an electrical stiffness, K_{el} and electrical damping C_{el}.

In a similar manner, inserting equations B.19 and B.20 into B.15 and B.16, then squaring B.15 and B.16 and adding them, we obtain the equation for the square of the amplitude of motion, r_1^2. Rearrangement of the terms yields

$$r_1^2 = \frac{M_{\text{eq}}^2 |A|^2}{\left[K_1 + K_3\left(\frac{3}{4}r_1^2 + 3b_0^2\right) + K_{\text{el}} - \omega^2 M_{\text{eq}}\right]^2 + \omega^2\left(C + C_{\text{el}}\right)^2}, \tag{B.22}$$

which is the implicit equation of the square of the amplitude. The solution for r_1 is obtained by solving a sixth order polynomial expression after substitution of b_0 by one of its solution obtained from B.14. The multiple solutions of this expression are presented in section A.2.1.

B.2 Equivalent linearization

Equivalent linearization is an alternate approach to find the equivalent stiffness of the nonlinear restoring force. The idea is to replace the nonlinear restoring force by an equivalent linear force that minimizes the error. The equivalent stiffness is finally obtained by a least square regression. The approach is demonstrated here for the monostable Duffing oscillator and the piecewise oscillator.

B.2.1 Duffing oscillator stiffening/softening spring

As stated, the goal is to replace the nonlinear restoring force, $K_3\varphi(t)^3$, by an equivalent linear force, $\bar{K}_3\varphi(t)$. Thus, the equivalent stiffness $\bar{K}_3$ is obtained by doing a least square regression of the error $\varepsilon(t) = K_3\varphi(t)^3 - \bar{K}_3\varphi(t)$, which is expressed as

$$\frac{\mathrm{d}\overline{\varepsilon^2(t)}}{\mathrm{d}\bar{K}_3} = \frac{\mathrm{d}}{\mathrm{d}\bar{K}_3}\overline{(K_3\varphi(t)^3 - \bar{K}_3\varphi(t))^2} = 0. \tag{B.23}$$

Here, the overline denotes an average over a portion of a cycle, which will be defined shortly. Full development of this equation yields,

$$\bar{K}_3 = K_3\frac{\overline{\varphi(t)^4}}{\overline{\varphi(t)^2}}. \tag{B.24}$$

We now assume the system response to remain sinusoidal and of the form

$$\varphi = \varphi_0 \sin(\omega t), \tag{B.25}$$

where φ_0 is the amplitude. Replacing φ in equation B.24, and due to the symmetry of this function, the averaged value can be obtained by integration over one quarter of a cycle.

$$\bar{K}_3 = K_3\varphi_0^2\frac{\int_0^{\pi/2\omega}\sin^4(\omega t)dt}{\int_0^{\pi/2\omega}\sin^2(\omega t)dt}. \tag{B.26}$$

After simplification, the equivalent stiffness term $\bar{K}_3$ is

$$\bar{K}_3 = \frac{3}{4}K_3\varphi_0^2, \tag{B.27}$$

which is the same solution obtained from the harmonic balance method in equation A.6, obtained by assuming a single harmonic. This result therefore support the validity of the equivalent linearization method.

B.2.2 Piecewise oscillator spring

The method is now adapted for modeling the piecewise oscillator. The approach is the same as with equation B.23,

$$\frac{\mathrm{d}\overline{\varepsilon^2(\varphi)}}{\mathrm{d}\bar{K}} = \frac{\mathrm{d}}{\mathrm{d}\bar{K}}\overline{(f_R(\varphi) - \bar{K}\varphi)^2} = 0, \tag{B.28}$$

Further development yields,

$$\frac{\mathrm{d}\overline{\varepsilon^2(\varphi)}}{\mathrm{d}\bar{K}} = \int_0^{\frac{\pi}{2\omega}}\left[2\bar{K}\varphi(t)^2 - 2f_R(t)\varphi(t)\right]\mathrm{d}t \tag{B.29}$$

As the nature of the restoring force $f_R(t)$ is piecewise (Eq. A.5), so will be the integral involved. Computing the integral with respect to time requires assessment of the time t_S at which contact with the stoppers occur to get the intervals,

$$t_S = \frac{\arcsin\left(\frac{\varphi_s}{\varphi_0}\right)}{\omega}. \tag{B.30}$$

Equation B.29 therefore becomes,

$$\frac{\mathrm{d}\overline{\varepsilon^2(\varphi)}}{\mathrm{d}\bar{K}} = \int_0^{\frac{\pi}{2\omega}} 2\bar{K}\varphi_0^2 \sin^2(\omega t)\, dt + \int_0^{t_S} 2K_m\varphi_0^2 \sin^2(\omega t)\, dt + \int_{t_S}^{\frac{\pi}{2\omega}} \left[2(K_m + K_s)\varphi_0 \sin^2(\omega t) - 2K_s\varphi_s\varphi_0 \sin(\omega t)\right] \mathrm{d}t. \tag{B.31}$$

Evaluating these integrals and solving for $\bar{K}$ yields,

$$\bar{K} = K_m + K_s\left\{1 - \frac{2}{\pi}\left[\left(\frac{\varphi_s}{\varphi_0}\right)\sqrt{1-\left(\frac{\varphi_s}{\varphi_0}\right)^2} + \arcsin\left(\frac{\varphi_s}{\varphi_0}\right)\right]\right\}. \tag{B.32}$$

APPENDIX C
List of sensors in modern cars

A list of currently used automotive sensors is presented and grouped by functions in Table C.1. This list shows possible locations for vibration measurement based on two criteria: the data transmission rate (DTR) and the criticality level (CL) of the associated function. The data transmission rate is the frequency of communication between the sensor and the ECU, thus a higher rate is logically more energy demanding, which reduce the node autonomy or ask for high performances from the harvester. Alternatively, the criticality level of a sensor represents the severity of the consequences to the passenger's safety or vehicle condition if the sensor fails to transmit the information. Hence, critical sensors (*e.g.*, shock accelerometers, ABS yaw sensors, chemical sensors of the powertrain system, etc.) are considered riskier and less suited for wireless connection due to reliability concerns. Both criteria are weighted using a qualitative scale (1=low, 2=medium, 3=high) and are evaluated based on our own judgment. The final score is obtained from the product of both criteria.

Table C.1 List of current sensors in modern cars

Sensors	**Type**	**DTR**	**CL**	**Score**
Airbag system				
Front primary crash	Accelerometer	3	3	9
Seat pan bladder pressure	Pressure	1	1	1
Seat pan load/deflection	Load	1	1	1
Seat track limit detection	Hall effect	1	1	1
Seat-belt buckle detection	Reed switch	1	2	2
Seat-belt tension	Tension	1	2	2
Sides impact	Accelerometer	3	3	9
Vehicle rollovers lateral	Accelerometer	3	3	9
Antilock brake (ABS)				
Brake booster membrane displacement	Position	2	3	6
Brake fluid level	Reed switch	1	1	1
Brake-by-wire pedal depression	Position	3	3	9
Lateral/Longitudinal acceleration	Accelerometer	3	3	9
Wheel speed	Variable reluctance	3	3	9
Body control and suspension control				
Body vertical/lateral/longitudinal acceleration	Accelerometer	2	1	2
Chassis height	Position	2	1	2
Side mirror vertical/horizontal limit	Position	1	1	1
Front/rear/trunk door ajar	Proximity switch	1	1	1
Lateral Acceleration	Accelerometer	2	3	6
Power Windows Up/Down Detection	Reed switch	1	1	1
Steering wheel angle	AMR effect	2	2	4
Sunroof open/close detection	Hall effect switch	1	1	1
Washer fluid level	Reed switch	1	1	1

Continued on next page

Sensors	Type	DTR	CL	Score
Wheel speed	Variable reluctance	3	3	9
Yaw angular rate	Gyroscope	2	3	6
Comfort and security				
Glass breakage/shock detection	Accelerometer	1	1	1
Rain sensor switch	Photodiode	1	1	1
Sliding door anti-pinch	Ultrasonic	1	1	1
Vehicle tilt detection	Gyroscope	1	1	1
Tire pressure monitoring system (TPMS)				
Tire pressure	Pressure	1	1	1
Tire temperature	Temperature	1	1	1
HVAC system				
A/C front outlet temperature	Temperature	1	1	1
A/C pressure	Pressure	1	1	1
Air-flap position	Switch	1	1	1
Evaporator temperature	Temperature	1	1	1
Exterior/interior temperature/humidity	Temperature/humidity	1	1	1
Outdoor light for healight control	Photodiode	1	1	1
Sunload/twilight	Photodiode	1	1	1
Power steering				
Power steering fluid level	Reed switch	1	1	1
Power steering pressure switch	Pressure	3	3	9
Steering wheel column telescope position	Position	1	2	2
Steering wheel column tilt position	Position	1	2	2
Steering wheel position	Position	2	3	6
Powertrain control				
Accelerator pedal position	Position	1	3	3
Air intake mass flow	Flow	3	3	9
Boost air temperature	Temperature	1	2	2
Brake pedal depression switch	Reed switch	1	3	3
Camshaft rotational speed	Hall effect	3	3	9
Cylinder head temperature	Temperature	1	3	3
EGR valve position	Position	3	3	9
Engine coolant level	Reed switch	1	2	2
Engine coolant temperature	Temperature	1	2	2
Engine knock detection	Accelerometer	3	3	9
Engine oil level	Reed switch	1	2	2
Engine oil temperature	Temperature	1	2	2
Engine speed	Speed	3	3	9
Engine torque	Magnetostrictive	3	3	9
Exhaust gas nitrogen oxide (NOx)	Chemical	3	3	9
Exhaust gsa oxygen (EGO)	Chemical	2	3	6
Exhaust gas recirculation (EGR) temperature	Temperature	2	2	4
Exhaust gas DPFE	Pressure	2	2	4
Fuel level	Position	1	1	1
Fuel rail temperature	Temperature	1	3	3
Fuel tank pressure	Pressure	2	3	6

Continued on next page

Sensors	Type	DTR	CL	Score
Heated exhaust gas oxygen (HEGO)	Chemical	2	3	6
Intake air temperature	Temperature	1	3	3
Manifold absolute pressure (MAP)	Pressure	3	3	9
Throttle rotary position (TPS)	Switch	3	3	9
Top dead center (TDC) detection	Position	3	3	9
Transfer case speed	Speed	3	3	9
Transmission fluid temperature	Temperature	1	2	2
Transmission gear shift position	Position	3	3	9
Transmission range	Position	3	3	9
Transmission torque	Magnetostrictive	3	3	9
Turbine shaft speed (TSS)	Speed	3	3	9
Vehicle speed (VSS)	Speed	3	3	9
Parking aid and driving aid				
Adaptive cruise control sensor	Radar	3	3	9
Auto dimming mirror sensor	Optoelectronic	1	1	1
Blind spot surveillance	Beam width radar	2	3	6
Lateral lane detection	Magnetometer	3	3	9
Night vision	Infrared	3	3	9
Parking aid front	Ultrasonic	1	1	1
Parking aid rear right/left corner	Ultrasonic	1	1	1
Parking rear right/left center	Ultrasonic	1	1	1

References: [14, 74]

APPENDIX D

Supplementary material to chapter 4

D.1 Quasi-static beam model equations

The inertia of the beam is first considered as a constant distributed load $f_{\mathrm{b}}(t)$, whereas the tip mass applies a point force $F_{\mathrm{M}}(t)$ as well as a moment $M_{\mathrm{M}}(t)$ at the tip of the cantilever due to the mass centroid offset from the tip of the beam. These loads are respectively described by,

$$f_{\mathrm{b}}(t) = b\left(\rho_{\mathrm{s}} h_{\mathrm{s}} + \rho_{\mathrm{p}} h_{\mathrm{p}} + \rho_{\mathrm{el}} h_{\mathrm{el}}\right) a(t), \tag{D.1}$$

$$F_{\mathrm{M}}(t) = bL_{\mathrm{t}}\left(\rho_{\mathrm{s}} h_{\mathrm{t,S}} + \rho_{\mathrm{W}} h_{\mathrm{t,W}}\right) a(t) = M_{\mathrm{t}} a(t), \tag{D.2}$$

$$M_{\mathrm{M}}(t) = F_{\mathrm{M}}(t) L_{\mathrm{t}}/2. \tag{D.3}$$

The beam quasistatic deflection $w_{\mathrm{b}}(x,t)$ can be expressed as the superposition of each loading terms,

$$w_{\mathrm{b}}(x,t) = w_{\mathrm{b},f}(x,t) + w_{\mathrm{b},F}(x,t) + w_{\mathrm{b},M}(x,t) \tag{D.4}$$

where $w_{\mathrm{b},f}$, $w_{\mathrm{b},F}$, and $w_{\mathrm{b},M}$ are then given by [106] :

$$w_{\mathrm{b},f} = -f_{\mathrm{b}}(t)\left(x^4 - 4L_{\mathrm{b}}x^3 + 6L_{\mathrm{b}}^2 x^2\right)/\left(24YI\right), \tag{D.5}$$

$$w_{\mathrm{b},F} = -F_{\mathrm{M}}(t)\left(-x^3 + 3L_{\mathrm{b}}x^2\right)/\left(6YI\right), \tag{D.6}$$

$$w_{\mathrm{b},M} = -M_{\mathrm{M}}(t)x^2/\left(2YI\right) \tag{D.7}$$

and YI is the flexural rigidity of the composite cantilever. The flexural rigidity of a cantilever beam is linked to the bending moment $M_y(x,t)$ by:

$$M_y(x,t) = YI\frac{\partial^2 w(x,t)}{\partial x^2} \tag{D.8}$$

This moment is found by integrating the stress over the thickness of the beam, which requires knowing the position of the neutral axis. For the three layers composite beam depicted in

Fig. 4.1(a), one can find the position of each interfaces respectively to the neutral axis as:

$$h_a = -\frac{\frac{h_s^2}{2}Y_s + \left(h_s + \frac{h_p}{2}\right)h_pY_p + \left(h_s + h_p + \frac{h_{el}}{2}\right)h_{el}Y_{el}}{h_sY_s + h_pY_p + h_{el}Y_{el}} \tag{D.9a}$$

$$h_b = h_s - \frac{\frac{h_s^2}{2}Y_s + \left(h_s + \frac{h_p}{2}\right)h_pY_p + \left(h_s + h_p + \frac{h_{el}}{2}\right)h_{el}Y_{el}}{h_sY_s + h_pY_p + h_{el}Y_{el}} \tag{D.9b}$$

$$h_c = h_p + h_s - \frac{\frac{h_s^2}{2}Y_s + \left(h_s + \frac{h_p}{2}\right)h_pY_p + \left(h_s + h_p + \frac{h_{el}}{2}\right)h_{el}Y_{el}}{h_sY_s + h_pY_p + h_{el}Y_{el}} \tag{D.9c}$$

$$h_d = h_{el} + h_p + h_s - \frac{\frac{h_s^2}{2}Y_s + \left(h_s + \frac{h_p}{2}\right)h_pY_p + \left(h_s + h_p + \frac{h_{el}}{2}\right)h_{el}Y_{el}}{h_sY_s + h_pY_p + h_{el}Y_{el}} \tag{D.9d}$$

where h_a, h_b, h_c, and h_d refer respectively to the positions of the bottom of the silicon beam, the silicon/AlN interface, the AlN/Al electrode interface, and the top of the electrode. After integrating the tensile stress over the beam thickness, the flexural rigidity is finally obtained as:

$$YI = \frac{b}{3}\left[Y_s\left(h_b^3 - h_a^3\right) + Y_p\left(h_c^3 - h_b^3\right) + Y_{el}\left(h_d^3 - h_c^3\right)\right]. \tag{D.10}$$

D.2 Effective mass calculations

We consider the displacement of the tip mass as a rigid body motion; therefore, the equivalent mass of the system must also account for the inertia of the tip mass in both translation and rotation. To this end, we define a referential O' located at the intersection of the mass attach point and the beam neutral axis, as shown on Fig. D.1, and where $\vec{i}$, $\vec{j}$ and $\vec{k}$ are the unit vectors respectively associated to its x, y and z axis.

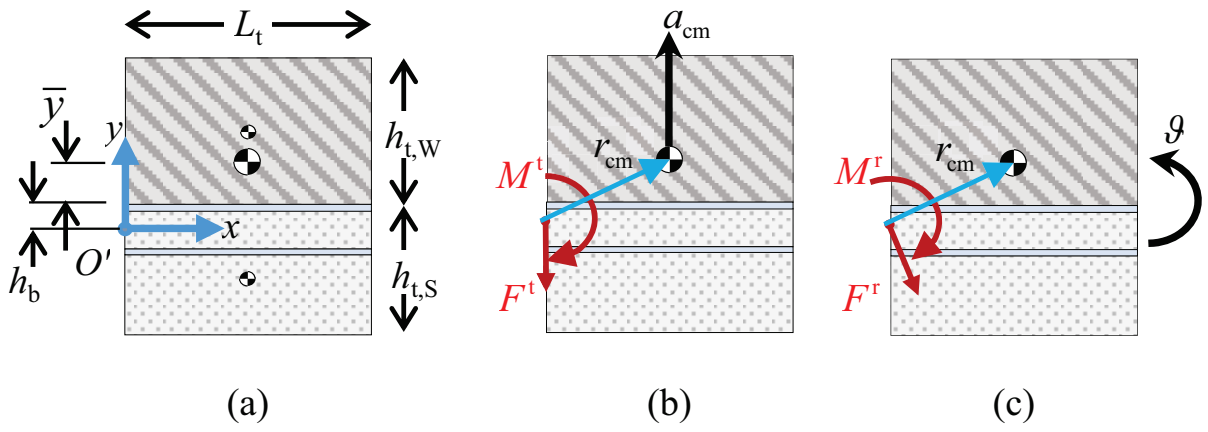

Figure D.1 Schematic representation of the tip mass as a rigid body on point O′ with (a) the characteristics dimensions, with the loads from (b) translation and (c) rotation.

The effect of translation and rotation can then be analyzed separately to evaluate the resulting load on the beam tip. We consider a linear acceleration of the center of mass, noted a_{cm}, equal to the acceleration at the tip of the beam, and an angular acceleration, noted $\ddot{\vartheta}(t)$. While the beam is vibrating, the linear and angular acceleration are therefore expressed in vector form as

$$\vec{a}_{\mathrm{cm}}(t) = \left[\hat{w}(L_{\mathrm{b}})\ddot{\varphi}(t) + a(t)\right]\vec{j}, \tag{D.11}$$

$$\vec{\ddot{\vartheta}} = \frac{\mathrm{d}\hat{w}(L_{\mathrm{b}})}{\mathrm{d}x}\ddot{\varphi}(t)\vec{k}. \tag{D.12}$$

We then note the force and moment induced by linear acceleration by $F^{\mathrm{t}}(t)$ and $M^{\mathrm{t}}(t)$, whereas the force and moment induced by the angular acceleration are noted by $F^{\mathrm{r}}(t)$ and $M^{\mathrm{r}}(t)$:

$$\vec{F}^{\mathrm{t}}(t) = -M_{\mathrm{t}}\vec{a}_{\mathrm{cm}}, \tag{D.13}$$

$$\vec{M}^{\mathrm{t}}(t) = -M_{\mathrm{t}}\left(\vec{a}_{\mathrm{cm}} \times \vec{a}_{\mathrm{cm}}\right), \tag{D.14}$$

$$\vec{F}^{\mathrm{r}}(t) = -M_{\mathrm{t}}\left(\vec{\ddot{\vartheta}} \times \vec{r}_{\mathrm{cm}}\right), \tag{D.15}$$

$$\vec{M}^{\mathrm{r}}(t) = -\vec{\ddot{\vartheta}}\left(J_O + M_{\mathrm{t}}r_{\mathrm{cm}}^2\right), \tag{D.16}$$

with $\vec{r}_{\mathrm{cm}}$ the vector positioning the center of mass of the tip mass with respect to O' axis and J_O the polar moment of inertia of the mass with respect to its center of mass. The position of the center of mass is found by

$$\vec{r}_{\mathrm{cm}} = \left(\frac{L_{\mathrm{t}}}{2}\right)\vec{i} + (\bar{y} + h_b)\,\vec{j} \tag{D.17}$$

where $\bar{y}$ is the vertical position of the center of mass with respect to the silicon/tungsten interface,

$$\bar{y} = \frac{\rho_{\mathrm{W}}h_{\mathrm{t,W}}^2 - \rho_{\mathrm{S}}h_{\mathrm{t,S}}^2}{2\left(\rho_{\mathrm{S}}h_{\mathrm{t,S}} + \rho_{\mathrm{W}}h_{\mathrm{t,W}}\right)} \tag{D.18}$$

The moment of inertia J_O for the whole tip mass is therefore given by

$$J_O = (\rho_{\mathrm{W}}L_{\mathrm{t}}bh_{\mathrm{t,W}})\left[\frac{1}{12}\left(L_{\mathrm{t}}^2 + h_{\mathrm{t,W}}^2\right) + \left(\frac{h_{\mathrm{t,W}}}{2} - \bar{y}\right)^2\right] + (\rho_{\mathrm{S}}L_{\mathrm{t}}bh_{\mathrm{t,S}})\left[\frac{1}{12}\left(L_{\mathrm{t}}^2 + h_{\mathrm{t,S}}^2\right) + \left(\bar{y} + \frac{h_{\mathrm{t,S}}}{2}\right)^2\right]. \tag{D.19}$$

By combining the linear and angular components using Eqs. D.11-D.16 to get the balance of forces and moments, we find

$$\vec{F}^{\mathrm{c}}(t) = M_{\mathrm{t}}\left\{\left[\frac{\mathrm{d}\hat{w}(L_{\mathrm{b}})}{\mathrm{d}x}\ddot{\varphi}(t)\,(\bar{y}+h_b)\right]\vec{i} - \left[\hat{w}(L_{\mathrm{b}})\ddot{\varphi}(t) + a(t) + \frac{\mathrm{d}\hat{w}(L_{\mathrm{b}})}{\mathrm{d}x}\ddot{\varphi}(t)\left(\frac{L_{\mathrm{t}}}{2}\right)\right]\vec{j}\right\}, \tag{D.20}$$

$$\vec{M}^{\mathrm{c}} = -M_{\mathrm{t}}\left\{\left(\frac{L_{\mathrm{t}}}{2}\right)\left[\hat{w}(L_{\mathrm{b}})\ddot{\varphi}(t) + a(t)\right] + \frac{\mathrm{d}\hat{w}(L_{\mathrm{b}})}{\mathrm{d}x}\ddot{\varphi}(t)\left(\frac{J_O}{M_{\mathrm{t}}} + r_{\mathrm{cm}}^2\right)\right\}\vec{k}. \tag{D.21}$$

The first term in Eq. D.20, which causes an axial force along the x axis due to the mass centroid offset out of the beam plane, can be neglected. We then rearrange Eqs. D.20 and D.21 to express the balance of forces and moments as a combination of inertial terms, $F_{\mathrm{i}}(t)$ and $M_{\mathrm{i}}(t)$, and the external excitation terms $F_{\mathrm{M}}(t)$ and $M_{\mathrm{M}}(t)$ presented in Appendix D.1.

$$F^{\mathrm{c}} \approx F_{\mathrm{i}}(t) - F_{\mathrm{M}}(t), \tag{D.22}$$

$$M^{\mathrm{c}} = M_{\mathrm{i}}(t) - M_{\mathrm{M}}(t). \tag{D.23}$$

where

$$F_{\mathrm{i}}(t) \approx -M_{\mathrm{t}}\left[\hat{w}_{\mathrm{b}}(L_{\mathrm{b}}) + \frac{\mathrm{d}\hat{w}_{\mathrm{b}}(L_{\mathrm{b}})}{\mathrm{d}x}\left(\frac{L_{\mathrm{t}}}{2}\right)\right]\ddot{\varphi}(t), \tag{D.24}$$

$$M_{\mathrm{i}}(t) = -M_{\mathrm{t}}\left[\left(\frac{L_{\mathrm{t}}}{2}\right)\hat{w}(L_{\mathrm{b}}) + \frac{\mathrm{d}\hat{w}(L_{\mathrm{b}})}{\mathrm{d}x}\left(\frac{J_O}{M_{\mathrm{t}}} + r_{\mathrm{cm}}^2\right)\right]\ddot{\varphi}(t). \tag{D.25}$$

The equivalent tip mass M_{t}' is then derived from the virtual work done by these inertial terms, δW_{i}, over a virtual displacement $\delta w(L_{\mathrm{b}})$ and rotation $\delta\vartheta$. Based on Eq. 4.1,

$$\delta w(L_{\mathrm{b}}) = \hat{w}(L_{\mathrm{b}})\delta\varphi, \tag{D.26}$$

$$\delta\vartheta = \frac{d\hat{w}(L_{\mathrm{b}})}{\mathrm{d}x}\delta\varphi, \tag{D.27}$$

hence δW_{i} is given by

$$\delta W_{\mathrm{i}} = \left[F_{\mathrm{i}}(t)\hat{w}(L_{\mathrm{b}}) + M_{\mathrm{i}}(t)\frac{d\hat{w}(L_{\mathrm{b}})}{\mathrm{d}x}\right]\delta\varphi = M_{\mathrm{t}}'\ddot{\varphi}(t)\delta\varphi. \tag{D.28}$$

Putting Eqs. D.24-D.25 into Eq. D.28 and rearranging, we find the effective tip mass M_{t}' as

$$M_{\mathrm{t}}' = M_{\mathrm{t}}\left[\hat{w}_{\mathrm{b}}^2(L_{\mathrm{b}}) + L_{\mathrm{t}}\hat{w}_{\mathrm{b}}(L_{\mathrm{b}})\frac{d\hat{w}_{\mathrm{b}}L_{\mathrm{b}}}{\mathrm{d}x} + \left(\frac{d\hat{w}(L_{\mathrm{b}})}{\mathrm{d}x}\right)^2\left(\frac{J_O}{M_{\mathrm{t}}} + r_{\mathrm{cm}}^2\right)\right] \tag{D.29}$$

and by replacing the angle terms with the equivalent normalized notation from Eq. 4.6 in Eq. D.29 we get

$$M'_{\mathrm{t}} = M_{\mathrm{t}} \left[1 + \frac{L_{\mathrm{t}}}{L_{\mathrm{b}}} \hat{\vartheta} + \frac{r^2_{O'}}{L^2_{\mathrm{b}}} \hat{\vartheta}^2 \right]. \tag{D.30}$$

The value of $r^2_{O'}$ is then derived from Eqs. D.17-D.19,

$$\begin{aligned} r^2_{O'} &= \frac{J_O}{M_{\mathrm{t}}} + r^2_{\mathrm{cm}} \\ &= \frac{L^2_{\mathrm{t}}}{3} + \frac{\left(\rho_{\mathrm{s}} h^3_{\mathrm{t,S}} + \rho_{\mathrm{W}} h^3_{\mathrm{t,W}}\right)}{3\left(\rho_{\mathrm{s}} h_{\mathrm{t,S}} + \rho_{\mathrm{W}} h_{\mathrm{t,W}}\right)} + \frac{\rho_{\mathrm{s}} h_{\mathrm{t,S}} \left(h^2_b - h_b h_{\mathrm{t,S}}\right) + \rho_{\mathrm{W}} h_{\mathrm{t,W}} \left(h^2_b + h_b h_{\mathrm{t,W}}\right)}{\left(\rho_{\mathrm{s}} h_{\mathrm{t,S}} + \rho_{\mathrm{W}} h_{\mathrm{t,W}}\right)} \end{aligned} \tag{D.31}$$

The equivalent mass M_{eq} of the harvester is finally obtained by including the beam effective mass, which gives

$$M_{\mathrm{eq}} = \left(\rho_{\mathrm{s}} h_{\mathrm{s}} + \rho_{\mathrm{p}} h_{\mathrm{p}} + \rho_{\mathrm{el}} h_{\mathrm{el}}\right) \int_0^{L_{\mathrm{b}}} \left(\hat{w}(x)\right)^2 \mathrm{d}x + M_{\mathrm{t}} \left[1 + \frac{L_{\mathrm{t}}}{L_{\mathrm{b}}} \hat{\vartheta} + \frac{r^2_{O'}}{L^2_{\mathrm{b}}} \hat{\vartheta}^2 \right].$$

D.3 Squeeze film model equations

By considering the mass motion in Eq. 4.5, we can express the gap function h_{g} as:

$$h_{\mathrm{g}}(x,t) = h_0 \left(1 - \hat{w}_{\mathrm{m}}(x) \frac{\varphi(t)}{h_0} \right), \tag{D.32}$$

and based on our general assumptions, we can also linearize the Reynolds equation for small pressure and gap variations. The following normalization are applied to the gap function, $\tilde{h} = h_{\mathrm{g}}/h_0$, and the pressure field, $P^* = P/P_{\mathrm{a}}$. Doing so yields the linearized differential equation of the normalized pressure field P^* for a compressible 2D squeeze film, which is described by the classic Reynolds equation [19],

$$\frac{\partial^2 P^*}{\partial x^2} + \frac{\partial^2 P^*}{\partial y^2} - \frac{12\mu_{h_{0,\mathrm{eff}}}}{h^2_0 P_{\mathrm{a}}} \frac{\partial P^*}{\partial t} = \frac{12\mu_{h_{0,\mathrm{eff}}}}{h^2_0 P_{\mathrm{a}}} \frac{\partial \tilde{h}(x,t)}{\partial t}, \tag{D.33}$$

where $\mu_{h_{0,\mathrm{eff}}}$ is the fluid effective viscosity defined with respect to the gap. The derivative of the normalized gap function is expressed by:

$$\frac{\partial \tilde{h}(x,t)}{\partial t} = -\left[1 + \left(\frac{x}{L_{\mathrm{b}}} - 1 \right) \hat{\vartheta} \right] \frac{\varphi(t)}{h_0}. \tag{D.34}$$

Equation D.33 is then solved assuming ideal venting at the edges ($P = 0$) and using the Green function approach presented by Darling *et al.* [43] to solve for $P^*(x,y,t)$, expressed as a sum of

eigenmodes:

$$P^*(x,y,t) = \tilde{P}(x,y)\frac{\varphi_0}{h_0}\cos(\omega t + \psi). \tag{D.35}$$

$\tilde{P}(x,y)$ is the normalized spatial distribution of the pressure field:

$$\tilde{P}(x,y) = \sum_{mn} \phi_{mn} c_m c_n \begin{matrix}\cos\\ \sin\end{matrix}\left(\frac{m\pi(x-L_\mathrm{b})}{L_\mathrm{t}} - \frac{m\pi}{2}\right)\begin{matrix}\cos\\ \sin\end{matrix}\left(\frac{n\pi y}{b}\right), \tag{D.36}$$

where cos and sin are respectively used for odd and even indices of m,n. The coefficients c_m are computed from Eq. D.37

$$\begin{aligned} c_m &= \frac{2}{L_\mathrm{t}}\int_{L_\mathrm{b}}^{L_\mathrm{b}+L_\mathrm{t}} \left[1+\left(\frac{x}{L_\mathrm{b}}-1\right)\hat{\vartheta}\right] \begin{matrix}\cos\\ \sin\end{matrix}\left(\frac{m\pi(x-L_\mathrm{b})}{L_\mathrm{t}} - \frac{m\pi}{2}\right)\mathrm{d}x, \\ &= \begin{cases} (-1)^{(m-1)/2}\left[2\left(\frac{L_\mathrm{t}}{L_\mathrm{b}}\hat{\vartheta}+2\right)\right]/(\pi m) & \text{odd} \\ (-1)^{(m/2+1)} 2\frac{L_\mathrm{t}}{L_\mathrm{b}}\hat{\vartheta}/(\pi m) & \text{even} \end{cases}, \end{aligned} \tag{D.37}$$

whereas the values for c_n are given by Eq. D.38

$$c_n = \frac{2}{b}\int_{-b/2}^{b/2} \begin{matrix}\cos\\ \sin\end{matrix}\left(\frac{n\pi y}{b}\right)\mathrm{d}y = \begin{cases} (-1)^{(n-1)/2}4/(\pi n) & \text{odd} \\ 0 & \text{even.} \end{cases} \tag{D.38}$$

Equation D.39 finally provides the values of ϕ_{mn}

$$\phi_{mn} = \sigma_{mn}/(1+j\sigma_{mn}), \tag{D.39}$$

where

$$\sigma_{mn} = \frac{12\mu_{h_0,\mathrm{eff}}\omega}{\left[P_\mathrm{a}\pi^2 h_0^2\left(\frac{m^2}{L_\mathrm{t}^2}+\frac{n^2}{b^2}\right)\right]}. \tag{D.40}$$

Here σ_{mn} are equivalent to squeeze numbers for each of the converging sum terms. For large σ_{mn}, the fluid is compressible and contributes to an increased stiffness. Conversely, the pressure field is mainly dissipative for smaller σ_{mn}, which is the case for the geometries and frequency considered ($\sigma_{11} \approx 5\mathrm{E}-6$ at 1 atm), and therefore $P^* \approx \mathrm{Re}[P^*]$.

We can then derive $U_{\mathrm{D,f}}$ from Eq. 4.12 by using the pressure terms, from Eqs. D.35 to D.39, and mass displacement from Eq. 4.5. After integrating relatively to time, we get:

$$U_{\mathrm{D,f,squeeze}} = \frac{\pi P_\mathrm{a}\varphi_0^2}{h_0}\int_{L_\mathrm{b}}^{L_\mathrm{b}+L_\mathrm{t}}\int_{-b/2}^{b/2}\tilde{P}(x,y)\left[1+\left(\frac{x}{L_\mathrm{b}}-1\right)\hat{\vartheta}\right]\mathrm{d}y\mathrm{d}x \tag{D.41}$$

We finally obtain Q_{f} for the squeeze film by taking Eq. D.41 and Eq. 4.11 into Eq. 4.10,

$$Q_{\mathrm{f,squeeze}} = \frac{M_{\mathrm{eq}}\omega^2 h_0}{P_{\mathrm{a}} \int_{L_{\mathrm{b}}}^{L_{\mathrm{b}}+L_{\mathrm{t}}} \int_{-b/2}^{b/2} \tilde{P}(x,y) \left[1 + \left(\frac{x}{L_{\mathrm{b}}} - 1\right) \hat{\vartheta}\right] \mathrm{d}y\mathrm{d}x}. \tag{D.42}$$

APPENDIX E

Process flow parameters and mask layouts

This appendix consists in a detailed presentation of the process flow, which includes most of the recipe parameters and informations regarding the mask layouts.

Part A: Tungsten wafer preparation

Step 0: Tungsten wafer cleaning

- Tungsten wafers with 99% purity, 500 µm thickness, are bought from American Elements.
- Polished at Valley Design Corp, down to a final thickness of 440 µm.
- All substrates are cleaned before further processing.

W

	Process step	Parameters	Comments
1)	Surface degreasing/cleaning	Immerse in warm Remover 1165 (70°C, 24h)	
2)	Acetone rinse with ultrasonic agitation	5 min/side	
3)	IPA rinse	5 min/side	
4)	DI water rinse		Clean surface is hydrophilic. Gently scrub surface with wet cloth to remove residual slurry or tungsten particles. Concentrated HF or KOH can also be used to remove silica or alumina slurries from the surface, they don't attack W.
5)	Plasma O2 clean	5min, 300 mTorr, 150W	

Initial wafer

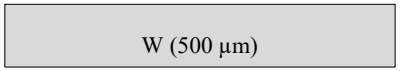

Step 1: Tungsten surface etching (1)

Mask M1 (align_etch)

- Dark field mask with positive photoresist. The dark areas are exposed and etched to produce three alignment marks

W

	Process step	Parameters	Comments
1)	Dehydrate on hot plate	5 min, >100°C	Wait for wafer to cool down
2)	Spin and bake MCC Primer	5s @ 500 RPM 30s @ 5000 RPM Bake 60s @ 110°C	Wait for wafer to cool down before spinning again
3)	Spin AZ 9245 (+) on front	60s @ 4000 RPM	Gives ~4 µm thick
4)	EBR	10s @ 1000 RPM	Gently scrub soaked Q-tip to wafer edge and spin dry
5)	Soft bake on hot plate	2min, 110°C	
6)	Expose resist using mask M1	40s @ 22,7 mW/cm^2	~2x exposition due to rough metal surface
7)	Develop resist	AZ400K:H2O (1:4) Immersion 2min30s	DI water rinse, nitrogen dry
8)	RIE etch	SF6, 100% flow O2, 10% 150W, 2min	Approx. 300 nm etch depth
9)	Strip resist	Acetone immersion	Scrub resist residue with cloth
10)	IPA rinse, nitrogen dry		
11)	Plasma O2 clean	150W, 5min, 300 mTorr	

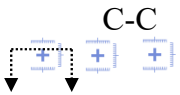

Crosses are etched on front for alignment

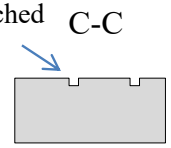

Step 2: Tungsten surface etching (2) + silicon nitride deposition

Mask M3 (oxide_etch)

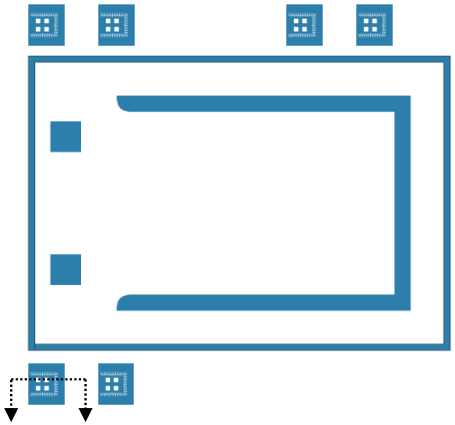

- Dark field mask with positive photoresist. The dark areas are exposed and etched.
- Front to back alignment, two sets of alignment marks are etch on the other side for future bond alignment
- Marks reused only for the alignment marks

Si3N4

W

	Process step	Parameters	Comments
1)	Dehydrate on hot plate	5 min, >100°C	Wait for wafer to cool down
2)	Spin and bake MCC Primer	5s @ 500 RPM 30s @ 5000 RPM Bake 60s @ 110°C	Wait for wafer to cool down before spinning again
3)	Spin AZ 9245 (+) on front	60s @ 4000 RPM	Gives ~4 µm thick
4)	EBR	10s @ 1000 RPM	Gently scrub soaked Q-tip to wafer edge and spin dry
5)	Soft bake on hot plate	2min, 110°C	
6)	Expose resist using mask M1	40s @ 22,7 mW/cm^2	~2x exposition due to rough metal surface
7)	Develop resist	AZ400K:H2O (1:4) Immersion 2min30s	DI water rinse, nitrogen dry
8)	RIE etch	SF6, 100% flow O2, 10% 150W, 2min	Approx. 300 nm etch depth
9)	Strip resist	Acetone immersion	Scrub resist residue with cloth
10)	IPA rinse, nitrogen dry		
11)	Plasma O2 clean	150W, 5min, 300 mTorr	
12)	PECVD of Si3N4 on front and back	Recipe: HFSiN 9min 200 nm thick	Hard mask

A-A

C-C

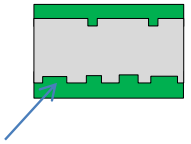

Squares are etched on back for alignment

Step 3: Top hard mask patterning

M10 (mass_top)

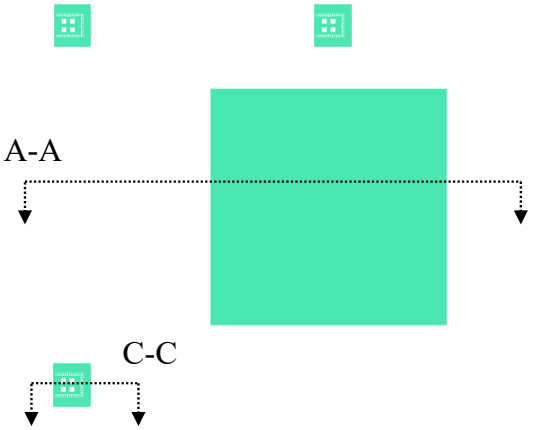

- Dark field mask with negative photoresist. The dark areas are protected from the wet etchant.
- A second exposure is done on the alignment marks using a special window mask (M13:exposition_window). The resist on top of the marks is fully exposed to protect them from the etch.
- 1 set of alignment marks is used for top alignment.

	Process step	Parameters	Comments
1)	Dehydrate on hot plate	5 min, >100°C	Wait for wafer to cool down
2)	Spin and bake MCC Primer	5s @ 500 RPM 30s @ 5000 RPM Bake 60s @ 110°C	Wait for wafer to cool down before spinning again
3)	Spin KMPR1005 (-) on front	30s @ 3000 RPM	Gives ~5 µm thick
4)	Soft bake on hot plate	5min, 100°C	
5)	Front alignment. Expose resist using mask M10	20s @ 22,7 mW/cm^2	~2x exposition due to metal surface
6)	Front alignment, expose resist using special exposition window	20s @ 22,7 mW/cm^2	~2x exposition due to metal surface. Protects align marks
7)	Post exposure bake on hot plate	2min @ 100°C	
8)	Develop resist	SU8 dev. Immersion 2min	DI water rinse, nitrogen dry
9)	RIE	CF4 (74% mass flow) 200W, 3 min 135 mTorr	Etches nitride but not tungsten
10)	Strip resist	Warm Remover 1165 immersion (70°C, 24h)	Scrub resist residue with cloth
11)	Acetone immersion, IPA rinse, nitrogen dry		
12)	Plasma O2 clean	150W, 5min, 300 mTorr	

Si3N4
W

A-A

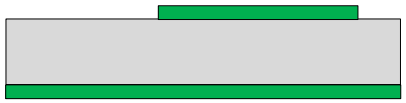

C-C

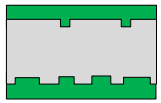

Step 4: Bottom hard mask patterning

M9 (mass_bottom)

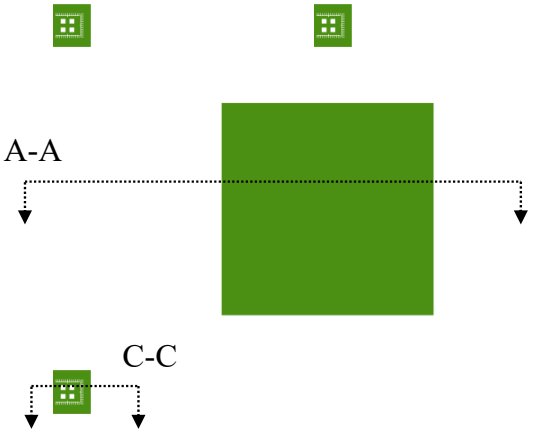

- Dark field mask with negative photoresist. The dark areas are protected from the wet etchant.
- A second exposure is done on the alignment marks using a special window mask (M13: exposition_window). The resist on top of the marks is fully exposed to protect them from the etch.
- Same set of alignment marks is used for bottom alignment. Mask M9 and M10 differ slightly to account for different undercut.

	Process step	Parameters	Comments
1)	Dehydrate on hot plate	5 min, >100°C	Wait for wafer to cool down
2)	Spin and bake MCC Primer	5s @ 500 RPM 30s @ 5000 RPM Bake 60s @ 110°C	Wait for wafer to cool down before spinning again
3)	Spin KMPR1005 (-) on back	30s @ 3000 RPM	Gives ~5 µm thick
4)	Soft bake on hot plate	5min, 100°C	
5)	*Front to* back alignment. Expose resist using mask M9	20s @ 22,7 mW/cm^2	~2x exposition due to metal surface
6)	Front to back alignment, expose resist using special exposition window	20s @ 22,7 mW/cm^2	~2x exposition due to metal surface. Protects align marks
7)	Post exposure bake on hot plate	2min @ 100°C	
8)	Develop resist	SU8 dev. Immersion 2min	DI water rinse, nitrogen dry
9)	RIE	CF4 (74% mass flow) 200W, 3 min 135 mTorr	Etches nitride but not tungsten
10)	Strip resist	Warm Remover 1165 immersion (70°C, 24h)	Scrub resist residue with cloth
11)	Acetone immersion, IPA rinse, nitrogen dry		
12)	Plasma O2 clean	150W, 5min, 300 mTorr	

Si3N4
W

A-A

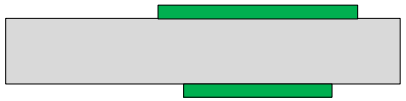

C-C

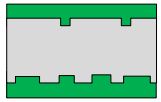

Step 5: W deep isotropic etching

Si3N4
W

	Process step	Parameters	Comments
1)	Wet etch	Buffered ferrocyanide solution immersion for at least 6h @ 60°C. DI water rinse	Put in special agitation container Rotate wafer regularly to enhance uniformity of etch. Should etch approx. 180 µm on each side (Est. Etch rate=0.5 to 0.6 µm/min) **Pin hole defects may appear at this step**
2)	DI water rinse		

A-A

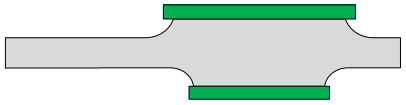

C-C

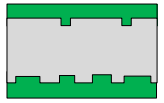

Etched motifs are protected on front and back

Part B: Device wafer preparation

Step 0: Initial device wafer

- 200 mm SOI wafers are bought from OKMETIC
- Piezoelectric aluminum nitride is deposited by RF sputtering. Supplied by Teledyne Dalsa
- Laser diced into smaller 100 mm and 3 inches wafers

AlN
SiO2
Si

A-A

Initial stack

AlN (1 µm)
<100> oriented doped Si (30 µm)
SiO_2 (0,5 µm)
<100> oriented Si (675 µm)

Step 1: Protective oxide and top electrode deposition

Cr
AlN
SiO2
Si

	Process step	Parameters	Comments
1)	O2 plasma clean	150W, 5 minutes	
2)	PECVD SiO2 deposition	Recipe: HFSiO Duration: 3 minutes 100 nm thick	AlN protection from resist developer
3)	Piranha etch (H2SO4:H2O2, 3:1)	15 minutes	
4)	DI water rinse		
5)	100 nm Cr evaporation	0.4 nm/s deposition rate	Blanket deposition top electrode metal

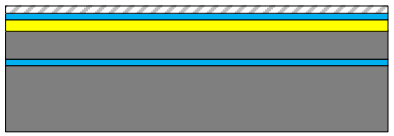

Mask M2 (top_metal)

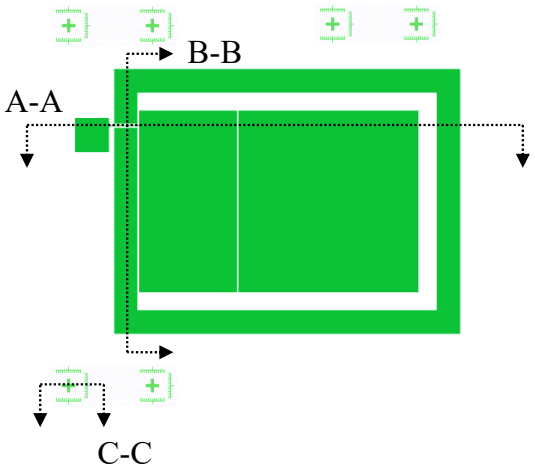

Step 2: Top Cr etching

- Bright field mask with positive photoresist. The shaded areas are where the Cr patterns are created.
- 2 sets of alignment marks patterned on top Cr layer.
- Top electrode is separated from mass area and frame area. Small gap is filled by PECVD deposited dielectric material.
- Metal is left on frame to keep same level for mass bonding and potential cap bonding

Cr
AlN
SiO2
Si

	Process step	Parameters	Comments
1)	Dehydrate on hot plate	5 min, >110°C	Wait for wafer to cool down
2)	Spin and bake MCC Primer on front	5s @ 500 RPM 30s @ 5000 RPM Bake 60s @ 110°C	Wait for wafer to cool down before spinning again
3)	Spin S1818 (+) on front	30s @ 5000 RPM	Gives ~1,5 µm thick (Brewer)
4)	Soft bake on hot plate	1min, 115°C	
5)	Expose resist using mask M2	8s @ 22,7 mW/cm^2	
6)	Develop resist	MF319 Immersion 40s	
7)	DI water rinse, nitrogen dry		
8)	Chrome etch	Immersion 1min15s	DI water rinse, iso etch
9)	Strip resist	Acetone	
10)	IPA/DI water rinse		
11)	O2 plasma clean	150W, 5 minutes	

A-A

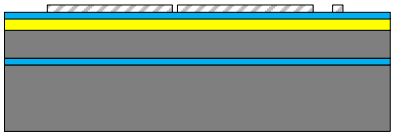

B-B

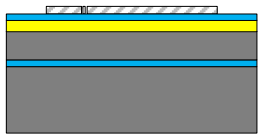

C-C

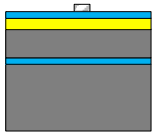

Step 3: Wafer thinning

- Wafer thinned down from the back side. Handle layer thinned from 675 µm down to 400 µm.
- Done externally by Aptek Industries
- Wafer edges are polished manually with wet fiber optic polishing paper and then rinse in DI water
- Thoroughly cleaned before further processing

	Process step	Parameters	Comments
1)	Solvent clean	Opticlear, 5 min Acetone, 5 min IPA, 5 min DI water rinsed, 2min	Ultrasonic agitation used with acetone
2)	Piranha clean	H2O2:H2SO4, 1:1 15 min DI water rinsed	
3)	SC1 clean	H2O:NH4OH:H2O2 (5:1:1) 75C, 15 min DI water rinsed	To remove particles
4)	DI water rinsed and nitrogen dried		

A-A

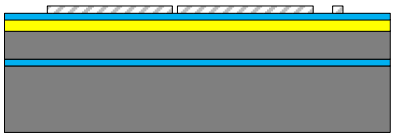

<100> oriented Si (400 µm)

Step 4: Backside marks etching

Mask M12 (backside_marks)

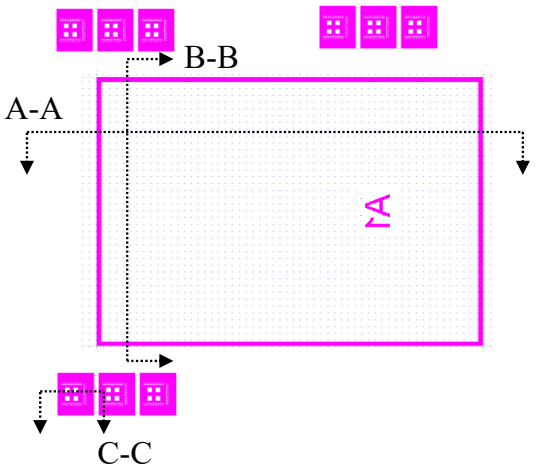

- Dark field mask with positive photoresist. The shaded areas are where the Si patterns are etched.
- 3 sets of alignment marks patterned on bottom Si layer.
- Dicing lines and device identification numbers are etched on wafer backside

	Process step	Parameters	Comments
1)	Dehydrate on hot plate	5 min, >110°C	Wait for wafer to cool down
2)	Spin and bake MCC Primer on front	5s @ 500 RPM 30s @ 5000 RPM Bake 60s @ 110°C	Wait for wafer to cool down before spinning again
3)	Spin AZ9245 (+) on back	60s @ 4000 RPM	Gives ~4,5 µm thick
4)	Soft bake on hot plate	2min, 110°C	
5)	Front to back alignement. Expose resist using mask M12	30s @ 22,7 mW/cm^2	
6)	Develop resist	AZ400K:H2O (1:4) Immersion 120s	
7)	DI water rinse, nitrogen dry		
8)	RIE etch	SF6, 100% flow, 160mTorr, 1 min, 200 W	~400 nm etch depth
9)	Strip resist	Acetone	
10)	IPA/DI water rinse		

A-A

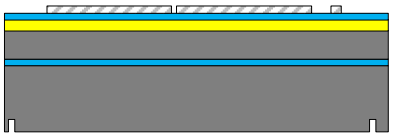

B-B

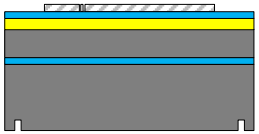

C-C

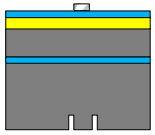

Step 5: SiO2 and Si3N4 PECVD deposition

Cr
AlN
SiO2
Si
Si3N4

	Process step	Parameters	Comments
1)	Piranha etch (H2SO4:H2O2, 3:1)	15min immersion	Remove resist residue DI water rinse
2)	PECVD of SiO2 on front	Recipe: Predep Time: 5min50s 2 µm thick	Surface passivation, planarize
3)	PECVD of Si3N4 on front	Recipe: HFSiN 9min 100 nm thick	Metal diffusion barrier, adhesion layer
4)	PECVD of SiO2 on back	Recipe: Predep 12min15s 4 µm thick	To make DRIE hard mask

A-A

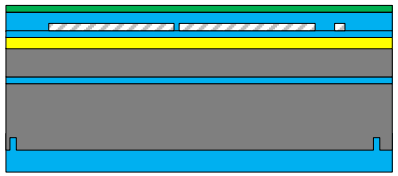

B-B

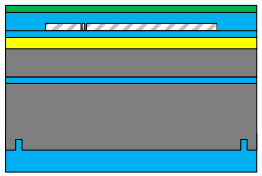

Step 6: Bottom oxide etching

Mask M11 (handle_si)

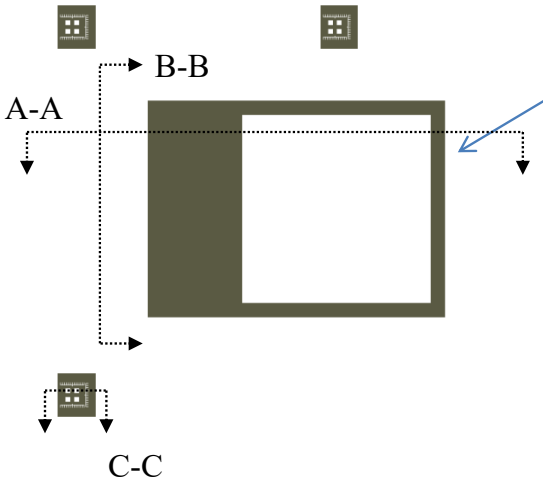

- Dark field mask with positive resist. The dark areas are exposed and etched.
- Front to back alignment realized using 1st set of align marks.
- Backside DRIE oxide hard mask definition

	Process step	Parameters	Comments
1)	Plasma O2	10 min, 150W, 300mTorr	Promote adhesion on oxide
2)	Spin and bake MCC Primer on front	5s @ 500 RPM 30s @ 5000 RPM Bake 60s @ 110°C	Wait for wafer to cool down before spinning again
3)	Spin AZ9245 (+) on backside	60s @ 2000 RPM	Gives ~6 µm thick
4)	Soft bake on hot plate	3min, 110°C	
5)	Alignment and expose resist using mask M11	30s @ 31,8 mW/cm^2	
6)	Develop resist	AZ400K:H2O (1:4) Immersion 5min	
7)	DI water rinse, nitrogen dry		
8)	Bond to support wafer	Crystal bond	
9)	Dry etch in AOE	Recipe: CF4Etch Time: 12min15s Depth: 4 um	
10)	Debond from support wafer	Heat wafer to 80°C to debond. Remove Crystal Bond with water rinse	
11)	Strip resist	Immerse in acetone	
12)	IPA rinse, nitrogen dry		

Cr
AlN
SiO2
Si
Si3N4

A-A

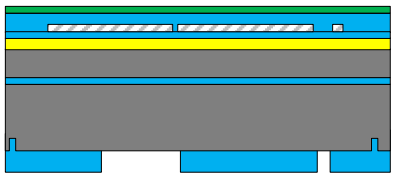

B-B

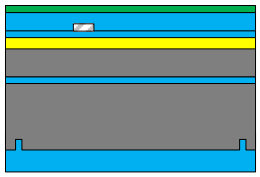

C-C

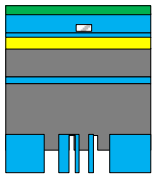

Step 7: Top nitride and oxide etching

Mask M3 (oxide etch)

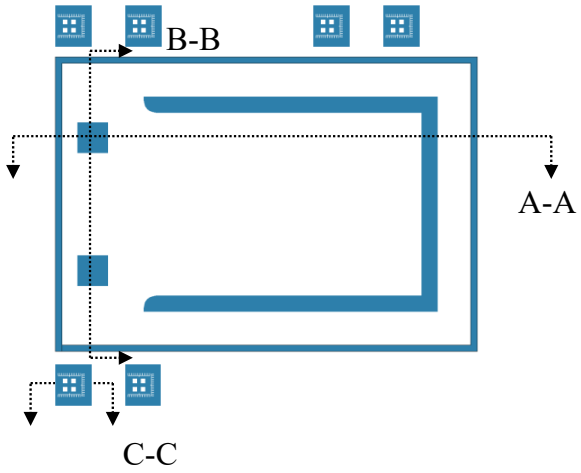

- Dark field mask with positive photoresist. The filled areas are exposed and etched away.
- 1st set of 3 alignment marks is used to align etching pattern, second etched marks used to create pit for Al mark deposition
- Side trenches area and wire bonding pads region exposed
- Etch stopped on protective oxide for AlN dry etch patterning

	Process step	Parameters	Comments
1)	Plasma O2	15 min, 150W, 300mTorr	Promote adhesion on oxide
2)	Spin and bake MCC Primer on front	5s @ 500 RPM 30s @ 5000 RPM Bake 60s @ 110°C	Wait for wafer to cool down before spinning again
3)	Spin AZ9245 (+) on front	60s @ 2000 RPM	Gives ~6 µm thick
4)	Soft bake on hot plate	3min, 110°C	
5)	Front alignment. Expose resist using mask M3	30s @ 31,8 mW/cm^2	
6)	Develop resist	AZ400K:H2O (1:4) Immersion 5min	
7)	DI water rinse, nitrogen dry		
8)	Bond to support wafer	Crystal bond	
9)	Dry etch in AOE	Recipe: CF4Etch Time: 4min30s Depth: 1.5um	Stop etch on protection SiO2, before exposing AlN
10)	Debond from support wafer	Heat wafer to 80°C to debond. Remove Crystal Bond with water rinse	
11)	Strip resist	Immerse in acetone	
12)	IPA rinse, nitrogen dry		
13)	Piranha etch (H2SO4:H2O2, 3:1)	15 min	Remove resist residue. DI water rinse

Cr
AlN
SiO2
Si
Si3N4

A-A

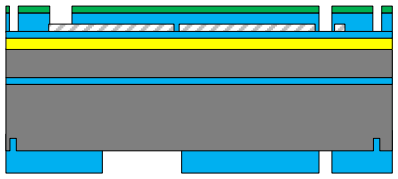

B-B

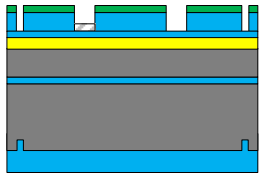

C-C

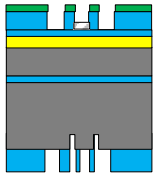

Step 8: AlN dry etching

Mask M4 (AlN_dry_etch)

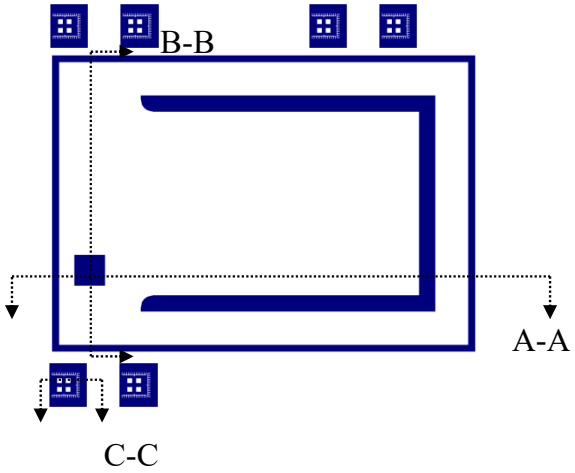

- Dark field mask with positive photo resist. The dark areas are exposed and etched.
- The photoresist stays on the top electrode top protect during the dry etch, but a window is etched to expose the bottom pad area
- Again, 1st and 2nd sets of marks are used for alignment.
- Wide side trenches are defined around the beam
- Protective oxide is removed before etching AlN

	Process step	Parameters	Comments
1)	Plasma O2	15 min, 150W, 300mTorr	Promote adhesion on oxide
2)	Spin and bake MCC Primer on front	5s @ 500 RPM 30s @ 5000 RPM Bake 60s @ 110°C	Wait for wafer to cool down before spinning again
3)	Spin AZ9245 (+) on front	60s @ 2000 RPM	Gives ~6 µm thick
4)	Soft bake on hot plate	3min, 110°C	
5)	Front alignment. Expose resist using mask M3	30s @ 31,8 mW/cm^2	
6)	Develop resist	AZ400K:H2O (1:4) Immersion 5min	Watch for attack of AlN by developer
7)	DI water rinse, nitrogen dry		
8)	Residual SiO2 RIE	CF4, 74%, 200W, 3 min	Removes any SiO2 before etching AlN
9)	Bond to support wafer	Crystal bond	
10)	Dry etch in ICP III-V	BCl3+Cl2+Ar recipe. Approx 4min etch time	
11)	Debond from support wafer	Heat wafer to 80°C to debond. Remove Crystal Bond with water rinse	
12)	Strip resist	Immerse in acetone	
13)	IPA rinse, nitrogen dry		
14)	Piranha etch (H2SO4:H2O2, 3:1)	15 min	Remove resist residue. DI water rinse

Cr
AlN
SiO2
Si
Si3N4

A-A

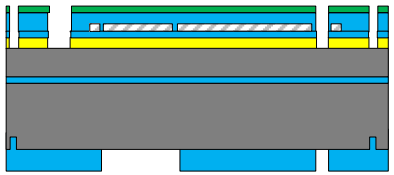

B-B

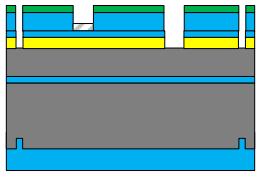

C-C

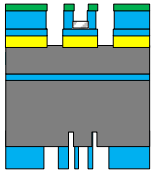

Step 9: Al pad lift-off and anneal

Mask M5 (pad metal)

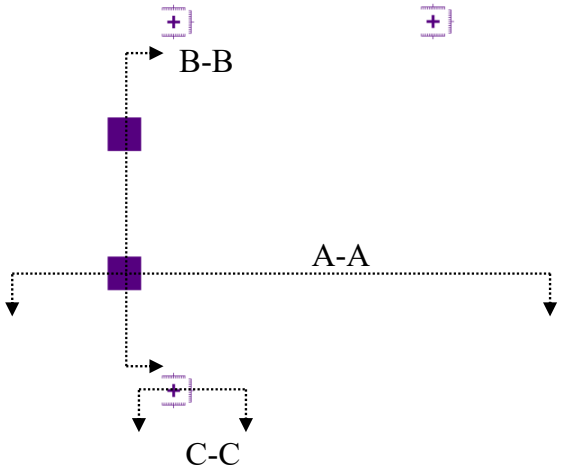

- Bright field mask with negative photoresist. The filled areas are masked and show where the resist is removed and Al is sputtered.
- Second set of three alignment marks used.
- Al pad deposition for good adhesion and contact with wire bonded Al wire
- Remaining oxide is etched just before Al deposition

	Process step	Parameters	Comments
1)	Dehydrate on hot plate	5 min, >100°C	Wait for wafer to cool down
2)	Spin and bake MCC Primer on front	5s @ 500 RPM 30s @ 5000 RPM Bake 60s @ 110°C	Wait for wafer to cool down before spinning again
3)	Spin NR4-8000P (-) on front	30s @ 4000 RPM	Gives ~6 µm thick
4)	Soft bake on hot plate	4min, 130°C	(plate temperature)
5)	Front alignment. Expose resist using mask M5	60s @ 31,8 mW/cm^2	
6)	Post exposure bake on hot plate	5 min, 90°C	
7)	Develop resist	MF319 Immersion 2 to 3 min	DI water rinse, nitrogen dry
8)	O2 plasma (descum)	50W, 3minutes	
9)	Desox, HF:H2O (1:10)	Immersion 1 min	To remove any oxide from pad area
10)	Al + Cap layer sputtering deposition	1 um Al + 50 nm cap layer	Cap layer: **Si3N4**, SiO2 or TiN
11)	Strip resist	Warm Remover 1165 (70°C)	To minimize flakes, avoid ultrasonic agitation and use sucessive remover bath before drying
12)	Acetone immersion, IPA rinse, nitrogen dry		
13)	Plasma O2 clean	150W, 5min, 300 mTorr	
14)	Thermal annealing in furnace	450°C, 30min, forming gaz	Form ohmic contact with silicon

Cr
AlN
SiO2
Si
Si3N4
Al

A-A

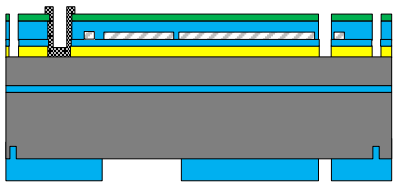

B-B

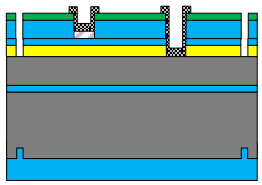

C-C

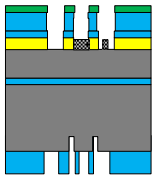

Step 10: Metal bonding layers lift-off (optional)

Mask M6 (bond_metal_1)

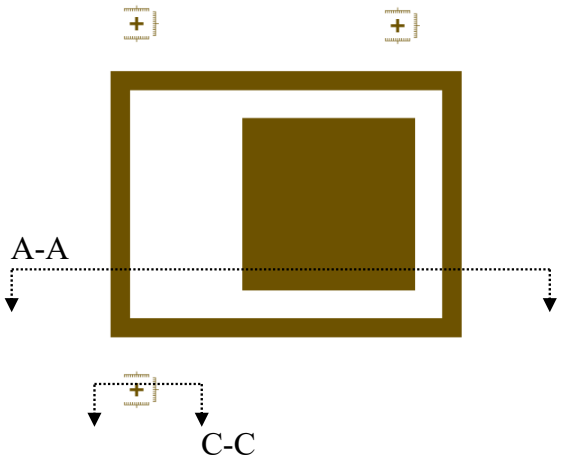

- Bright field mask with negative photoresist. The filled areas are masked and show where the resist is removed and metals are evaporated.
- 2nd set of alignment marks is reused to align lift-off pattern.
- Mass bonding area defined on the beam
- 400-200 µm wide seal ring is defined on the frame for potential vacuum packaging

	Process step	Parameters	Comments
1)	Dehydrate on hot plate	5 min, >100°C	Wait for wafer to cool down
2)	Spin and bake MCC Primer on front	5s @ 500 RPM 30s @ 5000 RPM Bake 60s @ 110°C	Wait for wafer to cool down before spinning again
3)	Spin NR4-8000P (-) on front	30s @ 4000 RPM	Gives ~6 µm thick
4)	Soft bake on hot plate	4min, 130°C	
5)	Front alignment. Expose resist using mask M6	60s @ 31,8 mW/cm^2	
6)	Post exposure bake on hot plate	5min, 90°C	
7)	Develop resist	MF319 Immersion 2min	DI water rinse, nitrogen dry
8)	Cr/Au deposition by e-beam evaporation	Cr: 20 nm thick Au: 500 nm thick	If Al flakes present, etch with Metal Etch E6 before deposition.
9)	Strip resist	Warm Remover 1165 (70°C) or acetone	To minimize flakes, avoid ultrasonic agitation, use sucessive remover bath before drying
10)	DI water rinse, IPA rinse, nitrogen dry		
11)	Plasma O2 clean	150W, 5min, 300 mTorr	

Cr
AlN
SiO2
Si
Si3N4
Al
Au

A-A

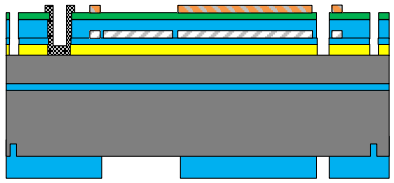

C-C

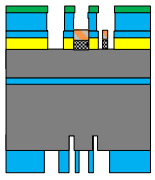

Step 11: Device layer deep silicon etching

Mask M7 (device_si)

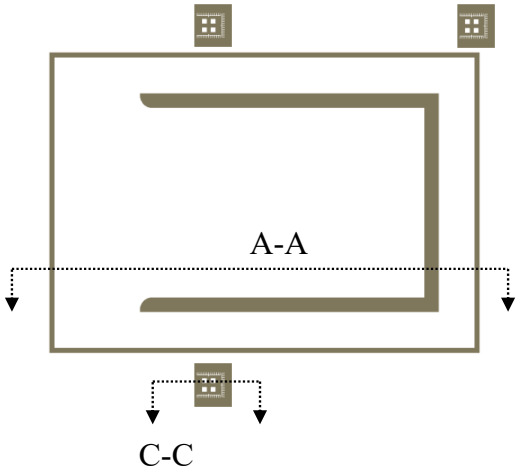

- Dark field mask with positive photoresist. The shaded areas are exposed and show where the device layer Si is etched.
- 3rd set of alignment marks is used to align etching pattern. Surface is protected by oxide to avoid contamination
- Wide side trenches are defined around the beam
- All exposed metallic contaminants are etched just before DRIE

	Process step	Parameters	Comments
1)	Dehydrate on hot plate	5 min, >100°C	Wait for wafer to cool down
2)	Spin and bake MCC Primer on front	5s @ 500 RPM 30s @ 5000 RPM Bake 60s @ 110°C	Wait for wafer to cool down before spinning again
3)	Spin AZ9245 (+) on front + Soft bake on hot plate	5s @ 500 RPM 60s @ 2000 RPM Bake: 120 s, 110°C	Gives ~6 µm thick Dynamic spread to avoid bubble formation
4)	Front alignment. Expose resist using mask M6	30s @ 22,7 mW/cm^2	
5)	Develop resist	AZ400K (1:4) Immersion 3min or more	DI water rinse, nitrogen dry
6)	Au/Cr wet etch	Gold etch, 21min RT, agitate Cr etch, 20s RT, agitate	To avoid metal residues and ASE-STS chamber contamination
7)	Cap Si3N4 RIE	CF4, 74%, 200W, 5 min	Remove nitride capping before etching Al
8)	Al wet etch	Al etch 16:2:2:1, 70°C, 3min, agitate	To avoid metal residues and ASE-STS chamber contamination
7)	Temporary bonding on glass+DRIE	Recipe: DEEP Time: 8:26	30 µm etch depth
8)	Acetone immersion, IPA rinse, nitrogen dry		Resist strip

Cr
AlN
SiO2
Si
Si3N4
Al
Au

A-A

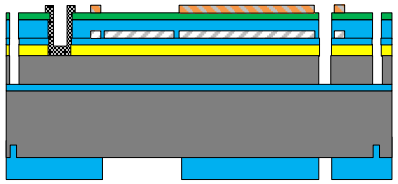

C-C

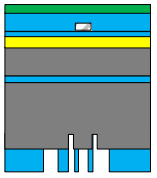

Part C: Wafer bonding (eutectic)

Step 1: Metal bond deposition with shadow mask

- Metal deposition on patterned wafer using a shadow mask
- The shadow mask has no alignment marks
- Coarse alignment done using the rectangular features under a microscope

	Process step	Parameters	Comments
1)	Bottom Si3N4 RIE	74% mass flow, 200W, 3min	Bottom nitride mask is removed before metal deposition to improve adhesion
2)	Cr/Au/Sn/Au deposition by e-beam evaporation	Cr: 20 nm thick Au: 300 nm thick Sn: 500 nm thick A: 50 nm thick	Stack thicknesses calculated to have 81.7%wt Au after bonding (Au rich relative to eutectic). Top Au layer to prevent Sn oxidation.

Si3N4
W
AuSn

A-A

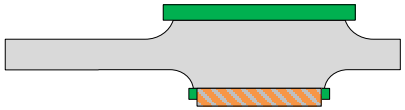

C-C

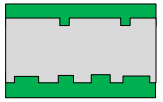

Step 2: Wafer bonding

- Flux-less bonding due to gold capping layer
- Requires optical alignment (can be done on EVG620)

	Process step	Parameters	Comments
1)	Clean wafer surfaces	Diluted HF (10:1), 1min	
2)	Optical alignement	EVG60 aligner No flags	
3)	Wafer bonding	300°C 1 kN 20 minutes dwell time	*Process not validated*

Cr
AlN
SiO2
Si
Si3N4
Al
Au
W

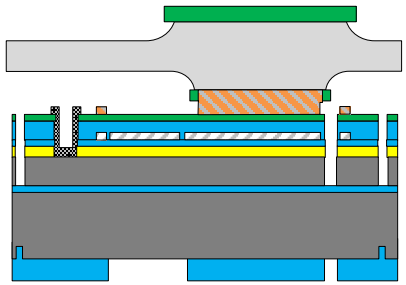

Part D: Mass and cantilever definition

Step 1: W wet etch and mass release

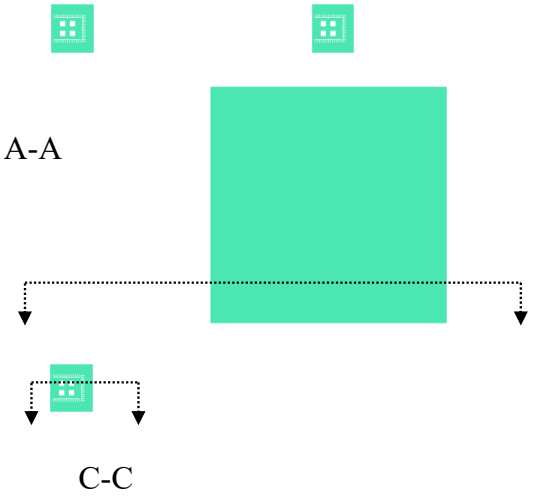

- Shaded areas are protected from the etchant by the hard mask. Etch is completed from the top only

	Process step	Parameters	Comments
1)	Wet etch	Buffered ferrocyanide solution immersion for at approx. 6 hours @ ~60°C. DI water rinse	Put in special agitation container Rotate wafer regularly to enhance uniformity of etch. **Est. etch rate ~0.5 to 0.6 µm/min**
2)	DI water rinse, nitrogen dry		

A-A

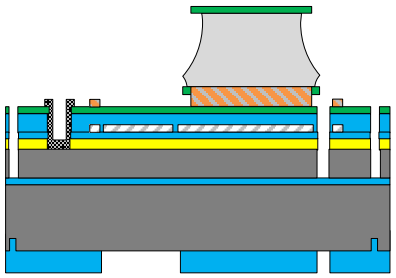

C-C

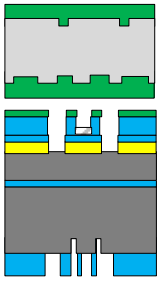

Step 2: Temporary carrier bond, handle layer deep silicon etching, BOX etching

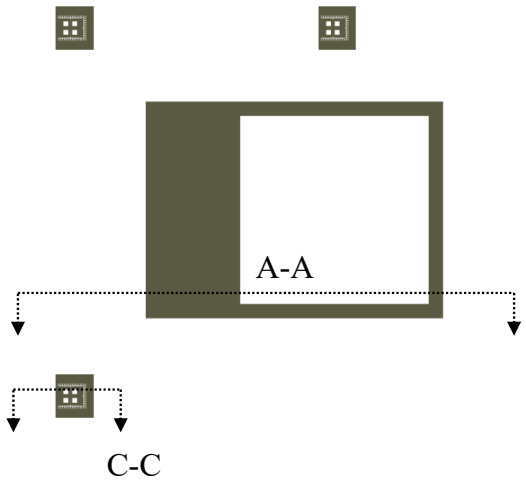

- Hard mask patterned on the back of the wafer previously is used for the DRIE etch.
- The wafer is mounted on a temporary glass carrier for this processing step.

	Process step	Parameters	Comments
1)	Glass carrier bonding	Heat wafer over 120°C on hot plate Speard thick Crystalbond 509 layer over metal proof masses Repeat on glass carrier Stack both wafers on hot plate	Put in vacuum and heat to remove trapped air Put weight (e.g. 1kg) over stack while hot to push trapped bubles out Clean stack edges to remove excess crystalbond
2)	Handle layer DRIE	Recipe: DEEP Time: 1h40 min	400 µm etch depth
3)	Acetone immersion, IPA rinse, nitrogen dry		Resist strip
4)	Backside oxide etch	HF:H2O (10:1), 20 min	Remove BOX and expose dicing lines
5)	Wafer dicing		
6)	Acetone immersion, IPA rinse, water rinse, air dry		Die separation from carrier glass. Do not use water or nitrogen jet
NOTE	For the DRIE step, after bonding to the carrier, a resist mask can also be used with these parameters		
*	Spin AZ9245 (+) on device wafer + Soft bake on hot plate (dual layer process)	5s @ 500 RPM 60s @ 2000 RPM (x2) Bake 1: 100s, 110°C Bake 2: 180s, 110°C	Gives ~14,5 µm thick Bake between each spin Dynamic spread to avoid bubble formation in bottom layer

Cr
AlN
SiO2
Si
Si3N4
Al
Au
W

A-A

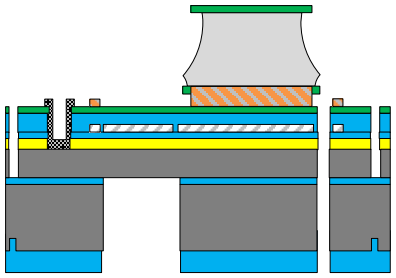

C-C

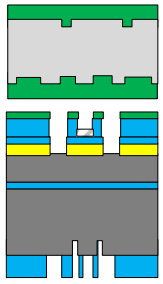

Mask layouts

Mask M1: align_etch

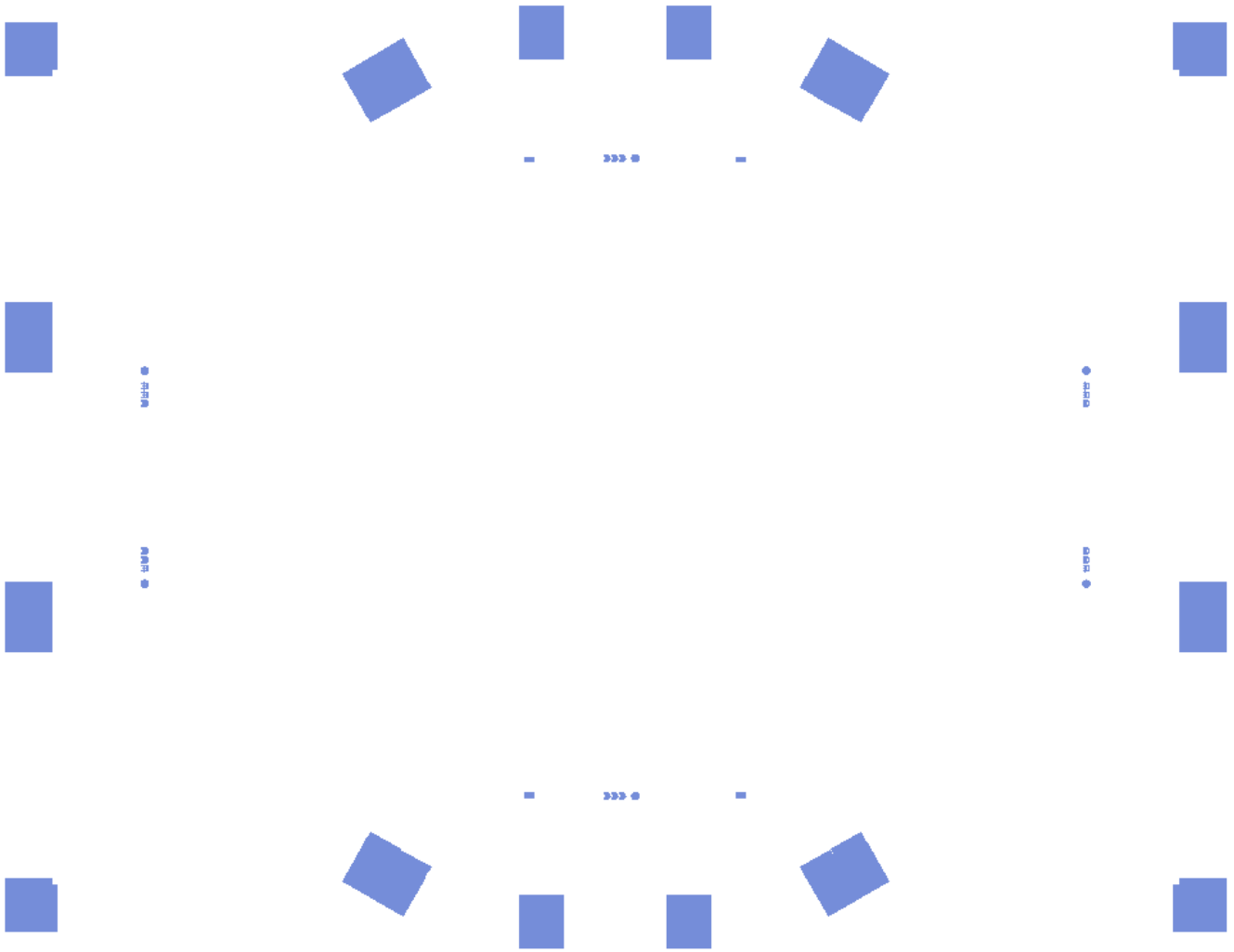

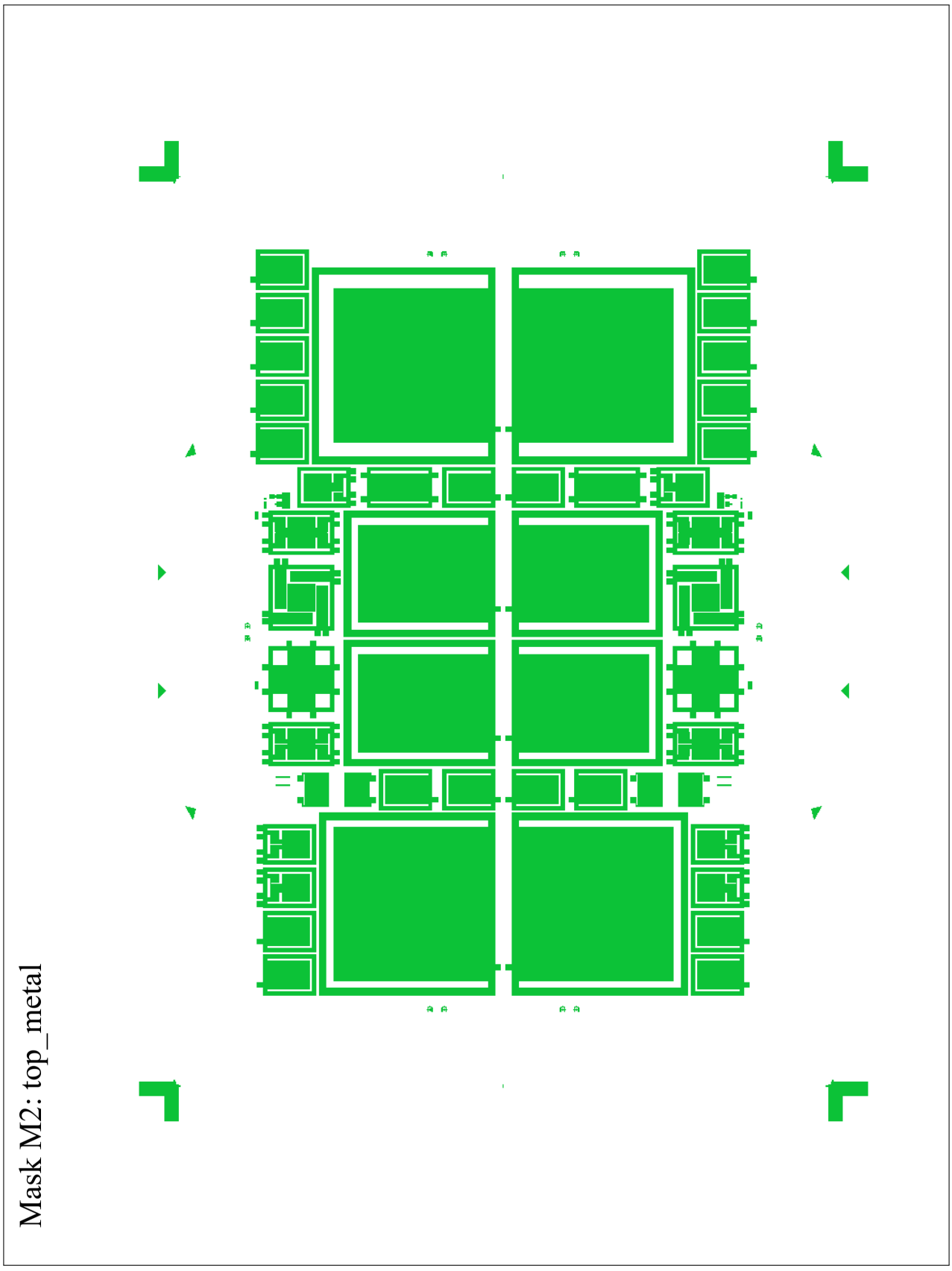

Mask M2: top_metal

Mask M3: oxide_etch

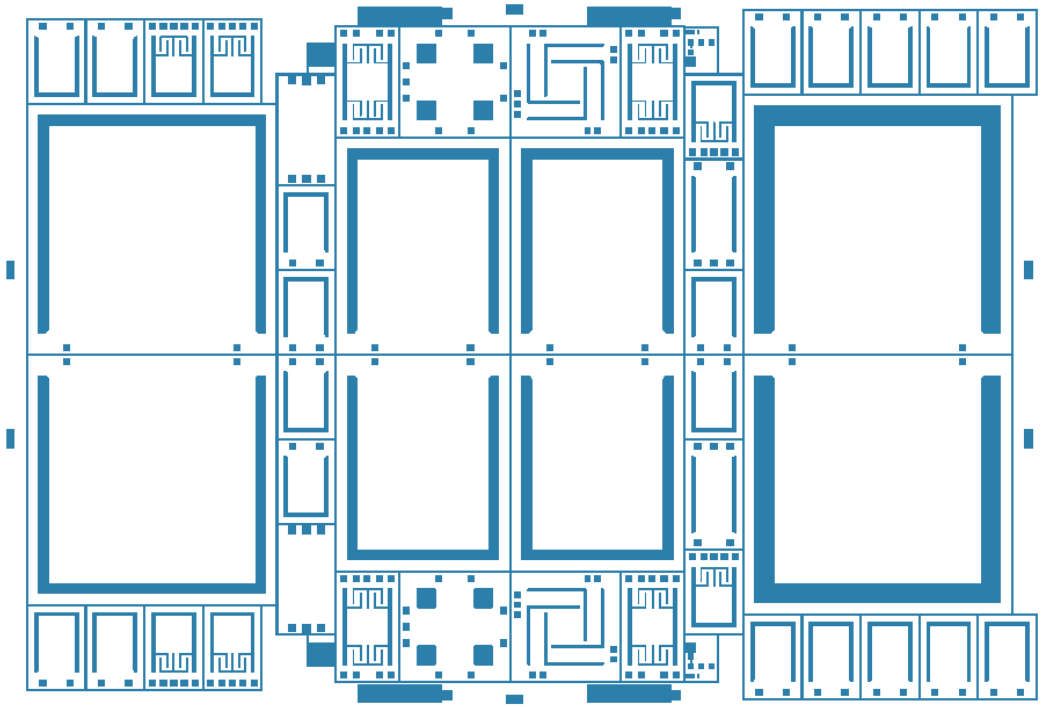

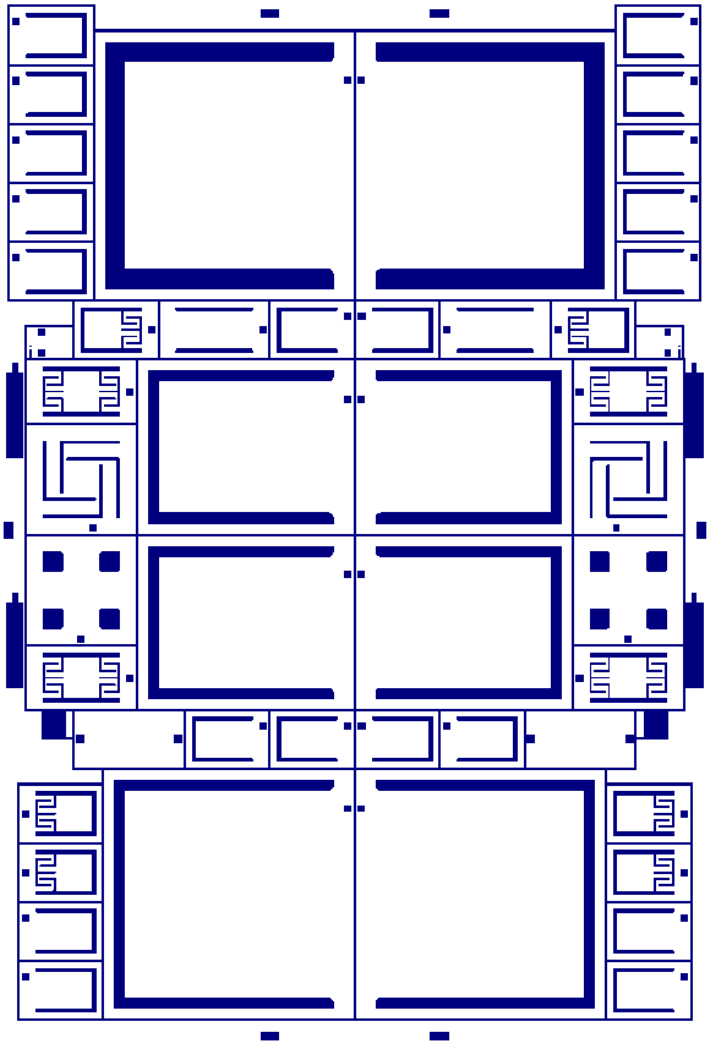

Mask M4: AlN_dry_etch

Mask M5: pad_metal

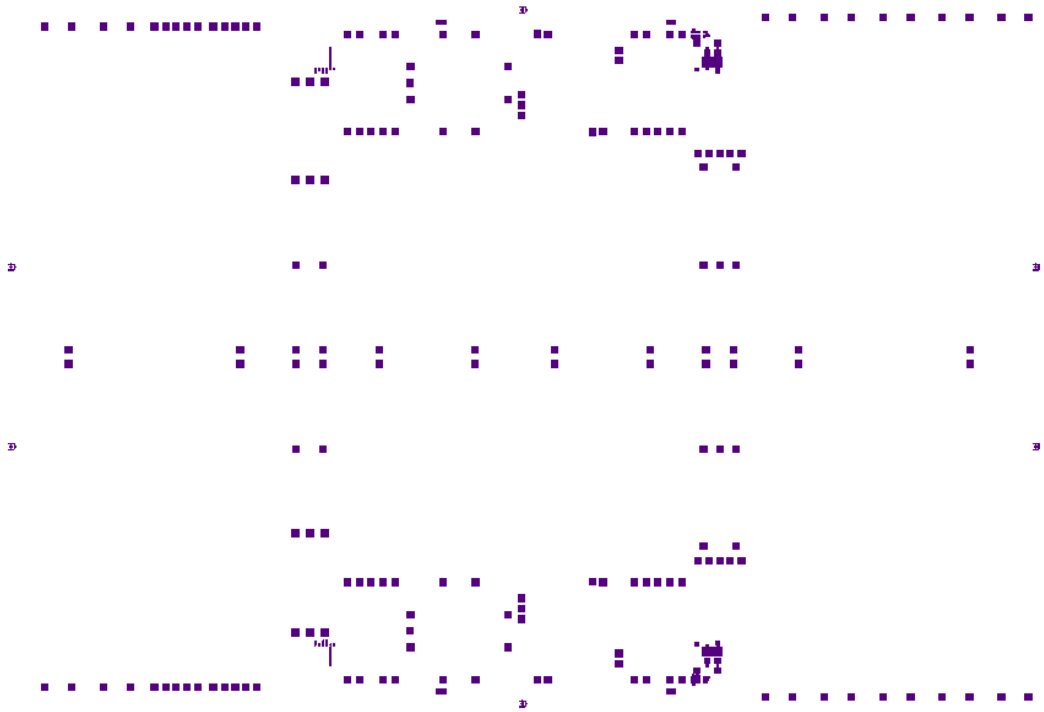

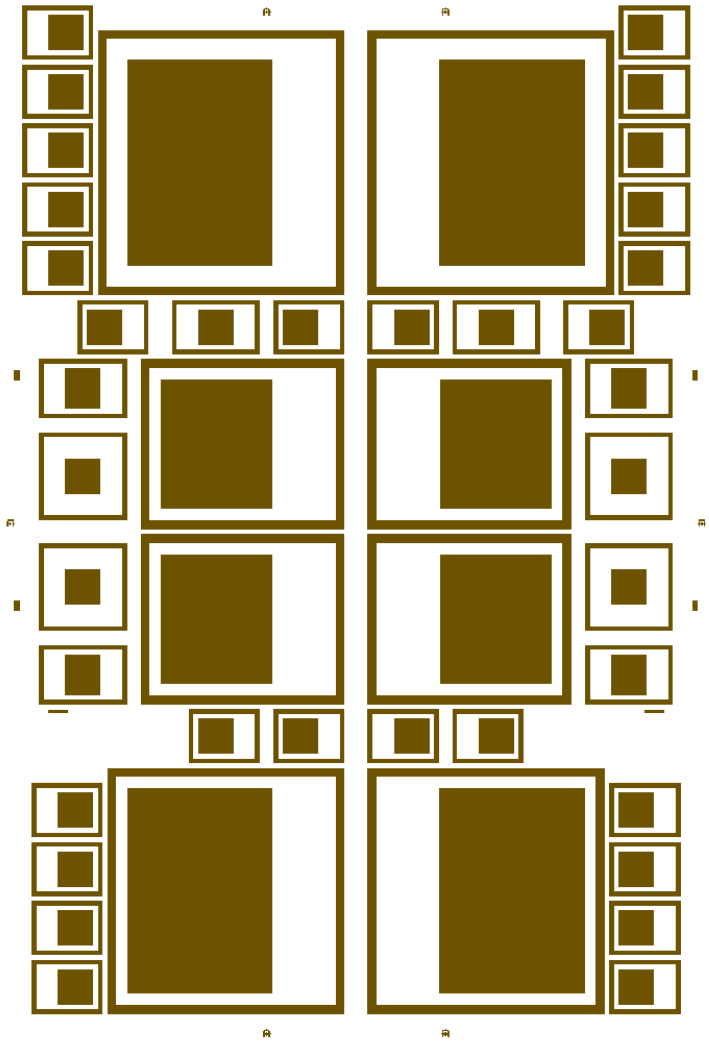

Mask M6: metal_bond_1

Mask M7: device_si

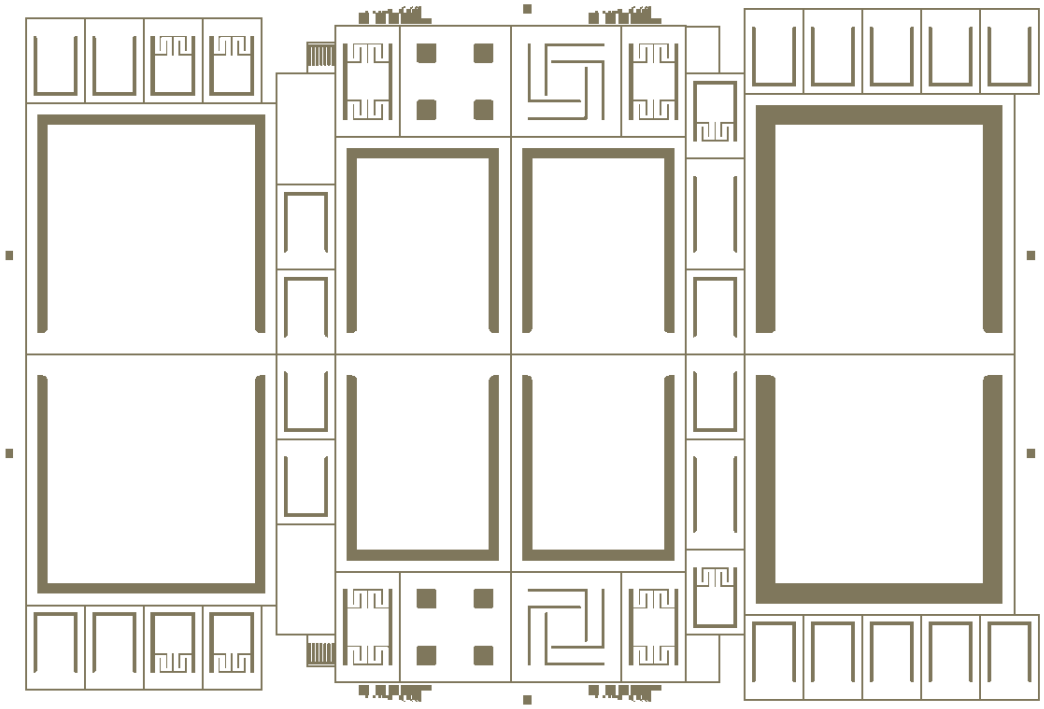

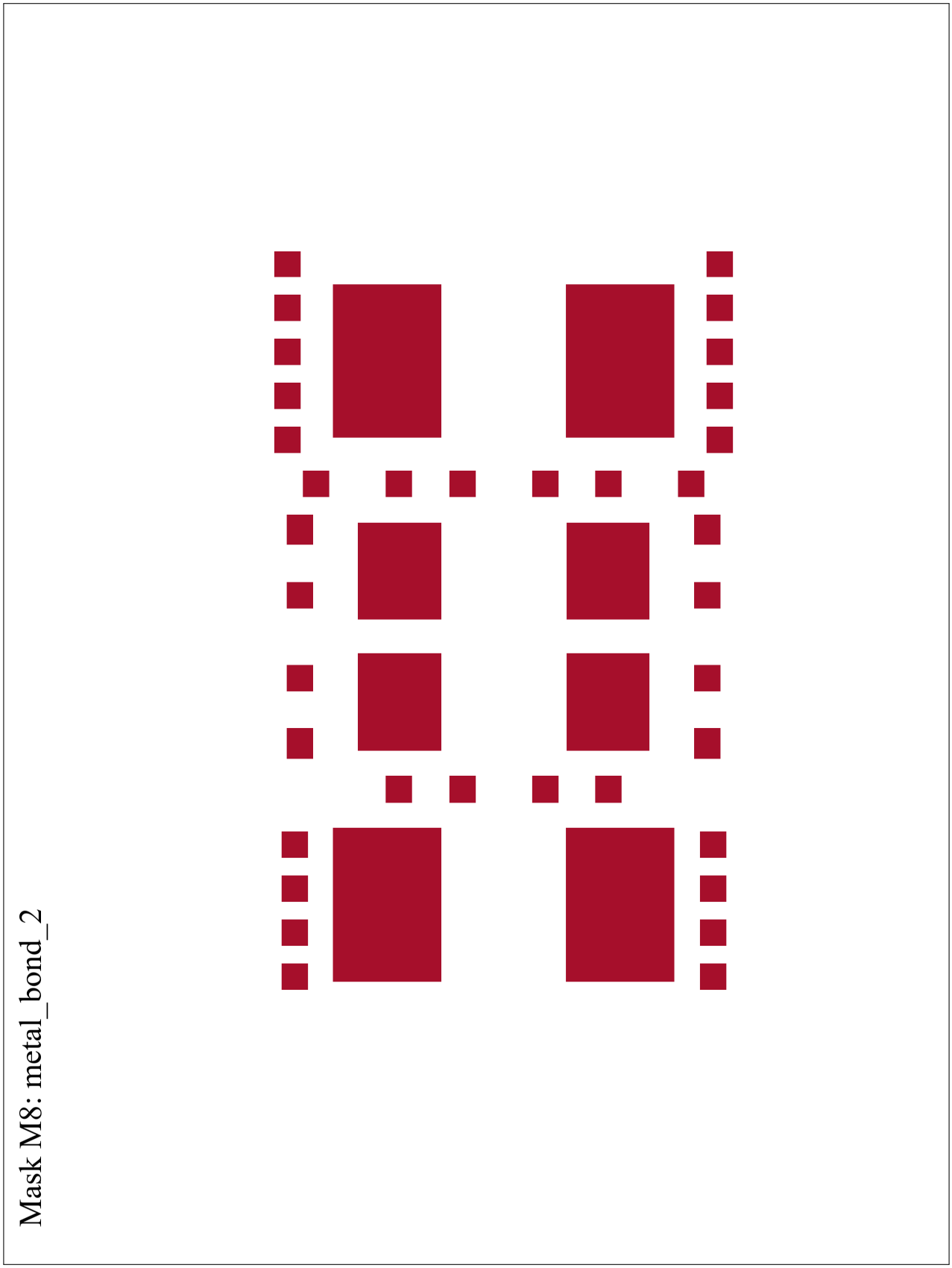
Mask M8: metal_bond_2

Mask M9: mass_bottom

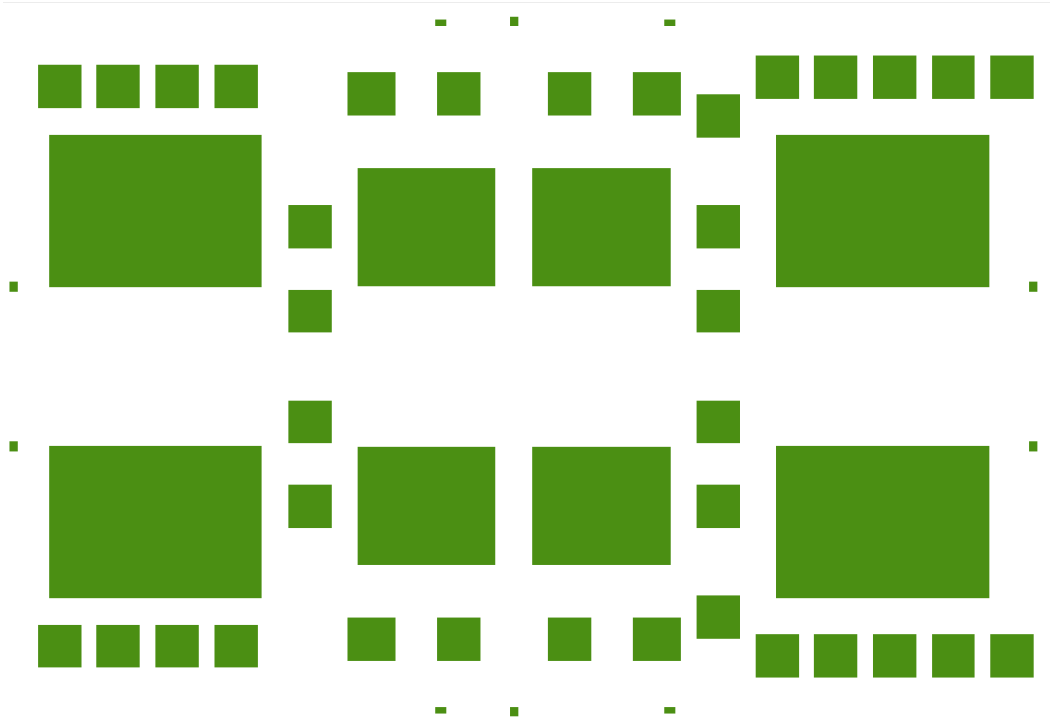

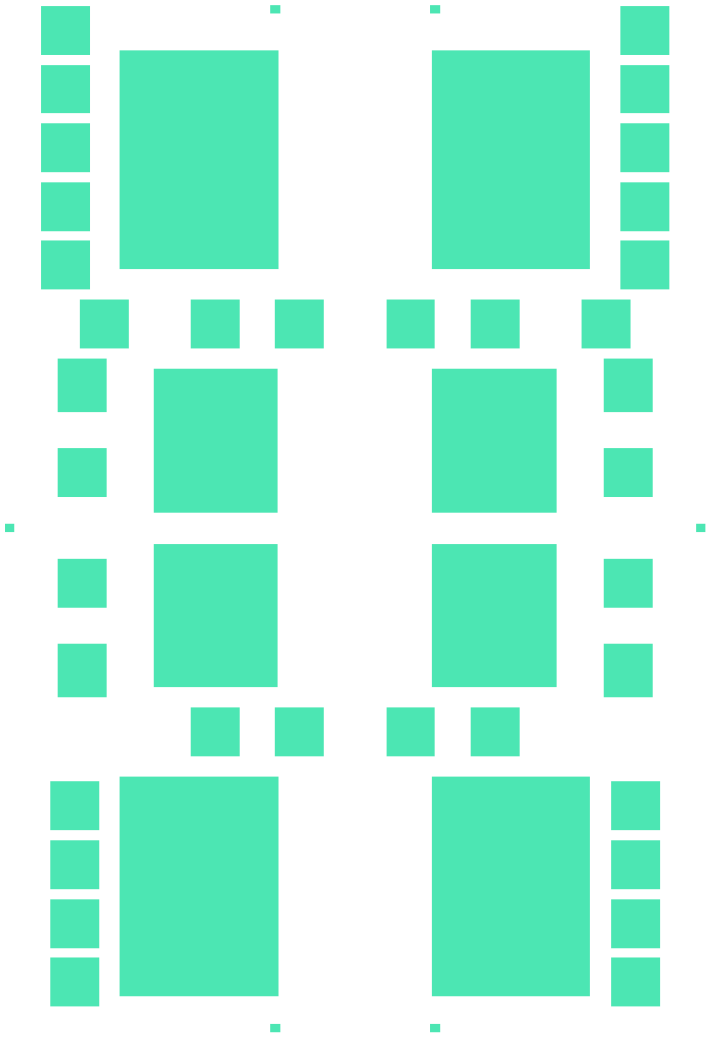

Mask M10: mass_top

Mask M11: handle_si

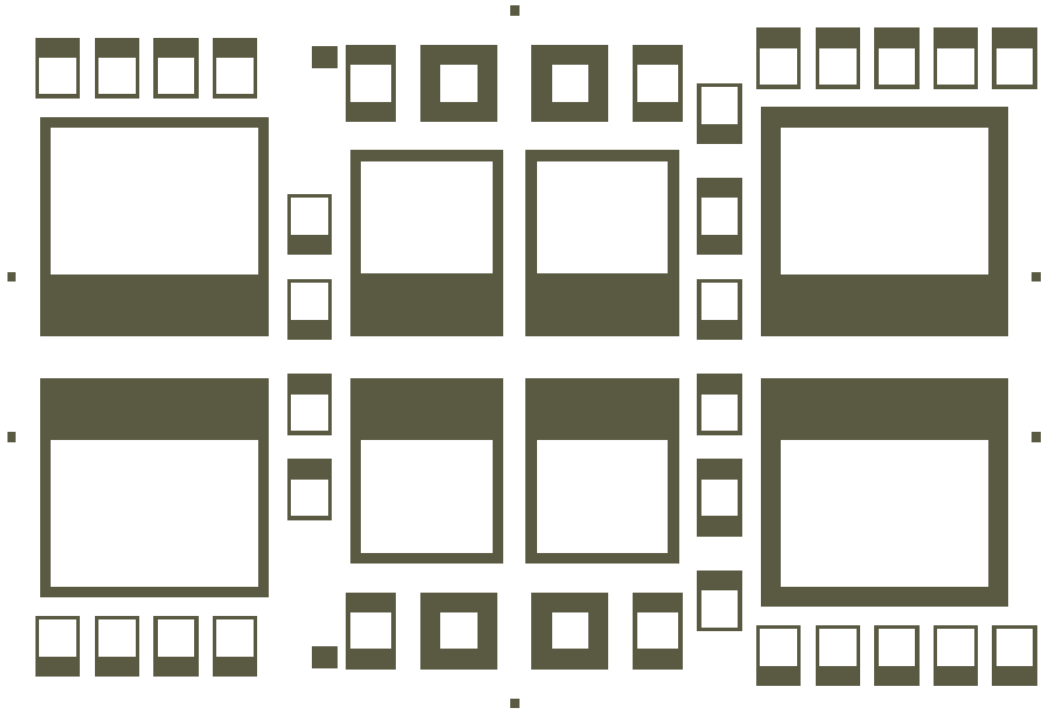

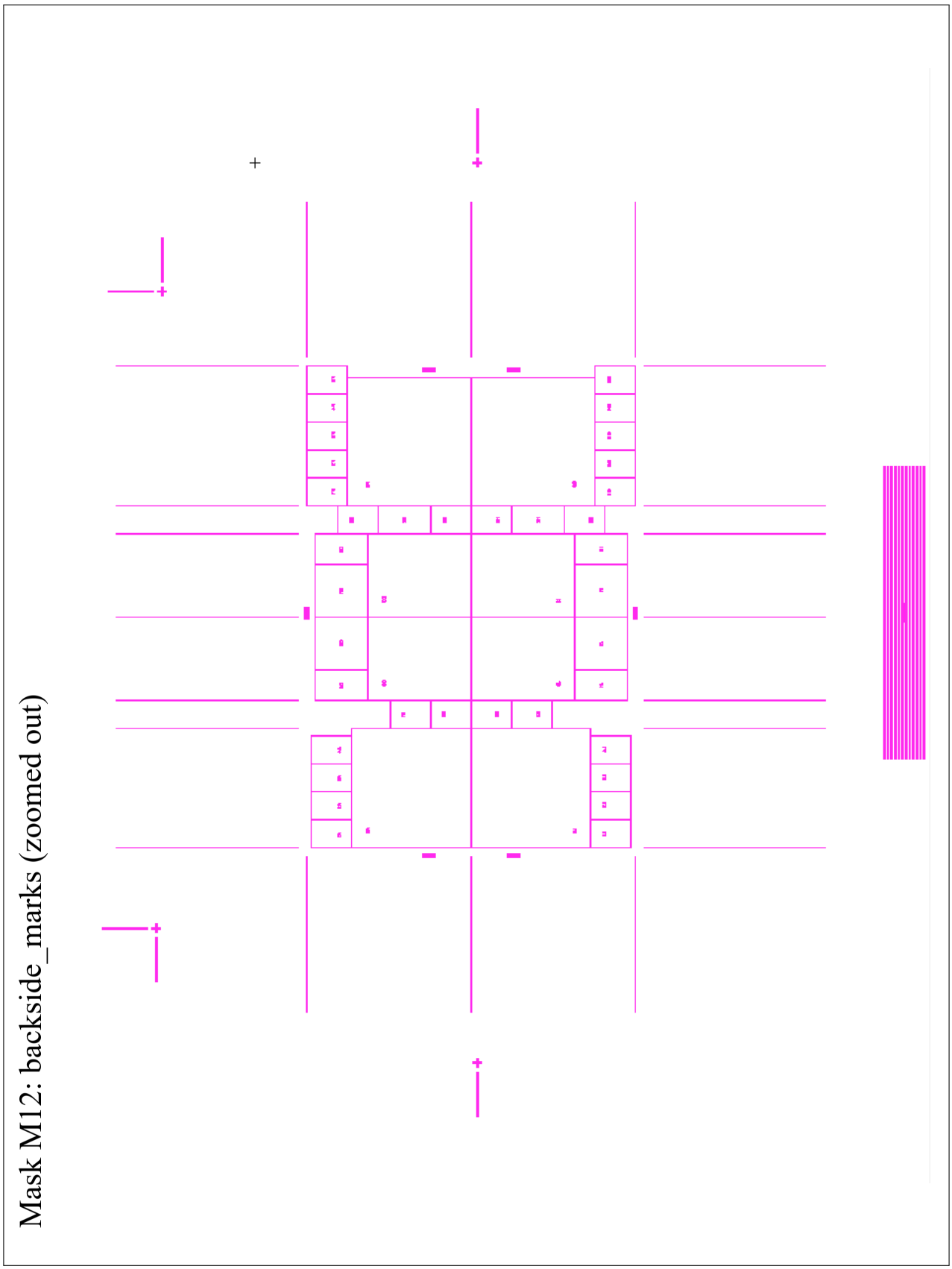

Mask M12: backside_marks (zoomed out)

Mask M13: exposition_window

APPENDIX F

Experimental results for all test devices

F.1 Voltage and power FRF variations with the resistance

As stated in section 6.2.1, our designs have been tested with various acceleration levels and frequency ranges. Plotting the FRFs compensate for the acceleration input that is not always flat over the full duration of each test and mostly fluctuate close to resonance. Nevertheless, the nominal level of acceleration for each test run is provided for reference. The FRFs and the peak output values for each load of each device are plotted in Figures F.1 to F.8.

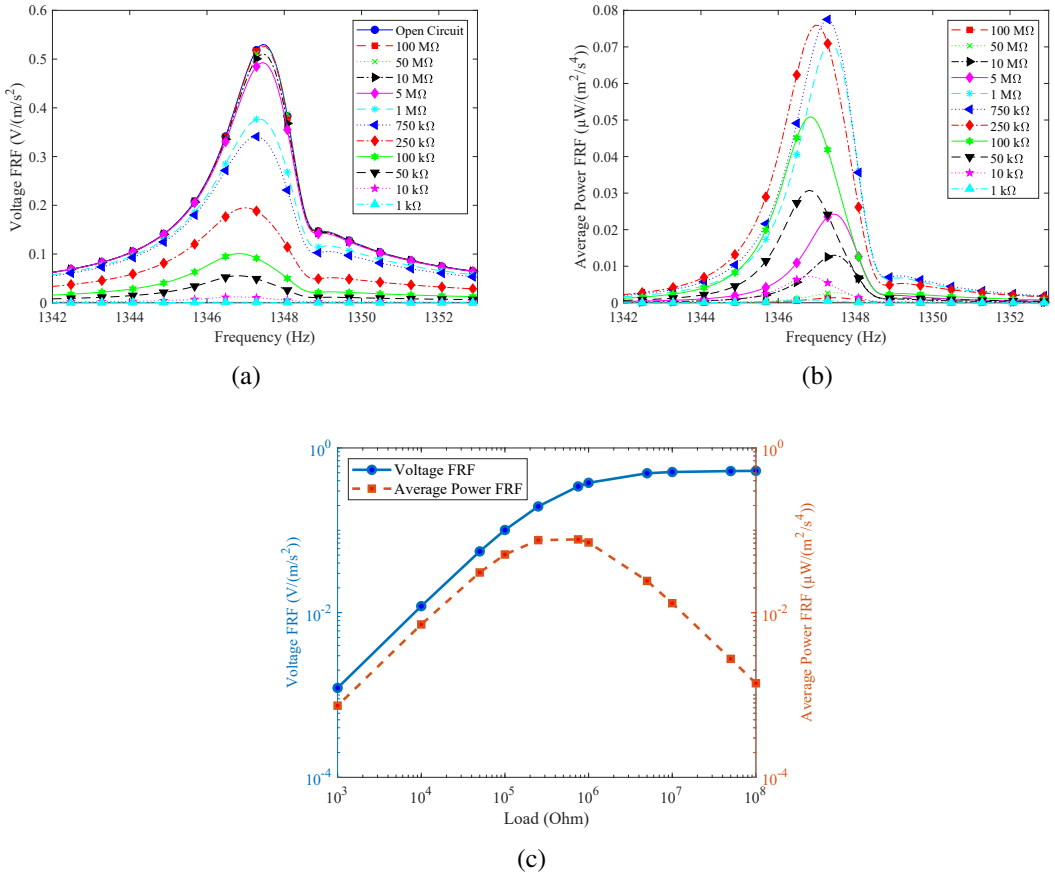

Figure F.1 Device G5 voltage FRF (a), average power FRF (b) and outputs at peaks (c) as a function of the connected resistance. Nominal amplitude of acceleration: 5 m/s^2.

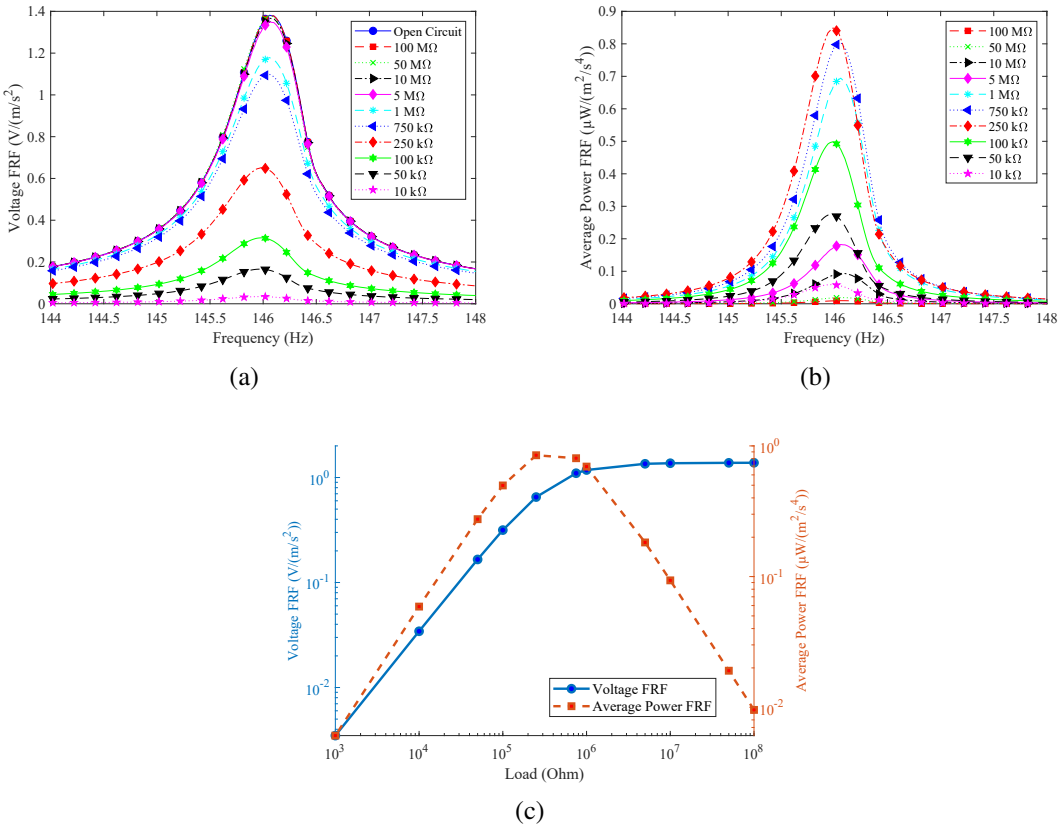

Figure F.2 Device J3 voltage FRF (a), average power FRF (b) and outputs at peaks (c) as a function of the connected resistance. Nominal amplitude of acceleration: 1 m/s^2.

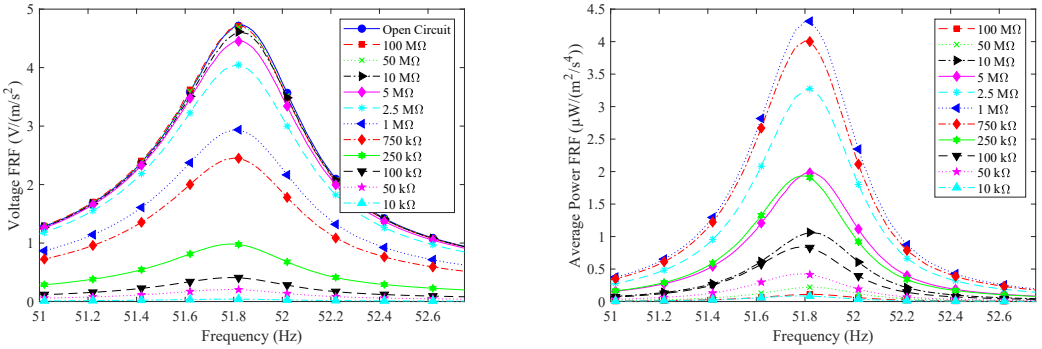

(a)

(b)

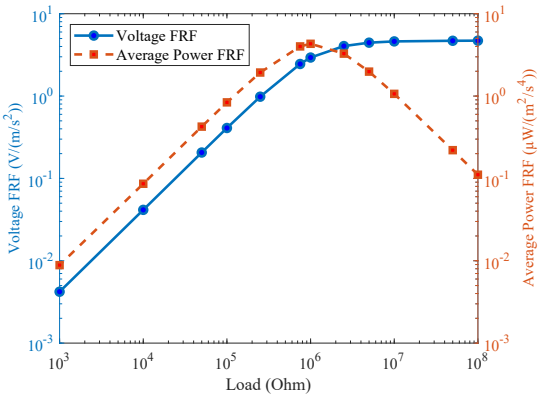

(c)

Figure F.3 Device J3′ voltage FRF (a), average power FRF (b) and outputs at peaks (c) as a function of the connected resistance. Nominal amplitude of acceleration: 1 m/s^2.

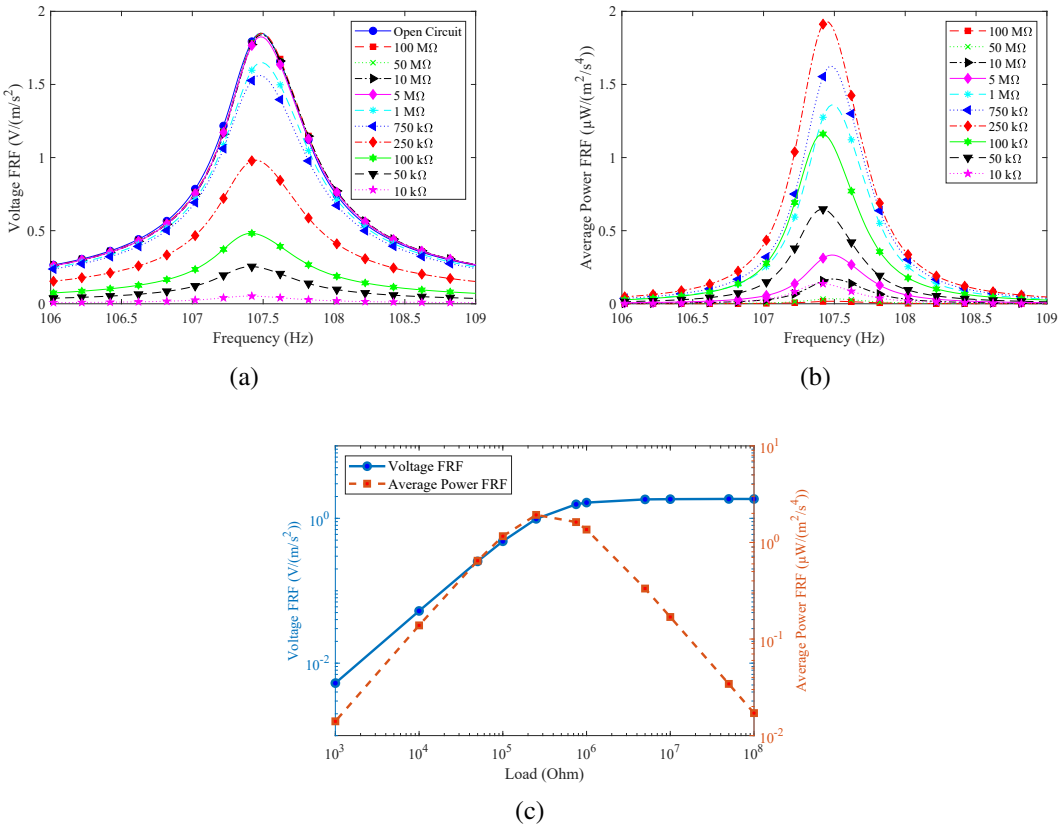

Figure F.4 Device G6 voltage FRF (a), average power FRF (b) and outputs at peaks (c) as a function of the connected resistance. Nominal amplitude of acceleration: 1 m/s^2.

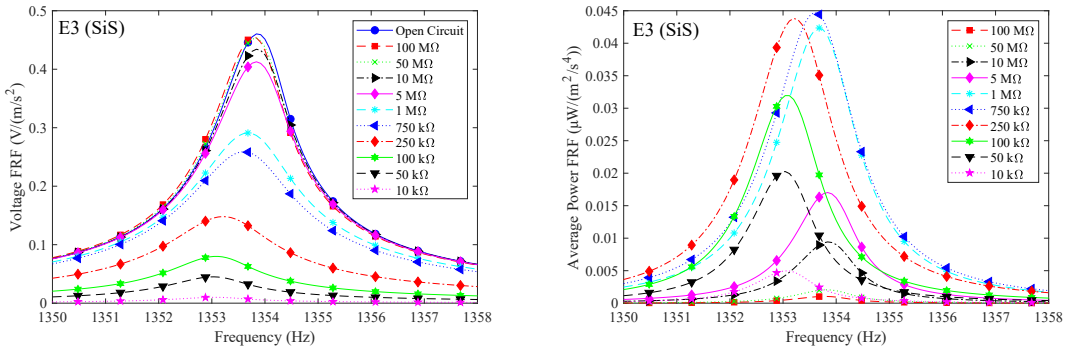

(a) (b)

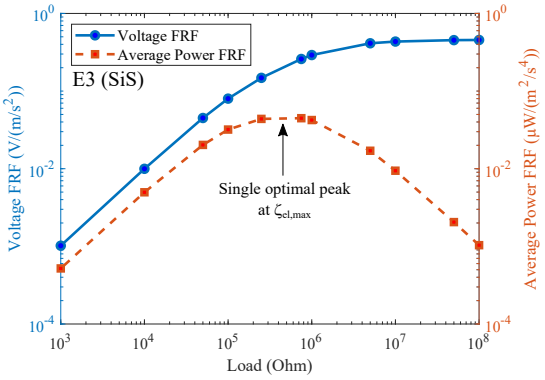

(c)

Figure F.5 Device E3 voltage FRF (a), average power FRF (b) and outputs at peaks (c) as a function of the connected resistance. Nominal amplitude of acceleration: 5 m/s^2.

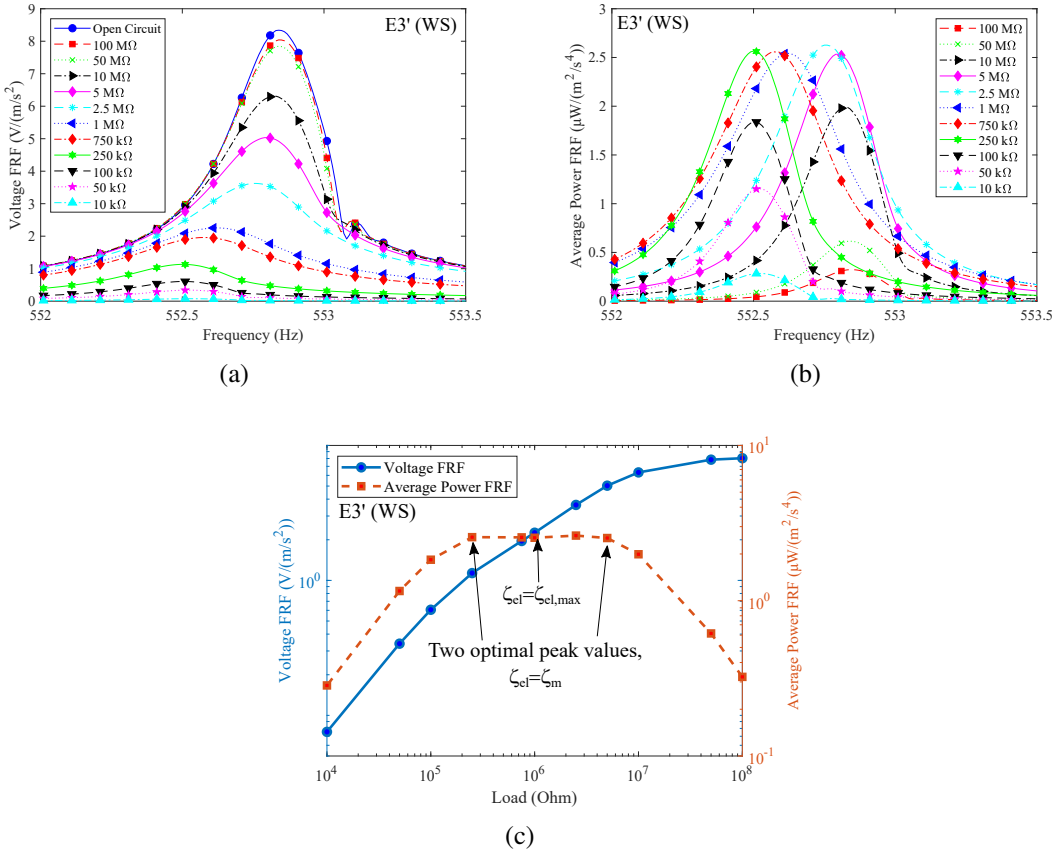

Figure F.6 Device E3′ voltage FRF (a), average power FRF (b) and outputs at peaks (c) as a function of the connected resistance. Nominal amplitude of acceleration: 0.5 m/s^2.

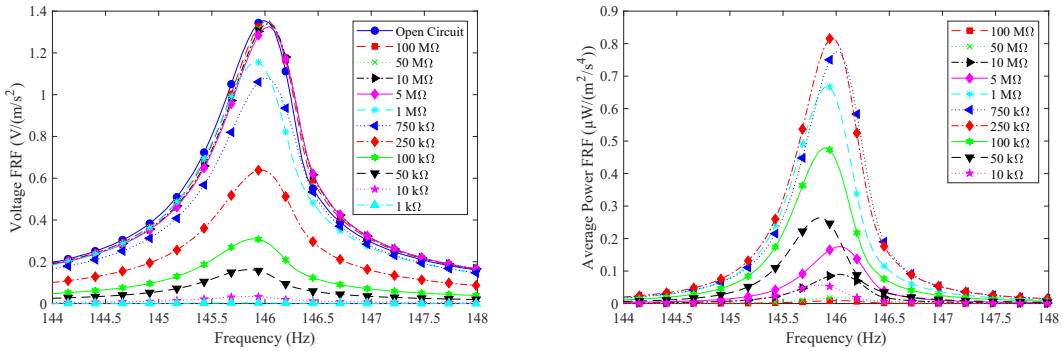

(a) (b)

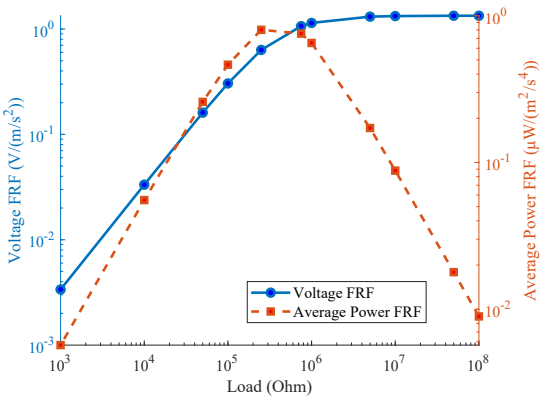

(c)

Figure F.7 Device I3 voltage FRF (a), average power FRF (b) and outputs at peaks (c) as a function of the connected resistance. Nominal amplitude of acceleration: 1 m/s^2.

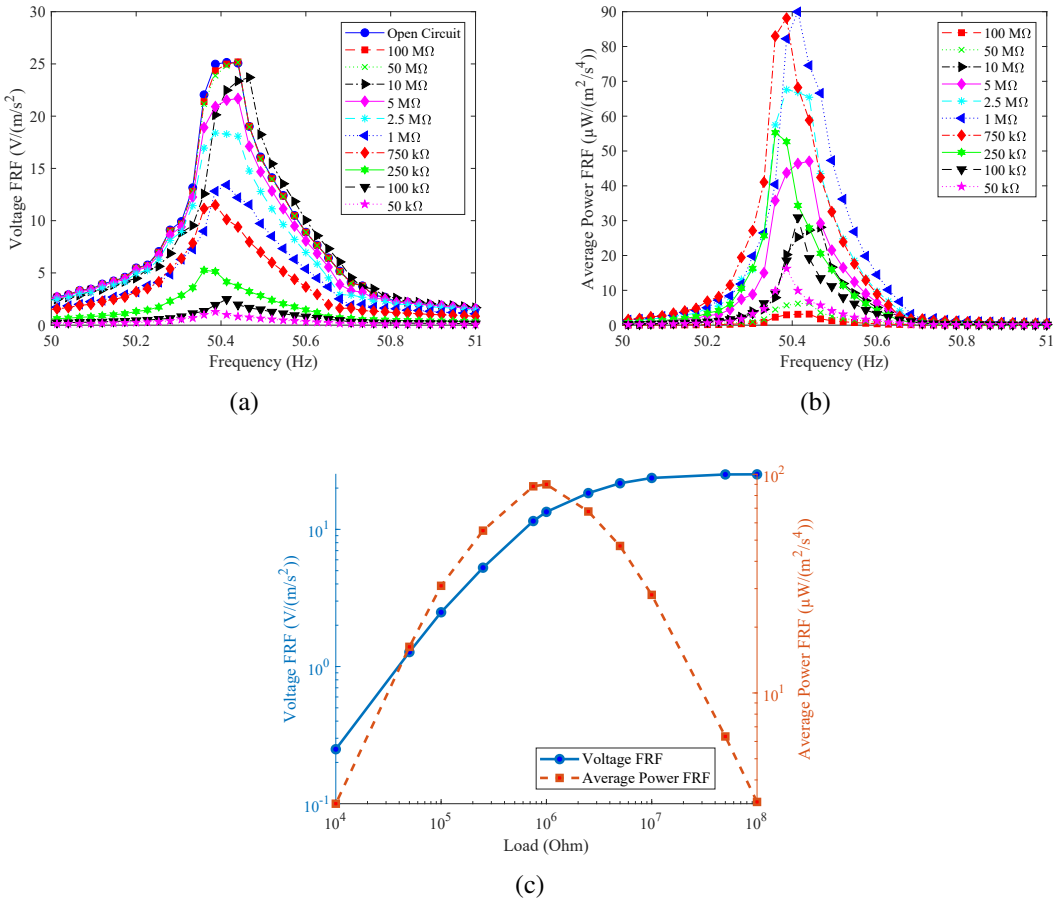

Figure F.8 Device I3′ voltage FRF (a), average power FRF (b) and outputs at peaks (c) as a function of the connected resistance. Nominal amplitude of acceleration: 0.1 m/s^2.

F.2 Voltage and power output frequency response variations with acceleration

In this section, the voltage and power outputs measured versus the frequency and at various levels of acceleration are presented for all the devices. The load is kept constant and maintained to the optimal value between runs. Contrary to the other graphs previously presented, here the results are not normalized by the input vibration to provide a direct sense of the devices outputs. Also note that the acceleration levels indicated are the nominal values (*i.e.*, away from the resonance). These results highlight how some devices exhibit nonlinearities, mainly from increased damping at higher amplitudes seen by a decreased peak sharpness. This is especially visible for devices J3 (Fig. F.10), G6 (Fig. F.12), and I3 (Fig. F.15). Figure F.14 also illustrate the point of failure observed for E3′.

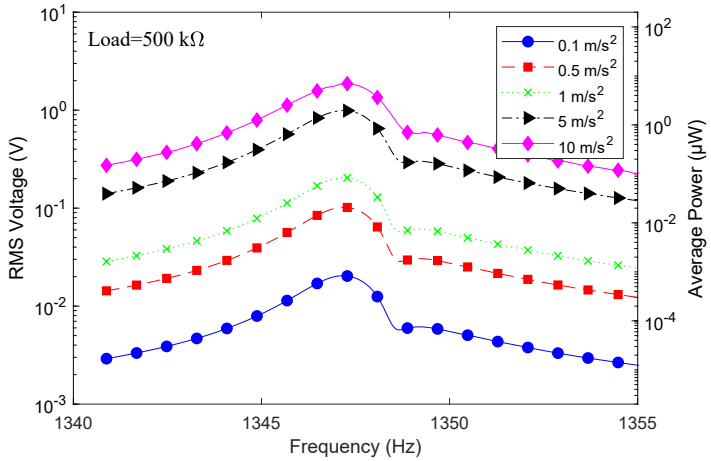

Figure F.9 Device G5 voltage and power output spectrum as a function of the acceleration (nominal).

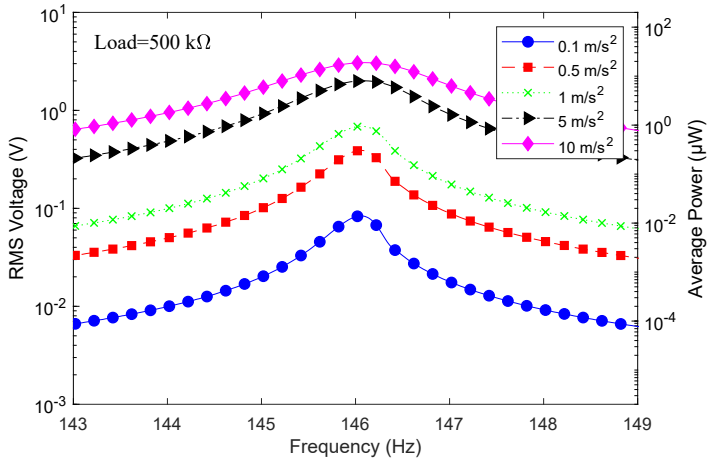

Figure F.10 Device J3 voltage and power output spectrum as a function of the acceleration (nominal).

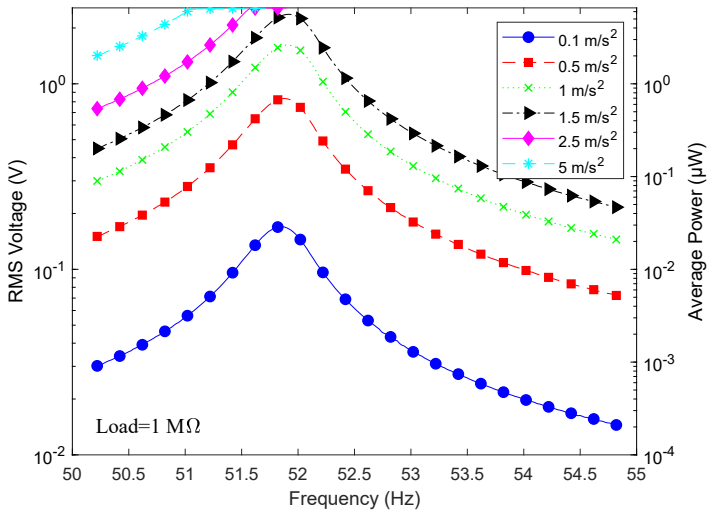

Figure F.11 Device J3′ voltage and power output spectrum as a function of the acceleration (nominal).

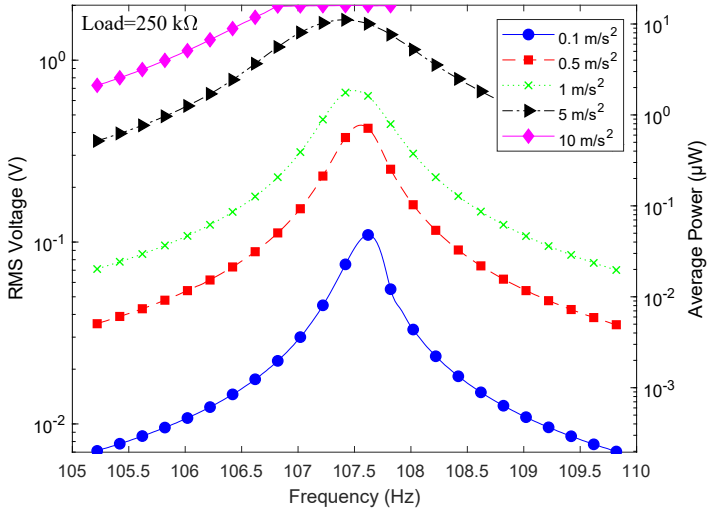

Figure F.12 Device G6 voltage and power output spectrum as a function of the acceleration (nominal).

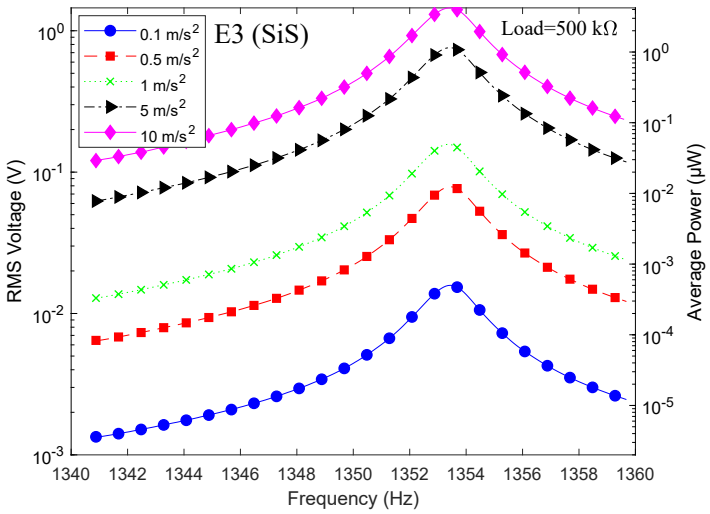

Figure F.13 Device J3′ voltage and power output spectrum as a function of the acceleration (nominal).

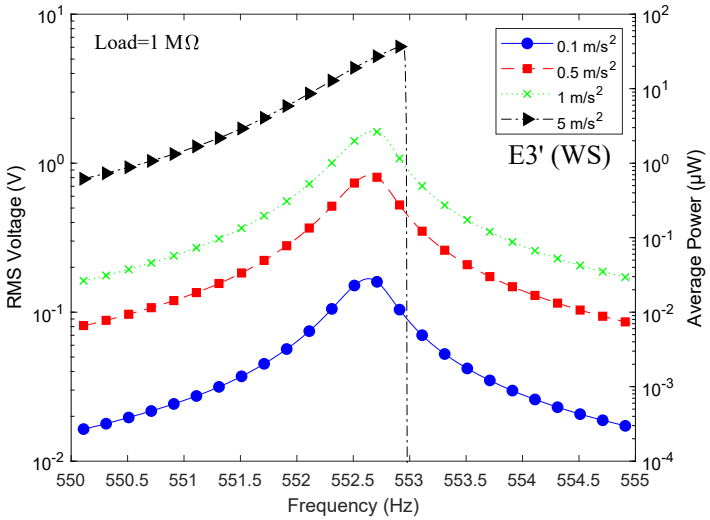

Figure F.14 Device E3′ voltage and power output spectrum as a function of the acceleration (nominal).

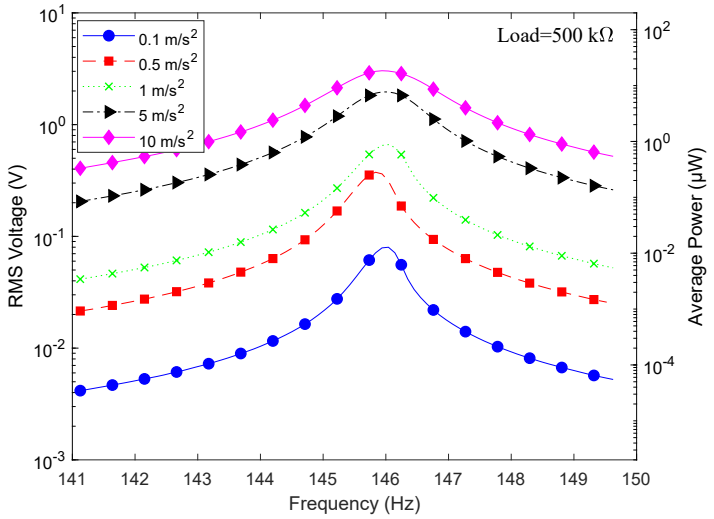

Figure F.15 Device I3 voltage and power output spectrum as a function of the acceleration (nominal).

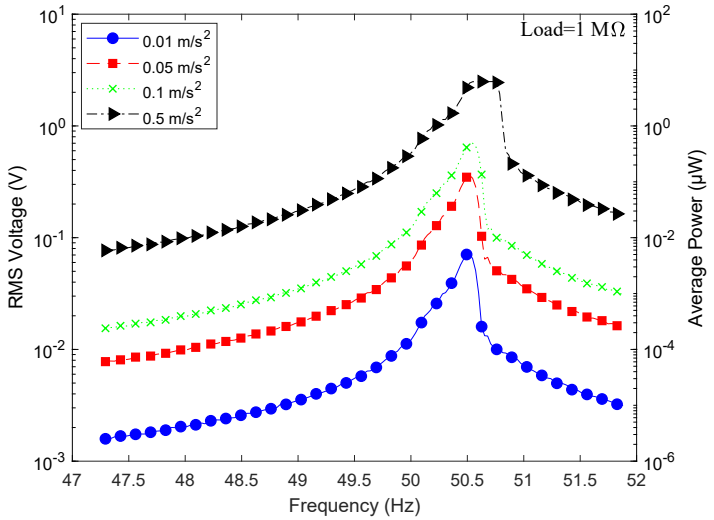

Figure F.16 Device I3′ voltage and power output spectrum as a function of the acceleration (nominal).

LIST OF REFERENCES

[1] 8power Limited. (2017) Cambridge-based 8power launches Track 200 Self-Powered Sensors for Global Wireless Applications. [Online]. Available: https://www.prnewswire.com/news-releases/cambridge-based-8power-launches-track-200-self-powered-sensors-for-global-wireless-applications-300546302.html

[2] ——. (2018) 8power - Powering the sensor revolution. [Online]. Available: https://www.8power.com/

[3] Advanced Cerametrics Inc. (2011) Advanced Cerametrics - Harvestor Power Module. [Online]. Available: http://www.advancedcerametrics.com/pages/harvestor_power_module

[4] E. E. Aktakka and K. Najafi, "A Micro Inertial Energy Harvesting Platform With Self-Supplied Power Management Circuit for Autonomous Wireless Sensor Nodes," *IEEE Journal of Solid-State Circuits*, vol. 49, no. 9, pp. 2017–2029, Sept. 2014. [Online]. Available: http://ieeexplore.ieee.org/lpdocs/epic03/wrapper.htm?arnumber=6845376

[5] E. E. Aktakka, R. L. Peterson, and K. Najafi, "Multi-layer PZT stacking process for piezoelectric bimorph energy harvesters," in *Proceedings of PowerMEMS 2011, Seoul, South Korea*, vol. 10. KAIST, 2011, p. 8000. [Online]. Available: http://cap.ee.ic.ac.uk/~pdm97/powermems/2011/Oral/5A-1.pdf

[6] E. E. Aktakka, R. L. Peterson, and K. Najafi, "Thinned-PZT on SOI process and design optimization for piezoelectric inertial energy harvesting," in *Solid-State Sensors, Actuators and Microsystems Conference (TRANSDUCERS), 2011 16th International*. IEEE, June 2011, pp. 1649–1652. [Online]. Available: http://ieeexplore.ieee.org/document/5969857/

[7] American Elements. (2018) American Elements - The Advanced Materials Manufacturer. [Online]. Available: https://www.americanelements.com/

[8] B. Ando, S. Baglio, C. Trigona, N. Dumas, L. Latorre, and P. Nouet, "Nonlinear mechanism in MEMS devices for energy harvesting applications," *Journal of Micromechanics and Microengineering*, vol. 20, no. 12, p. 125020, Dec. 2010. [Online]. Available: http://stacks.iop.org/0960-1317/20/i=12/a=125020?key=crossref.c0732cdbdb3ae4bef6fba01ec4d90738

[9] B. Ando, S. Baglio, G. L'Episcopo, and C. Trigona, "Investigation on Mechanically Bistable MEMS Devices for Energy Harvesting From Vibrations," *Journal of Microelectromechanical Systems*, vol. 21, no. 4, pp. 779–790, Aug. 2012. [Online]. Available: http://ieeexplore.ieee.org/document/6189362/

[10] R. Andosca, T. G. McDonald, V. Genova, S. Rosenberg, J. Keating, C. Benedixen, and J. Wu, "Experimental and theoretical studies on MEMS piezoelectric vibrational energy harvesters with mass loading," *Sensors and Actu-*

ators A: Physical, vol. 178, pp. 76–87, May 2012. [Online]. Available: http://linkinghub.elsevier.com/retrieve/pii/S0924424712001410

[11] J. Antonio, "Power flow in structures during steady-state forced vibration," Ph.D. dissertation, University of London, London, UK, 1984. [Online]. Available: http://hdl.handle.net/10044/1/37293

[12] APC International Ltd. Specifications of pmn-pt single crystal (pmn-32pt). [Online]. Available: http://www.americanpiezo.com/product-service/pmn-pt.html

[13] Aptek Industries. (2018) Aptek Industries Inc. [Online]. Available: http://www.wafer2chip.com/

[14] Autoenginuity.com. (2012) Enhanced Ford Module List. [Online]. Available: https://www.autoenginuity.com/images/vehicle_samples/Ford/Ford-All-Systems-List.html

[15] A. Badel, "Récupération d'énergie et contrôle vibratoire par éléments piézoélectriques suivant une approche non linéaire," Ph.D. dissertation, Université de Savoie, Chambéry, France, Oct 2005. [Online]. Available: https://tel.archives-ouvertes.fr/tel-00303823/document

[16] A. Badel, A. Benayad, E. Lefeuvre, L. Lebrun, C. Richard, and D. Guyomar, "Single crystals and nonlinear process for outstanding vibration-powered electrical generators," *IEEE transactions on ultrasonics, ferroelectrics, and frequency control*, vol. 53, no. 4, pp. 673–684, Apr. 2006.

[17] S. H. Baek, J. Park, D. M. Kim, V. A. Aksyuk, R. R. Das, S. D. Bu, D. A. Felker, J. Lettieri, V. Vaithyanathan, S. S. N. Bharadwaja, N. Bassiri-Gharb, Y. B. Chen, H. P. Sun, C. M. Folkman, H. W. Jang, D. J. Kreft, S. K. Streiffer, R. Ramesh, X. Q. Pan, S. Trolier-McKinstry, D. G. Schlom, M. S. Rzchowski, R. H. Blick, and C. B. Eom, "Giant Piezoelectricity on Si for Hyperactive MEMS," *Science*, vol. 334, no. 6058, pp. 958–961, Nov. 2011. [Online]. Available: http://www.sciencemag.org/cgi/doi/10.1126/science.1207186

[18] K. Baert, B. Gyselinckx, T. Torfs, V. Leonov, F. Yazicioglu, S. Brebels, S. Donnay, J. Vanfleteren, E. Beyne, and C. Van Hoof, "Technologies for highly miniaturized autonomous sensor networks," *Microelectronics Journal*, vol. 37, no. 12, pp. 1563–1568, Dec. 2006. [Online]. Available: http://linkinghub.elsevier.com/retrieve/pii/S0026269206001637

[19] M. Bao and H. Yang, "Squeeze film air damping in MEMS," *Sensors and Actuators A: Physical*, vol. 136, no. 1, pp. 3–27, May 2007. [Online]. Available: http://linkinghub.elsevier.com/retrieve/pii/S0924424707000118

[20] S. P. Beeby, M. J. Tudor, and N. M. White, "Energy harvesting vibration sources for microsystems applications," *Measurement Science and Technology*, vol. 17, no. 12, pp. R175–R195, Dec. 2006. [Online]. Available: http://stacks.iop.org/0957-0233/17/i=12/a=R01?key=crossref.ff55f78e312657545b6c23c0fad808ad

[21] S. Beeby, R. Torah, M. Tudor, P. Glynne-Jones, T. O'Donnell, C. Saha, and S. Roy, "A micro electromagnetic generator for vibration energy harvesting," *Journal of Micromechanics and Microengineering*, vol. 17, no. 7, p. 1257, 2007.

[22] S. P. Beeby, L. Wang, D. Zhu, A. S. Weddell, G. V. Merrett, B. Stark, G. Szarka, and B. M. Al-Hashimi, "A comparison of power output from linear and nonlinear kinetic energy harvesters using real vibration data," *Smart Materials and Structures*, vol. 22, no. 7, p. 075022, July 2013. [Online]. Available: http://stacks.iop.org/0964-1726/22/i=7/a=075022?key=crossref.64d8f3916efe442ad33bdc1422766dd6

[23] F. R. Blom, "Dependence of the quality factor of micromachined silicon beam resonators on pressure and geometry," *Journal of Vacuum Science & Technology B: Microelectronics and Nanometer Structures*, vol. 10, no. 1, p. 19, Jan. 1992. [Online]. Available: http://scitation.aip.org/content/avs/journal/jvstb/10/1/10.1116/1.586300

[24] L.-C. J. Blystad, E. Halvorsen, and S. Husa, "Piezoelectric MEMS energy harvesting systems driven by harmonic and random vibrations," *IEEE Transactions on Ultrasonics, Ferroelectrics and Frequency Control*, vol. 57, no. 4, pp. 908–919, Apr. 2010. [Online]. Available: http://ieeexplore.ieee.org/document/5442885/

[25] L. Blystad and E. Halvorsen, "An energy harvester driven by colored noise," *Smart Materials and Structures*, vol. 20, p. 025011, 2011.

[26] A. Bodensohn, R. Falsett, M. Haueis, and M. Pulvermüller, "Autonomous sensor systems for car applications," in *Advanced Microsystems for Automotive Applications 2004*, J. Valldorf and W. Gessner, Eds. Springer, 2004, ch. 3, pp. 225–232.

[27] M. G. Cain, M. Stewart, and M. Gee, "Degradation of piezoelectric materials," National Physical Lab., Tech. Rep. NPL-R-CMMT/A–148, 1999. [Online]. Available: http://inis.iaea.org/Search/search.aspx?orig_q=RN:30035183

[28] N. B. Caldwell and M. F. Daqaq, "Exploiting the principle parametric resonance of an electric oscillator for vibratory energy harvesting," *Applied Physics Letters*, vol. 110, no. 9, p. 093903, Feb. 2017. [Online]. Available: http://aip.scitation.org/doi/10.1063/1.4977835

[29] A. Cammarano, S. G. Burrow, D. A. W. Barton, A. Carrella, and L. R. Clare, "Tuning a resonant energy harvester using a generalized electrical load," *Smart Materials and Structures*, vol. 19, no. 5, p. 055003, May 2010. [Online]. Available: http://stacks.iop.org/0964-1726/19/i=5/a=055003?key=crossref.43842ffa5a797629c788511d47f49873

[30] A. Cammarano, S. A. Neild, S. G. Burrow, and D. J. Inman, "The bandwidth of optimized nonlinear vibration-based energy harvesters," *Smart Materials and Structures*, vol. 23, no. 5, p. 055019, May 2014. [Online]. Available: http://stacks.iop.org/0964-1726/23/i=5/a=055019?key=crossref.b19b6e0cb8b223005bba606c90756214

[31] B.-Y. Cao, "Non-maxwell slippage induced by surface roughness for microscale gas flow: a molecular dynamics simulation," *Molecular Physics*, vol. 105, no. 10, pp. 1403–1410,

2007.

[32] B.-Y. Cao, J. Sun, M. Chen, and Z.-Y. Guo, "Molecular momentum transport at fluid-solid interfaces in MEMS/NEMS: a review," *International journal of molecular sciences*, vol. 10, no. 11, pp. 4638–4706, 2009.

[33] H. Cao, V. H. Schmidt, R. Zhang, W. Cao, and H. Luo, "Elastic, piezoelectric, and dielectric properties of 0.58Pb(Mg1/3Nb2/3)O3-0.42PbTiO3 single crystal," *Journal of Applied Physics*, vol. 96, no. 1, pp. 549–554, July 2004. [Online]. Available: http://aip.scitation.org/doi/10.1063/1.1712020

[34] Z. Cao, J. He, Q. Wang, M. Hara, H. Oguchi, and H. Kuwano, "High output power aln vibration-driven energy harvesters," in *Journal of Physics: Conference Series*, vol. 476. IOP Publishing, 2013, p. 012034.

[35] G. Carlotti, G. Socino, A. Petri, and E. Verona, "Elastic Constants of Sputtered ZnO Films," in *IEEE 1987 Ultrasonics Symposium*. IEEE, 1987, pp. 295–300. [Online]. Available: http://ieeexplore.ieee.org/document/1535912/

[36] T. K. Caughey, "Derivation and application of the Fokker-Planck equation to discrete nonlinear dynamic systems subjected to white random excitation," *The Journal of the Acoustical Society of America*, vol. 35, no. 11, pp. 1683–1692, 1963.

[37] Ceracomp. single crystal, single crystal transducer, single crystal devices. [Online]. Available: http://www.ceracomp.com/

[38] A. Chandrasekaran, "Intra-Vehicle Channel Characterization in the 5 GHz Band," Master's thesis, Ohio University, Ohio, USA, 2011. [Online]. Available: https://etd.ohiolink.edu/pg_10?0::NO:10:P10_ETD_SUBID:61671

[39] Q. Chen, L. Qin, and Q.-M. Wang, "Property characterization of AlN thin films in composite resonator structure," *Journal of Applied Physics*, vol. 101, no. 8, p. 084103, Apr. 2007. [Online]. Available: http://aip.scitation.org/doi/10.1063/1.2716391

[40] F. Cottone, L. Gammaitoni, H. Vocca, M. Ferrari, and V. Ferrari, "Piezoelectric buckled beams for random vibration energy harvesting," *Smart Materials and Structures*, vol. 21, no. 3, p. 035021, Mar. 2012. [Online]. Available: http://stacks.iop.org/0964-1726/21/i=3/a=035021?key=crossref.97728923a5d377e5e7876b8e4754f0cf

[41] A. Cowen, G. Hames, K. Glukh, and B. Hardy, "Piezomumps design handbook," *MEMSCAP Inc*, vol. 1, 2012.

[42] M. F. Daqaq, R. Masana, A. Erturk, and D. D. Quinn, "On the role of nonlinearities in vibratory energy harvesting: a critical review and discussion," *Applied Mechanics Reviews*, vol. 66, no. 4, p. 040801, 2014.

[43] R. B. Darling, C. Hivick, and J. Xu, "Compact analytical modeling of squeeze film damping with arbitrary venting conditions using a Green's function approach," *Sensors and Actuators A: Physical*, vol. 70, no. 1-2, pp. 32–41, Oct. 1998. [Online]. Available: http://linkinghub.elsevier.com/retrieve/pii/S0924424798001095

[44] L. D. David, "Review of ferricyanide etching of molybdenum: Ozone recycling and etching at neutral pH," in *Proceedings of the Symposium on High Rate Metal Dissolution Processes*. The Electrochemical Society, 1995, pp. 316–323.

[45] L. D. David and M. T. Kurdziel, "Ozone Reoxidation of a Ferricyanide Bath for Etching Molybdenum," *Metal Finishing*, vol. 86, no. 5, pp. 47–49, 1988. [Online]. Available: http://infohouse.p2ric.org/ref/28/27995.pdf

[46] C. W. De Silva, *Vibration: fundamentals and practice*. Boca Raton, FL: CRC Press, 2000.

[47] C. W. De Silva, Ed., *Vibration and shock handbook*, ser. Mechanical engineering series. Boca Raton: Taylor & Francis, 2005.

[48] T. Delaunay, E. Le Clezio, M. Guennou, H. Dammak, Mai Pham Thi, and G. Feuillard, "Full tensorial characterization of PZN-12%PT single crystal by resonant ultrasound spectroscopy," *IEEE Transactions on Ultrasonics, Ferroelectrics and Frequency Control*, vol. 55, no. 2, pp. 476–488, Feb. 2008. [Online]. Available: http://ieeexplore.ieee.org/document/4460881/

[49] J. Dias, C. De Marqui Jr, and A. Erturk, "Hybrid piezoelectric-inductive flow energy harvesting and dimensionless electroaeroelastic analysis for scaling," *Applied Physics Letters*, vol. 102, no. 4, p. 044101, 2013.

[50] A. Dompierre and L. Fréchette, "Improvement of vibration energy harvesters mechanical Q-factor through high density proof mass integration," in *Journal of Physics: Conference Series*, vol. 773, IOP Publishing. Institute of Physics, 2016, p. 012095.

[51] A. Dompierre, M. Traore, and L. Fréchette, "Measurements of car vibrations under real-life driving conditions and assessment of energy harvesting for wireless sensor nodes," in *ASME 2013 International Mechanical Engineering Congress and Exposition*, American Society of Mechanical Engineers. American Society of American Engineers, 2013, pp. V014T15A023–V014T15A023.

[52] A. Dompierre, S. Vengallatore, and L. Fréchette, "Power density limits and benchmarking of resonant piezoelectric vibration energy harvesters," in *Novel Advances in Microsystems Technologies and Their Applications*. CRC Press, 2013, pp. 293–333.

[53] A. Dompierre, "Modélisation et conception de microrésonateurs piézoélectriques pour la récupération d'énergie vibratoire," Master's thesis, Université de Sherbrooke, Département de Génie Mécanique, Sherbrooke, Quebec, august 2011.

[54] A. Dompierre and L. Fréchette, "Inertial devices with wafer-level integration of higher density proof masses and method of manufacturing," PCT Patent WO2 018 227 308, 2018.

[55] A. Dompierre and L. G. Fréchette, "A wafer-level process for bulk tungsten integration in MEMS vibration energy harvesters and inertial sensors," in *Solid-State Sensors, Actuators and Microsystems (TRANSDUCERS), 2017 19th International Conference on*, IEEE. IEEE, 2017, pp. 2127–2130.

[56] A. Dompierre, S. Vengallatore, and L. G. Fréchette, "Compact Model Formulation and Design Guidelines for Piezoelectric Vibration Energy Harvesting with Geometric and Material Considerations," in *Proc. of the 10th Workshop on Micro and Nanotechnology for Power Generation and Energy Conversion Applications - PowerMEMS 2010 December 1-3, Leuven, Belgium, Technical Digest Poster Sessions*. Micropower Generation Group, imec/Holst Centre, December 2010, pp. 99–102.

[57] A. Dompierre, S. Vengallatore, and L. G. Fréchette, "Theoretical and practical limits of power density for piezoelectric vibration energy harvesters," in *Proceedings of PowerMEMS 2011, Seoul, South Korea*. KAIST, 2011.

[58] A. Dompierre, S. Vengallatore, and L. G. Fréchette, "Piezoelectric vibration energy harvesters: Modeling, design, limits and benchmarking," in *Energy Harvesting with Functional Materials*, M. Bhaskaran, S. Srira, and K. Iniewski, Eds. CRC Press, 2013, ch. 9, pp. 215–264.

[59] A. Dompierre, S. Vengallatore, and L. G. Fréchette, "Achieving high quality factor without vacuum packaging by high density proof mass integration in vibration energy harvesters," *Journal of Microelectromechanical Systems*, in press.

[60] eFunda. Piezo material data. [Online]. Available: http://www.efunda.com/materials/piezo/material_data/matdata_index.cfm

[61] R. Elfrink, T. M. Kamel, M. Goedbloed, S. Matova, D. Hohlfeld, Y. van Andel, and R. van Schaijk, "Vibration energy harvesting with aluminum nitride-based piezoelectric devices," *Journal of Micromechanics and Microengineering*, vol. 19, no. 9, p. 094005, Sept. 2009. [Online]. Available: http://stacks.iop.org/0960-1317/19/i=9/a=094005?key=crossref.b9d8fea7c7178e0aa602e1473194bd84

[62] R. Elfrink, S. Matova, C. de Nooijer, M. Jambunathan, M. Goedbloed, J. van de Molengraft, V. Pop, R. Vullers, M. Renaud, and R. van Schaijk, "Shock induced energy harvesting with a MEMS harvester for automotive applications," in *2011 International Electron Devices Meeting*. IEEE, Dec. 2011, pp. 29.5.1–29.5.4. [Online]. Available: http://ieeexplore.ieee.org/document/6131639/

[63] R. Elfrink, M. Renaud, T. M. Kamel, C. de Nooijer, M. Jambunathan, M. Goedbloed, D. Hohlfeld, S. Matova, V. Pop, L. Caballero, and R. van Schaijk, "Vacuum-packaged piezoelectric vibration energy harvesters: damping contributions and autonomy for a wireless sensor system," *Journal of Micromechanics and Microengineering*, vol. 20, no. 10, p. 104001, Oct. 2010. [Online]. Available: http://stacks.iop.org/0960-1317/20/i=10/a=104001?key=crossref.cb4c35b78c18adcc59261cd375c8fa00

[64] Energy Harvesting Network. (2011) Energy Harvesting Network Data Repository. [Online]. Available: http://eh-network.org/data/index.php

[65] EnOcean. (2011) Energy Harvesting Wireless Sensor Solutions and Networks from EnOcean. [Online]. Available: http://www.enocean.com/home/

[66] A. Erturk, "Electromechanical modeling of piezoelectric energy harvesters," Ph.D. dissertation, Virginia Polytechnic Institute and State University, Department of Engineering Science and Mechanics, Blacksburg, Virginia, USA, november 2009.

[67] A. Erturk, O. Bilgen, and D. J. Inman, "Power generation and shunt damping performance of a single crystal lead magnesium niobate-lead zirconate titanate unimorph: Analysis and experiment," *Applied Physics Letters*, vol. 93, no. 22, p. 224102, Dec. 2008. [Online]. Available: http://aip.scitation.org/doi/10.1063/1.3040011

[68] A. Erturk, J. Hoffmann, and D. J. Inman, "A piezomagnetoelastic structure for broadband vibration energy harvesting," *Applied Physics Letters*, vol. 94, no. 25, p. 254102, June 2009. [Online]. Available: http://aip.scitation.org/doi/10.1063/1.3159815

[69] A. Erturk and D. J. Inman, "A Distributed Parameter Electromechanical Model for Cantilevered Piezoelectric Energy Harvesters," *Journal of Vibration and Acoustics*, vol. 130, no. 4, p. 041002, 2008. [Online]. Available: http://VibrationAcoustics.asmedigitalcollection.asme.org/article.aspx?articleid=1471147

[70] A. Erturk and D. J. Inman, "Issues in mathematical modeling of piezoelectric energy harvesters," *Smart Materials and Structures*, vol. 17, no. 6, p. 065016, Dec. 2008. [Online]. Available: http://stacks.iop.org/0964-1726/17/i=6/a=065016?key=crossref.2c9ea418f2ce70369a621285b33432a8

[71] A. Erturk, P. Tarazaga, J. Farmer, and D. J. Inman, "Effect of strain nodes and electrode configuration on piezoelectric energy harvesting from cantilevered beams," *Journal of Vibration and Acoustics*, vol. 131, no. 1, p. 011010, 2009.

[72] H.-B. Fang, J.-Q. Liu, Z.-Y. Xu, L. Dong, L. Wang, D. Chen, B.-C. Cai, and Y. Liu, "Fabrication and performance of MEMS-based piezoelectric power generator for vibration energy harvesting," *Microelectronics Journal*, vol. 37, no. 11, pp. 1280–1284, Nov. 2006. [Online]. Available: http://linkinghub.elsevier.com/retrieve/pii/S0026269206001911

[73] J. Fleming and C. Barron, "Novel silicon fabrication process for high-aspect-ratio micromachined parts," *Proc. SPIE Micromachining and Microfabrication '95*, vol. 2639, p. 185, 1995. [Online]. Available: http://proceedings.spiedigitallibrary.org/pdfaccess.ashx?url=/data/conferences/spiep/58206/185_1.pdf

[74] W. J. Fleming, "Overview of automotive sensors," *IEEE sensors journal*, vol. 1, no. 4, pp. 296–308, 2001.

[75] T. Galchev, E. E. Aktakka, and K. Najafi, "A Piezoelectric Parametric Frequency Increased Generator for Harvesting Low-Frequency Vibrations," *Journal of Microelectromechanical Systems*, vol. 21, no. 6, pp. 1311–1320, Dec. 2012. [Online]. Available: http://ieeexplore.ieee.org/document/6251992/

[76] T. Galchev, H. Kim, and K. Najafi, "Micro Power Generator for Harvesting Low-Frequency and Nonperiodic Vibrations," *Journal of Microelectromechan-*

ical Systems, vol. 20, no. 4, pp. 852–866, 2011. [Online]. Available: http://ieeexplore.ieee.org/document/5961600/

[77] J. A. Geen, G. M. Molnar, G. S. Davis, B. Ma, K. J. Cole, J. Timony, and K. Flanders, "Fabrication of tungsten MEMS structures," U.S. Patent 9,878,901, 2018.

[78] G. Gloth and M. Sinapius, "Analysis of swept-sine runs during modal identification," *Mechanical systems and signal processing*, vol. 18, no. 6, pp. 1421–1441, 2004.

[79] F. Goldschmidtboeing and P. Woias, "Characterization of different beam shapes for piezoelectric energy harvesting," *Journal of Micromechanics and Microengineering*, vol. 18, no. 10, p. 104013, Oct. 2008. [Online]. Available: http://stacks.iop.org/0960-1317/18/i=10/a=104013?key=crossref.2445fd414557e8034ffc4521c2527fbe

[80] L. Gu and C. Livermore, "Impact-driven, frequency up-converting coupled vibration energy harvesting device for low frequency operation," *Smart Materials and Structures*, vol. 20, no. 4, p. 045004, 2011.

[81] D. Guyomar and M. Lallart, "Recent Progress in Piezoelectric Conversion and Energy Harvesting Using Nonlinear Electronic Interfaces and Issues in Small Scale Implementation," *Micromachines*, vol. 2, no. 4, pp. 274–294, June 2011. [Online]. Available: http://www.mdpi.com/2072-666X/2/2/274/

[82] A. Hajati, "Ultra wide-bandwidth micro energy harvester," Ph.D. dissertation, Massachusetts Institute of Technology, Department of Electrical Engineering and Computer Science, Boston, USA, february 2011.

[83] A. Hajati, S. P. Bathurst, H. J. Lee, and S. G. Kim, "Design and fabrication of a nonlinear resonator for ultra wide-bandwidth energy harvesting applications," in *2011 IEEE 24th International Conference on Micro Electro Mechanical Systems (MEMS)*, IEEE. IEEE, 2011, pp. 1301–1304.

[84] A. Haji Hosseinloo and K. Turitsyn, "Fundamental Limits to Nonlinear Energy Harvesting," *Physical Review Applied*, vol. 4, no. 6, p. 064009, Dec 2015. [Online]. Available: https://link.aps.org/doi/10.1103/PhysRevApplied.4.064009

[85] M. A. Halim and J. Y. Park, "Theoretical modeling and analysis of mechanical impact driven and frequency up-converted piezoelectric energy harvester for low-frequency and wide-bandwidth operation," *Sensors and Actuators A: Physical*, vol. 208, pp. 56–65, Feb. 2014. [Online]. Available: http://linkinghub.elsevier.com/retrieve/pii/S0924424713006316

[86] E. Halvorsen and T. Dong, "Analysis of tapered beam piezoelectric energy harvesters," in *Proceedings of PowerMEMS 2008 + microEMS 2008, Sendai, Japan, November 9-12*, 2008, pp. 241–244.

[87] E. Halvorsen, "Fundamental issues in nonlinear wideband-vibration energy harvesting," *Physical Review E*, vol. 87, no. 4, p. 042129, Apr. 2013. [Online]. Available: https://link.aps.org/doi/10.1103/PhysRevE.87.042129

[88] R. Harne and K. Wang, "A review of the recent research on vibration energy harvesting via bistable systems," *Smart materials and structures*, vol. 22, no. 2, p. 023001, 2013.

[89] T. Hehn and Y. Manoli, "Piezoelectricity and energy harvester modelling," in *CMOS Circuits for Piezoelectric Energy Harvesters*. Springer, 2015, pp. 21–40.

[90] B. Homeijer, D. Lazaroff, D. Milligan, R. Alley, J. Wu, M. Szepesi, B. Bicknell, Z. Zhang, R. Walmsley, and P. Hartwell, "Hewlett packard's seismic grade MEMS accelerometer," in *2011 IEEE 24th International Conference on Micro Electro Mechanical Systems*. IEEE, jan 2011, pp. 585–588. [Online]. Available: http://ieeexplore.ieee.org/document/5734492/

[91] H. Hosaka, K. Itao, and S. Kuroda, "Damping characteristics of beam-shaped micro-oscillators," *Sensors and Actuators A: Physical*, vol. 49, no. 1-2, pp. 87–95, June 1995. [Online]. Available: http://linkinghub.elsevier.com/retrieve/pii/092442479501003J

[92] Y. Hu, H. Xue, and H. Hu, "A piezoelectric power harvester with adjustable frequency through axial preloads," *Smart Materials and Structures*, vol. 16, p. 1961, 2007.

[93] IMEC. (2014) Compact vibration harvester power supply with highest efficiency opens door to "fix-and-forget" sensor nodes. [Online]. Available: https://phys.org/news/2014-07-compact-vibration-harvester-power-highest.html

[94] N. Izyumskaya, Y. I. Alivov, S. J. Cho, H. Morkoc, H. Lee, and Y. S. Kang, "Processing, Structure, Properties, and Applications of PZT Thin Films," *Critical Reviews in Solid State and Materials Sciences*, vol. 32, no. 3, pp. 111–202, July 2007. [Online]. Available: http://www.tandfonline.com/doi/abs/10.1080/10408430701707347

[95] H. Jaffe and D. A. Berlincourt, "Piezoelectric transducer materials," *Proceedings of the IEEE*, vol. 53, no. 10, pp. 1372–1386, Oct. 1965.

[96] Y. Jia, S. Du, and A. A. Seshia, "Twenty-Eight Orders of Parametric Resonance in a Microelectromechanical Device for Multi-band Vibration Energy Harvesting," *Scientific Reports*, vol. 6, no. 1, Sept. 2016. [Online]. Available: http://www.nature.com/articles/srep30167

[97] Y. Jia, J. Yan, K. Soga, and A. A. Seshia, "Parametrically excited MEMS vibration energy harvesters with design approaches to overcome the initiation threshold amplitude," *Journal of Micromechanics and Microengineering*, vol. 23, no. 11, p. 114007, Nov. 2013. [Online]. Available: http://stacks.iop.org/0960-1317/23/i=11/a=114007?key=crossref.9c5314d1dc23c4ee957cc7aff4ce89a5

[98] Y. Jia, J. Yan, K. Soga, and A. A. Seshia, "Parametric resonance for vibration energy harvesting with design techniques to passively reduce the initiation threshold amplitude," *Smart Materials and Structures*, vol. 23, no. 6, p. 065011, June 2014. [Online]. Available: http://stacks.iop.org/0964-1726/23/i=6/a=065011?key=crossref.f771ca44ad4e847b0c2bf6945945d246

[99] W. Jiang, R. Zhang, B. Jiang, and W. Cao, "Characterization of piezoelectric materials with large piezoelectric and electromechanical coupling coefficients," *Ul-*

trasonics, vol. 41, no. 2, pp. 55–63, Mar. 2003. [Online]. Available: http://linkinghub.elsevier.com/retrieve/pii/S0041624X02004365

[100] Jordan Novet. (2015) Venture Beat - Google has reportedly acquired sensor company Lumedyne for $85M. [Online]. Available: https://venturebeat.com/2015/06/02/google-has-reportedly-acquired-sensor-company-lumedyne-for-85m/

[101] S. Joshi, S. Hung, and S. Vengallatore, "Design strategies for controlling damping in micromechanical and nanomechanical resonators," *EPJ Techniques and Instrumentation*, vol. 1, no. 1, Dec. 2014. [Online]. Available: http://epjtechniquesandinstrumentation.springeropen.com/articles/10.1186/epjti5

[102] T. M. Kamel, R. Elfrink, M. Renaud, D. Hohlfeld, M. Goedbloed, C. de Nooijer, M. Jambunathan, and R. van Schaijk, "Modeling and characterization of MEMS-based piezoelectric harvesting devices," *Journal of Micromechanics and Microengineering*, vol. 20, no. 10, p. 105023, Oct. 2010. [Online]. Available: http://stacks.iop.org/0960-1317/20/i=10/a=105023?key=crossref.bc20b0958deceb585ed623c03c883195

[103] I. Kanno, H. Kotera, and K. Wasa, "Measurement of transverse piezoelectric properties of PZT thin films," *Sensors and Actuators A: Physical*, vol. 107, no. 1, pp. 68–74, Oct. 2003. [Online]. Available: http://linkinghub.elsevier.com/retrieve/pii/S0924424703002346

[104] H. Karadeniz, M. P. Saka, and V. Togan, "Introduction to Random Vibration and Stochastic Analysis," in *Stochastic Analysis of Offshore Steel Structures*. London: Springer London, 2013, pp. 121–176. [Online]. Available: http://link.springer.com/10.1007/978-1-84996-190-5_2

[105] A. Kasyap, "Development of MEMS-based Piezoelectric Cantilever Arrays for Vibrational Energy Harvesting," Ph.D. dissertation, University of Florida, Department of Aerospace Engineering, Mechanics and Engineering Science, Gainesville, USA, 2007.

[106] V. Kempe, *Inertial MEMS: principles and practice*. Cambridge ; New York: Cambridge University Press, 2011.

[107] M. T. Khbeis, "Development of a simplified, mass producible hybridized ambient, low frequency, low intensity vibration energy scavenger (half-lives)," Ph.D. dissertation, University of Maryland, College Park, 2010. [Online]. Available: http://drum.lib.umd.edu/handle/1903/10778

[108] D. Kobor, "Synthèse, dopage et caractérisation de monocristaux ferroélectriques type PZN-PT par la méthode du flux," Thèse doctorat, LGEF - Laboratoire de Génie Electrique et Ferroélectricité, France, 2005.

[109] K. Kokubun, M. Hirata, H. Murakami, Y. Toda, and M. Ono, "A bending and stretching mode crystal oscillator as a friction vacuum gauge," *Vacuum*, vol. 34, no. 8-9, pp. 731–735, 1984.

[110] H. Kulah and K. Najafi, "Energy Scavenging From Low-Frequency Vibrations by Using Frequency Up-Conversion for Wireless Sensor Applications," *IEEE Sen-*

sors Journal, vol. 8, no. 3, pp. 261–268, 2008. [Online]. Available: http://ieeexplore.ieee.org/document/4448348/

[111] M. Lallart and D. Guyomar, "Piezoelectric conversion and energy harvesting enhancement by initial energy injection," *Applied Physics Letters*, vol. 97, no. 1, p. 014104, July 2010. [Online]. Available: http://aip.scitation.org/doi/10.1063/1.3462304

[112] M. Lallart and D. Guyomar, "Nonlinear energy harvesting," *IOP Conference Series: Materials Science and Engineering*, vol. 18, no. 9, p. 092006, Oct. 2011. [Online]. Available: http://stacks.iop.org/1757-899X/18/i=9/a=092006?key=crossref.e55fda7b542d6ea4015a2bc080efa2fc

[113] R. Langley, "A general mass law for broadband energy harvesting," *Journal of Sound and Vibration*, vol. 333, no. 3, pp. 927–936, Feb. 2014. [Online]. Available: http://linkinghub.elsevier.com/retrieve/pii/S0022460X13007906

[114] R. Langley, "Bounds on the vibrational energy that can be harvested from random base motion," *Journal of Sound and Vibration*, vol. 339, pp. 247–261, Mar. 2015. [Online]. Available: http://linkinghub.elsevier.com/retrieve/pii/S0022460X14009092

[115] L. Lebrun, G. Sebald, B. Guiffard, C. Richard, D. Guyomar, and E. Pleska, "Investigations on ferroelectric PMN-PT and PZN-PT single crystals ability for power or resonant actuators," *Ultrasonics*, vol. 42, no. 1-9, pp. 501–505, Apr. 2004. [Online]. Available: http://linkinghub.elsevier.com/retrieve/pii/S0041624X04000459

[116] E. Lefeuvre, G. Sebald, D. Guyomar, M. Lallart, and C. Richard, "Materials, structures and power interfaces for efficient piezoelectric energy harvesting," *Journal of Electroceramics*, vol. 22, no. 1-3, pp. 171–179, Feb. 2009. [Online]. Available: http://link.springer.com/10.1007/s10832-007-9361-6

[117] Libelium. (2013) Libelium Smart World Infographic - Sensors for smart cities, Internet of Things and beyond. [Online]. Available: http://www.libelium.com/libelium-smart-world-infographic-smart-cities-internet-of-things/

[118] I. C. Lien and Y. C. Shu, "Array of piezoelectric energy harvesting by the equivalent impedance approach," *Smart Materials and Structures*, vol. 21, no. 8, p. 082001, Aug. 2012. [Online]. Available: http://stacks.iop.org/0964-1726/21/i=8/a=082001?key=crossref.dc534761d4cb31a62e61891a60bcced6

[119] I. Lien, Y. Shu, W. Wu, S. Shiu, and H. Lin, "Revisit of series-SSHI with comparisons to other interfacing circuits in piezoelectric energy harvesting," *Smart Materials and Structures*, vol. 19, no. 12, p. 125009, 2010.

[120] J.-T. Lin, B. Lee, and B. Alphenaar, "The magnetic coupling of a piezoelectric cantilever for enhanced energy harvesting efficiency," *Smart Materials and Structures*, vol. 19, no. 4, p. 045012, Apr. 2010. [Online]. Available: http://stacks.iop.org/0964-1726/19/i=4/a=045012?key=crossref.be8dca5a4dba0ddfcbd3d7de5cf3f0ac

[121] H. Liu, C. J. Tay, C. Quan, T. Kobayashi, and C. Lee, "Piezoelectric MEMS Energy Harvester for Low-Frequency Vibrations With Wideband Operation Range

and Steadily Increased Output Power," *Journal of Microelectromechanical Systems*, vol. 20, no. 5, pp. 1131–1142, Oct. 2011. [Online]. Available: http://ieeexplore.ieee.org/document/6007034/

[122] H. Liu, C. J. Tay, C. Quan, T. Kobayashi, and C. Lee, "A scrape-through piezoelectric MEMS energy harvester with frequency broadband and up-conversion behaviors," *Microsystem Technologies*, vol. 17, no. 12, pp. 1747–1754, Dec. 2011. [Online]. Available: http://link.springer.com/10.1007/s00542-011-1361-4

[123] Y. Liu, "Active energy harvesting," Ph.D. dissertation, Pennsylvania State University, Old Main, USA, 2006.

[124] N. K. Mandal, "Vibration Power Flow: A Critical Review," *The Shock and Vibration Digest*, vol. 37, no. 1, pp. 3–11, Jan. 2005. [Online]. Available: http://svd.sagepub.com/cgi/doi/10.1177/0583102404049168

[125] B. Marinkovic and H. Koser, "Smart Sand - A wide bandwidth vibration energy harvesting platform," *Applied Physics Letters*, vol. 94, no. 10, p. 103505, march 2009.

[126] M. Marzencki, "Conception de microgénérateurs intégrés pour systèmes sur puce autonomes," phdthesis, Université Joseph-Fourier - Grenoble I, Grenoble, France, Mar. 2007. [Online]. Available: https://tel.archives-ouvertes.fr/tel-00163796/document

[127] M. Marzencki, M. Defosseux, and S. Basrour, "MEMS Vibration Energy Harvesting Devices With Passive Resonance Frequency Adaptation Capability," *Journal of Microelectromechanical Systems*, vol. 18, no. 6, pp. 1444–1453, Dec. 2009. [Online]. Available: http://ieeexplore.ieee.org/document/5325874/

[128] Matweb. Online Materials Information Resource - Matweb. [Online]. Available: http://www.matweb.com/

[129] B. J. Merchant, "MEMS applications in seismology," in *Seismic Instrumentation Technology Symposium*, vol. 11, 2009.

[130] microGen, "Bolt Industrial Piezo-MEMS Vibration Energy Harvesting Products Overview," 2013. [Online]. Available: https://www.cornestech.co.jp/images/uploads/file/products/pdf/bolt.pdf

[131] microGen. (2017) News Flash! microGen Systems. [Online]. Available: https://www.microgensystems.com/wireless-sensor-solutions-acquires-microgen-systems-inc/

[132] microGen Systems. (2011) microGen Systems. [Online]. Available: http://www.microgensystems.com/

[133] microGen Systems, "AC Power Cell OPP-00002-00 Datasheet," 2016. [Online]. Available: http://www.microgensystems.com/wp-content/uploads/microGen_AC_Power_Cell_Datasheet_v1-1.pdf

[134] microGen Systems, "DC Power Cell MPC-00010-00 Datasheet," 2016. [Online]. Available: http://www.microgensystems.com/wp-content/uploads/microGen_DC_PowerCell_Flyer_v1.pdf

[135] MicroStrain, "Magnetoinductive vibration energy harvester datasheet," http://files.microstrain.com/MVEH_Datasheet_Rev_1.02d.pdf, 2011.

[136] MicroStrain, "Piezoelectric vibration energy harvester datasheet," http://files.microstrain.com/PVEH_Datasheet_Rev_1.01f.pdf, 2011.

[137] Midé. (2017) Vibration Energy Harvesting With Piezoelectrics. [Online]. Available: https://www.mide.com/collections/vibration-energy-harvesting-with-protected-piezos

[138] L. V. Minh, M. Hara, T. Yokoyama, T. Nishihara, M. Ueda, and H. Kuwano, "Highly piezoelectric mgzr co-doped aluminum nitride-based vibrational energy harvesters [correspondence]," *IEEE Transactions on Ultrasonics, Ferroelectrics, and Frequency Control*, vol. 62, no. 11, pp. 2005–2008, November 2015.

[139] P. D. Mitcheson, E. K. Reilly, T. Toh, P. K. Wright, and E. M. Yeatman, "Performance limits of the three MEMS inertial energy generator transduction types," *Journal of Micromechanics and Microengineering*, vol. 17, no. 9, pp. S211–S216, Sept. 2007. [Online]. Available: http://stacks.iop.org/0960-1317/17/i=9/a=S01?key=crossref.a869f2c9ecd2b54a1a1b0885b85933b5

[140] P. Mitcheson, T. Green, E. Yeatman, and A. Holmes, "Architectures for Vibration-Driven Micropower Generators," *Journal of Microelectromechanical Systems*, vol. 13, no. 3, pp. 429–440, June 2004. [Online]. Available: http://ieeexplore.ieee.org/document/1303621/

[141] P. Mitcheson, E. Yeatman, G. Rao, A. Holmes, and T. Green, "Energy Harvesting From Human and Machine Motion for Wireless Electronic Devices," *Proceedings of the IEEE*, vol. 96, no. 9, pp. 1457–1486, Sept. 2008. [Online]. Available: http://ieeexplore.ieee.org/document/4618735/

[142] A. Moghimi, Hsin-Mu Tsai, C. Saraydar, and O. Tonguz, "Characterizing Intra-Car Wireless Channels," *IEEE Transactions on Vehicular Technology*, vol. 58, no. 9, pp. 5299–5305, Nov. 2009. [Online]. Available: http://ieeexplore.ieee.org/document/4914870/

[143] K. Morimoto, I. Kanno, K. Wasa, and H. Kotera, "High-efficiency piezoelectric energy harvesters of c-axis-oriented epitaxial PZT films transferred onto stainless steel cantilevers," *Sensors and Actuators A: Physical*, vol. 163, no. 1, pp. 428–432, Sept. 2010. [Online]. Available: http://linkinghub.elsevier.com/retrieve/pii/S0924424710003067

[144] E. Mounier, "MEMS markets & applications focus on wireless sensor networks & energy harvesting," in *2nd Workshop on design, control and software implementation for distributed MEMS*, 2012.

[145] E. Mounier, C. Troader, G. Girardin, and J. Mouly, "Status of the MEMS industry," Yole Development," Market Report, 2016.

[146] A. G. Moura and A. Erturk, "Combined piezoelectric and flexoelectric effects in resonant dynamics of nanocantilevers," *Journal of Intelligent Material Systems and Structures*, p. 1045389X18803441, 2018.

[147] P. Muralt, J. Antifakos, M. Cantoni, R. Lanz, and F. Martin, "Is there a better material for thin film BAW applications than AlN?" in *Ultrasonics Symposium, 2005 IEEE*, vol. 1. IEEE, 2005, pp. 315–320. [Online]. Available: http://ieeexplore.ieee.org/document/1602858/

[148] P. Muralt, M. Marzencki, B. Belgacem, F. Calame, and S. Basrour, "Vibration Energy Harvesting with PZT Micro Device," *Procedia Chemistry*, vol. 1, no. 1, pp. 1191–1194, Sept. 2009. [Online]. Available: http://linkinghub.elsevier.com/retrieve/pii/S1876619609002988

[149] P. Muralt, "Piezoelectric thin films for mems," *Integrated Ferroelectrics*, vol. 17, no. 1-4, pp. 297–307, Sept. 1997. [Online]. Available: http://www.tandfonline.com/doi/abs/10.1080/10584589708013004

[150] H. Nguyen, L. Van Minh, H. Oguchi, and H. Kuwano, "High figure of merit (MgHf)x Al1-x N thin films for miniaturizing vibrational energy harvesters," in *Journal of Physics: Conference Series*, vol. 1052. IOP Publishing, 2018, p. 012018.

[151] H. H. Nguyen, H. Oguchi, and H. Kuwano, "Development of highly efficient micro energy harvesters with mghf-codoped aln piezoelectric films," in *Micro Electro Mechanical Systems (MEMS), 2018 IEEE*. IEEE, 2018, pp. 222–225.

[152] NIPS Lab. (2011) Home - Real Vibrations. [Online]. Available: http://realvibrations.nipslab.org/

[153] S. C. of the IEEE UFFCS, *IEEE Standard on Piezoelectricity*, Standards Committee of the IEEE Ultrasonics, Ferroelectrics, and Frequency Control Society Std., 1988.

[154] A. K. Pandey and R. Pratap, "Coupled nonlinear effects of surface roughness and rarefaction on squeeze film damping in MEMS structures," *Journal of micromechanics and microengineering*, vol. 14, no. 10, p. 1430, 2004.

[155] A. K. Pandey and R. Pratap, "A semi-analytical model for squeeze-film damping including rarefaction in a MEMS torsion mirror with complex geometry," *Journal of Micromechanics and Microengineering*, vol. 18, no. 10, p. 105003, 2008.

[156] J. Peng, H. Luo, T. He, H. Xu, and D. Lin, "Elastic, dielectric, and piezoelectric characterization of 0.70Pb(Mg1/3Nb2/3)O3-0.30PbTiO3 single crystals," *Materials Letters*, vol. 59, no. 6, pp. 640–643, Mar. 2005. [Online]. Available: http://linkinghub.elsevier.com/retrieve/pii/S0167577X04008006

[157] M. Perlmutter and L. Robin, "High-performance, low cost inertial MEMS: A market in motion!" in *Proceedings of the 2012 IEEE/ION Position, Location and Navigation Symposium*. IEEE, April 2012, pp. 225–229.

[158] Perpetuum. (2013) The World Leader in Vibration Harvester Powered Wireless Sensing Systems. [Online]. Available: https://perpetuum.com/about/

[159] Perpetuum, "Vibration Energy Harvesters - PMG Perpetuum," 2013. [Online]. Available: https://perpetuum2016.files.wordpress.com/2016/09/perpetuum-ltd-vibration-energy-harvester-data-sheet-21october2013.pdf

[160] G. Petit Bois, *Tables of indefinite integrals*, ser. Dover books. New York: Dover Publ, 1961, no. S225, oCLC: 845481992.

[161] K. L. Phan, P. G. Steeneken, M. J. Goossens, G. E. J. Koops, G. J. A. M. Verheijden, and J. T. M. van Beek, "Spontaneous mechanical oscillation of a DC driven single crystal," *Nature Physics*, vol. 7, no. 4, pp. 354–359, Apr. 2011, arXiv: 0904.3748. [Online]. Available: http://arxiv.org/abs/0904.3748

[162] PI. Pi piezo tutorial: Mechanical considerations. [Online]. Available: http://www.physikinstrumente.com/tutorial/4_22.html

[163] K. S. J. Pister, "Smart dust," UC Berkeley, Tech. Rep. BAA 97-43, Oct. 1997. [Online]. Available: https://people.eecs.berkeley.edu/~pister/SmartDust/SmartDustBAA97-43-Abstract.pdf

[164] A. Preumont, *Random Vibration and Spectral Analysis*, ser. Solid Mechanics and Its Applications. Dordrecht: Springer Netherlands, 1994, vol. 33. [Online]. Available: http://link.springer.com/10.1007/978-94-017-2840-9

[165] A. Preumont, *Random Vibration and Spectral Analysis/Vibrations aléatoires et analyse spectral*. Springer Science & Business Media, 2013, vol. 33.

[166] Printed Electronics World. (2009) Vibration energy harvester. [Online]. Available: https://www.printedelectronicsworld.com/articles/1491/vibration-energy-harvester

[167] A. Rahafrooz and S. Pourkamali, "Thermal-Piezoresistive Energy Pumps in Micromechanical Resonant Structures," *IEEE Transactions on Electron Devices*, vol. 59, no. 12, pp. 3587–3593, Dec. 2012.

[168] M. Renaud, R. Elfrink, M. Jambunathan, C. de Nooijer, Z. Wang, M. Rovers, R. Vullers, and R. van Schaijk, "Optimum power and efficiency of piezoelectric vibration energy harvesters with sinusoidal and random vibrations," *Journal of Micromechanics and Microengineering*, vol. 22, no. 10, p. 105030, Oct. 2012. [Online]. Available: http://stacks.iop.org/0960-1317/22/i=10/a=105030?key=crossref.86765576fb5de5a2bfdc4567d9b61bee

[169] M. Renaud, R. Elfrink, B. Op het Veld, and R. van Schaijk, "Power Optimization Using Resonance and Antiresonance of MEMS Piezoelectric Vibration Energy Harverters," in *Proc. of the 10th Workshop on Micro and Nanotechnology for Power Generation and Energy Conversion Applications - PowerMEMS 2010 December 1-3, Leuven, Belgium, Technical Digest Oral Sessions*. Micropower Generation Group, imec/Holst Centre, December 2010, pp. 23–26.

[170] M. Renaud, P. Fiorini, R. van Schaijk, and C. van Hoof, "Harvesting energy from the motion of human limbs: the design and analysis of an impact-based piezoelectric generator," *Smart Materials and Structures*, vol. 18, no. 3, p. 035001, Mar. 2009. [Online]. Available: http://stacks.iop.org/0964-1726/18/i=3/a=035001?key=crossref.628c5b92432c62e08a2c6b72b767a2f6

[171] J. M. Renno, M. F. Daqaq, and D. J. Inman, "On the optimal energy harvesting from a vibration source," *Journal of Sound and Vibration*, vol. 320, no. 1-2, pp. 386–405, Feb. 2009. [Online]. Available: http://linkinghub.elsevier.com/retrieve/pii/S0022460X0800669X

[172] ReVibe Energy. (2018) ReVibe Energy - Powering the industrial IoT. [Online]. Available: https://revibeenergy.com/

[173] C. D. Richards, M. J. Anderson, D. F. Bahr, and R. F. Richards, "Efficiency of energy conversion for devices containing a piezoelectric component," *Journal of Micromechanics and Microengineering*, vol. 14, no. 5, pp. 717–721, May 2004. [Online]. Available: http://stacks.iop.org/0960-1317/14/i=5/a=009?key=crossref.b0d1820ab31fd21d102108ca1e7d4f6a

[174] S. Roundy, "On the Effectiveness of Vibration-based Energy Harvesting," *Journal of Intelligent Material Systems and Structures*, vol. 16, no. 10, pp. 809–823, Oct. 2005. [Online]. Available: http://jim.sagepub.com/cgi/doi/10.1177/1045389X05054042

[175] S. Roundy and P. K. Wright, "A piezoelectric vibration based generator for wireless electronics," *Smart Materials and Structures*, vol. 13, no. 5, pp. 1131–1142, Oct. 2004. [Online]. Available: http://stacks.iop.org/0964-1726/13/i=5/a=018?key=crossref.8cb539ef2c04efdc61df2fae9dc8e48c

[176] S. Roundy, P. K. Wright, and J. Rabaey, "A study of low level vibrations as a power source for wireless sensor nodes," *Computer Communications*, vol. 26, no. 11, pp. 1131–1144, july 2003. [Online]. Available: http://dx.doi.org/10.1016/S0140-3664(02)00248-7

[177] S. Roundy and Y. Zhang, "Toward self-tuning adaptive vibration-based microgenerators," in *Smart Structures, Devices, and Systems II*, vol. 5649, International Society for Optics and Photonics. SPIE, 2005, pp. 373–385.

[178] S. J. Roundy, "Energy Scavenging for Wireless Sensor Nodes with a Focus on Vibration to Electricity Conversion," Ph.D. dissertation, University of California, Berkeley, CA, USA, 2003, google-Books-ID: qpduGwAACAAJ.

[179] P. Salvo, R. Verplancke, F. Bossuyt, D. Latta, B. Vandecasteele, C. Liu, and J. Vanfleteren, "Adhesive bonding by su-8 transfer for assembling microfluidic devices," *Microfluidics and nanofluidics*, vol. 13, no. 6, pp. 987–991, 2012.

[180] T. Schumacher, M. Stadelmayer, T. Faseth, and H. Pretl, "A review of ultra-low-power and low-cost transceiver design," in *Microelectronics (Austrochip), 2017 Austrochip Workshop on*, IEEE. IEEE, 2017, pp. 29–34.

[181] G. Sebald, H. Kuwano, D. Guyomar, and B. Ducharne, "Experimental Duffing oscillator for broadband piezoelectric energy harvesting," *Smart Materials and Structures*, vol. 20, no. 10, p. 102001, Oct. 2011. [Online]. Available: http://stacks.iop.org/0964-1726/20/i=10/a=102001?key=crossref.31a21cd6ac9c177dcfd2485fc5a49abf

[182] G. Sebald, H. Kuwano, D. Guyomar, and B. Ducharne, "Simulation of a Duffing oscillator for broadband piezoelectric energy harvesting," *Smart Materials and Structures*, vol. 20, no. 7, p. 075022, July 2011. [Online]. Available: http://stacks.iop.org/0964-1726/20/i=7/a=075022?key=crossref.9634269f540c2c51d74583e59e2c2c9e

[183] Seung-Eek Park and T. Shrout, "Characteristics of relaxor-based piezoelectric single crystals for ultrasonic transducers," in *IEEE Transactions on Ultrasonics, Ferroelectrics, and Frequency Control*, vol. 2. IEEE, 1996, pp. 935–942. [Online]. Available: http://ieeexplore.ieee.org/document/584146/

[184] T. A. Shankoff, "High Resolution Tungsten Patterning Using Buffered, Mildly Basic Etching Solutions," *Journal of The Electrochemical Society*, vol. 122, no. 2, p. 294, 1975. [Online]. Available: http://jes.ecsdl.org/cgi/doi/10.1149/1.2134198

[185] D. Shen, J.-H. Park, J. Ajitsaria, S.-Y. Choe, H. C. Wikle, and D.-J. Kim, "The design, fabrication and evaluation of a MEMS PZT cantilever with an integrated Si proof mass for vibration energy harvesting," *Journal of Micromechanics and Microengineering*, vol. 18, no. 5, p. 055017, May 2008. [Online]. Available: http://stacks.iop.org/0960-1317/18/i=5/a=055017?key=crossref.e4feca47995d41b2d45d8112136294ad

[186] Y. C. Shu and I. C. Lien, "Efficiency of energy conversion for a piezoelectric power harvesting system," *Journal of Micromechanics and Microengineering*, vol. 16, no. 11, pp. 2429–2438, Nov. 2006. [Online]. Available: http://stacks.iop.org/0960-1317/16/i=11/a=026?key=crossref.b7add69dfcb3c8a33eaeb63109054caa

[187] Y. Shu, I. Lien, and W. Wu, "An improved analysis of the SSHI interface in piezoelectric energy harvesting," *Smart Materials and Structures*, vol. 16, p. 2253, 2007.

[188] J. Siang, M. Lim, and M. Salman Leong, "Review of vibration-based energy harvesting technology: Mechanism and architectural approach," *International Journal of Energy Research*, vol. 42, no. 5, pp. 1866–1893, 2018.

[189] M. Soliman, "Wideband Micro-Power Generators for Vibration Energy Harvesting," Ph.D. dissertation, University of Waterloo, Waterloo, Ontario, Canada, Aug. 2009. [Online]. Available: https://uwspace.uwaterloo.ca/handle/10012/4584

[190] L. Song, N. Li, S. Zhang, J. Luo, J. Hu, Y. Zhang, S. Chen, and J. Chen, "Inductively coupled plasma etching of bulk tungsten for MEMS applications," in *2014 IEEE 27th International Conference on Micro Electro Mechanical Systems (MEMS)*. IEEE, Jan. 2014, pp. 502–505. [Online]. Available: http://ieeexplore.ieee.org/document/6765687/

[191] M. Sridi, "Développement d'un système d'alimentation d'un noeud de capteur sans fils à partir d'un récupérateur piézoélectrique pour des applications dans l'automobile," Master's thesis, Université de Sherbrooke, Sherbrooke, Canada, 2014.

[192] M. Stamos, N. Nicoleau, R. Torah, J. Tudor, N. R. Harris, A. Niewiadomski, and S. P. Beeby, "Screen printed piezoelectric generator for helicopter health and usage monitoring systems," in *8th International Workshop on Micro and Nanotechnology for Power Generation and Energy Conversion Applications (PowerMEMS 2008)*, 2008, p. 4. [Online]. Available: https://eprints.soton.ac.uk/266982/

[193] S. C. Stanton, B. A. Owens, and B. P. Mann, "Harmonic balance analysis of the bistable piezoelectric inertial generator," *Journal of Sound and Vibration*, vol. 331, no. 15, pp. 3617–3627, 2012.

[194] M. Stewart, P. M. Weaver, and M. Cain, "Charge redistribution in piezoelectric energy harvesters," *Applied Physics Letters*, vol. 100, no. 7, p. 073901, Feb. 2012. [Online]. Available: http://aip.scitation.org/doi/10.1063/1.3685701

[195] A. Tabesh and L. G. Fréchette, "On the concepts of electrical damping and stiffness in design of a piezoelectric bending beam energy harvester," *Proc. Power MEMS 2009*, pp. 368–371, 2009.

[196] W. T. Thomson, "The response of mechanical systems to random excitation," Thompson Ramo Wooldridge Inc., Tech. Rep. AM-5-13, Nov. 1955. [Online]. Available: http://www.dtic.mil/docs/citations/AD0607716

[197] M. M. Torunbalci, E. C. Demir, I. Donmez, S. E. Alper, and T. Akin, "Gold-tin eutectic bonding for hermetic packaging of MEMS devices with vertical feedthroughs," in *SENSORS, 2014 IEEE*, IEEE. IEEE, 2014, pp. 2187–2190.

[198] S. Trolier-McKinstry, F. Griggio, C. Yaeger, P. Jousse, Dalong Zhao, S. S. N. Bharadwaja, T. N. Jackson, S. Jesse, S. V. Kalinin, and K. Wasa, "Designing piezoelectric films for micro electromechanical systems," *IEEE Transactions on Ultrasonics, Ferroelectrics and Frequency Control*, vol. 58, no. 9, pp. 1782–1792, Sept. 2011. [Online]. Available: http://ieeexplore.ieee.org/document/6020846/

[199] S. Trolier-McKinstry and P. Muralt, "Thin Film Piezoelectrics for MEMS," *Journal of Electroceramics*, vol. 12, no. 1/2, pp. 7–17, Jan. 2004. [Online]. Available: http://link.springer.com/10.1023/B:JECR.0000033998.72845.51

[200] H.-M. Tsai, "Intra-car Wireless Sensor Networks," Ph.D. dissertation, Carnegie Mellon University, Pittsburgh, PA, USA, 2010.

[201] Y. Tsujiura, E. Suwa, F. Kurokawa, H. Hida, K. Suenaga, K. Shibata, and I. Kanno, "Lead-free piezoelectric MEMS energy harvesters of (k, na) nbo3 thin films on stainless steel cantilevers," *Japanese Journal of Applied Physics*, vol. 52, no. 9S1, p. 09KD13, 2013.

[202] Valley Design. (2018) Optical Polishing, Lapping, Dicing and Optical Components Polishing Services. [Online]. Available: http://www.valleydesign.com/

[203] T. Veijola, A. Pursula, and P. Råback, "Extending the validity of squeezed-film damper models with elongations of surface dimensions," *Journal of Micromechanics and Microengineering*, vol. 15, no. 9, pp. 1624–1636, Sept.

2005. [Online]. Available: http://stacks.iop.org/0960-1317/15/i=9/a=003?key=crossref.35582dbfa7365cd9e315b421161a7abb

[204] T. Veijola, H. Kuisma, J. Lahdenperä, and T. Ryhänen, "Equivalent-circuit model of the squeezed gas film in a silicon accelerometer," *Sensors and Actuators A: Physical*, vol. 48, no. 3, pp. 239–248, 1995.

[205] R. Vullers, R. van Schaijk, I. Doms, C. Van Hoof, and R. Mertens, "Micropower energy harvesting," *Solid-State Electronics*, vol. 53, no. 7, pp. 684–693, July 2009. [Online]. Available: http://linkinghub.elsevier.com/retrieve/pii/S0038110109000720

[206] R. Vullers, R. van Schaijk, M. Goedbloed, R. Elfrink, Z. Wang, and C. Van Hoof, "Process challenges of MEMS harvesters and their effect on harvester performance," in *2011 International Electron Devices Meeting*. IEEE, Dec. 2011, pp. 10.2.1–10.2.4. [Online]. Available: http://ieeexplore.ieee.org/document/6131526/

[207] H. Wang and Q. Meng, "Analytical modeling and experimental verification of vibration-based piezoelectric bimorph beam with a tip-mass for power harvesting," *Mechanical Systems and Signal Processing*, vol. 36, no. 1, pp. 193–209, 2013.

[208] X. Wang, "Vehicle vibration measurement and analysis," in *Vehicle Noise and Vibration Refinement*. Elsevier, 2010, pp. 33–67.

[209] Z. Wang and Y. Xu, "Vibration energy harvesting device based on air-spaced piezoelectric cantilevers," *Applied Physics Letters*, vol. 90, no. 26, pp. 263 512–263 512, 2007.

[210] K. Wasa, S. Ito, K. Nakamura, T. Matsunaga, I. Kanno, T. Suzuki, H. Okino, T. Yamamoto, S. H. Seo, and D. Y. Noh, "Electromechanical coupling factors of single-domain 0.67Pb(Mg13Nb23)O3-0.33PbTiO3 single-crystal thin films," *Applied Physics Letters*, vol. 88, no. 12, p. 122903, Mar. 2006. [Online]. Available: http://aip.scitation.org/doi/10.1063/1.2188588

[211] K. Wasa, T. Matsushima, H. Adachi, I. Kanno, and H. Kotera, "Thin-Film Piezoelectric Materials For a Better Energy Harvesting MEMS," *Journal of Microelectromechanical Systems*, vol. 21, no. 2, pp. 451–457, Apr. 2012. [Online]. Available: http://ieeexplore.ieee.org/document/6142000/

[212] A. C. Waterbury and P. K. Wright, "Vibration energy harvesting to power condition monitoring sensors for industrial and manufacturing equipment," *Proceedings of the Institution of Mechanical Engineers, Part C: Journal of Mechanical Engineering Science*, vol. 227, no. 6, pp. 1187–1202, 2013.

[213] R. L. Waters, P. M. Sullivan, and B. R. Hunt, "Micro-electro-mechanical system (MEMS) and apparatus for generating power responsive to mechanical vibration," U.S. Patent 7,501,726, Mar. 10, 2009.

[214] Wikipedia. (2012, March) Energy Harvesting. [Online]. Available: http://en.wikipedia.org/wiki/Energy_harvesting

[215] C. B. Williams and R. B. Yates, "Analysis of a micro-electric generator for microsystems," *Sensors and Actuators A: Physical*, vol. 52, no. 1-3, pp. 8–11, 1996.

[216] S. S. Won, J. Lee, V. Venugopal, D.-J. Kim, J. Lee, I. W. Kim, A. I. Kingon, and S.-H. Kim, "Lead-free Mn-doped (K0.5, Na0.5) NbO3 piezoelectric thin films for MEMS-based vibrational energy harvester applications," *Applied Physics Letters*, vol. 108, no. 23, p. 232908, 2016.

[217] M. Xie, K. C. Aw, and W. Gao, "Polydimethylsiloxane structure as a broadband vibrational energy harvester," in *2014 IEEE/ASME International Conference on Advanced Intelligent Mechatronics (AIM)*. IEEE, July 2014, pp. 766–770. [Online]. Available: http://ieeexplore.ieee.org/document/6878171/

[218] D. Yamane, T. Matsushima, T. Konishi, H. Toshiyoshi, K. Masu, and K. Machida, "A dual-axis MEMS capacitive inertial sensor with high-density proof mass," *Microsystem Technologies*, vol. 22, no. 3, pp. 459–464, Mar. 2016. [Online]. Available: http://link.springer.com/10.1007/s00542-015-2539-y

[219] T.-T. Yen, T. Hirasawa, P. K. Wright, A. P. Pisano, and L. Lin, "Corrugated aluminum nitride energy harvesters for high energy conversion effectiveness," *Journal of Micromechanics and Microengineering*, vol. 21, no. 8, p. 085037, Aug. 2011. [Online]. Available: http://stacks.iop.org/0960-1317/21/i=8/a=085037?key=crossref.53208445bd6fea4157a2650cd97048d5

[220] L. Yu, F. E. H. Tay, G. Xu, B. Chen, M. Avram, and C. Iliescu, "Adhesive bonding with SU-8 at wafer level for microfluidic devices," *Journal of Physics: Conference Series*, vol. 34, pp. 776–781, Apr. 2006. [Online]. Available: http://stacks.iop.org/1742-6596/34/i=1/a=128?key=crossref.382f53c3293277d7594990b733d9fd5d

[221] R. Zhang, "Elastic, Dielectric and Piezoelctric Coefficients of Domain Engineered 0.70Pb(Mg1/3Nb2/3)O3-0.30PbTiO3 Single Crystal," in *AIP conference proceedings*, vol. 626. AIP, 2002, pp. 188–197. [Online]. Available: http://aip.scitation.org/doi/abs/10.1063/1.1499567

[222] R. Zhang, B. Jiang, and W. Cao, "Elastic, piezoelectric, and dielectric properties of multidomain 0.67Pb(Mg1/3Nb2/3)O3-0.33PbTiO3 single crystals," *Journal of Applied Physics*, vol. 90, no. 7, pp. 3471–3475, Oct. 2001. [Online]. Available: http://aip.scitation.org/doi/10.1063/1.1390494

[223] R. Zhang, B. Jiang, W. Jiang, and W. Cao, "Complete set of elastic, dielectric, and piezoelectric coefficents of 0.93Pb(Zn13Nb2/3)O3-0.07PbTiO3 single crystal poled along [011]," *Applied Physics Letters*, vol. 89, no. 24, p. 242908, Dec. 2006. [Online]. Available: http://aip.scitation.org/doi/10.1063/1.2404613

[224] X. Zhang and M. W. Judy, "Silicon-based MEMS devices including wells embedded with high density metal," U.S. Patent 14/695,421, June 23, 2016.

[225] D. Zhu, S. P. Beeby, M. J. Tudor, and N. R. Harris, "A credit card sized self powered smart sensor node," *Sensors and Actuators A: Physical*, vol. 169, no. 2, pp. 317–325, Oct. 2011.

[Online]. Available: http://linkinghub.elsevier.com/retrieve/pii/S0924424711000574